# PROBING THE SOLID-LIQUID INTERFACE OF FLUORINATED THIN FILMS WITH SUM FREQUENCY GENERATION SPECTROSCOPY

A Dissertation Presented to

the Faculty of the Department of Chemistry

University of Houston

In Partial Fulfillment

of the Requirements for the Degree of

Doctor of Philosophy

By

Daniela Deleon

May 2019

# PROBING THE SOLID-LIQUID INTERFACE OF FLUORINATED THIN FILMS WITH SUM FREQUENCY GENERATION SPECTROSCOPY

_____
Daniela Deleon

APPROVED:

_____
Dr. T. Randall Lee, Chairman

_____
Dr. Steven Baldelli

_____
Dr. Ding-Shyue Yang

_____
Dr. Jakoah Brgoch

_____
Dr. Janelle Pennington

_____
Dr. Dan E. Wells, Dean, College of Natural Sciences and Mathematics

***Dedicated to my husband, parents, and sisters,***

***David Deleon, J. Paulo Rodríguez, Aleyda Murillo, Ariana, Valeria, and Melissa***

***For the love and the outstanding support during my***

***Academic endeavor.***

# ACKNOWLEDGMENTS

I must first acknowledge my Lord and Savior Jesus Christ without whom I would have never made it this far in life. My deepest thanks are for my advisors Dr. T. Randall Lee and Dr. Steven Baldelli for teaching me how to be a scientist and guiding me in my journey through graduate school. Thank you for taking me in as a student and supporting me as I earned my degree. I would also like to thank my committee, Dr. Yang, Dr. Brgoch, and Dr. Pennington for taking the time to provide feedback on my dissertation and attend my defense.

I would like to acknowledge Dr. Maria D. Marquez for the synthesis of the D1F6H10SH adsorbate in Chapter 3 and the characterization of the self-assembled monolayers in Chapter 5. I would also like to thank her for being my constant collaborator, for editing this dissertation, and for being my sweet friend and teaching me so much over the years. I would like to credit Thong Li for gathering the Raman spectra used throughout my studies, Dr. Oussama Zenasni for the synthesis of several fluorinated thiols used in these studies, Dr. Han Ju Lee for the synthesis of the adsorbates used in Chapter 4 of this dissertation, and Long Han for helping with the synthesis of the D1F6H10SH thiol. I would like to thank my friend Dr. Zhe (Joshua) Sun for all the fun conversations we had while we waited on our spectra to run, for teaching me/helping me so much with my work, and for his constant encouragement over the past six years. I would like to thank the all the people in the Baldelli and Lee groups who helped me in my Ph.D. journey. I would like to thank Jack, Ming, and Dien, for teaching me how to do electrochemistry, align the laser systems, run SFG spectra, showing me around the lab as

first year, and being my good friends. I will always treasure the memories of Ming singing to me and Dien yelling at him to stop. I would also like to thank Dillon, Shah, and Alex for chatting with me while we worked in the lab and making me laugh when the laser inevitably died or something went wrong with my experiments. I will be forever grateful for their friendship and conversation. Thank you to Anjeeta, Thong, Lisa, Hao, Yu Wei and Michelle for supporting me in the lab and helping me whenever I asked. In the Lee group, "the family we chose", I want to thank Oussama and Chris for teaching me how to do thorough research, and Amin and Johnson for always making me laugh. I appreciate the kindness of Han Ju who taught me about the evaporator and Chulsoon who was just so silly but hardworking at the same time. I want to thank the rest of the group, specifically Ging, Yi-Ting (Princess), Arati, Ting Ting, Sam, Riddhiman, Ploy, Will (Youngblood), Hung, and Mario for always supporting me and being my friends. I will always treasure the fun times we had in and out of the lab. Of course, I must also acknowledge Turkey the turtle, who was my constant companion during the long days and nights while I worked in the lab.

Finally, I would like to thank my husband, David, and my family and for supporting me in this very long process and always being there when I needed them most. I love you all very much and I could have never made it through so much school without your constant encouragement and prayers.

# PROBING THE SOLID-LIQUID INTERFACE OF FLUORINATED THIN FILMS WITH SUM FREQUENCY GENERATION SPECTROSCOPY

An Abstract of a Dissertation

Presented to

the Faculty of the Department of Chemistry

University of Houston

In Partial Fulfillment

of the Requirements for the Degree of

Doctor of Philosophy

By

Daniela Deleon

May 2019

# ABSTRACT

This dissertation investigates the interactions at the solid-liquid interface between contacting liquids and model fluorinated surfaces using self-assembled monolayers (SAMs) on gold. Sum frequency generation (SFG) spectroscopy was employed due to its inherent interface selectivity, which allows it to probe buried interfaces. In the first study, SFG spectroscopy was used to understand the influence of dipole-terminated surfaces on the orientation of contacting liquids by supplying the vibrational spectra of the molecules at the solid-liquid interface. Modulation of the dipole of the solid surface was achieved through selective fluorination of the molecules used for the self-assembly. The work presented here was the first in-situ analysis showing a polar liquid reorient in direct response to the orientation of the surface dipole.

To understand the effect of contacting liquids on the structure of the SAMs, SFG spectroscopy was used to determine the orientation of the terminal functional groups of specifically fluorinated SAMs at the solid-liquid interface. In this study, a difluoromethylene moiety was systematically buried into the film and analyzed with several contacting liquids. The orientation and orientational distribution of the terminal functional groups showed that wetting liquids significantly perturb the interfacial structure of the film. A comparison between the conformation of the monolayer in contact with liquids and the macroscopic contact angle suggested that disordered monolayers yielded the most wettable surfaces.

Finally, the effect of changing the substrate to which molecules adsorb on the structure of the SAM was determined by terminal group orientation of SAMs generated

from three series of molecules bound to gold and underpotentially-deposited silver surfaces. The orientation of the terminal functional group of a SAM on Au changed depending on the length of the alkane chain, and the observed "odd-even" effect in the wettability of the films was reversed by changing the substrate. However, the solid-liquid interface spectra using two contacting liquids did not show any differences, with respect to the substrate. Therefore, although monolayer structure is an important factor in influencing the wettability of the resulting thin film, other factors must be considered to obtain a complete understanding of the macroscopic wetting phenomena of surfaces.

# TABLE OF CONTENTS

# LIST OF FIGURES

# LIST OF SCHEMES

# LIST OF TABLES

# Chapter 1. Introduction to Sum Frequency Generation Spectroscopy of Partially Fluorinated Self-Assembled Monolayers

## 1.1. Self-Assembled Monolayers

The interface between two media, where molecules are exposed to a different environment than that found in the bulk, is where the chemistry of interaction occurs, which dictates how the two media will behave on a macroscopic level. For example, superhydrophobic materials, such as polytetrafluoroethylene (PTFE), are known to have poor chemical interactions between the chemical functional groups in the material and water molecules, leading to poor wetting of the polymer surface and allowing for water drops to easily roll off the surface.[1] Phenomena such as these can only be explained through the careful study of molecules at buried interfaces, specifically the solid-liquid interface, which contain information about the molecular interactions that influence the macroscale properties of a surface. Fundamental studies of solid-liquid interfaces have been performed using model surfaces composed of a monolayer of molecules self-assembled and chemically-bound onto a surface due to the ability of the monolayers to mirror the physical properties of more complex systems.[2-3]

Model surfaces formed by the self-assembly of alkanethiol molecules onto metal substrates have been widely used to obtain a fundamental understanding of physical properties such wetting, adhesion, and friction of more complex systems.[4] Exposure of the molecules to metal substrates allows for the formation of a thermodynamically-favorable sulfur–metal bond, with a distance of ~5 Å between adjacent sulfur atoms,[5] which produces densely-packed films with the terminal functional groups exposed at the interface.[2,4,6] This

system is depicted schematically in Figure 1.1, where the sulfur headgroups of alkanethiol molecules with different overall chain lengths are bound to a gold surface, with the methylene ($CH_2$) groups forming the bulk of the alkane monolayer and the methyl ($CH_3$) tailgroup pointing away from the surface and into the interface. The alkyl chains of thiols bound to gold surfaces have been shown to have a trans-extended configuration that are tilted ~30° from the surface normal in order to maximize attractive van der Waals forces between adjacent chains,[2,5,7-8] which allows for the development of thin films with well-defined surface structures. The terminal functional groups of alkanethiol molecules can also be synthetically modified to generate self-assembled monolayers (SAMs) onto different substrates to produce surfaces with tunable surface properties that match the desired application.[4,9-10]

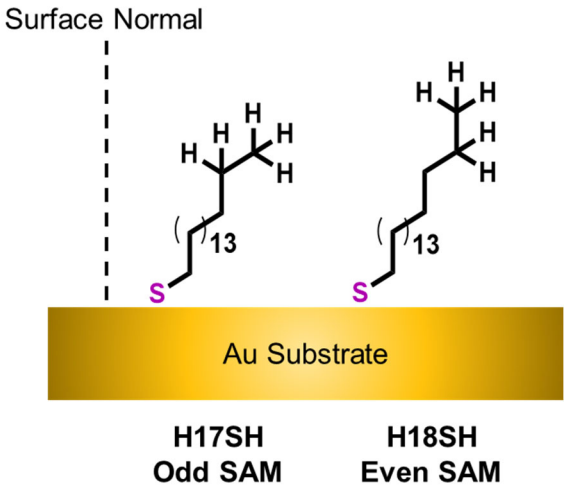


**Figure 1.1.** A schematic illustration of fully hydrocarbon alkanethiol molecules with overall alkane chain lengths of 17 and 18 total carbon atoms, denoted as **H17SH** and **H18SH**, respectively, bound to a gold substrate.

Wettability studies performed on model hydrophobic surfaces composed of alkanethiol self-assembled monolayers bound to gold have shown that the interfacial

structure of the thin films has important consequences on its wetting properties.[9,11] Changing the length of the alkanethiol by changing the number of carbon atoms in the chain induces a change in the orientation (upright or tilted) of the terminal functional group. This change in orientation of the terminal group has been shown to cause an "odd-even" effect in the wettability of the surfaces, as determined by advancing contact angle measurements.[9,11-12] In this effect, an odd number of carbon atoms in the alkyl chains (i.e. $CH_3(CH_2)_{16}SH$, labeled as **H17SH,** with H17 denoting 17 hydrocarbons in the chain) of thiol monolayers assembled onto gold, heretofore referred to as *odd SAMs*, have the final C–C axis tilted away from the surface normal. This is shown by **H17SH** in Figure 1.1 and indicates that the terminal methyl and methylene groups are exposed at the interface. With even-numbered carbon chains (i.e. $CH_3(CH_2)_{17}SH$, labeled as **H18SH)**, heretofore referred to as *even SAMs*, the terminal C–C axis has a more upright orientation, which minimizes exposure of the $CH_2$ at the interface,[5] as shown for **H18SH** in Figure 1.1. This difference in structure causes the odd SAM to be more wettable (lower advancing contact angle) by contacting liquids than the even SAMs on gold due to the increase in dispersive interactions between the liquid and the monolayer, with the exposure of the underlying methylene groups, producing what is termed the "odd-even" effect in wettability.

Besides modifying interfacial structure, altering the terminal functional group of a monolayer has been shown to change the physical properties of the resulting film.[9-10,13-19] Fluorination of the carbon chain has been shown to strongly influence the wettability of self-assembled monolayers.[3,13,20-24] Graupe et. al. used $CF_3$-terminated alkanethiols with the form $CF_3(CH_2)_nSH$, (where n = 9–15) to generate SAMs on Au and found that an array of oriented dipoles formed at the interface.[13] Their study concluded that ordered interfacial

dipoles strongly influence the wettability behavior of the thin films through the observation that the $CF_3$-terminated SAMs were more wettable (lower advancing contact angle) with polar contacting liquids and less wettable (higher advancing contact angle) with nonpolar contacting liquids than the corresponding chain length hydrocarbon SAM.[13] The "odd-even" effect observed in the wettability of $CF_3$-terminated surfaces was also found to be opposite to that of the analogous $CH_3$-terminated SAMs on Au.[22]

More recently, Zenasni et. al. manufactured films using trifluoromethyl-terminated alkanethiol SAMs (FSAMs) and also observed that the "odd-even" trends in the wettability of fully hydrocarbon SAMs were generally opposite for the $CF_3$-terminated surfaces.[25] In both studies, the presence of a fluorocarbon-hydrocarbon (FC–HC) dipole, with the negative pole pointing away from the surface (shown schematically in Figure 1.2), was attributed to the observed changes. Since the SAMs generated from $CF_3$-terminated thiols have been found to be structurally equivalent to the analogous fully hydrocarbon alkanethiols,[26] the orientation of the terminal dipole was considered to follow the orientation of the terminal C–C axis, as shown schematically in Figure 1.2. Thus, for an odd FSAM, the terminal dipole was considered to be tilted away from the surface normal, and for the even FSAM the dipole was considered to be more upright. The implications of the terminal group orientation are in the degree of compensation between adjacent dipoles, which for odd SAMs, due to the head-to-tail arrangement of dipoles, result in the exhibition of weaker dipole-dipole interactions with contacting liquids than for the more upright even SAMs.

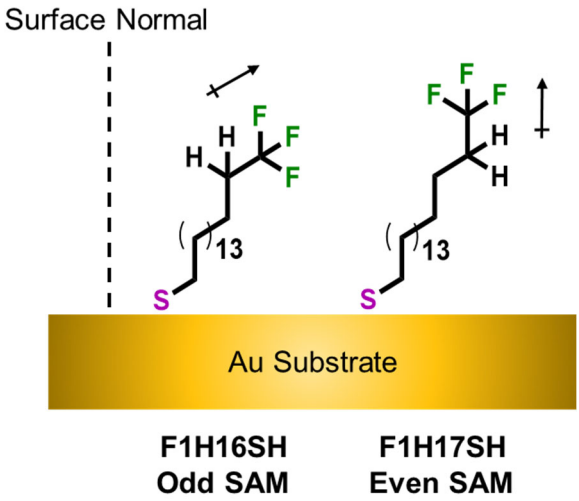


**Figure 1.2.** A schematic illustration of $CF_3$-terminated alkanethiol molecules with overall alkane chain lengths of 17 and 18 total carbon atoms, denoted as **F1H16SH** and **F1H17SH**, respectively, bound to a gold substrate.

To probe the effect of the terminal dipole, Zenasni and coworkers synthesized new adsorbates with the formula $CH_3(CF_2)_6H_nSH$ (n = 11–13) to generate a terminal hydrocarbon-fluorocarbon (HC-FC) dipole in which the positive pole points away from the surface, opposite to that of the $CF_3$-terminated films. With these "inverted-dipole" $CH_3$-capped FSAMs, the authors noted that the trends in wettability depended on several factors related to the surface, namely, the density of chains on the Au, the degree of compensation by adjacent dipoles, the strength of dipole-dipole interactions with the contacting liquid, as well as liquid-liquid interactions.[25]

## 1.2. Substrates for Monolayer Formation

Changing the substrate to which the molecules bind has been shown to alter the physical properties of the resulting film due to a modification in monolayer structure, which depends upon the most favorable binding geometry between the molecule and the

substrate.[4,12,27-36] Studies have demonstrated that SAMs form different tilted structures on silver versus gold.[5,30] Some researchers have credited the change in the SAM structure to a difference in the binding geometry of the S on Au and Ag which form C–S–metal bond angles of 109° and 180°, respectively.[28,37] A near edge X-ray absorption fine structure study on the orientation of octanethiol SAMs on Ag(111) determined that the S–C polar angle is canted at ~39° from the surface normal (compared to ~60° for S–C on Au (111)), enabling the adsorbate chains to align with the surface normal.[36]

Other studies have attributed the differences in SAM structure to preferential inter-thiolate distances on metal surfaces.[38] Sellers et. al. noted several reasons for the possible difference in bonding between thiolates on Ag and Au, including a lower ionization potential for Ag than Au and a larger spread in energies for the valence atomic orbitals for Ag than Au, leading to different hybridization tendencies for each metal.[5] Nevertheless, the studies of SAMs on Ag and Au agree that the hydrocarbon chains require less tilting on silver than gold, with tilt angles of 15° and 30° from the surface normal, respectively, to maximize favorable interactions with the substrate and neighboring adsorbates.[5,30,38] This assembly is illustrated schematically in Figure 1.3, and shows the possible differences in terminal C–C orientation with the alteration in molecular tilt.

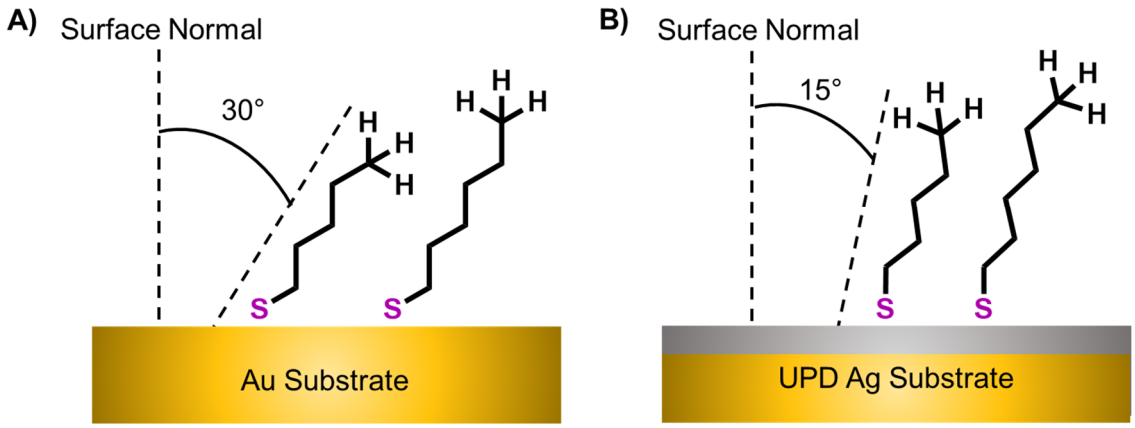


**Figure 1.3.** A schematic illustration of alkanethiol molecules with overall odd and even alkane chain lengths bound to A) Au and B) underpotentially-deposited (UPD) Ag substrates, along with their corresponding molecular tilt angles according to the literature.

The generation of SAMs from partially fluorinated thiols with the form $CF_3(CF_2)_9(CH_2)_nSH$ (where n = 2, 11, and 17) onto silver and gold has been studied by Frey et al.[39] As with the previous reports of alkanethiol tilt angles on Au vs Ag substrates, they found the tilt angle of the FSAMs on Ag to be 10°–12° compared to 32°–38° on Au. Because the ten-fluorocarbon-long tailgroups were bulky, increasing the space between adjacent adsorbates and reducing the interchain van der Waals interactions, the upright tilts of the chains on Ag, in comparison to Au, were attributed to different binding characteristics of the S with each metal.[39] As with the studies performed on self-assembled monolayers generated from thiols onto gold surfaces, "odd-even" effects in the wetting of SAMs on silver have been observed.[5,28,40] This kind of information aids in the design of surfaces with wettability behavior tailored to their application.

The use of readily-oxidizable metals such as silver and copper for surface studies presents challenges for the reproducibility in SAM formation, structure, and the resultant surface properties.[27-28] Therefore, studies have employed the electrochemical

underpotential deposition (UPD) of a monolayer of metal, such as silver, onto a more noble metal, such as gold, to generate substrates for the study of SAMs on different metal surfaces.[35,37,41-44] The deposition of one metal onto another at a potential less negative than the thermodynamic potential for bulk deposition can allow for precise control of the surface coverage, allowing for only a monolayer to be deposited.[45] Jennings and Laibinis noted that a UPD Ag monolayer atop Au did not appear to oxidize, due to the lack of oxygen peaks in their XPS spectra, and noted the superiority of the SAMs formed on UPD metal substrates to those formed on the corresponding bulk metals.[43] These advantages make the use of UPD metals on Au attractive substrates for SAM studies.

## 1.3. Analysis of SAMs on Metal Surfaces with SFG Spectroscopy

### 1.3.1. SFG Spectroscopy at the Solid-Air Interface

To probe buried interfaces such as the solid-liquid interface, an interface-specific technique, such as sum frequency generation (SFG) spectroscopy, is necessary. Sum frequency generation spectroscopy is detailed in Chapter 2, and briefly, is a second-order nonlinear optical technique from which the vibrational spectra of molecules at interfaces can be obtained.[46] It is performed using two high intensity pulsed laser beams incident on a surface which generate a new beam that oscillates at a frequency that is the sum of the two input frequencies, as illustrated in Figure 1.4, and which can only be generated from regions that display non-centrosymmetry, such as the boundary between a self-assembled monolayer and a liquid.[46] Therefore, SFG spectroscopy has been used in determining monolayer composition and structure at interfaces.[47] Several reviews exist which detail the uses of SFG spectroscopy,[46,48-51] and demonstrate the versatility of the technique.

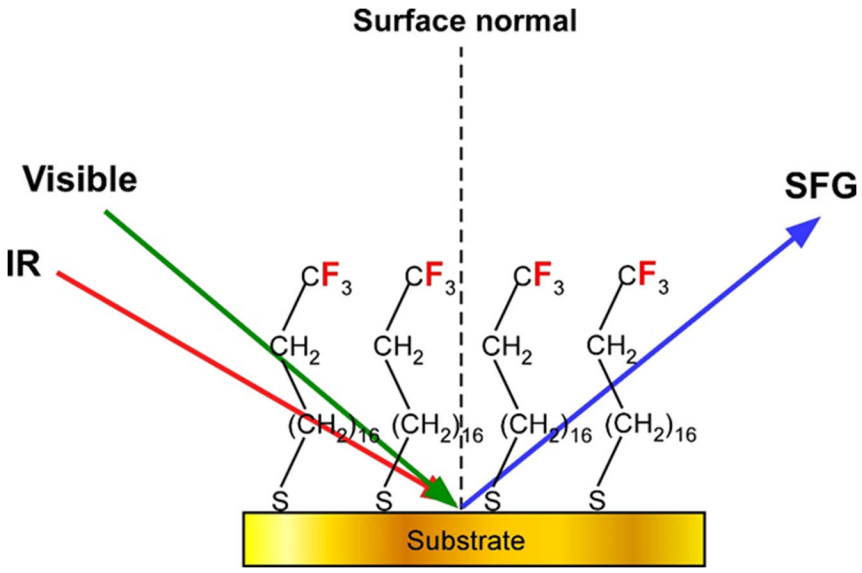


**Figure 1.4.** An illustration of two laser beams, one at a visible frequency (green arrow) and another at an infrared frequency (red arrow), incident on a $CF_3$-terminated self-assembled monolayer from which the sum frequency generation laser beam is generated. The illustration is not to scale; the area covered by the laser beams is on the order of millimeters whereas the SAM is less than a nanometer thick. Therefore, the beams are purposefully shown penetrating into the monolayer.

The SFG spectroscopy in the C–H stretching region of alkanethiol monolayers has been characterized before. The effects of alkyl chain length,[52-53] substrate roughness,[54] kinetics of formation,[55] and electrochemical desorption[56-57] on the structure of SAMs adsorbed to gold surfaces have been studied by determining the methyl group tilt angle with respect to the surface normal. The results demonstrate the same trends in the "odd-even" effect in the orientation of the terminal methyl group, as illustrated in Figure 1.1, with odd SAMs having a terminal C–C bond tilt angle of ~56° with respect to the surface normal, while the even SAMs have a terminal group tilt angle of ~34°.[53] Sum frequency generation spectroscopy has also been used to study the structure of alkanethiol self-assembled monolayers adsorbed to silver surfaces.[29-30,47] Because SFG is a coherent

spectroscopy, a change in the phase between the portion of the signal due to molecular vibrations, and the portion due to the metal substrate response to the input electric fields can affect the line shapes of the vibrational resonances in the spectra. This was readily apparent in the spectra of the same molecules adsorbed to silver and gold, indicating that the vibrationally nonresonant phase from the metal surface changed, depending on the metal, but did not prevent the analysis of the structure of the molecules on the different surfaces.[47] Further studies found that alkanethiol monolayers bound to silver surfaces displayed similar structural order at the interface as that of the same monolayers bound to gold.[29] However, monolayers formed from ether-terminated alkanethiols were found to contain gauche conformers at the interface, indicating disorder when bound to silver, which was not observed for gold surfaces.[30] The results obtained from the analysis of the structure of the monolayers at the air-solid interface were useful in forming conclusions about the wettability behavior of SAMs; a greater degree of disorder at the terminus of a SAM can lead to the partial solvation of the chains and increased wettability of the film.[30]

As with the studies on hydrocarbons in the C–H stretching region, SFG spectroscopy has been used to study fluorinated molecules in the C–F stretching region. Most of these studies have been limited to perfluorinated molecules oriented at the air-liquid interface,[58-62] and have shown the difficulties in the accurate assignment of the resonances in the spectra as well as determining the orientation of $CF_3$ groups at the interface. Tyrode et. al. were able to assign the resonances in their SFG spectra at 1320 and 1385 $cm^{-1}$ to $CF_3$ antisymmetric stretching modes and were able to determine that the $CF_3$ group at the terminus of a monolayer of ammonium perfluorononanoate on water was significantly tilted at high surface densities, indicating that surface micelles were formed.

The other studies at the air-solid interface were not so successful in the analysis of $CF_3$ orientation. In the last 5 years, several groups have collected SFG spectra for the C–F modes of perfluorinated molecules on solid surfaces, specifically glass,[63] Pt,[64] and Au,[65] but have been vague upon their interpretation of the spectra due to its relative complexity in comparison to hydrocarbon SFG spectra.

### 1.3.2. SFG Spectroscopy at the Solid-Liquid Interface

The strength of sum frequency generation spectroscopy lies in its ability to probe buried interfaces, such as the solid-liquid interface. The structure of self-assembled monolayers generated from regular hydrocarbon and alkoxy-terminated alkanethiols on gold and silver in contact with water, hexane, and acetonitrile, determined by the analysis of SFG data, offers rich details on the effect of liquid penetration into the monolayer on the structure of the terminal groups of the SAM.[17,66] Broadening of the vibrational modes observed in the SFG spectra upon the contact of liquids with the SAMs was attributed to rotation of the terminal methyl groups, induced by the solvent-monolayer interactions, while the increase of methylene group contributions to the SFG spectra indicated an increase in disorder of the films.

The above results indicate that the contacting liquids can significantly perturb the interfacial structure of the monolayers, as confirmed by other studies of SAMs in contact with wetting liquids probed with SFG.[67-68] A change in the orientation of ether-terminated molecules, according to the surface to which they were bound, had implications for the frequencies of the terminal group vibrational modes, indicating a change in interchain interactions.[17] Finally, as the polar ether terminal group was removed from the monolayer-

liquid interface, by the addition of a terminal alkyl chain of increasing length atop the oxygen atom, the depth dependence of molecular interactions was determined by comparison of the spectra of the alkoxy-terminated SAMs and those of fully hydrocarbon SAMs.[17] Studies of aqueous surfactants adsorbed onto hydrophobic surfaces composed of alkanethiol SAMs on gold showed that the orientation of the resonances in SFG spectra can be used to determine the orientation ($CH_3$ pointing towards or away from the SAM interface) of the surfactants.[69-71]

## 1.4. Dissertation Contents

The goal of this dissertation is to provide details about the interfacial phenomena that occur between liquids and model surfaces composed of alkanethiol self-assembled monolayers by taking advantage of the interfacial selectivity of sum frequency generation spectroscopy. Chapter 2 provides details on the theory of sum frequency generation as well as the methods used for the orientation analysis of the terminal functional groups of the self-assembled monolayers used in the studies detailed in Chapters 3–5. Chapter 2 also details the instrumental setups used to perform the SFG experiments.

Chapter 3 describes the SFG spectroscopy of liquid acetonitrile atop self-assembled monolayers generated from a deuterated hydrocarbon alkanethiol with the form $CD_3(CD_2)_{17}SH$ and partially fluorinated alkanethiols with the form $CF_3(CH_2)_{16}SH$, $CF_3(CH_2)_{17}SH$, and $CD_3(CF_2)_6(CH_2)_{10}SH$. The spectra were used to determine the role of interfacial dipoles on the structure of acetonitrile by discerning whether the $CH_3$ group in acetonitrile points towards or away from the SAM interface as it interacts with the dipole of SAM beneath it.

Chapter 4 presents the SFG spectroscopy at the solid-air and solid-liquid interface of partially fluorinated octadecanethiols in which a fluorinated methylene group is buried progressively deeper into the alkane chain, with the molecular formulas $CH_3CF_2(CH_2)_{16}SH$, $CH_3CH_2CF_2(CH_2)_{15}SH$, $CH_3(CH_2)_2CF_2(CH_2)_{14}SH$ and $CH_3(CH_2)_3CF_2(CH_2)_{13}SH$. The implications of the $CF_2$ position on the alkane chain with respect to the surface structure and film wetting properties are described using the relative order and orientation of the terminal methyl groups in the SAMs at the solid-liquid interface.

Chapter 5 presents the SFG spectroscopy of three series of molecules—fully hydrocarbon ($CH_3(CH_2)_nSH$, where n = 16–19), $CF_3$-terminated ($CF_3(CH_2)_nSH$, where n = 16–19), and $CH_3$-terminated partially-fluorinated alkanethiols ($CH_3(CF_2)_6(CH_2)_nSH$, where n = 10–13)—self-assembled onto gold and underpotentially deposited silver surfaces. The consequences of adsorption of the thiols onto different metal surfaces are detailed according to the orientation analysis of the terminal groups at the solid-air interface. The SFG spectra of the solid-liquid interfaces between the thiol monolayers and acetonitrile as well as perfluorodecalin are presented, along with a comparison of the interfacial structure to the macroscopic wettability of the films in the form of advancing contact angles.

## 1.5. References

1. Lee, S.; Park, J.-S.; Lee, T. R., The Wettability of Fluoropolymer Surfaces: Influence of Surface Dipoles. *Langmuir* **2008,** *24*, 4817–4826.

2. Porter, M. D.; Bright, T. B.; Allara, D. L.; Chidsey, C. E. D., Spontaneously Organized Molecular Assemblies. 4. Structural Characterization of *n*-Alkyl Thiol Monolayers on Gold by Optical Ellipsometry, Infrared Spectroscopy, and Electrochemistry. *J. Am. Chem. Soc.* **1987,** *109*, 3559–3568.

3. Colorado, R., Jr.; Lee, T. R., Wettabilities of Self-Assembled Monolayers on Gold Generated from Progressively Fluorinated Alkanethiols. *Langmuir* **2003,** *19*, 3288–3296.

4. Love, J. C.; Estroff, L. A.; Kriebel, J. K.; Nuzzo, R. G.; Whitesides, G. M., Self-Assembled Monolayers of Thiolates on Metals as a Form of Nanotechnology. *Chem. Rev.* **2005,** *105*, 1103–1170.

5. Sellers, H.; Ulman, A.; Shnidman, Y.; Eilers, J. E., Structure and Binding of Alkanethiolates on Gold and Silver Surfaces: Implications for Self-Assembled Monolayers. *J. Am. Chem. Soc.* **1993,** *115*, 9389–9401.

6. Himmelhaus, M.; Eisert, F.; Buck, M.; Grunze, M., Self-Assembly of *n*-Alkanethiol Monolayers. A Study by IR−Visible Sum Frequency Spectroscopy (SFG). *J. Phys. Chem. B* **2000,** *104*, 576–584.

7. Ulman, A.; Eilers, J. E.; Tillman, N., Packing and Molecular Orientation of Alkanethiol Monolayers on Gold Surfaces. *Langmuir* **1989,** *5*, 1147–1152.

8. Nuzzo, R. G.; Dubois, L. H.; Allara, D. L., Fundamental Studies of Microscopic Wetting on Organic Surfaces. 1. Formation and Structural Characterization of a Self-Consistent Series of Polyfunctional Organic Monolayers. *J. Am. Chem. Soc.* **1990,** *112*, 558–569.

9. Bain, C. D.; Troughton, E. B.; Tao, Y. T.; Evall, J.; Whitesides, G. M.; Nuzzo, R. G., Formation of Monolayer Films by the Spontaneous Assembly of Organic Thiols from Solution onto Gold. *J. Am. Chem. Soc.* **1989,** *111*, 321–335.

10. Bain, C. D.; Evall, J.; Whitesides, G. M., Formation of Monolayers by the Coadsorption of Thiols on Gold: Variation in the Head Group, Tail Group, and Solvent. *J. Am. Chem. Soc.* **1989,** *111*, 7155–7164.

11. Chang, S.-C.; Chao, I.; Tao, Y.-T., Structure of Self-Assembled Monolayers of Aromatic-Derivatized Thiols on Evaporated Gold and Silver Surfaces: Implication on Packing Mechanism. *J. Am. Chem. Soc.* **1994,** *116*, 6792–6805.

12. Tao, F.; Bernasek, S. L., Understanding Odd−Even Effects in Organic Self-Assembled Monolayers. *Chem. Rev.* **2007,** *107*, 1408–1453.

13. Graupe, M.; Takenaga, M.; Koini, T.; Colorado, R., Jr.; Lee, T. R., Oriented Surface Dipoles Strongly Influence Interfacial Wettabilities. *J. Am. Chem. Soc.* **1999,** *121*, 3222–3223.

14. Chidsey, C. E. D.; Loiacono, D. N., Chemical Functionality in Self-Assembled Monolayers: Structural and Electrochemical Properties. *Langmuir* **1990,** *6*, 682–691.

15. Zamborini, F. P.; Crooks, R. M., Corrosion Passivation of Gold by n-Alkanethiol Self-Assembled Monolayers: Effect of Chain Length and End Group. *Langmuir* **1998,** *14*, 3279–3286.

16. Tsao, M.-W.; Rabolt, J. F.; Schönherr, H.; Castner, D. G., Semifluorinated/Hydrogenated Alkylthiol Thin Films: A Comparison between Disulfides and Thiol Binary Mixtures. *Langmuir* **2000,** *16*, 1734–1743.

17. Ong, T. H.; Davies, P. B.; Bain, C. D., Sum-Frequency Spectroscopy of Monolayers of Alkoxy-Terminated Alkanethiols in Contact with Liquids. *Langmuir* **1993,** *9*, 1836–1845.

18. Dos Ramos, L.; de Beer, S.; Hempenius, M. A.; Vancso, G. J., Redox-Induced Backbiting of Surface-Tethered Alkylsulfonate Amphiphiles: Reversible Switching of Surface Wettability and Adherence. *Langmuir* **2015,** *31*, 6343-6350.

19. Wenzl, I.; Yam, C. M.; Barriet, D.; Lee, T. R., Structure and Wettability of Methoxy-Terminated Self-Assembled Monolayers on Gold. *Langmuir* **2003,** *19*, 10217–10224.

20. Fukushima, H.; Seki, S.; Nishikawa, T.; Takiguchi, H.; Tamada, K.; Abe, K.; Colorado, R., Jr.; Graupe, M.; Shmakova, O. E.; Lee, T. R., Microstructure, Wettability, and Thermal Stability of Semifluorinated Self-Assembled Monolayers (SAMs) on Gold. *J. Phys. Chem. B* **2000,** *104*, 7417–7423.

21. Weinstein, R. D.; Moriarty, J.; Cushnie, E.; Colorado, R., Jr.; Lee, T. R.; Patel, M.; Alesi, W. R.; Jennings, G. K., Structure, Wettability, and Electrochemical Barrier Properties of Self-Assembled Monolayers Prepared from Partially Fluorinated Hexadecanethiols. *J. Phys. Chem. B* **2003,** *107*, 11626–11632.

22. Colorado Jr, R.; Lee, T. R., Physical Organic Probes of Interfacial Wettability Reveal the Importance of Surface Dipole Effects. *J. Phys. Org. Chem.* **2000,** *13*, 796–807.

23. Yuan, Y.; Yam, C. M.; Shmakova, O. E.; Colorado, R., Jr.; Graupe, M.; Fukushima, H.; Moore, H. J.; Lee, T. R., Solution-Phase Desorption of Self-Assembled

Monolayers on Gold Derived From Terminally Perfluorinated Alkanethiols. *J. Phys. Chem. C* **2011,** *115*, 19749–19760.

24. Miura, Y. F.; Takenaga, M.; Koini, T.; Graupe, M.; Garg, N.; Graham, R. L.; Lee, T. R., Wettabilities of Self-Assembled Monolayers Generated from $CF_3$-Terminated Alkanethiols on Gold. *Langmuir* **1998,** *14*, 5821–5825.

25. Zenasni, O.; Marquez, M. D.; Jamison, A. C.; Lee, H. J.; Czader, A.; Lee, T. R., Inverted Surface Dipoles in Fluorinated Self-Assembled Monolayers. *Chem. Mater.* **2015,** *27*, 7433–7446.

26. Kim, H. I.; Graupe, M.; Oloba, O.; Koini, T.; Imaduddin, S.; Lee, T. R.; Perry, S. S., Molecularly Specific Studies of the Frictional Properties of Monolayer Films: A Systematic Comparison of $CF_3$-, $(CH_3)_2CH$-, and $CH_3$-Terminated Films. *Langmuir* **1999,** *15*, 3179–3185.

27. Laibinis, P. E.; Whitesides, G. M.; Allara, D. L.; Tao, Y. T.; Parikh, A. N.; Nuzzo, R. G., Comparison of the Structures and Wetting Properties of Self-Assembled Monolayers of *n*-Alkanethiols on the Coinage Metal Surfaces, Copper, Silver, and Gold. *J. Am. Chem. Soc.* **1991,** *113*, 7152–7167.

28. Walczak, M. M.; Chung, C.; Stole, S. M.; Widrig, C. A.; Porter, M. D., Structure and Interfacial Properties of Spontaneously Adsorbed n-Alkanethiolate Monolayers on Evaporated Silver Surfaces. *J. Am. Chem. Soc.* **1991,** *113*, 2370–2378.

29. Hines, M. A.; Todd, J. A.; Guyot-Sionnest, P., Conformation of Alkanethiols on Au, Ag(111), and Pt(111) Electrodes: A Vibrational Spectroscopy Study. *Langmuir* **1995,** *11*, 493–497.

30. Laibinis, P. E.; Bain, C. D.; Nuzzo, R. G.; Whitesides, G. M., Structure and Wetting Properties of ω-Alkoxy-*n*-Alkanethiolate Monolayers on Gold and Silver. *J. Phys. Chem.* **1995,** *99*, 7663–7676.

31. Zharnikov, M.; Frey, S.; Rong, H.; Yang, Y. J.; Heister, K.; Buck, M.; Grunze, M., The Effect of Sulfur–Metal Bonding on the Structure of Self-Assembled Monolayers. *Phys. Chem. Chem. Phys.* **2000,** *2*, 3359–3362.

32. Woodruff, D., The Role of Reconstruction in Self-Assembly of Alkylthiolate Monolayers on Coinage Metal Surfaces. *Appl. Surf. Sci.* **2007,** *254*, 76–81.

33. Sheen, C. W.; Shi, J. X.; Maartensson, J.; Parikh, A. N.; Allara, D. L., A New Class of Organized Self-Assembled Monolayers: Alkane Thiols on Gallium Arsenide (100). *J. Am. Chem. Soc.* **1992,** *114*, 1514–1515.

34. Allara, D. L.; Nuzzo, R. G., Spontaneously Organized Molecular Assemblies. 1. Formation, Dynamics, and Physical Properties of n-Alkanoic Acids Adsorbed from Solution on an Oxidized Aluminum Surface. *Langmuir* **1985,** *1*, 45–52.

35. Lin, S.-Y.; Tsai, T.-K.; Lin, C.-M.; Chen, C.-h.; Chan, Y.-C.; Chen, H.-W., Structures of Self-Assembled Monolayers of *n*-Alkanoic Acids on Gold Surfaces Modified by Underpotential Deposition of Silver and Copper: Odd−Even Effect. *Langmuir* **2002,** *18*, 5473–5478.

36. Rieley, H.; Kendall, G. K., X-ray Studies of Self-Assembled Monolayers on Coinage Metals. 3. Angularly Resolved Near Edge X-ray Absorption Fine Structure Determination of the Orientation in 1-Octanethiol SAMs on Ag(111) and Cu(111). *Langmuir* **1999,** *15*, 8867–8875.

37. Chen, I. W. P.; Chen, C.-C.; Lin, S.-Y.; Chen, C.-h., Effect of Underpotentially Deposited Adlayers on Sulfur Bonding Schemes of Organothiols Self-Assembled on Polycrystalline Gold: sp or sp3 Hybridization. *J. Phys. Chem. B* **2004,** *108*, 17497–17504.

38. Laibinis, P. E.; Fox, M. A.; Folkers, J. P.; Whitesides, G. M., Comparisons of Self-Assembled Monolayers on Silver and Gold: Mixed Monolayers Derived from $HS(CH_2)_{21}X$ and $HS(CH_2)_{10}Y$ (X, Y = $CH_3$, $CH_2OH$) have Similar Properties. *Langmuir* **1991,** *7*, 3167–3173.

39. Frey, S.; Heister, K.; Zharnikov, M.; Grunze, M.; Tamada, K.; Colorado, R., Jr.; Graupe, M.; Shmakova, O. E.; Lee, T. R., Structure of Self-Assembled Monolayers of Semifluorinated Alkanethiols on Gold and Silver Substrates. *Isr. J. Chem.* **2000,** *40*, 81–97.

40. Tao, Y. T., Structural Comparison of Self-Assembled Monolayers of n-Alkanoic Acids on the Surfaces of Silver, Copper, and Aluminum. *J. Am. Chem. Soc.* **1993,** *115*, 4350–4358.

41. Jennings, G. K.; Laibinis, P. E., Underpotentially Deposited Metal Layers of Silver Provide Enhanced Stability to Self-Assembled Alkanethiol Monolayers on Gold. *Langmuir* **1996,** *12*, 6173–6175.

42. Burgess, J. D.; Hawkridge, F. M., Octadecyl Mercaptan Sub-Monolayers on Silver Electrodeposited on Gold Quartz Crystal Microbalance Electrodes. *Langmuir* **1997,** *13*, 3781–3786.

43. Jennings, G. K.; Laibinis, P. E., Self-Assembled *n*-Alkanethiolate Monolayers on Underpotentially Deposited Adlayers of Silver and Copper on Gold. *J. Am. Chem. Soc.* **1997,** *119*, 5208–5214.

44. Aitchison, H.; Lu, H.; Hogan, S. W. L.; Früchtl, H.; Cebula, I.; Zharnikov, M.; Buck, M., Self-Assembled Monolayers of Oligophenylenecarboxylic Acids on Silver Formed at the Liquid–Solid Interface. *Langmuir* **2016,** *32*, 9397–9409.

45. Herrero, E.; Buller, L. J.; Abruña, H. D., Underpotential Deposition at Single Crystal Surfaces of Au, Pt, Ag and Other Materials. *Chem. Rev.* **2001,** *101*, 1897–1930.

46. Bain, C. D., Sum-Frequency Vibrational Spectroscopy of the Solid/Liquid Interface. *J. Chem. Soc., Faraday Trans.* **1995,** *91*, 1281–1296.

47. Bain, C. D.; Davies, P. B.; Ong, T. H.; Ward, R. N.; Brown, M. A., Quantitative Analysis of Monolayer Composition by Sum-Frequency Vibrational Spectroscopy. *Langmuir* **1991,** *7*, 1563–1566.

48. Buck, M.; Himmelhaus, M., Vibrational Spectroscopy of Interfaces by Infrared–Visible Sum Frequency Generation. *J. Vac. Sci. Technol., A* **2001,** *19*, 2717-2736.

49. Tian, C. S.; Shen, Y. R., Recent Progress on Sum-Frequency Spectroscopy. *Surf. Sci. Rep.* **2014,** *69*, 105–131.

50. Miranda, P. B.; Shen, Y. R., Liquid Interfaces: A Study by Sum-Frequency Vibrational Spectroscopy. *J. Phys. Chem. B* **1999,** *103*, 3292–3307.

51. Eisenthal, K. B., Liquid Interfaces Probed by Second-Harmonic and Sum-Frequency Spectroscopy. *Chem. Rev.* **1996,** *96*, 1343–1360.

52. Nishi, N.; Hobara, D.; Yamamoto, M.; Kakiuchi, T., Chain-Length-Dependent Change in the Structure of Self-Assembled Monolayers of n-Alkanethiols on Au(111) Probed by Broad-Bandwidth Sum Frequency Generation Spectroscopy. *J. Chem. Phys.* **2003,** *118*, 1904–1911.

53. Jacob, J. D. C.; Rittikulsittichai, S.; Lee, T. R.; Baldelli, S., Characterization of SAMs Derived from Octadecyloxyphenylethanethiols by Sum Frequency Generation. *J. Phys. Chem. C* **2013,** *117*, 9355–9365.

54. Uehara, T. M.; de Aguiar, H. B.; Bergamaski, K.; Miranda, P. B., Adsorption of Alkylthiol Self-Assembled Monolayers on Gold and the Effect of Substrate Roughness: A Comparative Study Using Scanning Tunneling Microscopy, Cyclic Voltammetry, Second-Harmonic Generation, and Sum-Frequency Generation. *J. Phys. Chem. C* **2014,** *118*, 20374–20382.

55. Yang, C. S. C.; Richter, L. J.; Stephenson, J. C.; Briggman, K. A., In Situ, Vibrationally Resonant Sum Frequency Spectroscopy Study of the Self-Assembly of Dioctadecyl Disulfide on Gold. *Langmuir* **2002,** *18*, 7549–7556.

56. Cai, X.; Baldelli, S., Surface Barrier Properties of Self-Assembled Monolayers as Deduced by Sum Frequency Generation Spectroscopy and Electrochemistry. *J. Phys. Chem. C* **2011,** *115*, 19178–19189.

57. Jacob, J. D. C.; Lee, T. R.; Baldelli, S., In Situ Vibrational Study of the Reductive Desorption of Alkanethiol Monolayers on Gold by Sum Frequency Generation Spectroscopy. *J. Phys. Chem. C* **2014,** *118*, 29126–29134.

58. Tyrode, E.; Johnson, C. M.; Rutland, M. W.; Day, J. P. R.; Bain, C. D., A Study of the Adsorption of Ammonium Perfluorononanoate at the Air−Liquid Interface by Vibrational Sum-Frequency Spectroscopy. *J. Phys. Chem. C* **2007,** *111*, 316–329.

59. Iwahashi, T.; Miyamae, T.; Kanai, K.; Seki, K.; Kim, D.; Ouchi, Y., Anion Configuration at the Air/Liquid Interface of Ionic Liquid [bmim]OTf Studied by Sum-Frequency Generation Spectroscopy. *J. Phys. Chem. B* **2008,** *112*, 11936–11941.

60. Karageorgiev, P.; Petrov, J. G.; Motschmann, H.; Moehwald, H., Why Fluorination of the Polar Heads Reverses the Positive Sign of the Dipole Potential of Langmuir Monolayers: A Vibrational Sum Frequency Spectroscopic Study. *Langmuir* **2013,** *29*, 4726–4736.

61. Volpati, D.; Chachaj-Brekiesz, A.; Souza, A. L.; Rimoli, C. V.; Miranda, P. B.; Oliveira, O. N.; Dynarowicz-Łątka, P., Semifluorinated Thiols in Langmuir Monolayers – A Study by Nonlinear and Linear Vibrational Spectroscopies. *J. Colloid Interface Sci.* **2015,** *460*, 290–302.

62. Even, M. A.; Lee, S.-H.; Wang, J.; Chen, Z., Detection and Spectral Analysis of Trifluoromethyl Groups at a Surface by Sum Frequency Generation Vibrational Spectroscopy. *J. Phys. Chem. B* **2006,** *110*, 26089–26097.

63. Kristalyn, C. B.; Watt, S.; Spanninga, S. A.; Barnard, R. A.; Nguyen, K.; Chen, Z., Investigation of Sub-Monolayer, Monolayer, and Multilayer Self-Assembled Semifluorinated Alkylsilane Films. *J. Colloid Interface Sci.* **2011,** *353*, 322–330.

64. Yagi, I.; Inokuma, K.; Kimijima, K. i.; Notsu, H., Molecular Structure of Buried Perfluorosulfonated Ionomer/Pt Interface Probed by Vibrational Sum Frequency Generation Spectroscopy. *J. Phys. Chem. C* **2014,** *118*, 26182–26190.

65. Kato, M.; Oyaizu, N.; Shimazu, K.; Yagi, I., Oxygen Reduction Reaction Catalyzed by Self-Assembled Monolayers of Copper-Based Electrocatalysts on a Polycrystalline Gold Surface. *J. Phys. Chem. C* **2016,** *120*, 15814–15822.

66. Ong, T. H.; Ward, R. N.; Davies, P. B.; Bain, C. D., Microscopic Basis of Wetting: an In Situ Study of the Interaction Between Liquids and an Organic Monolayer. *J. Am. Chem. Soc.* **1992,** *114*, 6243–6245.

67. Zolk, M.; Eisert, F.; Pipper, J.; Herrwerth, S.; Eck, W.; Buck, M.; Grunze, M., Solvation of Oligo(ethylene glycol)-Terminated Self-Assembled Monolayers Studied by Vibrational Sum Frequency Spectroscopy. *Langmuir* **2000,** *16*, 5849–5852.

68. Henry, M. C.; Wolf, L. K.; Messmer, M. C., In Situ Examination of the Structure of Model Reversed-Phase Chromatographic Interfaces by Sum-Frequency Generation Spectroscopy. *J. Phys. Chem. B* **2003,** *107*, 2765–2770.

69. Ward, R. N.; Davies, P. B.; Bain, C. D., Orientation of Surfactants Adsorbed on a Hydrophobic Surface. *J. Phys. Chem.* **1993,** *97*, 7141–7143.

70. Ward, R. N.; Duffy, D. C.; Davies, P. B.; Bain, C. D., Sum-Frequency Spectroscopy of Surfactants Adsorbed at a Flat Hydrophobic Surface. *J. Phys. Chem.* **1994,** *98*, 8536–8542.

71. Kett, P. J. N.; Casford, M. T. L.; Davies, P. B., Sum Frequency Generation (SFG) Vibrational Spectroscopy of Planar Phosphatidylethanolamine Hybrid Bilayer Membranes under Water. *Langmuir* **2010,** *26*, 9710–9719.

# Chapter 2. Sum Frequency Generation Spectroscopy Theory and Instrumentation

## 2.1. Theoretical Background for SFG Spectroscopy

### 2.1.1. The Interface Selectivity of SFG

Nonlinear optics have been used for decades to study surface phenomena.[1-4] The theory of the nonlinear emission of light from an excited material stems from the induced polarization, which is the dipole moment per unit volume of a material, by an electric field. If the material is excited using an intense light from a laser, the response of the material to the electric fields perturbing it is anharmonic and the expression for the dipole moment must include nonlinear terms.[2] This is shown by the following Taylor-expanded expression for the induced polarization, $\boldsymbol{P}_{total}$, of a material,

$$\boldsymbol{P}_{total} = \boldsymbol{P}^{(1)} + \boldsymbol{P}^{(2)} + \boldsymbol{P}^{(3)} + \cdots \tag{2.1}$$

where $\boldsymbol{P}^{(n)}$ denotes the order of the terms in the polarization. For example, $\boldsymbol{P}^{(1)}$ denotes the first order polarization which stems from the linear absorption of light by a material, quantified using Beer's law, and corresponds most of the optical phenomena seen in everyday life. The expression for $\boldsymbol{P}_{total}$ can be further defined to include response of the molecules to perturbation by the incident electric fields, $\boldsymbol{E}$, as detailed by the molecular susceptibility, $\chi^{(n)}$, (with its corresponding order) shown below,[2]

$$\boldsymbol{P}_{total} = \epsilon_0[\chi^{(1)}\boldsymbol{E} + \chi^{(2)}\vdots\boldsymbol{EE} + \chi^{(3)}\vdots\boldsymbol{EEE}\ldots]. \tag{2.2}$$

The second-order polarization, $\boldsymbol{P}^{(2)}$, gives the nonlinear interaction of coherent light in a medium and is expressed as,

$$\boldsymbol{P}^{(2)}(\omega_{SFG}) \propto \chi^{(2)}: \boldsymbol{E}(\omega_1)\boldsymbol{E}(\omega_2) \tag{2.3}$$

where $\boldsymbol{E}(\omega_1)$and $\boldsymbol{E}(\omega_2)$ correspond to two input electric fields with frequencies $\omega_1$ and $\omega_2$, and $\chi^{(2)}$ denotes the second-order nonlinear susceptibility tensor of the interaction.[2, 5] The induced polarization in the material oscillates with a frequency, $\omega_{SFG}$, that is at the sum of the two input frequencies and is called the sum frequency generation (SFG) beam.[5] The intrinsic symmetry of the $\chi^{(2)}$ forbids SFG emission from centrosymmetric media because as a third rank tensor, $\chi^{(2)}$ changes sign under the inversion operation.[2] Centrosymmetric materials are invariant under the inversion operation, meaning the susceptibility would have to equal its negative; therefore, in centrosymmetric media the susceptibility must be zero.[2] The implications of this selection rule in sum frequency generation from interfaces indicate that molecules in an isotropic bulk environment will not produce SFG signal, but interfacial molecules can at the boundaries where the centrosymmetry of the system is broken and where $\chi^{(2)}$ will be nonzero.[3]

In the experiments performed in this dissertation, SFG signal was generated using a fixed-frequency electric field in the visible wavelength range, denoted by $\omega_{vis}$, and a variable-frequency electric field in the infrared wavelength range, $\omega_{IR}$, overlapping at an interface, such as a surface of self-assembled monolayers exposed to air, as depicted in Figure 2.1. The electric fields taking the form of laser beams cause the interfacial molecules to oscillate and emit a new coherent electric field, the SFG beam, with a frequency $\omega_{SFG}$,[6] so that the expression for the polarization becomes,

$$\boldsymbol{P}^{(2)}(\omega_{SFG}) \propto \chi^{(2)}: \boldsymbol{E}(\omega_{vis})\boldsymbol{E}(\omega_{IR}) \tag{2.4}$$

where $\omega_{SFG}$ is given by,

$$\omega_{SFG} = \omega_{vis} + \omega_{IR}. \tag{2.5}$$

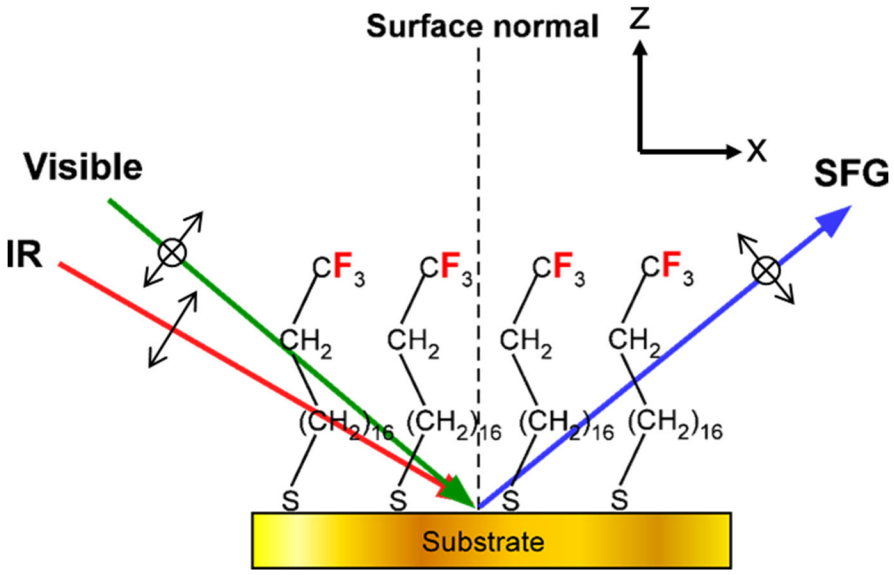


**Figure 2.1.** Schematic of the input visible and infrared laser beams as well as the emitted SFG beam from a gold surface covered by a self-assembled monolayer of fluorinated alkanethiol molecules. The laboratory coordinate system is defined in the top right of the figure, with the z-axis pointing in the direction of the surface normal. The z-x axes form the surface normal plane along which the p-polarized beams propagate. The s-polarized beams are in the direction of the y-axis, perpendicular to the x-axis.

### 2.1.2. The Macroscopic Susceptibility

The intensity of the generated SFG beam, $I_{SFG}$, is proportional to the square of the second-order polarization, and thereby also proportional to the square of the macroscopic effective susceptibility, $\chi_{eff}^{(2)}$, for the system, as shown by the following relationship,[3]

$$I_{SFG} \propto \left|\boldsymbol{P}^{(2)}(\omega_{SFG})\right|^2 \propto \left|\chi_{eff}^{(2)}\right|^2 I(\omega_{vis}) I(\omega_{IR}) \tag{2.6}$$

where $I(\omega_{vis})$ and $I(\omega_{IR})$ are the intensities of the incident electric fields with the frequencies $\omega_{vis}$ and $\omega_{IR}$. The effective susceptibility is described, as shown in Equation 2.7, in terms of $\chi_{NR}^{(2)}$, a vibrationally non-resonant component coming from the interaction

of the metal surface with the intense light fields, and a vibrationally resonant component, $\chi_R^{(2)}$, which contains molecular orientation information,

$$\left|\chi_{eff}^{(2)}\right|^2 \propto \left|\chi_{NR}^{(2)} + \chi_R^{(2)}\right|^2. \tag{2.7}$$

The $\chi_{NR}^{(2)}$ has an amplitude $\mathrm{A}_{NR}$ and phase $\epsilon$, and can be described as,

$$\chi_{NR}^{(2)} = \mathrm{A}_{NR} * e^{i\epsilon} \tag{2.8}$$

while the $\chi_R^{(2)}$ follows the relationship,

$$\chi_R^{(2)} = \sum_q \frac{\mathrm{A}_q}{\omega_q - \omega_{\mathrm{IR}} - i\Gamma_q} \tag{2.9}$$

where $\mathrm{A}_q$, $\omega_q$, $\Gamma_q$ are the amplitude, frequency, and linewidth of the q$^{\text{th}}$ vibrational mode. The resonance amplitude, $\mathrm{A}_q$, is related to the Raman polarizability tensor, $\alpha$, and the IR transition dipole moment, $\mu$, of the q$^{\text{th}}$ vibrational mode in coordinate system, Q, by,

$$\mathrm{A}_q \propto \frac{\partial \alpha}{\partial Q_q}\frac{\partial \mu}{\partial Q_q} \tag{2.10}$$

signifying that in order for SFG signal to be generated, the vibrational mode must be both Raman and IR active. Because the rule of mutual exclusion is violated in centrosymmetric media, this also explains why SFG can only be generated from non-centrosymmetric environments.[2]

### 2.1.3. Fitting Procedure for the SFG Spectra

Equation 2.9 shows that when the frequency of the IR beam is the same as the frequency of a normal mode the susceptibility is maximized, as is the intensity of the emitted SFG beam. Because $I_{SFG}$ directly, although not linearly, depends on whether or not the input IR beam is in resonance with one or more of the vibrational modes of the

molecules at the interface, the frequency of the IR beam can be scanned and plotted with respect to the SFG intensity to produce a surface vibrational spectrum with functional group specificity.[2] The resulting relationship for the intensity of the SFG beam,

$$I_{SFG} \propto \left| \mathrm{A}_{NR} * e^{i\epsilon} + \sum_{q} \frac{\mathrm{A}_q}{\omega_q - \omega_{\mathrm{IR}} - i\Gamma_q} \right|^2 \tag{2.11}$$

was used to fit the SFG spectra collected. The intensities of the resonances were then calculated from the data fits according to the following equation:

$$I_{SFG}(\omega_q) = \left(\frac{A_q}{\Gamma_q}\right)^2. \tag{2.12}$$

Because the susceptibility is a complex quantity, the shape of the resonances in the spectra can be influenced by the relative phases $\epsilon$ and $\delta$ of the non-resonant and resonant components of the susceptibility, as shown by the expansion of equation 2.7,[2]

$$\left|\chi^{(2)}_{eff}\right|^2 \propto \left|\chi^{(2)}_{NR}\right|^2 + \left|\chi^{(2)}_{R}\right|^2 + 2\left(\left|\chi^{(2)}_{NR}\right|\left|\chi^{(2)}_{R}\right|\cos(\epsilon - \delta(\omega)\right). \tag{2.13}$$

Thus, constructive interference between the phases of the resonant and non-resonant contributions to the susceptibility tensor gives rise to upward-pointing resonances (peaks), while destructive interference produces downward-pointing resonances (dips) in the SFG spectra.[2] Because the $\chi^{(2)}_{NR}$ has a constant phase for the substrates used in the studies described in this dissertation, a change in the orientation of the resonances in SFG spectra can consequently be used to determine changes in the structure of functional groups at an interface.

### 2.1.4. The Microscopic Hyperpolarizability

Because the effective susceptibility, $\chi_{eff}^{(2)}$, is a third-rank tensor, it has 27 tensor elements[3] that are dependent on the Cartesian coordinates of the polarizations of the laser beams used in the experiment. Therefore, only certain polarization combinations (p-polarized or s-polarized with respect to the surface normal) will give non-zero elements of the susceptibility tensor. For rotationally isotropic surfaces, such as the gold slides used in the experiments outlined in this dissertation, there are seven non-zero components, namely, $\chi_{xxz}^{(2)} = \chi_{yyz}^{(2)}$, $\chi_{xzx}^{(2)} = \chi_{yzy}^{(2)}$, $\chi_{zxx}^{(2)} = \chi_{zyy}^{(2)}$, and $\chi_{zzz}^{(2)}$, where the subscripts correspond to the laboratory coordinate system (x, y, z) in which z is along the surface normal and x is in the plane of incidence, as defined in Figure 2.1.[3] For the experiments outlined in this dissertation only the ssp and ppp polarization combinations, denoting the SFG, visible, and IR beam polarizations, in that order, were considered. This was according to the available non-zero components of $\chi_{eff}^{(2)}$ and due to the fact that s-polarized infrared light could not be used, because it changes phase upon reflection from metal surfaces, so that the beam destructively interferes and produces no significant intensity.[7] Therefore, the following relationships for the susceptibility were used,[3]

$$\chi_{eff,ssp}^{(2)} = L_{yy}(\omega_{SFG})\, L_{yy}(\omega_{vis})\, L_{zz}(\omega_{IR})\, \sin\beta_{IR}\, \chi_{yyz}^{(2)} \tag{2.14}$$

$$\begin{aligned}\chi_{eff,ppp}^{(2)} = &-L_{xx}(\omega_{SFG})L_{xx}(\omega_{vis})\, L_{zz}(\omega_{IR})\cos\beta_{SFG}\cos\beta_{vis}\sin\beta_{IR}\ \chi_{xxz}^{(2)} \\ &- L_{xx}(\omega_{SFG})L_{zz}(\omega_{vis})\, L_{xx}(\omega_{IR})\cos\beta_{SFG}\sin\beta_{vis}\cos\beta_{IR}\ \chi_{xzx}^{(2)} \\ &+ L_{zz}(\omega_{SFG})L_{xx}(\omega_{vis})\, L_{xx}(\omega_{IR})\sin\beta_{SFG}\cos\beta_{vis}\cos\beta_{IR}\ \chi_{zxx}^{(2)} \\ &+ L_{zz}(\omega_{SFG})L_{zz}(\omega_{vis})\, L_{zz}(\omega_{IR})\sin\beta_{SFG}\sin\beta_{vis}\sin\beta_{IR}\ \chi_{zzz}^{(2)}\end{aligned} \tag{2.15}$$

where $L_{ii}(\omega_i)$ correspond to the Fresnel factors at the frequencies, $\omega_{SFG}$, $\omega_{vis}$, and $\omega_{IR}$, of the SFG, visible, and IR beams, respectively, and the β values correspond to the angles of incidence of the denoted beams. The Fresnel factors between two media with a molecularly thin layer in between, such as air (medium 1) above an alkanethiol monolayer assembled onto gold (medium 2), can be calculated using,[3]

$$L_{xx}(\omega_i) = \frac{2n_1(\omega_i)\cos\gamma_i}{n_1(\omega_i)\cos\gamma_i + n_2(\omega_i)\cos\beta_i} \tag{2.16}$$

$$L_{yy}(\omega_i) = \frac{2n_1(\omega_i)\cos\beta_i}{n_1(\omega_i)\cos\beta_i + n_2(\omega_i)\cos\gamma_i} \tag{2.17}$$

$$L_{zz}(\omega_i) = \frac{2n_2(\omega_i)\cos\beta_i}{n_1(\omega_i)\cos\gamma_i + n_2(\omega_i)\cos\beta_i}\left(\frac{n_1(\omega_i)}{n_m(\omega_i)}\right)^2 \tag{2.18}$$

where $n_1$ and $n_2$ are the frequency-dependent refractive indices of medium 1 and 2. The term $\gamma_i$ corresponds to the refractive angles into medium 2, as determined by Snell's law. The value for $n_m$, corresponding to the effective refractive index of the interface layer (i.e. the monolayer assembled onto gold), was calculated for each system using the method outlined by Zhuang et. al.,[1]

$$\left(\frac{1}{n_m}\right)^2 = \frac{4{n_{bulk}}^2 + 2}{{n_{bulk}}^2({n_{bulk}}^2 + 5)} \tag{2.19}$$

in which $n_{bulk}$ corresponds to the bulk refractive index of the molecules used for the monolayer assembly. Because the Fresnel factors of the $\chi^{(2)}_{xzx}$ and $\chi^{(2)}_{zxx}$ elements are quite small,[8] the susceptibility of the ppp polarization combination can be written as,

$$\begin{aligned}\chi^{(2)}_{eff,ppp} \cong\ & -L_{xx}(\omega_{SFG})L_{xx}(\omega_{vis})\,L_{zz}(\omega_{IR})\cos\beta_{SFG}\cos\beta_{vis}\sin\beta_{IR}\ \chi^{(2)}_{xxz} \\ & + L_{zz}(\omega_{SFG})L_{zz}(\omega_{vis})\,L_{zz}(\omega_{IR})\sin\beta_{SFG}\sin\beta_{vis}\sin\beta_{IR}\ \chi^{(2)}_{zzz}\end{aligned} \tag{2.20}$$

leaving only $\chi^{(2)}_{xxz}$ and $\chi^{(2)}_{zzz}$ as the contributing factors to the $\chi^{(2)}_{eff,ppp}$. The laboratory-scale susceptibility factors, $\chi^{(2)}_{ijk}$, where (i, j ,k = x, y, z) can be related to the molecular-scale elements of the hyperpolarizability $\beta^{(2)}_{\alpha\beta\gamma}$, where ($\alpha, \beta, \gamma$ = a, b, c), through a coordinate transformation via the following relationship,[3]

$$\chi^{(2)}_{ijk} = N \sum_{\alpha\beta\gamma} \langle R_{i\alpha} R_{j\beta} R_{k\gamma} \rangle \beta^{(2)}_{\alpha\beta\gamma} \tag{2.21}$$

where the angular brackets represent the ensemble average over all molecular orientations, N is the number of functional groups contributing to the signal at the interface, and $R_{i\alpha}$, etc. are the elements of the rotational transformation matrix from the molecular coordinate system at the microscale (a, b, c) to the lab (x, y, z) coordinate system at the macroscale, as defined for the $CH_3$ functional group shown in Figure 2.2. This shows how the molecular-scale vibrations described by the $\beta^{(2)}_{\alpha\beta\gamma}$ directly relate to the macroscopic measure of the input electric fields interacting with the surface molecules, $\chi^{(2)}_{ijk}$.

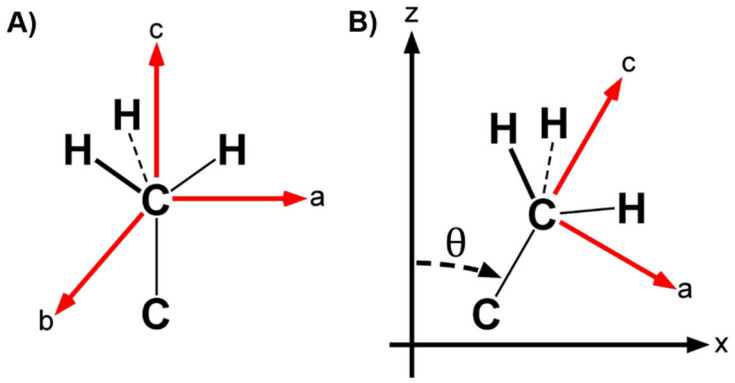


**Figure 2.2.** A) Schematic illustration of the molecular coordinate system (a, b, c) defined for a methyl ($CH_3$) group and B) the relationship between the molecular coordinate system (a, b, c) to the laboratory coordinate system (x, y, z). The average orientation angle, θ, is defined as the tilt angle of the C-axis of the functional group with respect to the surface normal along the z-axis.

There are only three independent symmetric hyperpolarizability elements, $\beta^{(2)}_{aac} = \beta^{(2)}_{bbc}$ and $\beta^{(2)}_{ccc}$, for the vibrational modes probed in the studies outlined in this dissertation, with local $C_{\infty v}$ and $C_{3v}$ symmetry.[3] If $R = \beta^{(2)}_{aac}/\beta^{(2)}_{ccc}$, the azimuthal angle over the x-y plane is averaged over, and a narrow distribution of functional group orientations is assumed, then the $\chi^{(2)}_{xxz}$ and $\chi^{(2)}_{zzz}$ for symmetric stretching vibrations can be found using,[3]

$$\chi^{(2),ss}_{xxz} = \chi^{(2),ss}_{yyz} = \frac{N\,\beta^{(2)}_{ccc}}{2}[(1+R)\langle\cos\theta\rangle - (1-R)\langle\cos^3\theta\rangle] \tag{2.22}$$

$$\chi^{(2),ss}_{zzz} = N\,\beta^{(2)}_{ccc}\,[R\langle\cos\theta\rangle + (1-R)\langle\cos^3\theta\rangle] \tag{2.23}$$

where θ is the average orientation angle, described as the tilt angle, of the functional group with respect to the surface normal, as shown for the case of a $CH_3$ group in Figure 2.2. For the antisymmetric stretching vibrations the $\chi^{(2)}_{xxz}$ and $\chi^{(2)}_{zzz}$ have the following relationships to θ,[3]

$$\chi^{(2),as}_{xxz} = \chi^{(2),as}_{yyz} = -N\,\beta^{(2)}_{aca}[\langle\cos\theta\rangle - \langle\cos^3\theta\rangle] \tag{2.24}$$

$$\chi^{(2),ss}_{zzz} = 2N\,\beta^{(2)}_{aca}\,[\langle\cos\theta\rangle - \langle\cos^3\theta\rangle]. \tag{2.25}$$

The value of the hyperpolarizability ratio, R, for a $CH_3$ group can be calculated according to the procedure outlined by Wang, et. al.,[3] in which,

$$R = \frac{\beta^{(2)}_{aac}}{\beta^{(2)}_{ccc}} = \frac{1+r-(1-r)\cos^2(\tau)}{2[r+(1-r)\cos^2(\tau)]} \tag{2.26}$$

where $\tau$ is the H–C–H bond angle of 109.5° and $r$ is the single bond polarizability derivative ratio. The value of $r$ is obtained from the Raman depolarization ratio, ρ, for the normal mode in question, which was not experimentally determined for the molecules used in this dissertation. Therefore, literature values for ρ from similar molecules were sought

out and used where appropriate. The following relationship between ρ and $r$ was used to determine the $r$ value used for the calculation of the hyperpolarizability ratio, R,[3]

$$\rho = \frac{3}{4 + 20\left[\frac{1+2r}{(1-r)(1-3\cos^2(\tau))}\right]^2} \tag{2.27}$$

Alternatively, the value of R was varied from 1 to 4 using the intensity ratios determined experimentally until a physically reasonable value was found.[3]

### 2.1.5. Functional Group Orientation Analysis

Equations 2.14–2.25 were used to generate theoretical curves that show the relationship between the intensity of the SFG beam, $I_{SFG}$, and the functional group tilt angle, θ, with respect to the surface normal. The intensities of the resonances in the SFG spectra corresponding to the vibrational modes of the functional groups probed in this dissertation were determined from the fits to the experimental data using Equation 2.11. The intensities from the experiment were compared to the simulated curves to determine the average orientation of the functional group with respect to the surface normal. Because not all the parameters used in the simulation of the orientation curves are known, such as the values for the individual hyperpolarizabilities, $\beta^{(2)}_{\alpha\beta\gamma}$, intensity ratios were used instead of direct intensities determined for a vibration in a spectrum. Two methods were used in determining functional group orientation: using the ratio of intensities for the same resonance from each of the polarization combinations collected, $\frac{I_{ssp}}{I_{ppp}}$, or using the intensity ratio between two resonances in the same spectrum, such as the symmetric and antisymmetric stretching modes, $\frac{I_{ss}}{I_{as}}$. The former method requires that the intensity ratios

be corrected for experimental differences due to using different polarization combinations. Therefore, the latter method, which is more self-consistent, was used when possible.

In order to determine the distribution in the average orientation angle, a Gaussian distribution function (with different widths) was applied to Equations 2.22–2.25 following the procedure outlined by Sun et. al.,[9] with the following expression,

$$\chi_{ijk}^{(2)} = N\beta_{\alpha\beta\gamma}^{(2)} \int g(\theta)\, f(\theta) d\theta \tag{2.28}$$

where $g(\theta)$ represents $\cos\theta$ or $\cos^3\theta$ and $f(\theta)$ is a Gaussian orientation distribution function with the form,

$$f(\theta) = \frac{1}{\sigma\sqrt{2\pi}} e^{\frac{-(\theta-\theta_0)}{2\sigma^2}} \tag{2.29}$$

in which $\sigma$ is the width of the distribution and $\theta_0$ is the average tilt angle of the functional group with respect to the surface normal. The average orientations and orientational distributions of the functional groups at an interface, determined from an SFG experiment, were used to understand how microscopic structure influences the macroscopic properties of films.

### 2.1.5.1. Determination of Methyl Group Tilt Angle

The orientation of the methyl ($CH_3$) groups at the terminus of self-assembled monolayers (SAMs) on metal surfaces generated from fully hydrocarbon alkanethiol molecules with the form $CH_3(CH_2)_nSH$ (**HnSH**, where n = 16–19) was determined using the ratio of resonance intensities for the symmetric and antisymmetric $CH_3$ stretches with frequencies of 2875 $cm^{-1}$ and 2965 $cm^{-1}$, respectively, in the ppp SFG spectra. Using this analysis, the average tilt angle along the terminal C–C bond of the methyl group, with

respect to the surface normal, hereafter described as the methyl group tilt angle, was determined. To generate the theoretical curves described above, a value of 1.45 for the refractive index, $n_{bulk}$, of an organic monolayer was used, consistent with the literature value used for SAMs.[10] For the hyperpolarizability ratio, R, a value of 3.4 was used, in accordance with previous reports that determined the tilt angle of $CH_3$ groups using SFG.[3, 11] Figure 2.3 displays the simulated orientation curves used in the analysis of $CH_3$ group tilt angle at the air-solid interface in the forthcoming chapters.

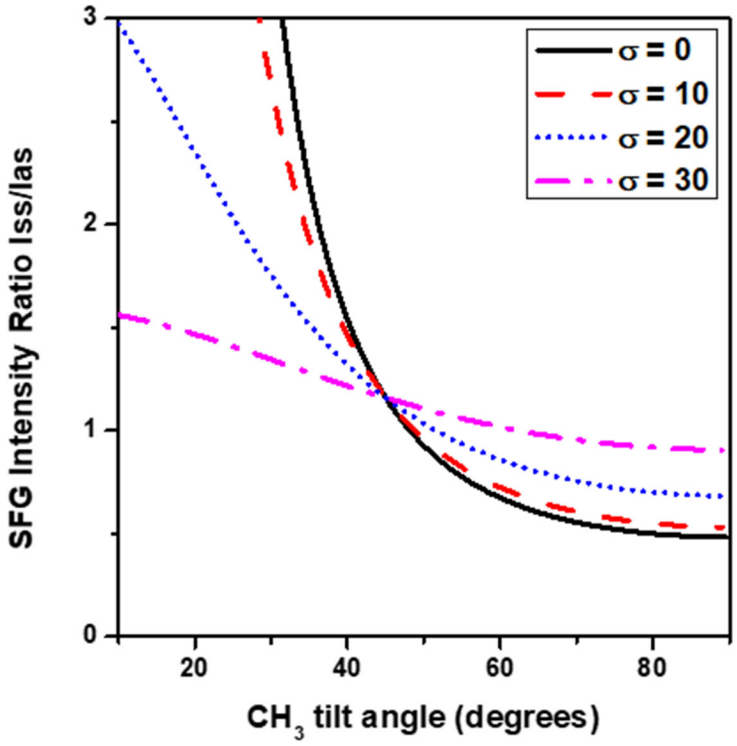


**Figure 2.3.** The relationship between the methyl group tilt angle and the SFG peak intensity ratio for the symmetric and antisymmetric methyl stretch. The black solid, red dash, blue dot, and pink dash-dot lines represent the width in the Gaussian distribution of the orientation angles with $\sigma$ = 0°, 10°, 20°, and 30°, respectively.

The resonance intensity ratios determined from the experimental SFG spectra can have relatively large errors attributed to variation in the spectrum fitting for the molecules.

Figure 2.4 shows one such case where a typical ppp SFG spectrum of octadecanethiol (**H18SH)** on gold was fit to different numbers of resonances, from three resonances corresponding to three methyl ($CH_3$) stretching frequencies, to six resonances that include contributions to the SFG spectrum from methylene ($CH_2$) groups. The figure shows the narrow distribution ($\sigma = 0°$) curve for the methyl group tilt angle as well as the intensity ratios and their errors determined from fitting the experimental SFG spectra. The average orientation angle was determined to be 28° for the spectrum fit to three resonances and 33° for the spectrum fit to five and six resonances.

The errors in the intensity ratios, shown by the error bars in Figure 2.4, were used to determine a range of possible tilt angles for the $CH_3$ group based on the error in the fit. While all three fits yield tilt angles that are the same within error, the error bars indicate that the tilt angles can diverge 2–6° away from the average tilt angle. The error bars also show that tilt angle ranges can span 6–9°. The different fitting procedures produced different average methyl tilt angles, and while the ranges of tilt angle values were lower for some fitting procedures, others show large variations between the average angle and range of angles. This illustrates a limitation of the SFG orientation analysis for the determination of the methyl group tilt angle. As such, the tilt angles obtained in the studies in this dissertation are meant to be understood as the range of angles that can vary.

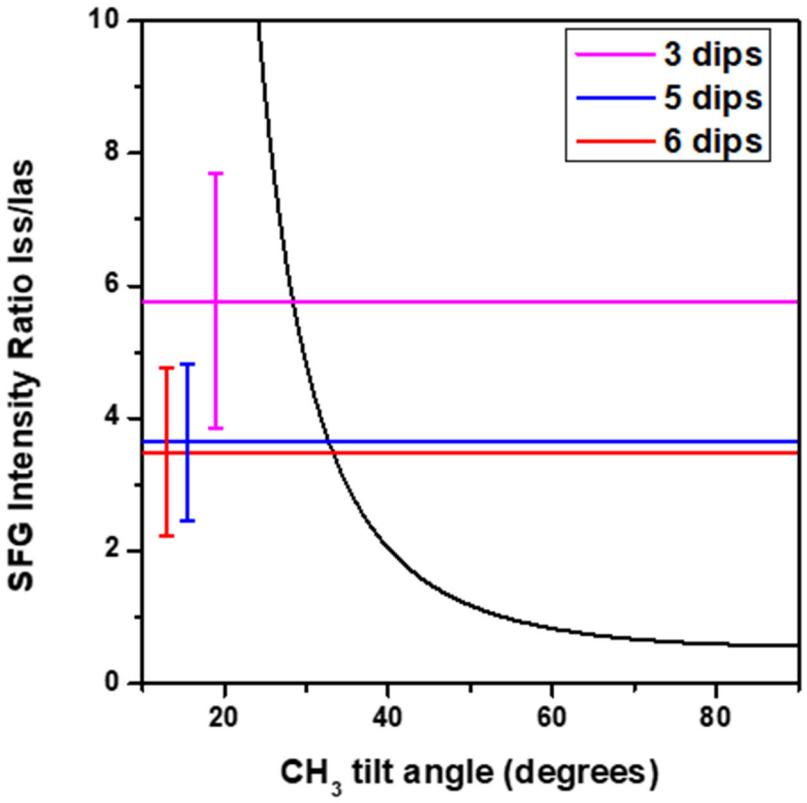


**Figure 2.4.** The relationship between the methyl group tilt angle and the SFG peak intensity ratio for the ppp symmetric and antisymmetric $CH_3$ stretch. The red, blue, and pink lines represent the intensity ratios, with their error, calculated from fitting the SFG spectrum of **H18SH** to six, five, and three resonances, respectively.

New simulations for the orientation curve were necessary for the solid-liquid interface between alkanethiol SAMs and contacting liquids, due to the change in Fresnel factors as the laser beams traveled through the liquid. The orientation curves used for the analysis of methyl group tilt angles while in contact with liquids are shown in Figure 2.5. The orientation curves for the methyl groups at solid-liquid interfaces were observed to shift slightly lower and towards lower tilt angles (more upright orientations of the methyl groups with respect to the surface normal), due to the change in refractive indices at the interface with the addition of a condensed phase at the interface.

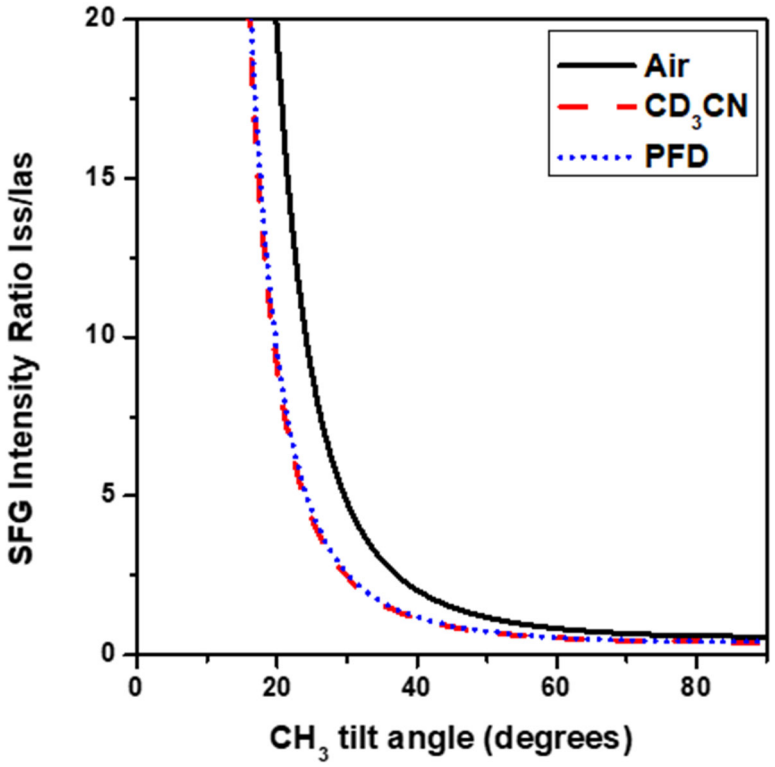


**Figure 2.5.** The relationship between the methyl group tilt angle and the SFG peak intensity ratio for the symmetric and antisymmetric methyl stretch for alkanethiol SAMs in contact with acetonitrile ($CD_3CN$) and perfluorodecalin (PFD).

### 2.1.5.2. Determination of $CF_3$ Group Tilt Angle

Determination of the orientation of the trifluoromethyl ($CF_3$) groups has been attempted before with varying success.[12-14] Tyrode et. al. noted that the orientation could not be determined accurately due to the lack of values for the hyperpolarizabilities of the resonances.[12] In the studies outline here, the orientation of the $CF_3$ at the terminus of partially fluorinated alkanethiols with the formula $CF_3(CH_2)_nSH$ (**F1HnSH**, where n = 16–19) self-assembled onto metal surfaces were attempted to be determined assuming the $CF_3$ group has local $C_{3v}$ symmetry so that the ratio of the symmetric stretching vibration of the $CF_3$ group in ssp and ppp polarization combinations could be used, due to the fact that it

was the most prominent vibration in the SFG spectra. The monolayer refractive index used was $n_m$ = 1.19, calculated using a bulk refractive index, $n_{bulk}$, of 1.431 ± 0.009 for $CF_3$-terminated alkanethiols.[15] Smith et. al. noted that the depolarization ratio for the $CF_2$ vibration is 0.05,[16] which gave r = 0.04, which was then used to get R = 3.91. This value was used to generate the simulated orientation curve for the intensity ratio versus the $CF_3$ tilt angle given in Figure 2.6, however the R value for a $CF_3$ group should be more appropriate.

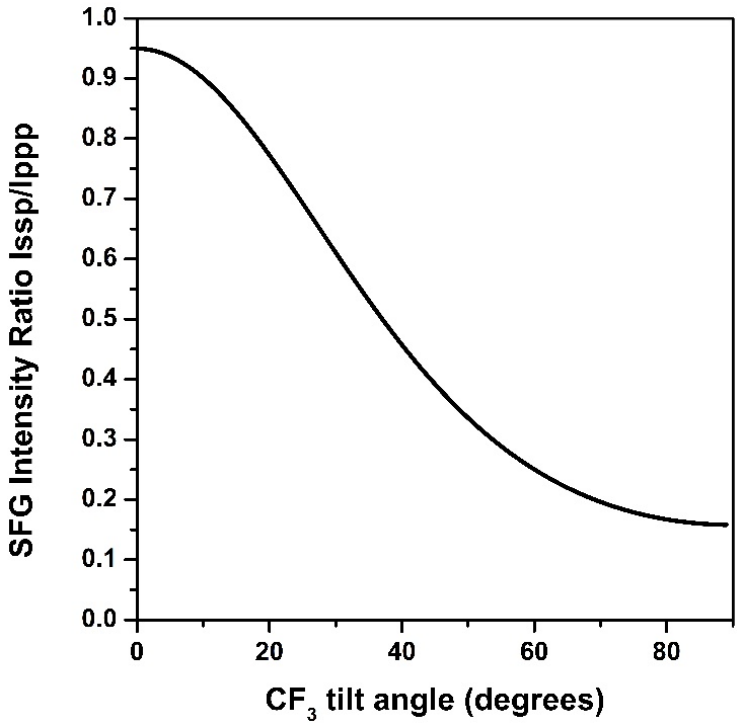


**Figure 2.6.** Simulated $\sigma$ = 0° distribution curve of the intensity ratio of the $CF_3$ symmetric stretch in ssp and ppp SFG spectra with respect to $CF_3$ orientation angles.

Raman studies of $CF_3$-terminated molecules have found that the depolarization ratio, ρ, of the $CF_3$ stretching vibration at ~1175 $cm^{-1}$ is ~0.7.[14, 17-18] Using this value leads to the calculation of a negative value for R, the hyperpolarizability ratio. Iwahashi, et.al.

arrived at the same result and used R = - 4.89 to determine the orientation angle for the $CF_3$ group in $CF_3SO_3^-$.[13] Karageorgiev et. al., who studied $CF_3$-terminated ethyl ether forming a Langmuir film on water, also calculated a negative value for R and justified its use by attributing the negative R value to phase shifts between the driving electric fields and the polarization response of a $CF_3$ group.[14] Although the electron-withdrawing nature of the $CF_3$ group is expected to reduce the value of the hyperpolarizabilities, the bond polarizability derivative model[3] used to determine the value of r assumes that the functional group in question has a polarizability so that $0 \leq r < 1$, therefore, a negative value for the hyperpolarizability ratio R does not make physical sense because it would indicate that the functional group is not polarizable.

Because a reasonable value for R was not found through the depolarization ratios available in the literature, the value of R in the simulation was allowed to vary until the orientation curve appeared to match the intensity ratios calculated from the experimental SFG data, producing a curve that agreed with the curve plotted in Figure 2.6. However, due to the coupled nature of the $CF_3$ vibrations to those of the C–C stretching and $CH_2/CH_3$ wagging vibrations,[18-19] the curve in Figure 2.6 did not fully match the intensity ratios determined from the SFG spectra, indicating that the model used to simulate the curve was insufficient. Potential energy distributions were sought out to determine the contribution of the $CF_3$ to the vibration at 1174 $cm^{-1}$, and found that the $CF_3$ symmetric stretching contribution does not exceed 25% for the band,[20] while other studies assigned the band with ~50% $CF_3$ antisymmetric stretching character,[17-19] implying that no matter the model used to generate orientation curves, the error in the tilt angle would be large due to strong coupling between the $CF_3$ vibrations and those of the chain.

Because the molecules studied in this dissertation are assembled on metal surfaces, the complex refractive index of a metal surface has a large influence on the Fresnel factors used in the simulation of the orientation curve; therefore, although the $CF_3$ vibrations are strongly coupled to other modes, unknown factors may have needed to be applied to the simulated curves to account for the use of electronically-resonant metal substrates and may have contributed to the error in the orientation analysis. Therefore, the $CF_3$ tilt angles were unable to be quantified successfully by SFG orientation analysis, however, the relative intensities of the $CF_3$ modes could still be used to qualitatively analyze the orientations of the functional groups, as described in Chapter 5.

#### 2.1.5.3. Determination of $CH_3$ Tilt Angle in Partially Fluorinated SAMs

The orientation of the methyl ($CH_3$) groups at the terminus of SAMs generated from partially fluorinated alkanethiols with the formula $CH_3(CF_2)_6(CH_2)_nSH$ (**H1F6HnSH**, where n = 10–13) assembled on metal surfaces was determined using the ratio of resonance intensities for the symmetric and antisymmetric $CH_3$ stretches in the ppp SFG spectra with frequencies of 2960 $cm^{-1}$ and 3024 $cm^{-1}$, respectively. Making no other changes to the values used in the simulation of the orientation curve for a $CH_3$ group, besides using the correct stretching frequencies for the $CH_3$ above a $CF_2$ moiety, made barely discernable changes to the orientation analysis curve for the methyl group orientation with a narrow distribution, shown in Figure 2.3. The monolayer refractive index was changed to $n_m = 1.18$, calculated using a bulk refractive index, $n_{bulk}$, of 1.40 ± 0.01 for a similar partially-fluorinated alkanethiol with the formula $CF_3(CF_2)_9(CH_2)_{11}SH$.[21] The depolarization ratio, ρ, for the $CH_3$ next to a $CF_2$ was found in the literature to be 0.02,[22]

and was used to calculate r = 0.21, which gives R = 1.88. This value for R is similar to the value for the methyl group in methanol, R =1.7.[3] Therefore, it was used in the orientation analysis for the SAMs derived from $CH_3$-terminated partially fluorinated alkanethiols to generate the narrow distribution curve shown in Figure 2.7 and used in the orientation analysis in Chapter 5.

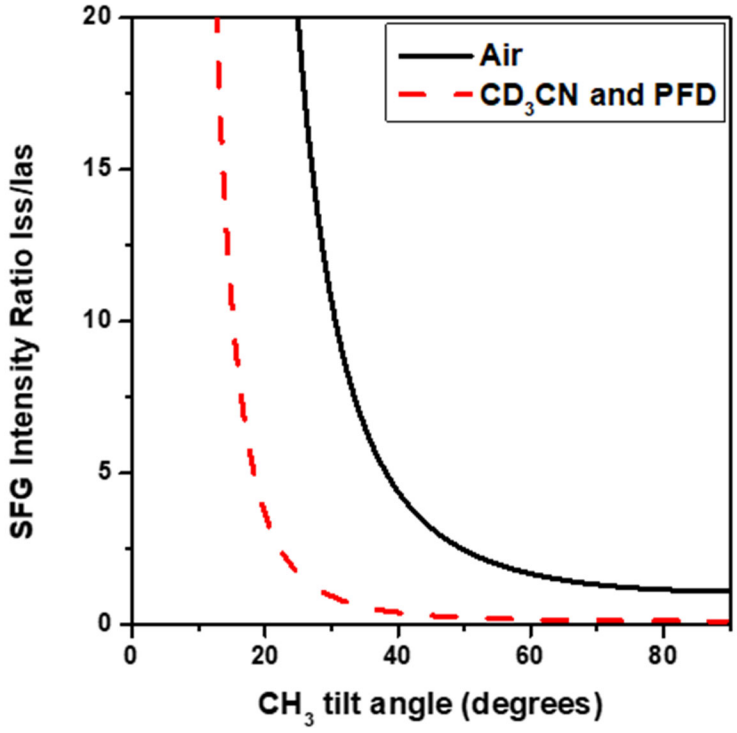


**Figure 2.7.** Simulated $\sigma = 0°$ distribution curve of the intensity ratio of the $CH_3$ symmetric and antisymmetric stretch with respect to $CH_3$ orientation angles for the SAMs generated from $CH_3(CF_2)_6(CH_2)_nSH$ (where n = 10–13), for the air-solid interface (black solid line) and solid-liquid interface (red dash line) between the SAMs and acetonitrile ($CD_3CN$) and perfluorodecalin (PFD).

For the partially-fluorinated molecule with a $CH_3$-$CF_2$ terminus used in Chapter 4 with a molecular formula of $CH_3CF_2(CH_2)_{16}SH$, the value of R = 1.88 was used as in the case of the series of SAMs generated from $CH_3(CF_2)_6(CH_2)_nSH$. A value of $n_{bulk}$, = 1.45,

giving $n_m$, = 1.2, was used due to the assumption that such limited fluorination would not have much of an effect on the refractive index of the monolayer, supported by the fact that the ellipsometric thickness of the SAM did not change in comparison to that of a fully alkane monolayer, as shown in Chapter 4. For the monolayer generated from $CH_3CH_2CF_2(CH_2)_{15}SH$, also used in Chapter 4, the value for ρ for the $CH_3$ adjacent to a $CH_2$-$CF_2$ was determined to be 0.05,[22] and was used to calculate r = 0.02, which gives R = 3.23. Once again a value of $n_m$ = 1.2 was used. The narrow distribution orientation curves for these two monolayers are compared to the curve for a regular alkanethiol, plotted in Figure 2.8, and were used in the orientation analysis in Chapter 4.

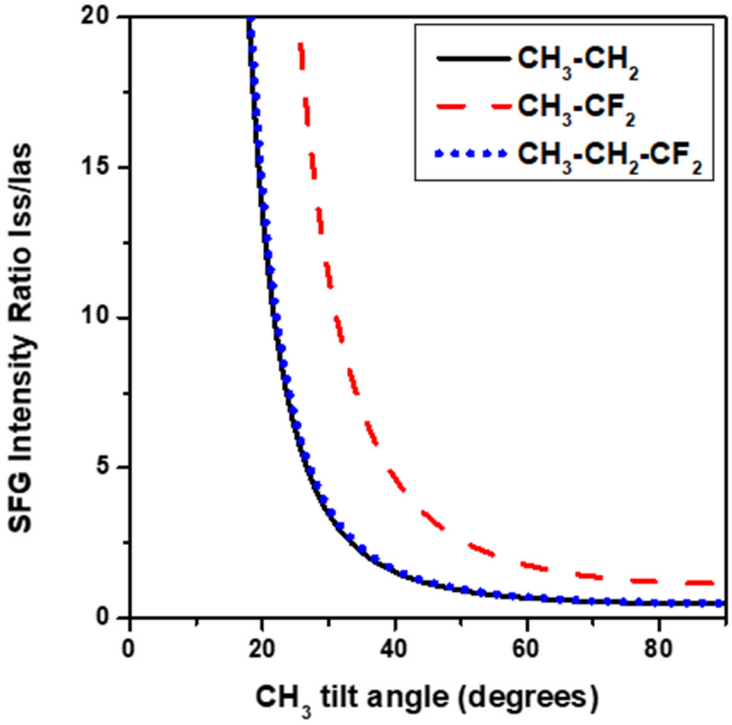


**Figure 2.8.** Simulated $\sigma$ = 0° distribution curves of the intensity ratio of the $CH_3$ symmetric and antisymmetric stretch with respect to $CH_3$ orientation angles for the SAMs with terminal groups of $CH_3$-$CH_2$ (black line), $CH_3$-$CF_2$ (red dash line), and $CH_3$-$CH_2$-$CF_2$ (blue dot line) at the air-solid interface.

At the solid-liquid interface, the Fresnel factors in the simulation were changed to account for the change in refractive index as the laser beams propagated through the contacting liquids. The tilt angles of the monolayers under acetonitrile and perfluorodecalin were determined using the orientation curves shown in Figure 2.9 and were used for the orientation analysis detailed in Chapter 4.

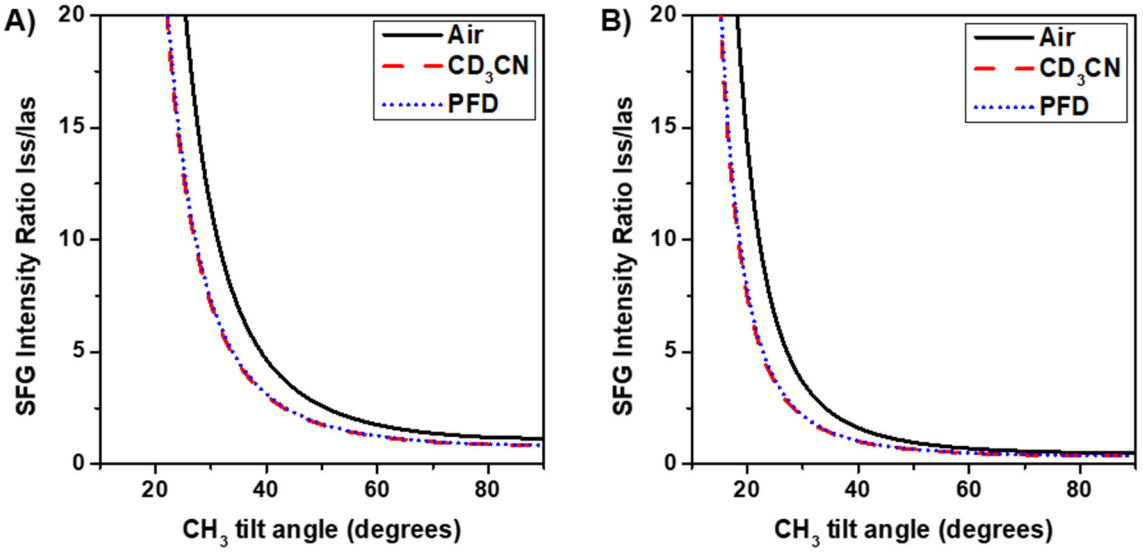


**Figure 2.9.** Simulated $\sigma$ = 0° distribution curves of the intensity ratio of the $CH_3$ symmetric and antisymmetric stretch with respect to $CH_3$ orientation angles for the SAMs generated from A) $CH_3CF_2(CH_2)_{16}SH$ and B) $CH_3CH_2CF_2(CH_2)_{15}SH$ at the air-solid interface (black solid line) and solid-liquid interface between the SAMs and acetonitrile ($CD_3CN$—red dash line) and perfluorodecalin (PFD—blue dot line).

### 2.1.6. Optical Parametric Generation and Amplification

Because the cross-section of the second-order nonlinear process is small, pulsed lasers with high peak power densities, and thus high intensities, are necessary to generate enough signal to be detected. Therefore, coherent (spatial and temporal) interaction of the input electric fields are necessary to obtain the SFG beam. To generate the fixed-frequency visible and the tunable infrared laser beams used for the sum frequency process, an optical

parametric generation and amplification system (OPG/OPA) was used. The visible beam for the experiment at 532 nm was generated by second harmonic generation (SHG) from a fundamental 1064 nm beam generated by an Nd:YAG laser used to pump the OPG/OPA, as shown in the instrumentation section. Second harmonic generation is a special case of SFG in which two input photons of the same frequency generate a new photon at twice the frequency of the original photons.

Optical parametric generation (OPG) and optical parametric amplification (OPA) by difference frequency generation (DFG) are also wave-mixing processes that involve energy conversion from a pump wave with a frequency, $\omega_{pump}$, into two new waves, a signal wave at a frequency of $\omega_{signal}$ and idler wave at a frequency of $\omega_{idler}$.[23-24] The $\omega_{signal}$ is defined as the higher frequency wave in comparison to the $\omega_{idler}$. As in the SFG process, the output frequencies of a parametric device are governed by energy ($\omega_{pump} = \omega_{signal} + \omega_{idler}$) and momentum ($k_{pump} = k_{signal} + k_{idler}$) conservation.[23-24] From these criteria come the phase-matching condition for the generation of new beams from nonlinear media, given by,

$$\omega_{pump} \sin\theta_{pump} = \omega_{signal} \sin\theta_{signal} + \omega_{idler} \sin\theta_{idler} \tag{2.30}$$

Optical parametric generation is thus the opposite process to SFG, generating two photons of lower frequency from one photon of higher frequency. When the process of generating new photons is coherent, the photons constructively add to create the signal and idler beams. In a seeded DFG process called optical parametric amplification, in which $\omega_{pump}$ and $\omega_{signal}$ are both incident on a non-centrosymmetric crystal, the signal beam at $\omega_{signal}$ is amplified because the pump beam will be broken down to make one more photon at

$\omega_{signal}$ as well as a photon at $\omega_{idler}$. Birefringent nonlinear crystals are used in OPG/OPA systems in order to take advantage of the dependence of the refractive index of the crystal on the direction of the polarization of the input radiation.[23-24] Equation 2.30 shows that by changing the angle at which the beams travel through the birefringent nonlinear crystals, the output frequencies $\omega_{signal}$ and $\omega_{idler}$ can be tuned.[23-24] This method of tuning is used to generate the IR beam that is scanned across a frequency range for SFG spectroscopy.

## 2.2. SFG Spectrometer Set-up and Characterization

### 2.2.1. OPG/OPA

Figure 2.10 shows the beam path beginning at the EKSPLA Nd:YAG, 20 ps pulse duration, 1064 nm laser used to pump a LaserVision optical parametric generation and amplification (OPG/OPA) system. This fundamental beam, depicted as black arrows pointing in the direction of propagation of the beam in Figure 2.10, is steered with mirrors 1 and 2 (M1 and M2) to a Galilean telescope made up of a plano-convex and a plano-concave lens (L1 and L2, respectively). The telescope takes the diverging beam from the laser and reshapes it to a small enough diameter to increase its peak power density so that when it pumps the parametric processes they can generate sufficient intensity for the SFG experiment. The beam is also collimated with the lenses to ensure a consistent output from the OPG/OPA.

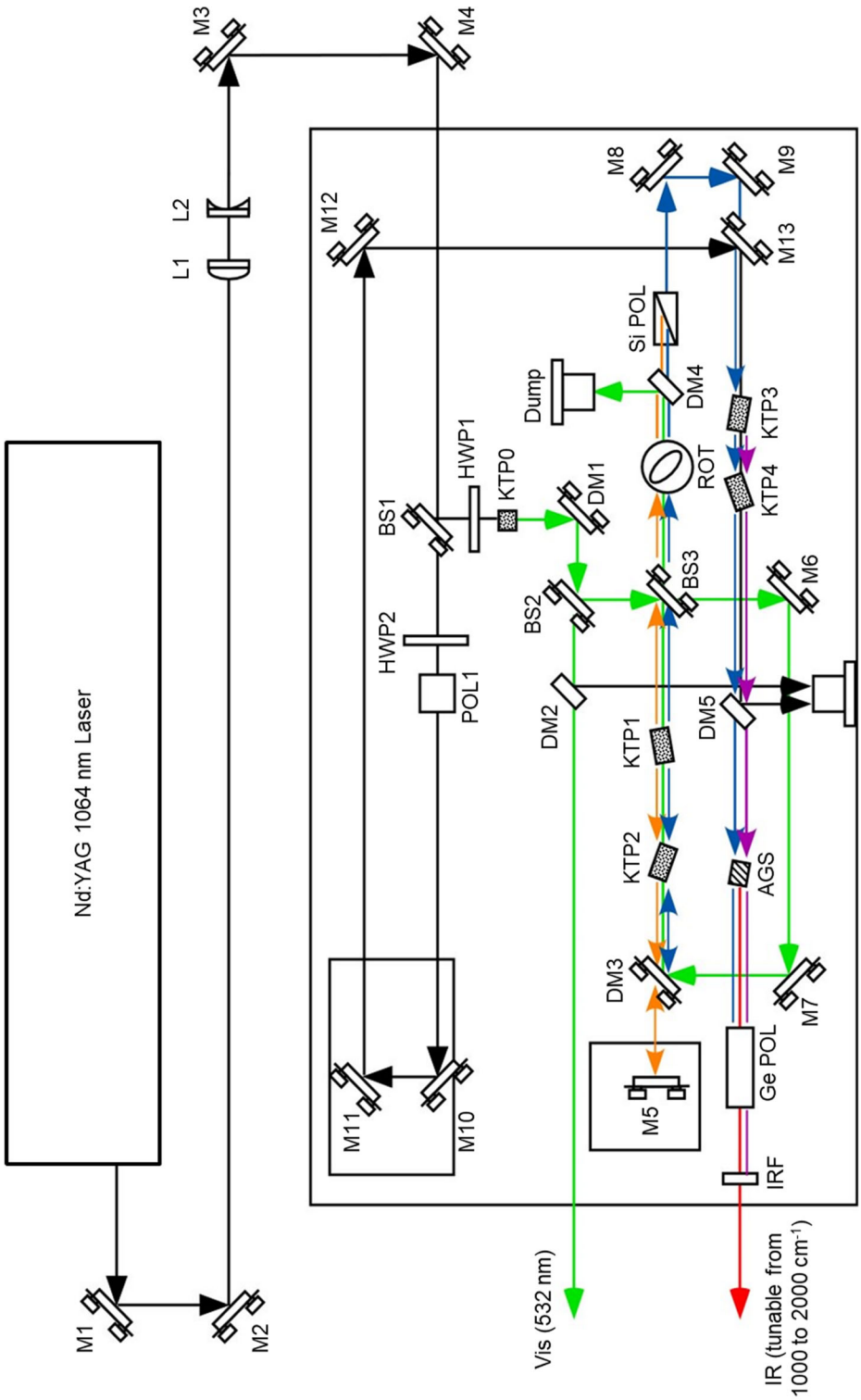


**Figure 2.10.** Top-view schematic of the optical parametric generation and amplification (OPG/OPA) set-up and the beam propagation throughout. This illustration is not to scale.

Mirrors M3 and M4 steer the beam into the OPG/OPA housing towards the first beam splitter (BS1) which reflects half of the fundamental beam towards the birefringent $KTiOPO_4$ (KTP) doubling crystal denoted as KTP0 in Figure 2.10 for second harmonic generation of the visible beam used in the SFG experiment. The KTP0 crystal requires both vertical and horizontal input beam polarizations to meet its phase-matching condition and generate the second harmonic of the fundamental beam. Therefore, a half-wave plate (HWP1) is used to rotate the horizontal polarization of the fundamental beam by 45°. Once the phase-matching condition is met, a 532 nm beam is generated and is sent towards the first dichroic mirror (DM1). Since the efficiency of the second harmonic process is not 100%, DM1 transmits the fundamental 1064 nm beam and steers the 532 nm beam towards BS2, and the transmitted beam from BS2 is further purified by going through DM2 which reflects the residual 1064 nm beam into a beam dump and transmits the 532 nm beam. The BS2 sends ~75% of the 532 nm beam towards the SFG set-up for use as the fixed visible frequency in the SFG experiment, and the other ~25% towards the first stage of crystals, mounted atop motorized stages for precise angle tuning and denoted as KTP1 and KTP2, for optical parametric generation.

These KTP crystals take the pump 532 nm beam and generate signal and idler beams of lower frequency, shown as the orange and blue arrows in Figure 2.10, respectively. The signal beam is at the higher-frequency of the generated beams, making the idler the lower-frequency beam. As BS3 sends a portion of the pump beam into the first stage crystals, the other portion goes to M6, M7, and finally DM3 which sends the pump beam back into the crystals along with the reflected signal beam from M5, which is on a translation stage to match the timing of the pulsed beams, in a seeding process to

amplify the generation of the beams. The amplified signal and idler then transmit through BS3 towards the rotator which turns their polarization in order to meet the polarization requirements for the second stage of KTP crystals (KTP3 and KTP4) used for optical parametric amplification through difference frequency generation. The DM4 reflects the unwanted 532 nm beam into a beam dump, and the undoped double-side polished silicon wafer used as a polarizer and set at the Brewster angle (Si POL) transmits only the idler beam (blue arrow) for use in the DFG process.

The other half of the pump 1064 nm beam transmitted through BS1 is sent through a delay (mirrors M10 and M11 which are on a translation stage, and mirror M12), to align both spatially and temporally at the second stage of KTP crystals, mounted atop motorized stages, along with the idler beam from the first stage, which is now considered the signal beam for the second stage, and steered by M8 and M9. By taking the difference of the input frequencies (1064 pump and idler beam from first stage), the KTP3 and KTP4 generate a new idler beam, designated by a purple arrow in Figure 2.10. This beam is tuned in the IR frequencies between 2000 and 4000 $cm^{-1}$ and can be used to probe the C≡N and C–H stretching regions of molecules. In order to study C–F bonds lower frequency infrared radiation is necessary, so the OPG/OPA illustrated in Figure 2.10 was outfitted with a third DFG stage that generates the necessary frequencies.

The dichroic mirror DM5 sends the 1064 nm beam to a beam dump, transmitting the signal and idler from the second stage (blue and purple arrows, respectively), now considered the pump and signal beams for the third stage, so that they align spatially at a $AgGaSe_2$ crystal mounted atop a motorized stage and denoted as AGS in Figure 2.10. The energy of the beams before the AGS crystal was measured to be ~2 mJ/pulse. The AGS

nonlinear crystal generates a new beam, the idler from the third stage shown as the red arrow in Figure 2.10, which is at the difference of the input frequencies and can be tuned from 1000 to 2000 $cm^{-1}$. A double-side polished undoped germanium wafer set at the Brewster-angle for the third-stage pump beam was used as a polarizer (Ge POL) to dump the beam, and an IR filter (IRF) was used to block the third-stage signal beam to separate out only the infrared radiation (third stage idler beam) that will be used in the SFG experiment. The motorized mounts for the three stages of crystals are connected to a computer through two 25-pin RS-232 serial cables attached to a board with motion control modules for each of the motors. This allows for angle-tuning of the crystals using the LaserVision motor controls software installed onto the computer. By careful alignment of the mirrors and angle tuning of the first, second, and third stage crystals on their motorized mounts, the energy and frequency of the final IR beam can be optimized, and is on the order of 15 to 45 μJ, as shown by the IR energy profile scanned from 1100–1800 $cm^{-1}$ and plotted in Figure 2.11.

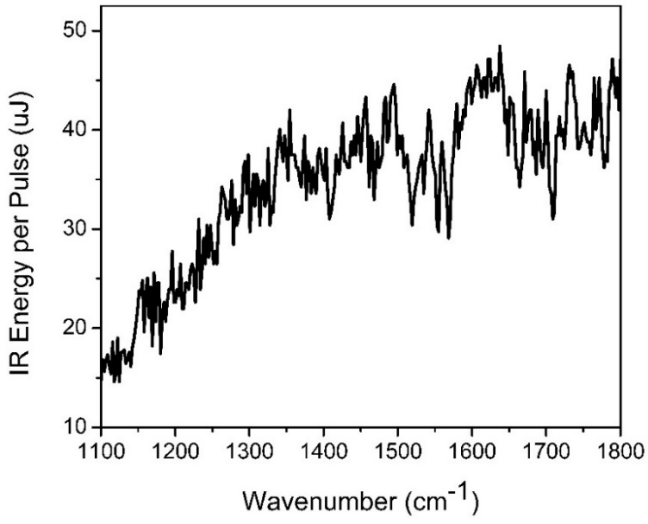


**Figure 2.11.** The energy profile of the IR radiation at the output of the OPG/OPA scanned from 1100–1800 $cm^{-1}$.

### 2.2.2. Low-Frequency SFG Spectrometer Set-up

Once the infrared and visible beams have been generated, they propagate into the SFG spectrometer as shown by the red and green arrows, respectively, in the schematics shown in Figure 2.12. The IR beam transmits through a second Ge polarizer, denoted as Ge POL2 in both illustrations, to ensure that only the frequencies between 1000–2000 $cm^{-1}$ are used in the low-frequency SFG experiment. The diverging IR beam from the OPG/OPA is then focused using a $BaF_2$ lens, designated as L3 in Figure 2.12B, and is steered using two evaporated-gold slides as mirrors M14 and M15 through a second $BaF_2$ lens (L4) to focus the beam to the sample. Commercially available gold mirrors were not used because they were found to have a coating that absorbs infrared radiation in the frequencies scanned in the experiments outlined in this dissertation.

As shown in Figure 2.12A, the visible beam is steered using M16 and M17 through a Galilean telescope (L5 and L6) to make the beam smaller and thereby more intense at the sample stage. Mirrors M18 and M19 are mounted on a translation stage to align the 532 nm beam temporally with the IR beam at the sample stage. The beam intensity is attenuated by changing the rotation of HWP1 while the polarizer cube POL2 is fixed, depending on the necessity for the sample. For all the SFG spectra presented in this dissertation, the beam was used at full intensity. Mirror M20 sends the beam through HWP2 which is used to tune the polarization of the visible beam at the sample stage. Mirrors M21 and M22 were used to steer the visible beam to the sample stage, as shown in Figure 2.12B.

The geometry of the system, illustrated schematically in Figure 2.12B, has incidence angles of 50° for visible beam and 60° for the IR beam, with respect to the surface normal. The samples were placed on the sample stage of the spectrometer and the laser

beams were aligned. Careful temporal alignment using the visible beam translation stage and spatial alignment of the two beams at the sample surface are necessary to optimize the emitted SFG signal. The generated SFG beam (shown as the blue arrows in Figure 2.12B) is steered by M23 and M24 through short-pass filters (F1 and F2) that transmit only the SFG wavelengths and absorb the visible beam. A Glan-Taylor polarizer cube, designated as POL3 in both schematics of Figure 2.12, dictates the polarization of the SFG beam for the experiments, and L7 focuses the weak SFG beam at the photomultiplier tube (PMT) used as the detector for the system.

The SFG signal collected by the PMT is processed by a gated boxcar integrator communicating with a computer where the averaged SFG signal is plotted versus the IR wavenumber using a homemade LabView program. The LabView program communicates with the OPG/OPA LaserVision software to mechanically adjust the angles of the crystals on their motorized mounts to scan the IR radiation from 1000 to 2000 $cm^{-1}$. The plot of infrared wavenumber versus SFG signal is the surface vibrational spectrum. The system described here is enclosed in a box that was purged with dry nitrogen gas for at least 30 minutes before the spectra were collected, and was continuously purged during the experiment to reduce the absorption of IR radiation by ambient water vapor.

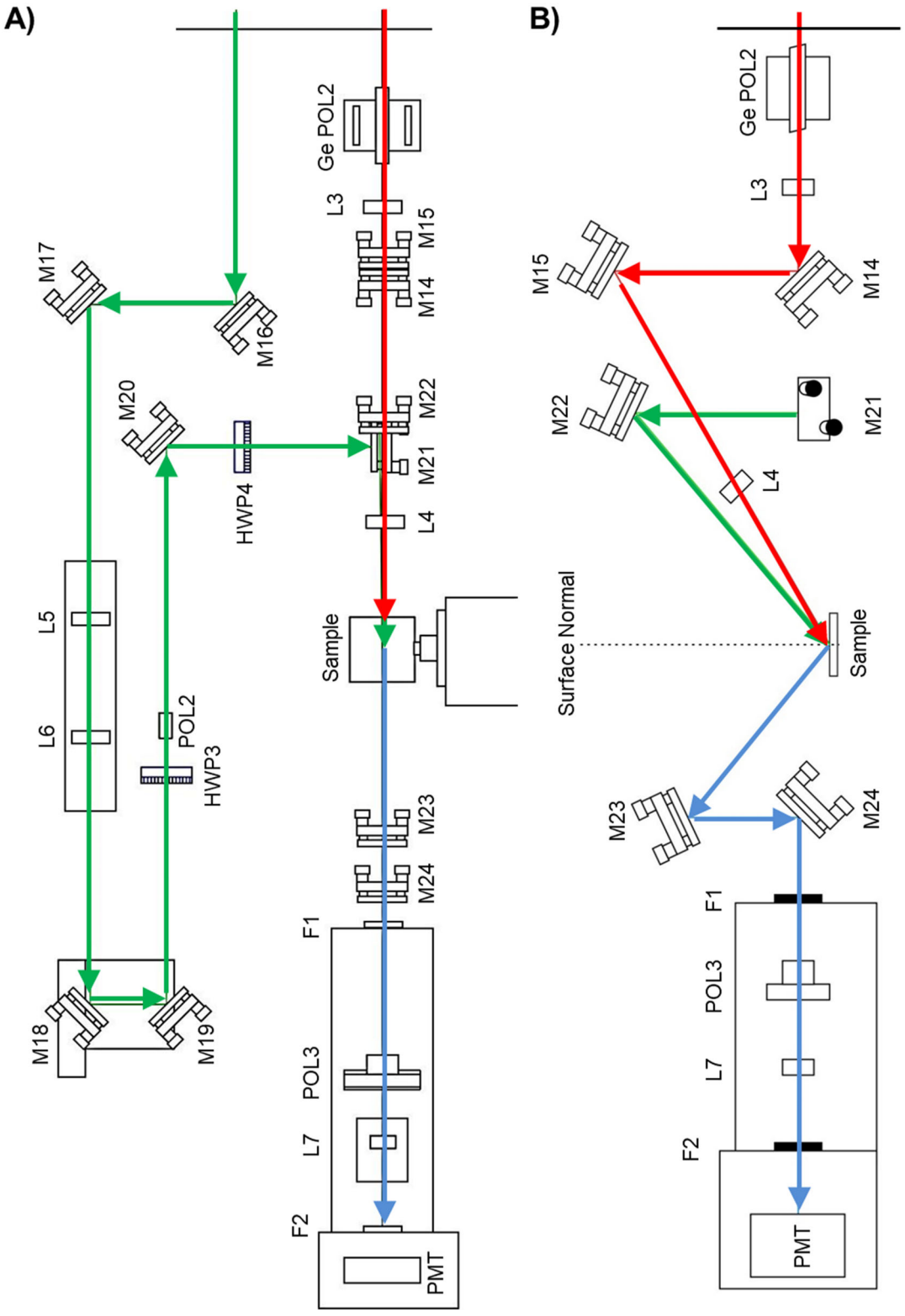


**Figure 2.12.** Schematic A) top view and B) side view of the low-frequency SFG spectrometer. This illustration is not to scale.

### 2.2.3. Low-Frequency SFG Spectrometer Characterization

Wavelength calibration of the SFG spectrometer was performed by placing a calibration standard polystyrene film in the path of the infrared beam as the SFG spectrum of a bare gold slide was collected. This procedure causes the IR radiation to be absorbed and large dips to be observed in the SFG spectrum of bare gold, as shown by the blue symbols in Figure 2.13A. The transmission FT-IR spectrum of the same polystyrene film was collected with 16 $cm^{-1}$ resolution and was used as a reference for resonance positions, as shown by the black solid line in Figure 2.13A. If the polystyrene resonance positions were found to be incorrect in the SFG spectrum of bare Au, the angles of the OPG/OPA crystals (only KTP2, KTP3, KTP4, and AGS) were adjusted using the LaserVision motor controls software to reflect the true wavelength of the IR beam. The resonances at 1370, 1450, 1493, and 1602 $cm^{-1}$ were used as calibration points and correspond to the aromatic C–C stretching and C–H bending modes of polystyrene. The similarities in the linewidth of the bands in the spectra of Figure 2.13A indicate that the resolution of the low-frequency spectrometer is on the order of ~15 $cm^{-1}$. The same procedure was carried out using polytetrafluoroethylene (PTFE) tape, as shown in Figure 2.13B, where the resonances at 1158 $cm^{-1}$ and 1227 $cm^{-1}$ correspond to the stretching vibrations of $CF_2$ groups.

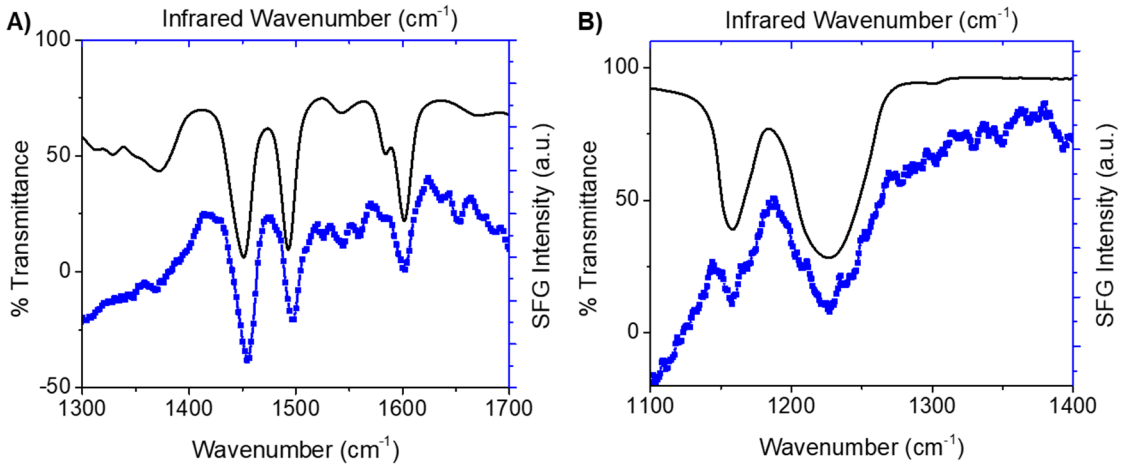


**Figure 2.13.** A) The transmission FT-IR spectrum of a polystyrene calibration standard collected using 16 $cm^{-1}$ resolution (black solid line) and the SFG spectrum of bare gold with the same polystyrene standard placed in the path of the IR beam (blue dashed line). B) The transmission FT-IR spectrum of a PTFE tape collected using 16 $cm^{-1}$ resolution (black solid line) and the SFG spectrum of bare gold with the same PTFE placed in the path of the IR beam (blue dashed line).

The SFG spectrum of a bare gold surface was collected daily to provide a background scan for the samples tested using the SFG spectrometer. Because SFG spectroscopy is a nonlinear technique, this spectrum cannot be background-subtracted from other spectra; however, the spectra can be taken as a ratio to account for the daily response function of the instrument to the gold surfaces. The bare gold spectra can thus be considered as a useful tool to determine the profile of the IR energy as the different frequencies are scanned.

### 2.2.4. High-Frequency SFG Spectrometer

The details of the high-frequency SFG spectrometer are found elsewhere.[25] Briefly, the pulsed, 20 Hz, 1064 nm beam from the EKSPLA laser is used to pump a second LaserVision optical parametric generation and amplification system that produces a

tunable-frequency infrared beam scanning from 2000–4000 $cm^{-1}$, and a 532 nm visible beam depicted as red and green arrows in the direction of the propagation of the beams, respectively. The two beams, with incidence angles of 60° and 50° from the surface normal, respectively, were spatially and temporally aligned at the sample surface to produce the SFG beam, as shown by blue arrows in Figure 2.14. This sum frequency (SFG) beam was filtered through a monochromator, collected using a PMT, and the resulting averaged data points were plotted using a LabView program. This high-frequency SFG spectrometer was used to scan the frequencies for the C≡N and C–H stretching vibrations, ranging from 2000–2300 $cm^{-1}$ and 2800–3050 $cm^{-1}$, respectively, in ppp and ssp polarization combinations where the letters denote the polarization of the SFG, visible, and IR beams, respectively. The final spectra of the samples are the average of at least 5 scans and have been normalized to the corresponding bare gold SFG spectrum to account for the gold response over the scanned frequencies.

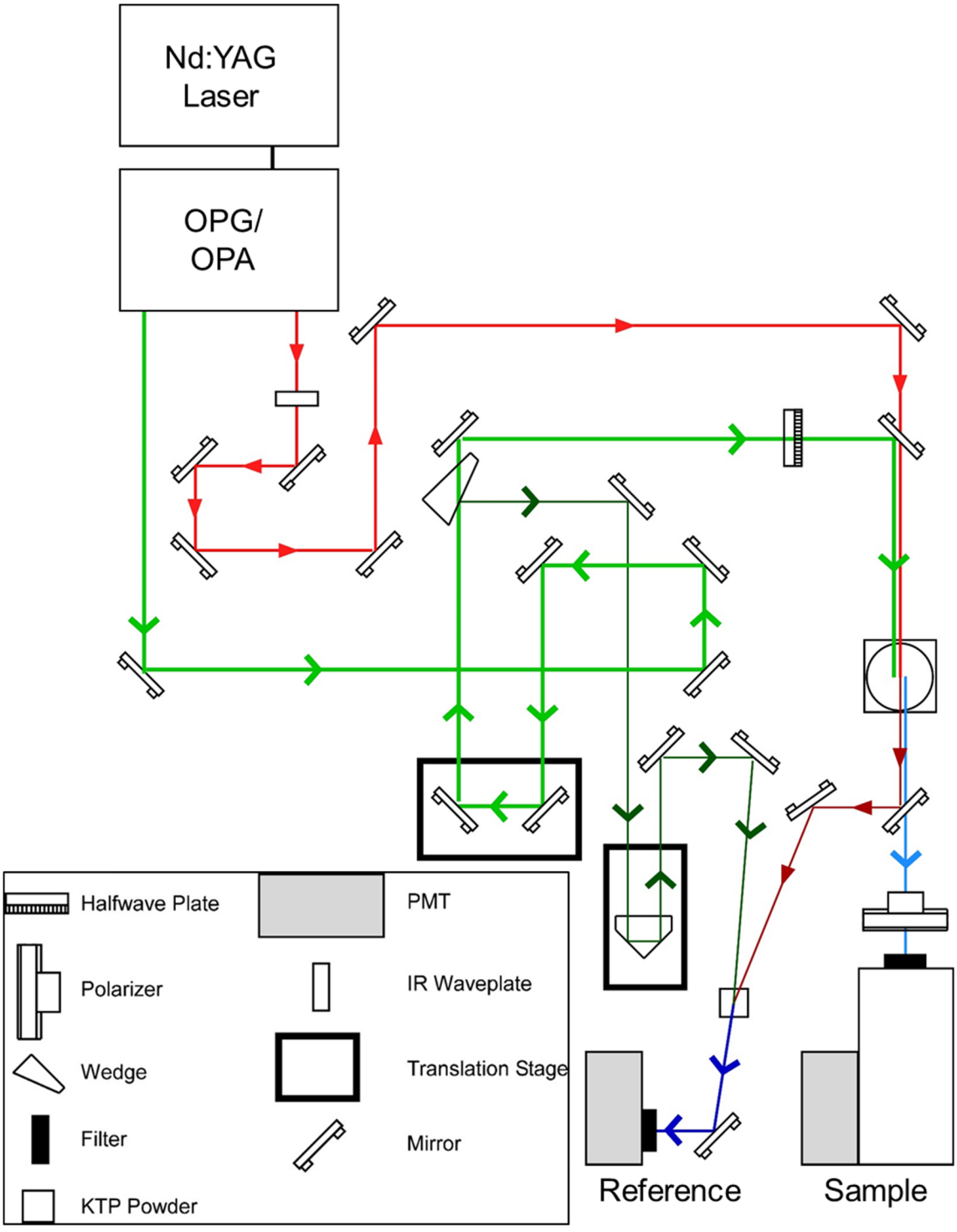


**Figure 2.14.** A schematic top view of the high-frequency SFG spectrometer. This illustration is not to scale. The spectrometer is built in three dimensions, therefore, some mirrors were excluded from this schematic. This illustration is meant only as a guide for the general beam propagation throughout the instrument.

The IR beam reflected from the sample surface as well as 10% of the input visible beam (diverted by use of a wedge set in the path of the visible beam) were used to generate a reference SFG beam from KTP powder, as shown schematically in Figure 2.14. This reference arm to the SFG spectrometer generates a profile of the IR energy throughout the surveyed frequency range, giving information about the absorption, or lack thereof, of the IR radiation by the liquids used in solid-liquid SFG experiments, as demonstrated by the spectra in Figures 3.7 and 3.8A in Chapter 3. The data from the reference arm was gathered simultaneously with the SFG signal from the sample surface and plotted separately during the experiment so that the spectra could be monitored for IR absorption as it was collected.

### 2.2.5. Cell for Solid-Liquid SFG Experiments

A homemade cell was designed and built for the solid-liquid SFG experiments and is illustrated schematically in Figure 2.15. The cell consisted of a PTFE body with a shelf to hold a fluoropolymer-coated silicon o-ring. Contacting liquids were dropped onto the gold slide containing the self-assembled monolayer. A small Kalrez o-ring under the gold slide helped to press the sample against a window so as to minimize the space, and therefore the amount of liquid, between the slide and the window. A $CaF_2$ window was used unless otherwise noted because it is does not absorb IR radiation in the frequency ranges surveyed. The window was drag-wiped with methanol and treated with UV light for an hour to remove as much organic contamination as possible before being placed into the cell. A thin, but sturdy, metal flange covered with PTFE tape was fastened over the window by tightening four nuts at the bottom of the cell to press all the components together, as shown in Figure 2.15. The cell was assembled in a glovebox under a $N_2$ atmosphere to prevent the absorption of water by the contacting liquids when necessary.

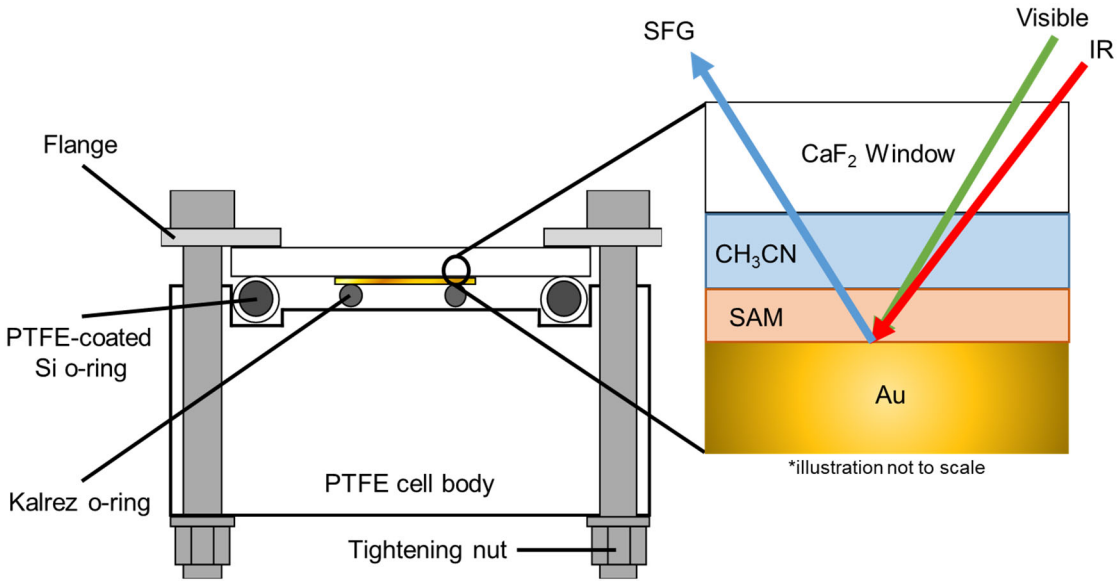


**Figure 2.15.** Schematic side view of the PTFE cell used for solid-liquid SFG experiments. This illustration is not to scale.

## 2.3. References

1. Zhuang, X.; Miranda, P. B.; Kim, D.; Shen, Y. R., Mapping Molecular Orientation and Conformation at Interfaces by Surface Nonlinear Optics. *Phys. Rev. B* **1999,** *59*, 12632–12640.

2. Bain, C. D., Sum-frequency Vibrational Spectroscopy of the Solid/Liquid Interface. *J. Chem. Soc., Faraday Trans.* **1995,** *91*, 1281–1296.

3. Wang, H.-F.; Gan, W.; Lu, R.; Rao, Y.; Wu, B.-H., Quantitative Spectral and Orientational Analysis in Surface Sum Frequency Generation Vibrational Spectroscopy (SFG-VS). *Int. Rev. Phys. Chem.* **2005,** *24*, 191–256.

4. Tian, C. S.; Shen, Y. R., Recent Progress on Sum-Frequency Spectroscopy. *Surf. Sci. Rep.* **2014,** *69*, 105–131.

5. Hirose, C.; Akamatsu, N.; Domen, K., Formulas for the Analysis of Surface Sum-Frequency Generation Spectrum by CH Stretching Modes of Methyl and Methylene Groups. *J. Chem. Phys.* **1992,** *96*, 997–1004.

6. Boyd, R. W., *Nonlinear Optics*. 3 ed.; Academic Press: 2008; p 640.

7. Born, M.; Wolf, E., *Principles of Optics*. 6 ed.; Pergamon: 1980.

8. Saito, K.; Peng, Q.; Qiao, L.; Wang, L.; Joutsuka, T.; Ishiyama, T.; Ye, S.; Morita, A., Theoretical and Experimental Examination of SFG Polarization Analysis at Acetonitrile–Water Solution Surfaces. *Phys. Chem. Chem. Phys.* **2017,** *19*, 8941–8961.

9. Sun, Z.; Zheng, D.; Baldelli, S., Study of the Wetting of Paraffin Films on the Metal Surface in the Dynamic Dip-Coating Process Using Compressive-Sensing Sum-Frequency Generation Microscopy. *J. Phys. Chem. C* **2018,** *122*, 26543–26553.

10. Porter, M. D.; Bright, T. B.; Allara, D. L.; Chidsey, C. E. D., Spontaneously Organized Molecular Assemblies. 4. Structural Characterization of *n*-Alkyl Thiol Monolayers on Gold by Optical Ellipsometry, Infrared Spectroscopy, and Electrochemistry. *J. Am. Chem. Soc.* **1987,** *109*, 3559–3568.

11. Jacob, J. D. C.; Lee, T. R.; Baldelli, S., In Situ Vibrational Study of the Reductive Desorption of Alkanethiol Monolayers on Gold by Sum Frequency Generation Spectroscopy. *J. Phys. Chem. C* **2014,** *118*, 29126–29134.

12. Tyrode, E.; Johnson, C. M.; Rutland, M. W.; Day, J. P. R.; Bain, C. D., A Study of the Adsorption of Ammonium Perfluorononanoate at the Air−Liquid Interface by Vibrational Sum-Frequency Spectroscopy. *J. Phys. Chem. C* **2007,** *111*, 316–329.

13. Iwahashi, T.; Miyamae, T.; Kanai, K.; Seki, K.; Kim, D.; Ouchi, Y., Anion Configuration at the Air/Liquid Interface of Ionic Liquid [bmim]OTf Studied by Sum-Frequency Generation Spectroscopy. *The Journal of Physical Chemistry B* **2008,** *112*, 11936–11941.

14. Karageorgiev, P.; Petrov, J. G.; Motschmann, H.; Moehwald, H., Why Fluorination of the Polar Heads Reverses the Positive Sign of the Dipole Potential of Langmuir Monolayers: A Vibrational Sum Frequency Spectroscopic Study. *Langmuir* **2013,** *29*, 4726–4736.

15. Miura, Y. F.; Takenaga, M.; Koini, T.; Graupe, M.; Garg, N.; Graham, R. L., Jr.; Lee, T. R., Wettabilities of Self-Assembled Monolayers Generated from $CF_3$-Terminated Alkanethiols on Gold. *Langmuir* **1998,** *14*, 5821–5825.

16. Smith, D. C.; Saunders, R. A.; Nielsen, J. R.; Ferguson, E. E., Infrared and Raman Spectra of Fluorinated Ethanes. IV. The Series $CH_3$–$CH_3$, $CH_3$–$CH_2F$, $CH_3$–$CHF_2$, and $CH_3$–$CF_3$. *J. Chem. Phys.* **1952,** *20*, 847-859.

17. Förner, W.; Badawi, H. M., Ab Initio Calculations of Vibrational Frequencies, Potential Functions of Internal Rotations and Vibrational Infrared and Raman Spectra for 3,3,3-Trifluoropropanal. *Molecular modeling annual* **2000,** *6*, 99-111.

18. Guirgis, G. A.; Horn, A.; Klaeboe, P.; Nielsen, C. J., Vibrational Spectroscopic Studies, Conformations and Ab Initio Calculations of 3,3,3-Trifluoropropyltrichlorosilane. *Spectrochim. Acta, Part A* **2005,** *61*, 1335–1346.

19. Gruodis, A.; Aleksa, V.; Powell, D. L.; Klaeboe, P.; Nielsen, C. J.; Guirgis, G. A.; Durig, J. R., Vibrational Spectroscopic Studies, Conformations and Ab Initio

Calculations of 1,1,1-Trifluoropropyltrifluorosilane. *J. Raman Spectrosc.* **2003,** *34*, 711–724.

20. Li, Y. S.; Cox, F. O.; Durig, J. R., Low-Resolution Microwave, Infrared, and Raman Spectra, Conformational Stability, and Vibrational Assignment of 2,2,2-Trifluoroethyl Methyl Ether. *J. Phys. Chem.* **1987,** *91*, 1334–1344.

21. Tamada, K.; Ishida, T.; Knoll, W.; Fukushima, H.; Colorado, R., Jr.; Graupe, M.; Shmakova, O. E.; Lee, T. R., Molecular Packing of Semifluorinated Alkanethiol Self-Assembled Monolayers on Gold: Influence of Alkyl Spacer Length. *Langmuir* **2001,** *17*, 1913–1921.

22. Durig, J. R.; Yu, Z.; Guirgis, G. A., Conformational Stability, Barriers to Internal Rotation, Vibrational Assignment, and Ab Initio Calculations of 2,2-Difluorobutane. *J. Mol. Struct.* **1999,** *509*, 115–135.

23. Zhang, J.-y.; Huang, J. Y.; Shen, Y.-R., *Optical parametric generation and amplification*. CRC Press: 1995; Vol. 19.

24. Zhang, J.; Huang, J.; Shen, Y. R., *Fundamentals of Optical Parametric Processes and Oscillations*. CRC Press: 1996; Vol. 20.

25. Zhang, H.; Romero, C.; Baldelli, S., Preparation of Alkanethiol Monolayers on Mild Steel Surfaces Studied with Sum Frequency Generation and Electrochemistry. *The Journal of Physical Chemistry B* **2005,** *109*, 15520-15530.

# Chapter 3. The Solid-Liquid Interface of Partially-Fluorinated Self-Assembled Monolayers on Gold and Acetonitrile: Surface Dipole Influence on Liquid Structure

## 3.1. Introduction

The wetting of solid surfaces is a complex phenomenon that is governed by a balance of interactions between the cohesion of the liquid molecules and their adhesion at the solid interface.[1] For a complete understanding of the interactions that govern such macroscale properties of surfaces, studies at the nanoscale solid-liquid interface are necessary. Several reviews on solid-liquid interfaces have been published[2-3] and have shown sum frequency generation spectroscopy to be a useful tool in selectively probing buried interfaces. Vibrational sum frequency generation (SFG) is a nonlinear spectroscopic technique that obtains signal from the second-order process forbidden in centrosymmetric media under the electric-dipole approximation.[3] By generating a vibrational spectrum at the interface between two media where there is no inversion symmetry, SFG provides information about the order and average orientation of functional groups at the molecular scale. SFG spectroscopy can be performed in-situ, allowing for the buried solid-liquid interface to be probed in real time and under ambient conditions.

Self-assembled monolayers (SAMs) of alkanethiol molecules on gold were used as the solid surfaces in this study due to the ability to tailor the functional groups at the end of the alkane chain used to generate the monolayer. Synthetic modification of the SAMs produces films with desirable physical properties for specific applications, such as anti-

adhesion and anti-corrosion. Studies undertaken to determine the SAM structure and organization when in contact with liquids have shown the effect of a change in the terminal group on the wettability of the thin films.[4-7] Recently, Zenasni, et. al., using selectively fluorinated SAMs on gold with oppositely oriented dipoles at the chain terminus, concluded that an inversion of the terminal dipole in a monolayer can cause a reversal of the "odd-even" effect in the film wetting behavior with polar contacting liquids.[7] Furthermore, increasing the length of the hydrocarbon chain atop the terminal dipole, effectively burying the dipole into the film, causes the contact angle to start anew -- with the fluorocarbon serving as a surrogate surface.[8]

These findings provide evidence for the influence of surface dipoles on the macroscopic wettability of surfaces, which was previously determined to be less significant than hydrogen bonding interactions.[4] Despite the many studies analyzing the structure of fluorinated SAMs in comparison to their contact angle (wettability) results,[5] there is insufficient information about the liquid structure at the SAM interface, possibly due to the limited number of techniques able to survey buried interfaces. Studies have shown water dipoles reorienting when in proximity to different charged groups using SFG,[9] and ethanol selectively wetting polar functional groups in a patterned surface using non-contact atomic force microscopy.[10]

This study aims to elucidate the role of terminal dipoles on the orientation of liquid molecules at the SAM interface and relate these findings to their macroscopic wetting phenomena. The adsorbates used in the study, shown in Figure 3.1, consist of two types of partially fluorinated alkanethiols -- $CF_3(CH_2)_nSH$, where n = 17 and 16 (**F1HnSH**), and $CD_3(CF_2)_6(CH_2)_{10}SH$ (**D1F6H10SH**) -- as well as a fully deuterated alkanethiol (**D18SH**)

to serve as a reference. In order to make full use of the spectroscopy and the need for clearly separated mode frequencies, the SAMs used in this study were deuterated where necessary.

Acetonitrile ($CH_3CN$) was selected as the liquid for this investigation due to its use as a polar probe in contact angle studies as well as its two distinct chromophores available to examine, providing a broad range of data for the purpose of determining its orientation at the surface. Previous studies using surface-sensitive spectroscopic methods, such as SFG, were undertaken to determine the organization and orientation of $CH_3CN$ at solid dielectric interfaces,[11-16] and metal electrode interfaces.[17-18] The interaction of acetonitrile and SAMs has also been examined, however, these studies describe only the SAM organization under the liquid.[19-22] Therefore, this study compares the interaction between acetonitrile and the terminal dipoles of partially-fluorinated self-assembled monolayers on gold in the C≡N and C–H stretching regions between 2000–2300 $cm^{-1}$ and 2800–3050 $cm^{-1}$, respectively. Intuition says that SAMs with oppositely oriented dipoles can cause a change in the interfacial structure of the acetonitrile, holding true for the systems probed in this study; the solid-liquid SFG spectra shown herein clearly show dipole-dipole interactions at the nanoscale between a polar contacting liquid and functionalized surfaces.

SFG at solid-liquid interfaces must be carried out carefully because the collected signal can be easily influenced by the laser beams traveling through several interfaces as well as through the bulk liquid. To that effect, spectra at each solid-liquid interface were gathered and a reference SFG setup, shown schematically in Figure 2.14 in Chapter 2, was built using the IR beam transmitted through the solid-liquid interface and reflected from

the sample surface to clearly show that interference from solvent absorption was not included in the collected SFG signal.

## 3.2. Experimental Procedures

### 3.2.1. Materials and Methods

Gold shot (99.999%) was purchased from Kamis, Inc. Chromium rods (99.9%) were purchased from R. D. Mathis Company. Single-side polished, single-crystal silicon (100) wafers were purchased from University Wafer. Tetrahydrofuran (THF) and dichloromethane (DCM) from Millipore Sigma, were dried over $CaH_2$ (Millipore Sigma) and distilled prior to use. The other solvents, toluene, 1,3-dimethyl-3,4,5,6-tetrahydro-2(1H)-pyrimidinone (DMPU), and ethyl acetate (Millipore Sigma); diethyl ether ($Et_2O$) and methanol (MeOH) both from Avantor Performance Materials; and ethanol (EtOH, Aaper Alcohol and Chemical Co.) were all used as received unless noted otherwise. Anhydrous acetonitrile ($CH_3CN$) was purchased from Sigma-Aldrich, distilled to remove impurities such as water, and kept under a nitrogen-atmosphere in a glove box. Triethyl amine ($Et_3N$), tributyl tin hydride ($Bu_3SnH$), azobisisobutyronitrile (AIBN), methanesulfonyl chloride (MsCl), potassium thioacetate (KSAc), and lithium aluminum hydride ($LiAlH_4$), were all purchased from Millipore Sigma and used as received. 4-Nitrobenzeneulfonyl chloride (NsCl, TCI America) and 10% Pd/C (Alfa Aesar) were used as received.

Magnesium sulfate ($MgSO_4$, Fisher Chemical); lithium chloride (LiCl, Acros Chemicals); sodium iodide (NaI), hydrochloric acid (HCl), both from Mallinckrodt Chemicals; sulfuric acid ($H_2SO_4$, J. T. Baker); and Celite (Millipore Sigma), were used as received. Dideuterosulfuric acid ($D_2SO_4$, Millipore Sigma), lithium aluminum deuteride

($LiAlD_4$, BOC Sciences), and deuterium oxide ($D_2O$, Cambridge Isotope Laboratories) were used as received; $LiAlD_4$ was stored under an inert atmosphere. Tributyl tin deuteride ($Bu_3SnD$) was prepared by treatment of $Bu_3SnH$ with 2.0 M cyclohexylmagnesium chloride solution (Millipore Sigma) and galvinoxyl (TCI America) followed by $D_2O$.[23] The intermediate methyl 17-(benzyloxy)-2,2,3,3,4,4,5,5,6,6,7,7-dodecafluoroheptadecanoate was prepared using a procedure found in the literature.[7] All $^1H$, $^{19}F$, and $^{13}C$ NMR spectra were collected using chloroform-d as the solven (Cambridge Isotope Laboratories). The chloroform ($CHCl_3$) used to collect $^2H$ NMR spectra was purchased from Millipore Sigma. The $CDCl_3$ and $CHCl_3$ was referenced at 7.26 ppm or 77.16 ppm for the $^1H$, $^2H$, and $^{13}C$ NMR spectra, respectively. The silica gel used for column chromatography was obtained from Sorbent Technologies. Absolute ethanol (200 proof, from Decon Labs, Inc.) and tetrahydrofuran (THF, from J.T. Baker) were used as received for the making of 1 mM alkanethiol solutions and rinsing of the generated SAMs on the gold slides.

The structures of the alkanethiols used as adsorbates to make the monolayer films on gold are depicted in Figure 3.1. Octadecane-$d_{37}$-1-thiol 99.1% (**D18SH**) was purchased from CDN Isotopes and used as received. The dipole-terminated adsorbates 17,17,17-Trifluoroheptadecane-1-thiol (**F1H16SH**) and 18,18,18-Trifluorooctadecane-1-thiol (**F1H17SH**) were synthesized following procedures found in the literature.[7]

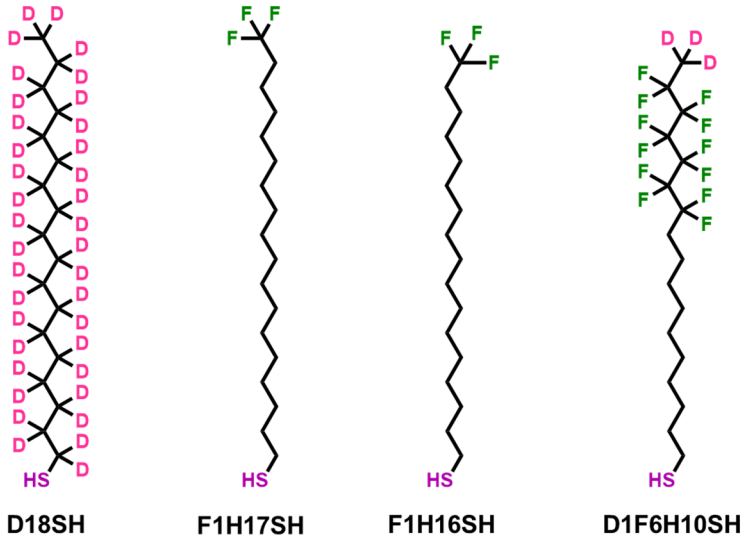


**Figure 3.1.** Molecular structures of the partially fluorinated alkanethiols (**F1H17SH**, **F1H16SH**, and **D1F6H10SH**) and deuterated alkanethiol (**D18SH**) used to generate self-assembled monolayers on gold in this study.

### 3.2.2. Synthesis of the Adsorbate D1F6H10SH

The deuterated adsorbate 11,11,12,12,13,13,14,14,15,15,16,16-dodecafluoroheptadecane-17,17,17-$d_3$-1-thiol (**D1F6H10SH**) was synthesized according to Scheme 3.1.

**Scheme 3.1.** Synthetic route used to prepare 11,11,12,12,13,13,14,14,15,15,16,16-dodecafluoroheptadecane-17,17,17-$d_3$-1-thiol (**D1F6H10SH**).

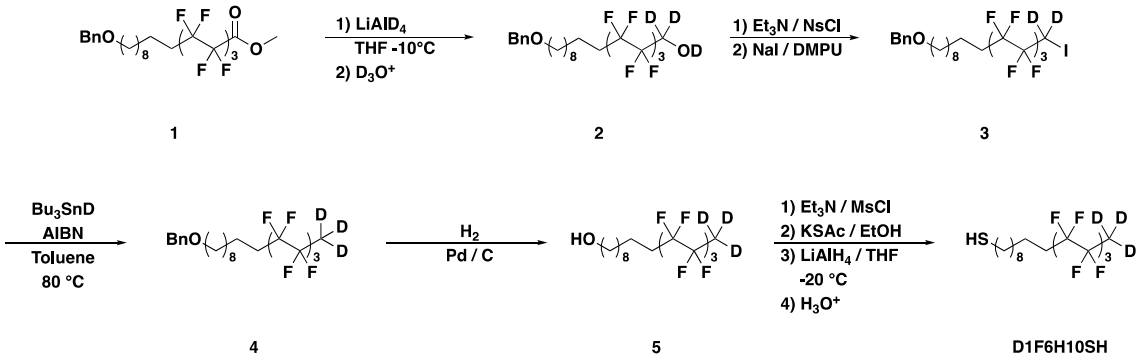

*17-(Benzyloxy)-2,2,3,3,4,4,5,5,6,6,7,7-dodecafluoroheptadecan-1,1-$d_2$-1-ol-d (2).* Into a 50 mL round-bottomed flask was added $LiAlD_4$ (0.0207 g, 0.500 mmol), inside a nitrogen-filled glove box; the flask was sealed with a rubber septum and subsequently removed from the glove box. THF (5 mL, previously degassed) was added into the round-bottomed flask to create a slurry at -20 °C. Afterward, intermediate **1** (0.197 g; 0.325 mmol), dissolved in THF (10 mL, previously degassed), was added dropwise, via syringe, into the $LiAlD_4$ slurry. The mixture was stirred at -20 °C for 4 h under a flow of argon. The reaction was then quenched with cold $D_2O$ (5 mL) at -20 °C and acidified with a 1M $D_2SO_4$ solution (prepared in $D_2O$). The mixture was extracted with $Et_2O$ (3 × 25 mL), and the combined organic phase was washed with $D_2O$ (1 × 25 mL), brine (1 × 25 mL, prepared in $D_2O$), and dried with $MgSO_4$. After removal of the solvent via rotary evaporation, the crude alcohol was purified by column chromatography on silica gel using hexanes/EtOAc (90/10) as the eluent to give **2** in 65% yield. $^1$H NMR (500 MHz, $CDCl_3$): δ 7.36–7.26 (m, 5H), 4.50 (s, 2H), 3.46 (t, $J$ = 6.59 Hz, 2H), 2.09–1.98 (m, 2H), 1.64–1.55 (m, 4H), 1.43–1.25 (m, 14H). $^2$H NMR (77 MHz, $CHCl_3$): δ 3.99 (broad peak, 2D).

*(((11,11,12,12,13,13,14,14,15,15,16,16-Dodecafluoro-17-iodoheptadecyl-17,17-$d_2$)oxy)methyl) benzene (3).* Intermediate **2** (0.1228 g, 0.02112 mmol) and NsCl (0.057 g, 0.26 mmol) were dissolved in anhydrous DCM, and at 0 °C $Et_3N$ (0.10 mL, 0.72 mmol) was added dropwise. The reaction was stirred at rt until consumption of the starting material (monitored by TLC). Then, the reaction was quenched with 1M HCl (5 mL) followed by water (10 mL). The mixture was extracted with DCM (3 × 25 mL), and the organic layer was washed with water (1 × 25 mL), brine (1 × 25 mL), and dried over

$MgSO_4$. After removing the solvent via rotary evaporation, the crude compound was purified by recrystallization with hexanes to give the nosylate in ~58% yield. The nosylate intermediate (0.4145 g, 0.5414 mmol) and NaI (2.4 g, 16 mmol) were dissolved in 10 mL of DMPU in a 50 mL round-bottomed flask equipped with a condenser. The reaction was heated at 100 °C for 18 h. The reaction was cooled down to rt, after which water (50 mL) was added. The mixture was extracted with $Et_2O$ (3 × 25 mL). The combined organic phases were washed with a 10% LiCl solution (1 × 25 mL), water (1 × 25 mL), brine (1 × 25 mL), dried over $MgSO_4$, and evaporated to dryness using a rotary evaporator. The crude compound was purified by column chromatography on silica gel using hexanes/EtOAc (98/2) as the eluent to give intermediate **3** in 70% yield. $^1$H NMR (500 MHz, $CDCl_3$): δ 7.35–7.27 (m, 5H), 4.50 (s, 2H), 3.46 (t, $J$ = 6.58 Hz, 2H), 2.09–1.98 (m, 2H), 1.64–1.57 (m, 4H), 1.41–1.25 (m, 14H). $^2$H NMR (77 MHz, $CHCl_3$): δ 3.63 (broad peak, 2D).

*(((11,11,12,12,13,13,14,14,15,15,16,16-Dodecafluoroheptadecyl-17,17,17-$d_3$)oxy)methyl)benzene (4).* Intermediate **3** (0.515 g, 0.746 mmol) and AIBN (10 mol %) were dissolved in anhydrous toluene. Afterward, $Bu_3SnD$ (1.188 g, 4.068 mmol) was added dropwise to the solution at rt, and the reaction was heated at 85 °C for 6 h. After cooling to rt, excess $Bu_3SnI$ salt was removed by diluting the reaction mixture with $Et_2O$ (100 mL) and filtering through a silica pad. The $Et_2O$/toluene solvent mixture was removed by rotary evaporation, and the resulting crude was purified by column chromatography on silica gel using hexanes as the eluent to give **4** in 100% yield. $^1$H NMR (500 MHz, $CDCl_3$): δ 7.35–7.28 (m, 5H), 4.50 (s, 2H), 3.46 (t, $J$ = 6.58 Hz, 2H), 2.08–1.99 (m, 2H), 1.64–1.57 (m, 4H), 1.41–1.25 (m, 14H). $^2$H NMR (77 MHz, $CHCl_3$): δ 1.82 (broad peak, 3D).

*11,11,12,12,13,13,14,14,15,15,16,16-Dodecafluoroheptadecan-17,17,17-$d_3$-1-ol (5).* A slurry of 10% Pd/C (0.171 g, 0.161 mmol) in anhydrous MeOH (10 mL) was prepared in an oven-dried 2-neck round-bottomed flask. The system was evacuated and refilled with $H_2$ gas and allowed to stir for 15 min. Then, intermediate **4** (0.363 g, 0.642 mmol) in 10 mL of anhydrous MeOH were transfered into the flask and allowed to stir at rt for 16 h. Afterward, $H_2$ was carefully removed from the system, and the reaction was diluted with $Et_2O$ (100 mL). To remove the Pd/C, the solution was filtered through Celite. Intermediate **5** was obtained after removing the solvent by rotary evaporation in 65% yield. $^1$H NMR (400 MHz, $CDCl_3$): δ 3.64 (q, $J$ = 6.11 Hz, 2H), 2.11–1.97 (m, 2H), 1.62–1.53 (m, 4H), 1.41–1.25 (m, 14H), 1.20 (t, $J$ = 5.27 Hz, 1H). $^2$H NMR (77 MHz, $CHCl_3$): δ 1.80 (broad peak, 3D).

*11,11,12,12,13,13,14,14,15,15,16,16-Dodecafluoroheptadecane-17,17,17-$d_3$-1-thiol* **(D1F6H10SH).** Alcohol **5** (0.300 g, 0.631 mmol) was dissolved in anhydrous THF, and the solution was cooled to 0 °C. Subsequently, $Et_3N$ (0.30 mL, 2.1 mmol) was added to the solution and allowed to stir for 10 min. Afterward, MsCl (0.20 mL, 2.6 mmol) was added dropwise, and the reaction was allowed to stir at rt for 6 h. To quench the reaction, cold water (50 mL) was added. The mesylate was extracted with $Et_2O$ (3 × 25 mL), and the combined organic layers were washed with 1M HCl (1 × 50 mL), water (1 × 50), and brine (1 × 50). The organic phase was dried over $MgSO_4$ followed by removal of the solvent with a rotary evaporator. The crude mesylate was carried to the next step without further purification. The crude mesylate and KSAc (0.117 g, 1.02 mmol) were dissolved in 50 mL of anhydrous EtOH. The reaction was stirred at 80 °C for 6 h. Then, the solvent

was reduced to ~10 mL using a rotary evaporator, and the remaining solution was diluted with 100 mL of water. The thioacetate was extracted with $Et_2O$ (3 × 50 mL), washed with water (1 × 75 mL), brine (1 × 75 mL), and dried with $MgSO_4$. The solvent was then removed by rotary evaporation. The crude thioacetate was carried to the next step without further purification. To an oven-dried flask equipped with an addition funnel was added $LiAlH_4$ (0.023 g, 0.61 mmol) under the flow of Ar. Anhydrous THF (15 mL, previously degassed) was added to the flask to create a slurry. A solution of the thioacetate (0.217 g, 0.407 mmol) dissolved in THF (15 mL, previously degassed) was added dropwise to the slurry at -20 °C.

The reaction was stirred at -20 °C for 3 h under an atmosphere of Ar. The reaction was quenched with cold water (10 mL, previously degassed), under Ar and acidified with 1M $H_2SO_4$ (15 mL, previously degassed). The solution remained under an atmosphere of Ar until a pH of ~1 was obtained. The solution was extracted with $Et_2O$ (3 × 50 mL), washed with 1 M $H_2SO_4$ (1 × 75 mL), water (1 × 75 mL), brine (1 × 75 mL), and dried with $MgSO_4$. The solvent was removed with a rotary evaporator, and the crude thiol was purified by column chromatography on silica gel using hexanes as the eluent. The thiol was obtained as a colorless waxy solid over 3 steps in 78 % yield. $^1$H NMR (MHz, $CDCl_3$): δ 2.52 (q, $J$ = 7.45 Hz, 2H), 2.09–1.98 (m, 2H), 1.63–1.57 (m, 4H), 1.37–1.28 (m, 14H). $^2$H NMR (77 MHz, $CHCl_3$): δ 1.80 (broad peak, 3D). $^{19}$F NMR (470 MHz, $CDCl_3$): δ -106.5 to -106.6 (m, 2F), -114.3 (m, 2F), -121.8 (m, 2F), -123.6 (m, 2F), -124.2 (m, 2F). $^{13}$C NMR (150 MHz, $CDCl_3$): δ 34.2, 31.1 (t, $J$ = 22.2 Hz), 29.5–29.2 (m), 28.5, 20.2, 17.9

(m). Broad peaks at δ120.5–109.3 are characteristic of a long perfluorocarbon chain.[24] HR-CI-MS, *m/z*: 490.1517 $[M-H]^+$.

### 3.2.3. Monolayer Formation and Characterization

#### 3.2.3.1. Substrate Preparation

The substrates used for the self-assembled monolayer (SAM) formation were prepared by the thermal evaporation of 100 Å of chromium followed by 1000 Å of gold onto silicon (100) wafers. The metals were evaporated under vacuum at a pressure of ~2 × $10^{-6}$ torr with a deposition rate of 0.5 Å/s. The gold wafers were cut into slides, rinsed with pure ethanol, and dried with a stream of ultra-pure nitrogen gas before measuring their optical constants with a Rudolph Auto EL III ellipsometer using a HeNe laser (632.8 nm) beam set at a 70° incident angle.

#### 3.2.3.2. Monolayer Formation

Immediately after the ellipsometric measurements, the gold slides were immersed in 1mM solutions of the alkanethiols in absolute ethanol and left to equilibrate for 48 h in the dark. The slides were then rinsed with THF followed by ethanol and dried with ultrapure nitrogen gas prior to taking ellipsometric thickness measurements. A value of 1.45 for the refractive index of an organic monolayer was used, consistent with the literature value used for SAMs.[25] The thicknesses reported are the average of nine measurements (three measurements per spot on the slide with three spots tested per slide) and are listed in Table 3.1.

**Table 3.1.** Ellipsometric Thicknesses of the SAMs Generated from Alkanethiols Bound to Gold.

| Adsorbate | Thickness (Å) |
|---|---|
| **D18SH** | 21 ± 1 |
| **F1H17SH** | 18 ± 2 |
| **F1H16SH** | 17 ± 1 |
| **D1F6H10SH** | 16 ± 1 |

### 3.2.3.3. Techniques for Monolayer Characterization

A PHI 5700 X-Ray photoelectron spectrometer using a monochromatic Kα X-ray source (hν = 1486.7 eV) set to 90° with respect to the axis of the hemispherical energy analyzer was used to collect the X-Ray photoelectron (XPS) spectra for the self-assembled monolayers. The photoelectron takeoff angle was set to 45° from the surface with a 23.5 eV pass energy. A survey spectrum was gathered before running high resolution spectra with a resolution of 0.1 eV. The high resolution spectra were aligned using the Au $4f_{7/2}$ peak at a binding energy of 84.0 eV.

Raman spectroscopy was collected using a home-built TIR Raman spectrometer which is detailed elsewhere.[26] The alkanethiols were stored in glass vials and the scattered light was collected with a spectrograph combined with a CCD camera (Andor iDus; Andor Technology) and resolved by high-frequency and low-frequency transmission gratings. The spectra were collected for 5 min each from 2000–2300 $cm^{-1}$ and 2750–3100 $cm^{-1}$ to probe the C–D and C–H stretching regions, respectively.

Attenuated total reflection infrared spectroscopy (ATR-IR) was measured using a Thermo Scientific Nicolet iS10 FT-IR spectrometer with an ATR accessory. Alkanethiol spectra were collected with a resolution of 2 $cm^{-1}$ from 600–4000 $cm^{-1}$ for 128 scans.

Polarization-modulation infrared reflection absorption spectroscopy (PM-IRRAS) was measured under a constant nitrogen purge using a Nicolet Nexus 670 Fourier transform spectrometer equipped with a Hinds Instruments PEM-90 photoelastic modulator adjusting a ZnSe window to modify the IR polarization. The spectra were collected with a mercury-cadmium-telluride (MCT) detector in reflection geometry at an IR beam incident angle of 80° from the surface normal. Sample spectra were collected with a resolution of 2 $cm^{-1}$ in the C–H stretching region from 2750–3100 $cm^{-1}$ for 512 scans.

Sum frequency generation (SFG) spectroscopy of the SAMs and $CH_3CN$ samples was measured using a home-built spectrometer for which the details can be found elsewhere,[27] and in Chapter 2. Briefly, a pulsed, 20 Hz, 1064 nm beam from an EKSPLA Nd:YAG laser is used to pump a LaserVision optical parametric generation and amplification system (OPG/OPA) to produce a tunable-frequency infrared beam as well as a 532 nm visible beam. The two beams, with corresponding incidence angles of 60° and 50° with respect to the surface normal, were spatially and temporally aligned at the sample surface to produce a new beam with a frequency equal to the sum of the two input frequencies. This sum frequency (SFG) beam was filtered for wavelength purity, collected using a PMT, processed using a boxcar integrator, and the resulting averaged data points were plotted using a LabView program. The samples were scanned in the C≡N (2000–2300 $cm^{-1}$) and C–H (2800–3050 $cm^{-1}$) stretching regions using ppp and ssp polarization combinations, where the letters denote the polarization of the SFG, visible, and IR beams, respectively. The final spectra are the average of at least 5 scans and have been normalized to the corresponding bare gold SFG spectrum to account for the gold response over the scanned IR frequencies.

A solid-liquid cell was designed and built for the SFG experiments and is described in Chapter 2. The cell consisted of a PTFE body into which the gold slide containing the SAM was placed. A cleaned glass and PTFE syringe was used to place a few drops of liquid acetonitrile onto the gold slide and a cleaned $CaF_2$ window was placed on top. A small Kalrez o-ring under the gold slide helped to press the sample against a $CaF_2$ window so as to minimize the amount of liquid between the slide and the window. A metal flange covered with PTFE tape was fastened over the window by tightening nuts at the bottom of the cell to press the window into an o-ring and seal all the components together as shown in Figure 2.15 in Chapter 2. The cell was assembled in a glovebox under a $N_2$ atmosphere to prevent the absorption of water by the acetonitrile. The final solid-liquid SFG spectra were compared to reference spectra, which show the profile of the IR energy throughout the surveyed frequency range, giving information about the absorption, or lack thereof, of the IR beam by the bulk liquid in the sample. The data from the reference arm was collected simultaneously with the SFG signal from the sample surface and plotted separately during the experiment so that the spectra could be monitored for IR absorption as it was collected.

The theory of sum frequency generation spectroscopy has been thoroughly described by several groups,[28-30] and is detailed in Chapter 2. Briefly, SFG is a coherent second-order nonlinear process that under the electric-dipole approximation is only allowed from media that are non-centrosymmetric. Therefore, molecules in an isotropic bulk environment will not produce SFG signal, but interfacial molecules can at the boundaries where the centrosymmetry of the system is broken. The intensity of the SFG signal, $I_{SFG}$, is related to the intensities of the incident beams $I(\omega_{vis})$ and $I(\omega_{IR})$ at the

frequencies $\omega_{vis}$ and $\omega_{IR}$ of the visible and infrared beams, respectively, as well as the effective second order nonlinear susceptibility, $\chi^{(2)}_{eff}$, via the following relationship,[28]

$$I_{SFG} \propto \left|\chi^{(2)}_{eff}\right|^2 I(\omega_{vis}) I(\omega_{IR}). \tag{3.1}$$

The susceptibility is the sample system's response to the optical fields perturbing it and is described by the sum of $\chi^{(2)}_{NR}$, the vibrationally non-resonant component coming from the interaction of the metal surface with the intense light fields, and the vibrationally resonant component, $\chi^{(2)}_{R}$, which contains molecular orientation information and which is maximized when the frequency of the IR beam is the same as the frequency of a normal mode. As described in Chapter 2, the resulting relationship between the intensity of the SFG beam and the susceptibility can be reduced to,

$$I_{SFG} \propto \left|\mathrm{A}_{NR} * e^{i\epsilon} + \sum_q \frac{\mathrm{A}_q}{\omega_q - \omega_{\mathrm{IR}} - i\Gamma_q}\right|^2 \tag{3.2}$$

where $\mathrm{A}_q$, $\omega_q$, $\Gamma_q$ are the amplitude, frequency, and line-width of the $q^{th}$ vibrational mode. Equation 3.2 was used to fit the SFG spectra and the intensities of the resonances were calculated. The ratio of intensities for same mode in two different polarizations was compared to the simulated curves that relate intensity to functional group tilt angle, as described in detail in Chapter 2.

## 3.3. Results and Discussion

### 3.3.1. Characterization of the SAMs

#### 3.3.1.1. Monolayer Thickness and Elemental Composition

Characterization of the self-assembled monolayers with ellipsometry showed that the film thicknesses listed in Table 1 are consistent with those found in the literature,[7] providing one piece of evidence for the successful formation of the self-assembled monolayers on gold. X-ray photoelectron spectra were then collected to examine the elemental composition of each film and provide detail about the SAM structure on the surface.[31] The high resolution spectra are plotted in Figure 3.2.

The XPS spectra in Figure 3.2 show that the binding energies of the peaks agree well with literature values for SAMs on Au.[7] The S 2p region in Figure 3.2B shows that there was minimal to no unbound thiol present in the SAMs due to the lack of a peak at a binding energy of 164 eV.[32] This spectra provide evidence for the successful formation of the monolayers. Figure 3.2C shows that the $CH_2/CD_3$ peak in the C 1s spectra for the SAMs generated from the fluorinated molecules shifts to lower binding energies in comparison to the SAM derived from **D18SH**. This is attributed to a lower packing density of the fluorinated chains due to the larger van der Waals diameter of the fluorinated groups, 2.7 Å, in comparison to the hydrocarbon groups, 2.0 Å. Among other contributing factors, the packing density of the SAMs has been shown to increase the wettability of the "inverted"-dipole surfaces, such as **D1F6H10SH**, by polar liquids; contacting liquids have more access to interact with the terminal dipole in comparison to the **F1HnSH** monolayers (where n=16–19) which form more densely-packed monolayers.[7]

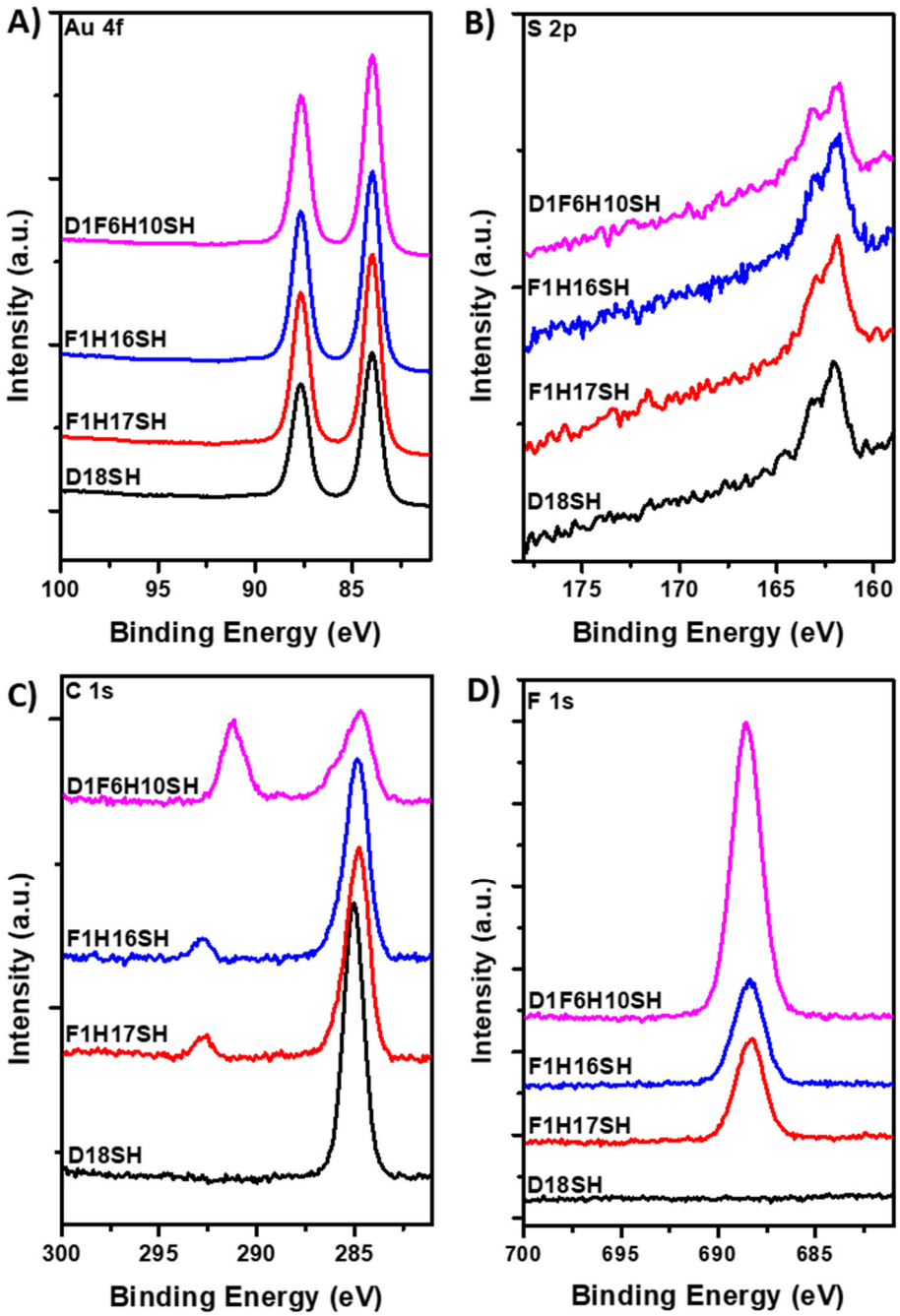


**Figure 3.2.** High-resolution XPS spectra in the A) Au 4f, B) S 2p, C) C 1s, and D) F 1s regions of the alkanethiol SAMs on gold substrates.

### 3.3.1.2. Vibrational Mode Assignments

Before testing the SAMs with surface infrared spectroscopy, the mode assignments for the fluorinated adsorbates are discussed from their bulk Raman and ATR-IR spectra.

Figure 3.3 shows the Raman spectra of the semi-fluorinated alkanethiols in the C–H stretching region between 2750–3100 $cm^{-1}$ and the C–D stretching region between 2025–2325 $cm^{-1}$. The bands in the C–H stretching region shown in Figure 3.3A for all three alkanethiols correspond to the symmetric methylene stretch, $\nu_{ss}^{CH_2}$, the symmetric stretch split by Fermi resonance, $\nu_{FR}^{CH_2}$, with the overtone of the symmetric $CH_2$ bending mode, and the methylene antisymmetric stretch, $\nu_{as}^{CH_2}$, in order of lowest to highest frequency. Further detail on the positions of these bands and the shape of the spectra can be found in Chapter 5.

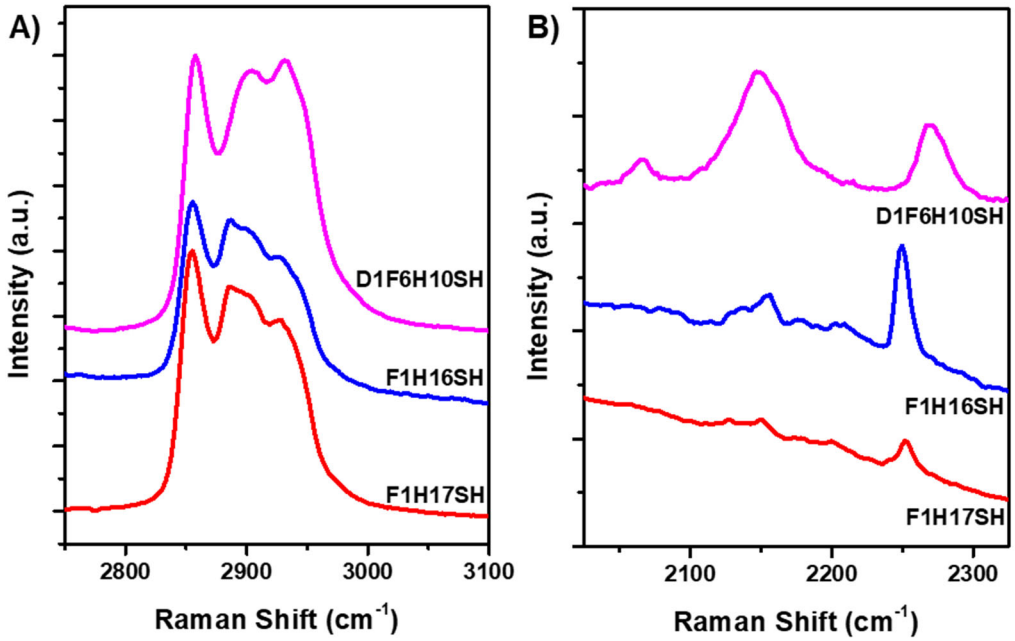


**Figure 3.3.** Raman spectra of the bulk alkanethiols in the A) C–H stretching region between 2750–3100 $cm^{-1}$, and B) the C–D stretching region between 2025–2325 $cm^{-1}$.

The Raman spectra shown in Figure 3.3A also do not have visible $CH_3$ stretches, however, in the $CD_3$ stretching region shown in Figure 3.3B, the methyl stretches of the **D1F6H10SH** molecule are clearly visible with the symmetric stretching peak at 2140 $cm^{-1}$ and the antisymmetric stretch at 2270 $cm^{-1}$.[33] The resonances for the $CF_3$-capped

molecules in the C–D region, specifically the higher intensity peaks at ~2150 and 2250 $cm^{-1}$, are attributed to a combination band of the C–C skeletal and $CF_3$ stretching mode and an overtone of the symmetric $CF_3$ stretching mode, respectively.[34]

The ATR-IR spectra shown in Figure 3.4 show that while the alkanethiols have strong resonances in the C–H stretching region (Figure 3.4A) corresponding the $CH_2$ stretching modes, the C–D stretching region (Figure 3.4B) shows no resonances for the **D1F6H10SH** molecule.

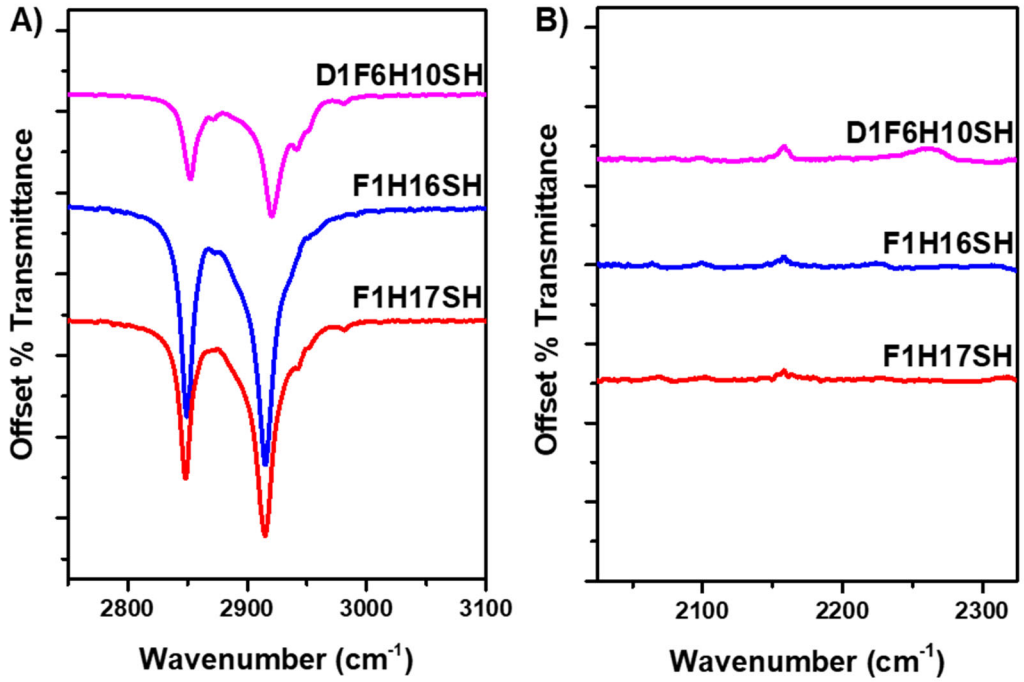


**Figure 3.4.** ATR-IR spectra of the bulk alkanethiols in the A) C–H stretching region between 2750–3100 $cm^{-1}$, and the B) C–D stretching region between 2000–2350 $cm^{-1}$ (right). The percent transmittance spectra are offset for clarity and both frequency regions are plotted with the same y-axis scale.

The absence of the $CD_3$ stretching bands in Figure 3.4B is attributed to a low IR cross-section; the methyl bands in the $CH_3$-terminated counterpart to this molecule (**H1F6H10SH**) have extremely low intensities compared to those of the methyl group in

fully hydrocarbon molecules,[7] plausibly due to the methyl group's proximity to the electron-withdrawing fluorocarbons.[35] If the $CH_3$ bands in **H1F6H10SH** have such low intensities, then the $CD_3$ bands are expected to be below the detection limit of the PM-IRRAS spectra. Since SFG intensities are the product of both the IR and Raman intensities for the transition in question, these results present a plausible reason why the $CD_3$ stretches for the monolayer formed from **D1F6H10SH** are not visible in the SFG spectra shown in Figure 3.6.

#### 3.3.1.3. Monolayer Conformation by PM-IRRAS

Polarization-modulation infrared reflection absorption spectroscopy (PM-IRRAS) uses the modulation of infrared light polarization incident at a grazing angle to the surface to determine the differential surface reflectivity ($\Delta R/R = (R_p - R_s)/(R_p + R_s)$) and generate a surface infrared spectrum of the molecules with the full bulk information of the thin film. PM-IRRAS is used to characterize the relative conformational order of the monolayers by using the peak position of the methylene antisymmetric stretch which has been shown to vary with the arrangement of the monolayers on the surface into crystalline-like (ordered) or liquid-like (disordered) environments.[25] Figure 3.5. shows the spectra in the C–H stretching region between 2750–3100 $cm^{-1}$ for the SAMs generated from the adsorbates shown in Figure 3.1. Only two resonances are shown, one at 2850 $cm^{-1}$ and the other at 2918 $cm^{-1}$ corresponding to the methylene symmetric and antisymmetric stretching vibrations, respectively. Figure 3.5 shows that all SAMs have the methylene antisymmetric stretch, $\nu_{as}^{CH_2}$, at 2918 $cm^{-1}$ which is indicative of well-ordered, trans-extended chains.[25, 36] Furthermore, the spectra fail to exhibit stretches associated with the methyl ($CH_3$) group

since the SAMs are terminated with either $CD_3$ or $CF_3$. There were no visible resonances in the C–D stretching region, in accordance with the ATR-IR spectra shown in Figure 3.4B.

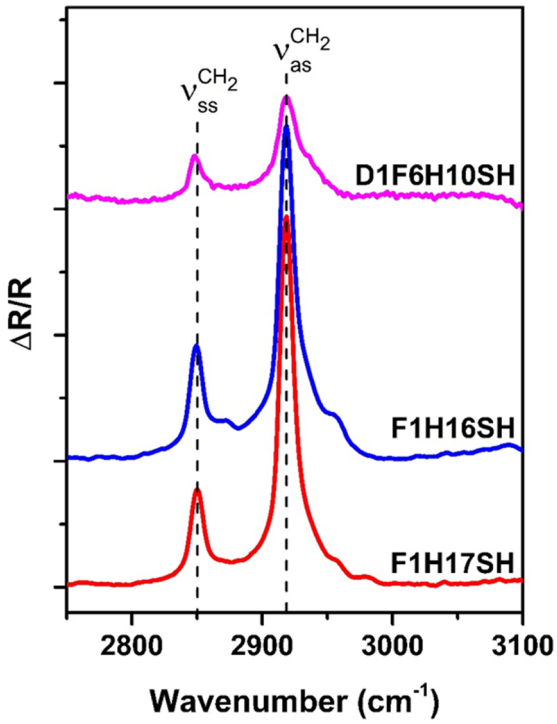


**Figure 3.5.** PM-IRRAS spectra of the alkanethiol SAMs on gold substrates in the C–H stretching region between 2750–3100 cm$^{-1}$.

### 3.3.1.4. Interfacial Structure at the Solid-Air Interface by SFG

To selectively probe the interfacial interactions between SAMs and a contacting liquid we employed sum frequency generation spectroscopy in the C–H and C≡N stretching regions. The spectra of the solid-air interface, shown in Figure 3.6, were included to provide contrast with the solid-liquid spectra shown later as well as a reference for peak positions and resonance orientations in the spectra. In this study, upward-pointing resonances are defined as "peaks", and downward-pointing resonances as "dips". Table 3.2 lists the observed vibrational mode frequencies for the spectra and their assignments taken from the literature and the bulk Raman and IR results.[22, 36-38]

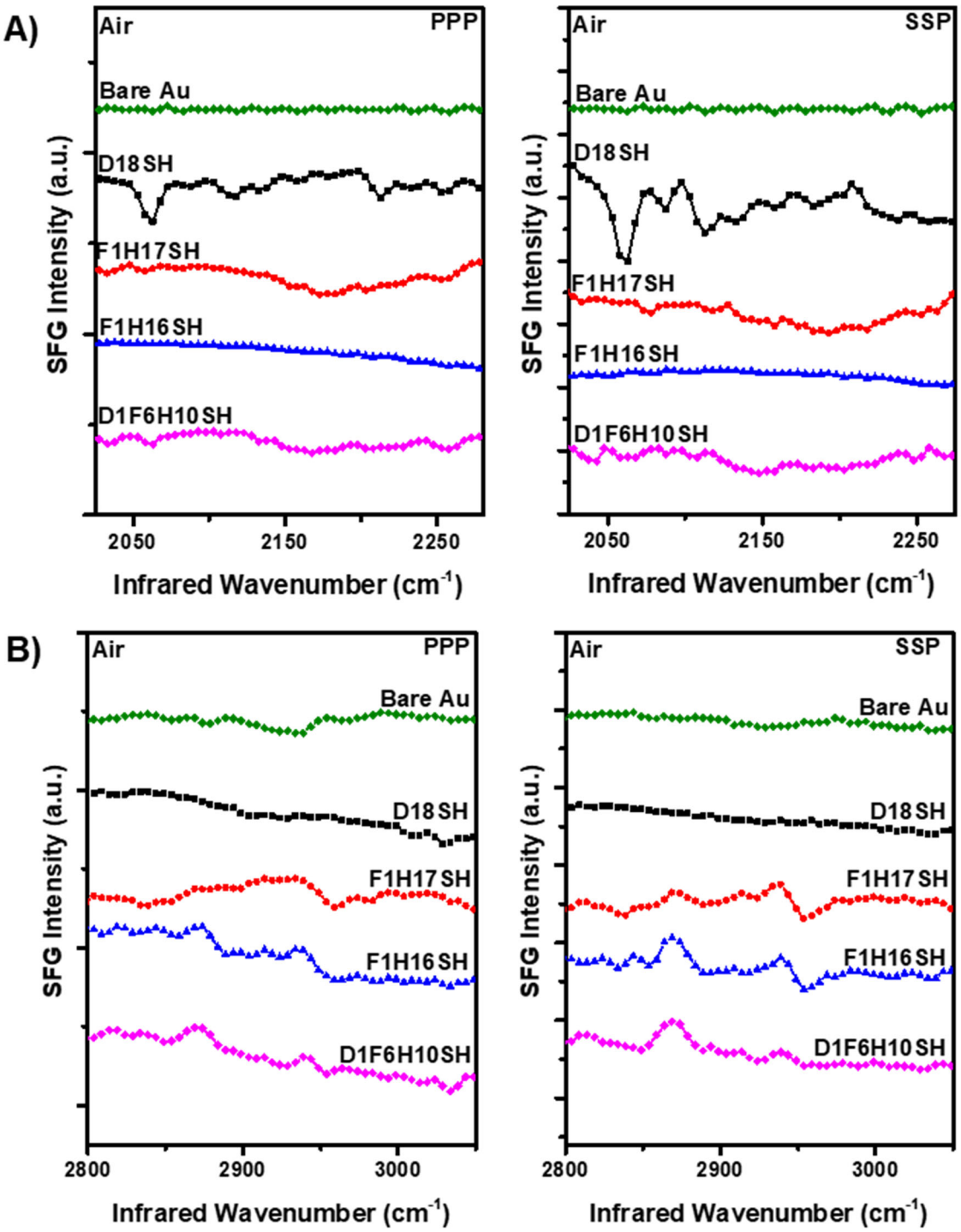


**Figure 3.6.** Solid-air SFG spectra in ppp and ssp polarization combinations for the SAMs and bare gold in the a) C–H and b) C≡N stretching regions.

**Table 3.2.** Observed Vibrational Mode Frequencies and their Assignments for the SAMs Generated from the Adsorbates in Figure 3.1 and Acetonitrile..[22, 36-38]

| Vibrational mode assignment | | Resonance position ($cm^{-1}$) |
|---|---|---|
| $CD_3$ symmetric stretch | $\nu_{ss}^{CD_3}$ | 2060 |
| $CD_3$ symmetric stretch split by Fermi resonance | $\nu_{FR}^{CD_3}$ | 2109 |
| $CD_3$ antisymmetric stretch | $\nu_{as}^{CD_3}$ | 2212 |
| $CH_3CN$: C≡N stretch | $\nu_{ss}^{CN}$ | 2245 |
| $CH_3CN$: $CH_3$ symmetric stretch | $\nu_{ss}^{CH_3}$ | 2942 |

Apparent from the spectra in Figure 3.6A is the lack of the C≡N stretch, in agreement with the absence of acetonitrile, on the surfaces. The fully hydrocarbon SAM, **D18SH**, shows the typical deuterated methyl stretching resonances, as listed in Table 3.2, as dips in the ppp and ssp SFG spectra in Figure 3.6A, and fails to exhibit resonances in the C–H stretching region as shown by Figure 3.6B. Representative SFG spectra in the C–H stretching region of a non-deuterated octadecanethiol monolayer on gold (**H18SH**) can be found in Chapters 4 and 5 with their corresponding peak assignments. Densely-packed self-assembled monolayers on gold, such as those used in this study, are known to be tilted almost perpendicular to the surface (~30° from the surface normal) so that their tailgroups are oriented facing away from the gold.[39] It is important to note that for the **D18SH** monolayer, the methyl group at the terminus of the SAM, which points away from the Au surface, produces dips in the spectrum. This is an important reference point for later analysis of the orientation of the acetonitrile molecules. The SAMs generated from the fluorinated molecules, **F1H17SH**, **F1H16SH**, and **D1F6H10SH** exhibit small resonances in the C–H stretching region attributed to the methylene group below the fluorinated

segment.[22] However, the methylene resonances are far from the acetonitrile methyl stretching peak and will not be analyzed in the current study, but are analyzed in Chapter 5.

### 3.3.2. SFG Spectroscopy of the Solid-Liquid Interface

To provide evidence that the resonances observed in the SFG spectra for the interface between acetonitrile and the self-assembled monolayers, heretofore labeled as the $CH_3CN$/SAM interface, do not arise from IR absorption by the bulk liquid, first, representative spectra for the case in which the IR light is absorbed by a thick liquid layer are shown in Figure 3.7. The thickness of the layer of acetonitrile was controlled by whether or not the window and sample were pressed together, as described in Chapter 2 for the preparation of the solid-liquid cell illustrated in Figure 2.15. For a cell that was not sealed, both the signal and reference SFG spectra in Figure 3.7A show large dips attributed to the C≡N stretching vibration at 2252 $cm^{-1}$ and a combination band of lower-frequency modes in acetonitrile at 2290 $cm^{-1}$.[17] In the C–H stretching region shown in Figure 3.7B, once again both the signal and reference SFG spectra display dips, attributed to the $CH_3$ symmetric and antisymmetric stretches of acetonitrile at 2940 and 3010 $cm^{-1}$, respectively.[40] Because the reference signal is produced using the IR light that has already transmitted through the sample, as shown schematically in Figure 2.15 in Chapter 2, the fact that both the reference and signal SFG spectra exhibit large dips indicates that the IR light was absorbed by bulk acetonitrile as it transmitted through a layer of liquid that was relatively too thick.

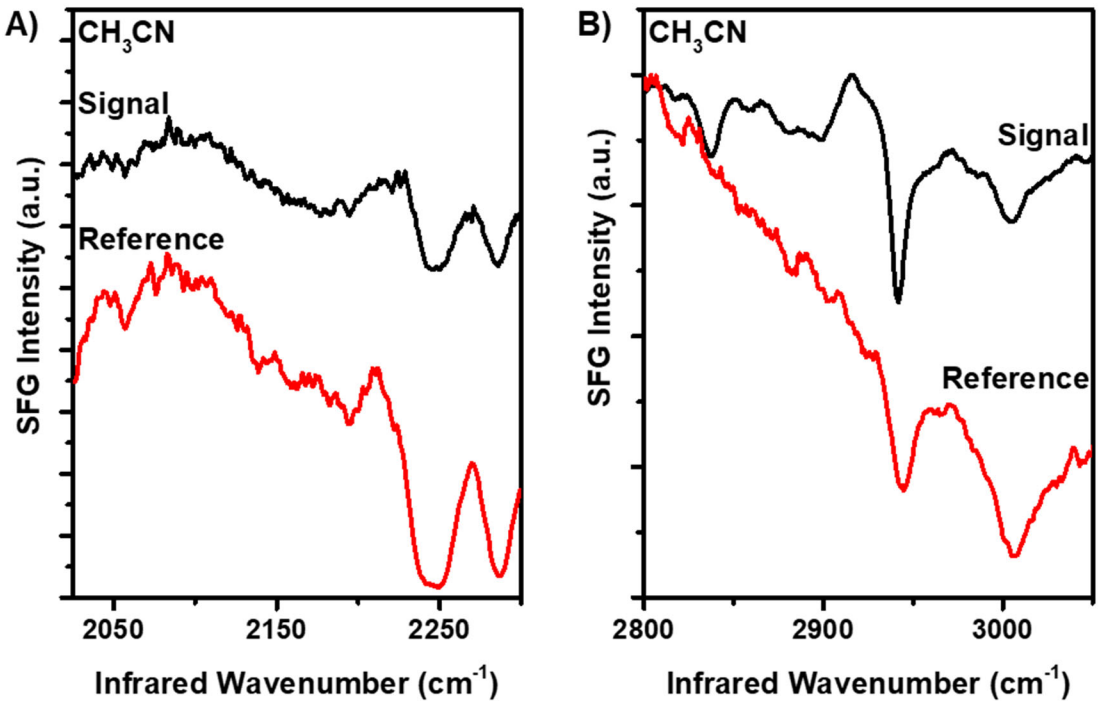


**Figure 3.7.** Infrared absorption by a thick layer of acetonitrile liquid in contact with a SAM in the A) C≡N and B) C–H stretching regions.

When the thickness of the liquid acetonitrile layer was minimized by sealing the solid-liquid cell shown schematically in Figure 2.15 in Chapter 2, the resulting simultaneously-collected sample and reference SFG signals are shown in Figure 3.8A and 3.8B. The solid lines in both sets of spectra represent the reference channel intensity while the connected symbols represent the $CH_3CN$/**D18SH** interface spectra. The sharp decline in the reference signal as the IR frequency is scanned to 2300 $cm^{-1}$, shown in Figure 3.8A, is due to IR absorption by the carbon dioxide gas present in air. The reference spectra show no significant resonances in the regions of the C≡N and $CH_3$ stretches, clearly demonstrating that there is no IR absorption by the layer of acetonitrile between the sample and the window.

Since SFG is a second-order nonlinear spectroscopy, by definition the signal will arise only from interfaces where the centrosymmetry of a system is broken. As shown in the illustration of the SFG solid-liquid cell in Figure 2.15, the input and output beams of the spectrometer travel through several interfaces before reaching the detector, therefore, the interface from which the SFG signal originates needs to be carefully defined.

The first interface encountered by the laser beams, the boundary between the $CaF_2$ window and the liquid $CH_3CN$, can generate SFG signal as shown by the small resonances in the $CH_3CN/CaF_2$ spectra plotted in Figures 3.8C and 3.8D. Note, the data were gathered from the $CaF_2/CH_3CN$ interface with no sample underneath. While it is apparent from the peaks in the ssp spectra that the $CH_3CN$ molecules gather at the boundary with the window, it is unlikely that this signal is contributing to the signal at the $CH_3CN$/SAM interface. As shown by the spectra in Figures 3.8C and 3.8D, the amount of signal arising from the resonances at the $CH_3CN/CaF_2$ interface is more than ten times lower than the signal of acetonitrile atop the **D18SH** SAM. Therefore, signal from the $CH_3CN/CaF_2$ is too weak to interfere with the signal produced from the $CH_3CN$/SAM interface.

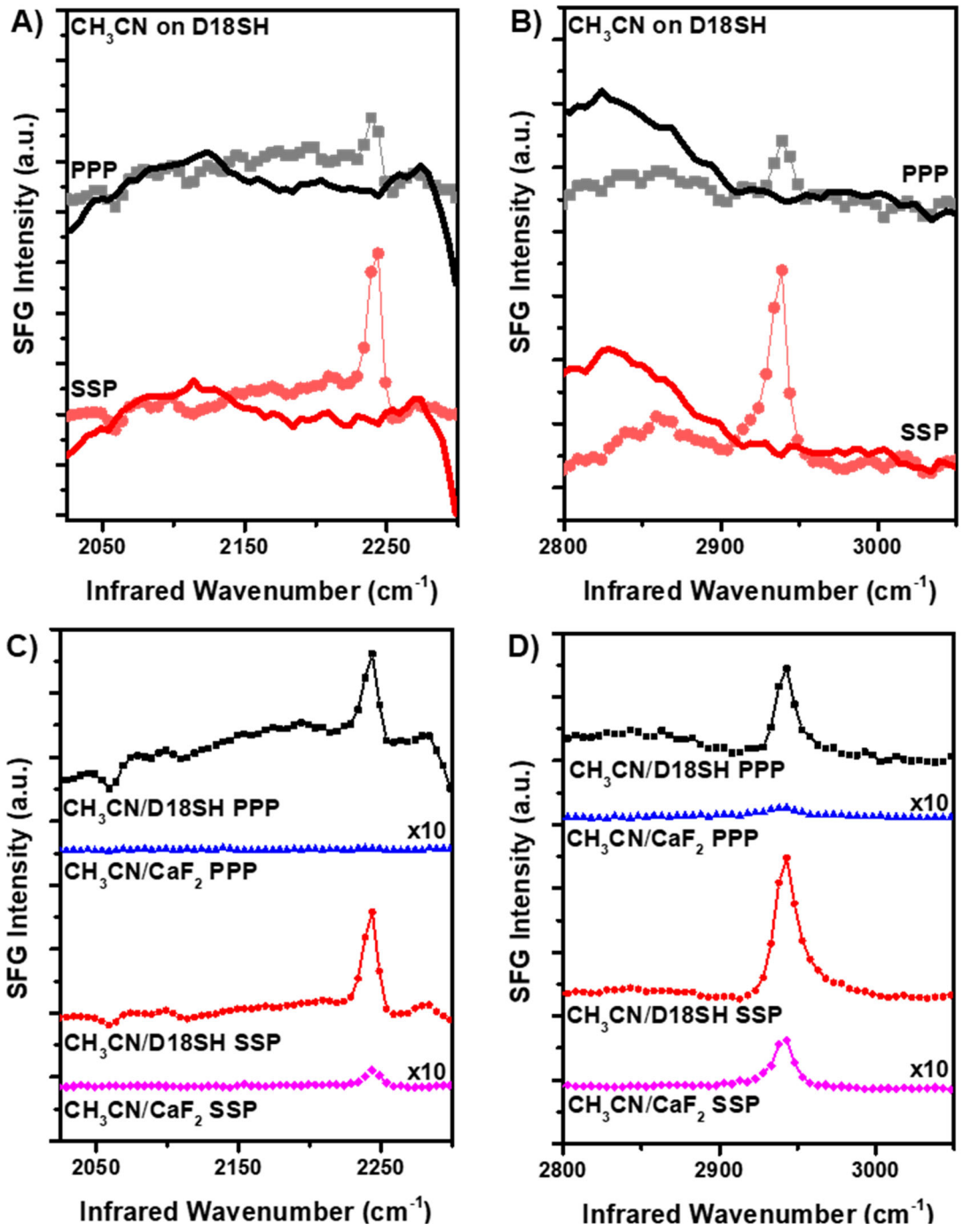


**Figure 3.8.** The solid-liquid SFG spectra in the A/C) C≡N and B/D) C–H stretching regions for ppp and ssp polarization combinations for acetonitrile in contact with A/B) the **D18SH** monolayer on gold and C/D) the $CaF_2$ window. *The thick solid lines are the reference channel SFG spectra, while the connected symbols represent the SFG spectra from the $CH_3CN$/surface interface.*

The second interface that could contribute to the signal is the acetonitrile interaction with the gold substrate. Using a bare piece of gold, the spectra at the $CH_3CN$/Au boundary were gathered and plotted as the green data points in Figure 3.9. There is a clear dip in the ppp C≡N spectrum and asymmetric resonance shapes in the ssp C≡N and both C–H spectra for the acetonitrile in contact with bare Au, in contrast to the shape of the resonances for the other $CH_3CN$/SAM interfaces tested as shown in Figure 3.9. This provides evidence for a different interaction, and possibly orientation, of the acetonitrile in response to a metal surface lacking a well-ordered alkanethiol monolayer. The literature presents experimental evidence for the preferential binding of acetonitrile to Au through the nitrile group, suggesting that the methyl group should be pointed away from the bare Au surface.[17, 41-42] Baldelli et. al. noted that the methyl symmetric stretching frequency red-shifts due to mode softening if the group interacts with a metal surface.[17] The resonances in Figure 3.9B are not shifted, pointing to a lack of interaction between the methyl group of the liquid and the metal surface. Therefore, because of the lack of frequency shifts in the C–H spectra and the asymmetric shape of the resonances implying that there could be multiple types of interactions at the surface, the nitrile group may be pointing toward the Au surface.

The solid-liquid interface SFG spectra of the acetonitrile in contact with the SAMs are plotted in Figure 3.9. The acetonitrile vibrational bands, the C≡N stretch at ~2250 $cm^{-1}$ and the $CH_3$ symmetric stretch at 2940 $cm^{-1}$, are clearly evident in each frequency region of the spectra, with the orientations of the resonance (peaks vs. dips) differing between the surfaces. Despite the strong antisymmetric methyl stretching band shown by the bulk acetonitrile at 3010 $cm^{-1}$ in Figure 3.7, the same resonance is not observed in the SFG spectra in Figure 3.9B.

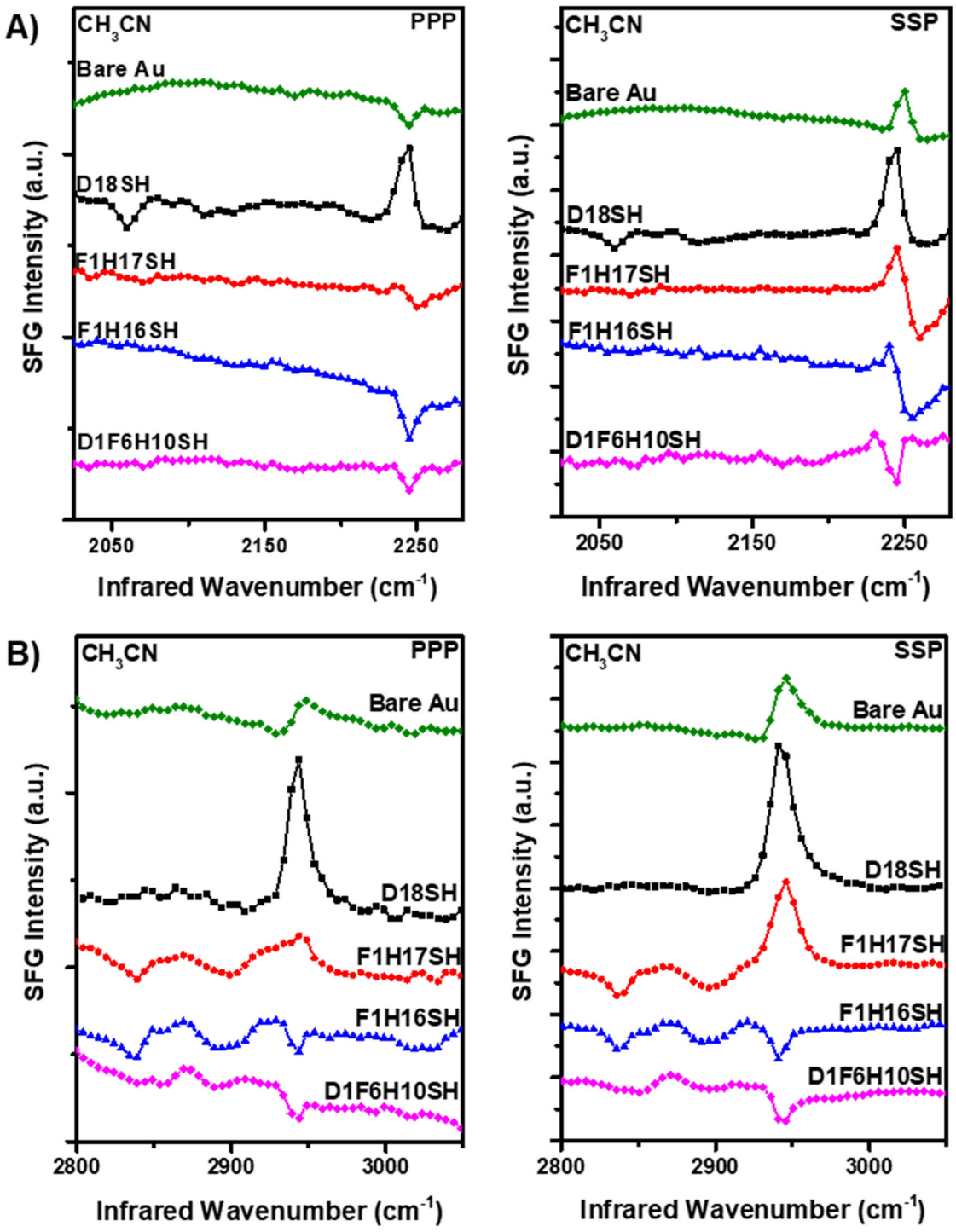


**Figure 3.9.** Solid-liquid SFG spectra in ppp and ssp polarization combinations for the acetonitrile in contact with SAMs and bare Au in the a) C≡N and b) C–H stretching regions.

The ssp and ppp spectra in Figure 3.9A for the **D18SH** SAM interacting with $CH_3CN$ shows dips for the methyl resonances, $\nu_{ss}^{CD_3}$ at 2060 $cm^{-1}$ and $\nu_{FR}^{CD_3}$ at 2109 $cm^{-1}$, originating from the $CD_3$ group which is pointing away from the surface. This is used as an internal reference to guide the interpretation of the consequently upward-pointing peaks of the C≡N and $CH_3$ vibrational bands of the acetonitrile exhibited at 2250 and 2940 $cm^{-1}$, respectively. Taking van der Waals forces as the main driving force for the interaction between **D18SH** and the liquid, the attraction of the $CH_3$ of the acetonitrile to the $CD_3$ of the SAM should lead to the methyl group of acetonitrile pointing downwards toward the surface.

Experimental evidence provided in the literature suggests favorable methyl-to-methyl interactions between hydrocarbon SAMs and acetonitrile.[13, 22, 43-44] Previously, Ward, et. al. analyzed the behavior of various surfactants adsorbed onto a **D18SH** on Au surface and noted that the surfactants preferred to orient with the methyl terminal group of the surfactants pointing toward the $CD_3$ termini of the **D18SH** surface.[43-44] Considering previous literature examples, if the $CD_3$ of the **D18SH** is oriented away from the surface and produces a dip in the spectrum, then the $CH_3$ of the acetonitrile pointed toward the surface should produce an oppositely-oriented, upward-pointing peak.[22, 43] Concurrently, the favorable dispersive interaction between the methyl groups will lead the C≡N group to point away from the surface and produce a peak. Following this model and intuition about permanent dipole-to-dipole interactions (i.e., Keesom forces), the expected resonance orientations as well as the observed orientations for the resonances of acetonitrile are listed in Table 3.3.

**Table 3.3.** Expected Versus Observed Resonance Orientations for the Acetonitrile Methyl and Nitrile Stretching Modes in the ppp and ssp SFG Spectra.

| Surface | Expected peak orientation | $\nu_{ss}^{CH_3}$ resonance orientation | | $\nu_{ss}^{CN}$ resonance orientation | |
|---|---|---|---|---|---|
| | | Observed, PPP | Observed, SSP | Observed, PPP | Observed, SSP |
| **Bare Au** | - | ↑ | ↑ | ↓ | ↑ |
| **D18SH** | ↑ | ↑ | ↑ | ↑ | ↑ |
| **F1H17SH** | ↑ | ↑ | ↑ | ↓ | ↑ |
| **F1H16SH** | ↓ | ↓ | ↓ | ↓ | ↓ |
| **D1F6H10SH** | ↓ | ↓ | ↓ | ↓ | ↓ |

A similar analysis in regards to the orientation of the acetonitrile liquid molecules atop the fluorinated surfaces can be made. The upward pointing peak in the C–H spectra of the $CH_3CN$/**F1H17SH** interface, shown in Figure 3.7B, is indicative of the acetonitrile adopting a similar orientation on this SAM as it does on the **D18SH** SAM. Furthermore, due to the nature of the oriented dipole at the termini the **F1H17SH** SAM with the negative pole at the F–C junction and the positive pole at the C–H junction, and the nature of the attraction between two dipoles -- head to tail alignment, where the positive pole is attracted to the negative pole of the methyl group of the acetonitrile, its positive pole is expected to point toward the SAM surface. This statement readily agrees with the observed C–H spectra and ssp C≡N spectrum, but qualitatively disagrees with the ppp C≡N spectrum. To understand the origin of the dip in the ppp C≡N spectrum of the $CH_3CN$/**F1H17SH** interface, the nonlinear susceptibility, $\chi_{eff,ppp}^{(2)}$, factors that govern the orientation of the resonances in SFG spectra must be taken into consideration:

$$I_{ppp} \propto \left|\chi^{(2)}_{eff,ppp}\right|^2 \propto \left|-\chi^{(2)}_{xxz} + \chi^{(2)}_{zzz}\right|^2 \quad (3.3)$$

where the ratio of the two susceptibility factors can be defined in order to determine their independent contribution to the effective susceptibility and finally the intensity shown in the SFG spectrum. The ratio between $\chi^{(2)}_{xxz}$ and $\chi^{(2)}_{zzz}$ is dependent on the value of the hyperpolarizability ratio, R, which is determined from the Raman depolarization ratio for acetonitrile, and the orientation of the molecule with respect to the surface normal as shown in a previous report by Saito, et. al.[45] In the case of the C≡N stretch, if R = 0.48,[14] the ratio $\frac{\chi^{(2)}_{zzz}}{\chi^{(2)}_{xxz}}$ vacillates between about 0.6 and 2.9 (as shown by the black solid line in Figure 3.10), implying that for most molecular orientations the $\chi^{(2)}_{zzz}$ will be greater than $\chi^{(2)}_{xxz}$.

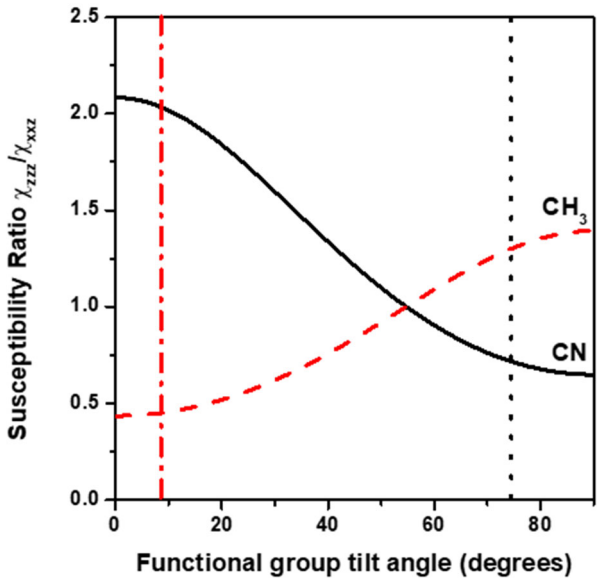


**Figure 3.10.** The simulated ratio of susceptibilities, $\frac{\chi^{(2)}_{zzz}}{\chi^{(2)}_{xxz}}$, with respect to tilt angle for the $CH_3$ (dashed red line) and C≡N (solid black line) groups. The vertical lines mark the average orientation of the $CH_3$ (red dash dot) and C≡N (black dot) groups of acetonitrile at the **F1H17SH** surface, derived from the SFG orientation analysis in section 3.3.3. A σ = 0° distribution of orientations is assumed and R values of 0.48 and 2.3 were used for the C≡N and $CH_3$ groups, respectively.[46-47]

Since the components in Equation 3.3 are opposite in sign, both the relative magnitude of the component and its corresponding Fresnel factors will contribute to the susceptibility. The spectra follow the relationships,

$$I_{ppp,CH} \propto \left|-(0.51 - 0.83i)\,\chi^{(2)}_{xxz} + (0.67 + 1.68i)\,\chi^{(2)}_{zzz}\right|^2 \tag{3.4}$$

$$I_{ppp,CN} \propto \left|-(0.51 - 0.88i)\,\chi^{(2)}_{xxz} + (0.63 + 1.62i)\,\chi^{(2)}_{zzz}\right|^2 \tag{3.5}$$

which show that the Fresnel factors in both regions of the infrared are greater for the $\chi^{(2)}_{zzz}$ component than for the $\chi^{(2)}_{xxz}$, thereby, the $\chi^{(2)}_{zzz}$ will have a greater contribution to the final intensity of the peak in the ppp SFG spectrum than the $\chi^{(2)}_{xxz}$, regardless of molecular orientation. The SFG spectra show that the ssp polarization combination, and therefore $\chi^{(2)}_{xxz}$, produces a peak for the $CH_3$ stretch and must have a "positive" value, therefore the lower intensity in the ppp can be attributed to an overall "negative" $\chi^{(2)}_{zzz}$ contribution. In terms of the $CH_3CN$/**F1H17SH** ppp C≡N spectrum in Figure 3.7, this information indicates that the dip in the ppp is due to the opposite sign and larger magnitude of the $\chi^{(2)}_{zzz}$ component of the effective susceptibility and its corresponding Fresnel factors. Therefore, the model suggested by the $CH_3CN$/**D18SH** data is still in line with the experimental results of the $CH_3CN$/**F1H17SH** interface and the resonance orientations in the ssp spectra can be considered a good basis for determining the relative orientation of the liquid in contact with the SAM.

The **F1H16SH** film has the same total number of carbon atoms as the **D1F6H10SH** SAM but an oppositely-oriented terminal dipole, yet shares similar characteristics with the spectra of the $CH_3CN$/**D1F6H10SH** interface. The C–H ssp spectrum in Figure 3.9B has

a clear dip signifying that the $CH_3$ is pointing away from the surface. The ssp C≡N spectrum has an asymmetric-shaped peak with a negative amplitude implying that the nitrile group points toward the surface as well. The terminal dipole of **F1H16SH** must be tilted to allow the dipoles of the acetonitrile molecules to interact and align differently than the head-to-tail manner described before. Because the analysis with the susceptibilities shed light onto the fact that the ssp spectra hold the key to the orientation of the liquid molecules, the results point to a model in which the $CH_3CN$/**F1H16SH** surface may have anti-parallel-oriented dipoles, allowing for the liquid molecules to orient at a more tilted angle than at the other interfaces.

The interpretation for the $CH_3CN$/**D1F6H10SH** interface is simplified due to the appearance of only dips in the both the C≡N and C–H spectra in Figure 3.9, opposite to that of the $CH_3CN$/**D18SH** spectra. The interaction must be opposite to that of the liquid on the fully hydrocarbon monolayer, and the methyl group of the acetonitrile molecules must be pointing away from the surface. This assumption agrees well with the model of head-to-tail alignment of the dipole vectors of the liquid and the SAM, due to the existence of the "inverted" dipole of the **D1F6H10SH** monolayer with the positive pole at the terminus of the chain.

The clear dips observed in the **F1H16SH** and **D1F6H10SH** spectra in Figure 3.9, provide more evidence that the $CH_3CN/CaF_2$ signal does not affect the $CH_3CN$/SAM signal. If the FSAM data was being influenced or was interfering with the acetonitrile at the window only positively-pointing peaks would be expected in the spectra. Because the $CH_3CN$ resonances in the solid-liquid spectra flip in orientation with a change in the SAM

underneath, the peaks/dips observed in the spectra belong to the molecules aligning at interface with the SAMs, not the window.

### 3.3.3. Orientation Analysis of Acetonitrile at the Solid-Liquid Interface

Orientation analysis was performed on the SFG spectra of the acetonitrile molecules to offer details about the structure of the liquid at the surface. Previous literature examples have used different models to fit the C≡N spectra. Therefore, the model used to fit the spectra must be specified because it can have an effect on the final analysis of the data. Hatch et. al. fit their acetonitrile C≡N spectra to two resonances, one at ~2254 $cm^{-1}$ which was attributed to the acetonitrile molecules weakly adsorbed to the substrate ($ZrO_2$) through polar interactions and the second at ~2250 $cm^{-1}$, which was attributed to polar intermolecular interactions between acetonitrile molecules.[12] Baldelli et. al., following a similar model, also fit their spectra to two peaks, a C≡N resonance at 2245 $cm^{-1}$ corresponding to the acetonitrile adsorbed to Pt, and an SFG active combination band at 2290 $cm^{-1}$.[17] The resonance at 2250 $cm^{-1}$ was attributed to the acetonitrile solution peak.

Another feature to note involves shifts in the frequency of the $CH_3$ peak of acetonitrile between the ssp and ppp polarization combinations, which Ding et al. have suggested that the spectra be fit assuming the peak is composed of two Lorentzian features of opposite sign; the features corresponded to a redistribution of intensity between the two features under different polarization conditions, due to the ability of liquid acetonitrile to reorganize into different environments, resulting in different peak frequencies.[13] The C–H spectra in Figure 3.9 did not exhibit a shift in frequency between ssp and ppp, and the C≡N spectrum for the reference system, $CH_3CN$/**D18SH,** does not appear to exhibit polar

interactions between the liquid and the SAM. Therefore, in light of the previous reports and the observations made from this study, the peaks/dips in the C–H spectra shown in Figure 3.9 were fit to one resonance at 2942 $cm^{-1}$, while the C≡N resonance appearing in $CH_3CN$/**D18SH** interface spectra was fit to one frequency at 2244 $cm^{-1}$. On the other hand, due to the suspected dipole-dipole interactions at the $CH_3CN$/FSAM interfaces and the asymmetric shape of the C≡N resonances, the C≡N spectra were fit to two resonances, one at 2244 $cm^{-1}$ corresponding to the interaction between the acetonitrile and the SAM and another at 2250 $cm^{-1}$ corresponding to dipole-dipole interactions between the liquid molecules.

The fitted data, shown in Figure 3.11, were then used to deduce the orientation of each functional group, defined by the tilt angle, θ, of the C-axis with respect to the surface normal, using the intensity ratio, Issp/Ippp**,** between the symmetric stretching vibration in the ssp and ppp SFG spectra of the acetonitrile in contact with the different SAMs. The fitting parameters used for each spectrum are listed in Tables 3.4–3.7 and were substituted into Equation 2.12 in Chapter 2 to calculate resonance intensity. The SFG intensity ratio Issp/Ippp was then calculated, and corrected using a scaling factor to account for the reflectivities of the laser beams at each interface through the cell. The final values of the intensity ratios and the average orientation angles are listed in Table 3.8 and the intensity ratios for both of the chromophores in acetonitrile are plotted in Figure 3.12.

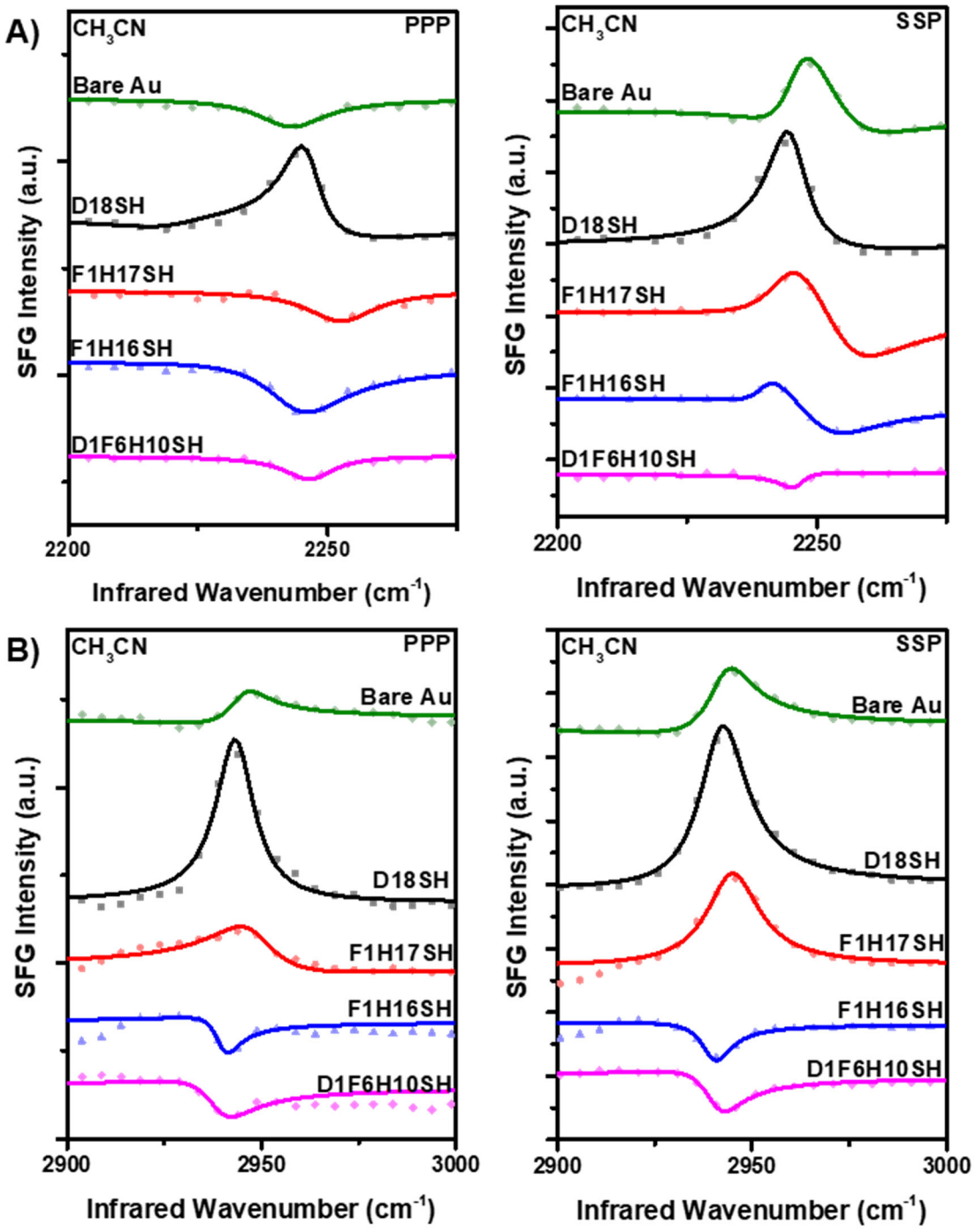


**Figure 3.11.** Spectrum fits to the solid-liquid SFG spectra in ppp and ssp polarization combinations for the acetonitrile in contact with SAMs and bare Au in the a) C≡N and b) C–H stretching regions. *The symbols represent the experimental data, and the solid lines are the best fits.*

**Table 3.4.** Fitting Parameters for the ppp SFG Spectra of the Solid-Liquid Interface of Acetonitrile and Alkanethiol SAMs on Gold for the C≡N Stretching Vibration.

| System | $\nu_{ss}^{CN}$ resonance, PPP | | | | |
|---|---|---|---|---|---|
| | **Anr*** | **ε** | **A** | **ω** | **Γ** |
| **Bare Au** | 1.36 | 2.53 ± 0.17 | -0.11 ± 0.07 | 2242.8 ± 0.8 | 3.03 ± 3.34 |
| **D18SH** | 0.80 | 1.22 ± 0.03 | 0.68 ± 0.02 | 2245.2 ± 0.1 | 5.23 ± 0.14 |
| **F1H17SH** | 0.97 | 1.58 ± 0.06 | -0.30 ± 0.02 | 2252.5 ± 0.6 | 8.03 ± 0.63 |
| **F1H16SH** | 0.91 | 1.97 ± 0.05 | -0.62 ± 0.03 | 2244.0 ± 0.6 | 9.42 ± 0.58 |
| **D1F6H10SH** | 0.84 | 1.59 ± 0.04 | -0.16 ± 0.01 | 2246.1 ± 0.3 | 4.95 ± 0.29 |

*Error in the non-resonant amplitude is below the listed significant figures.

**Table 3.5.** Fitting Parameters for the ssp SFG Spectra of the Solid-Liquid Interface of Acetonitrile and Alkanethiol SAMs on Gold for the C≡N Stretching Vibration.

| System | $\nu_{ss}^{CN}$ resonance, SSP | | | | |
|---|---|---|---|---|---|
| | **Anr*** | **ε** | **A** | **ω** | **Γ** |
| **Bare Au** | 1.34 | 2.76 ± 0.15 | 1.85 ± 0.36 | 2245.8 ± 0.4 | 5.24 ± 0.45 |
| **D18SH** | 0.65 | 1.02 ± 0.03 | 4.06 ± 0.12 | 2245.2 ± 0.1 | 4.98 ± 0.15 |
| **F1H17SH** | 1.01 | 2.25 ± 0.04 | 2.55 ± 0.26 | 2244.2 ± 0.2 | 7.25 ± 0.27 |
| **F1H16SH** | 0.88 | 2.32 ± 0.03 | -5.32 ± 0.79 | 2247.0 ± 0.9 | 10.4 ± 0.19 |
| **D1F6H10SH** | 0.72 | 1.56 ± 0.07 | -0.66 ± 0.07 | 2244.5 ± 0.3 | 3.95 ± 0.43 |

*Error in the non-resonant amplitude is below the listed significant figures.

**Table 3.6.** Fitting Parameters for the ppp SFG Spectra of the Solid-Liquid Interface of Acetonitrile and Alkanethiol SAMs on Gold for the $CH_3$ Stretching Vibration.

| System | $\nu_{ss}^{CH_3\ (CH_3CN)}$ resonance, PPP | | | | |
|---|---|---|---|---|---|
| | **Anr*** | **ε** | **A** | **ω** | **Γ** |
| **Bare Au** | 0.92 | 2.34 ± 0.07 | 0.12 ± 0.01 | 2944.7 ± 0.5 | 6.03 ± 0.55 |
| **D18SH** | 0.85 | 1.51 ± 0.03 | 0.61 ± 0.02 | 2943.4 ± 0.2 | 5.96 ± 0.23 |
| **F1H17SH** | 1.02 | 0.86 ± 0.06 | 0.25 ± 0.01 | 2948.3 ± 0.6 | 9.99 ± 0.52 |
| **F1H16SH** | 0.90 | 2.26 ± 0.07 | -0.09 ± 0.01 | 2939.9 ± 0.3 | 3.79 ± 0.29 |
| **D1F6H10SH** | 0.87 | 2.41 ± 0.12 | -0.17 ± 0.02 | 2939.0 ± 0.8 | 7.10 ± 0.73 |

*Error in the non-resonant amplitude is below the listed significant figures.

**Table 3.7.** Fitting Parameters for the ssp SFG Spectra of the Solid-Liquid Interface of Acetonitrile and Alkanethiol SAMs on Gold for the $CH_3$ Stretching Vibration.

| System | $\nu_{ss}^{CH_3\ (CH_3CN)}$ resonance, SSP | | | | |
|---|---|---|---|---|---|
| | **Anr*** | **ε** | **A** | **ω** | **Γ** |
| **Bare Au** | 0.97 | 2.23 ± 0.02 | 1.64 ± 0.03 | 2942.6 ± 0.1 | 6.99 ± 0.16 |
| **D18SH** | 0.70 | 1.83 ± 0.01 | 4.62 ± 0.05 | 2942.0 ± 0.1 | 7.39 ± 0.10 |
| **F1H17SH** | 1.03 | 1.66 ± 0.02 | 2.49 ± 0.05 | 2944.8 ± 0.2 | 8.19 ± 0.17 |
| **F1H16SH** | 0.78 | 1.86 ± 0.03 | -1.03 ± 0.03 | 2940.1 ± 0.2 | 4.74 ± 0.18 |
| **D1F6H10SH** | 0.70 | 2.18 ± 0.02 | -1.54 ± 0.04 | 2940.7 ± 0.2 | 5.94 ± 0.18 |

*Error in the non-resonant amplitude is below the listed significant figures.

**Table 3.8.** Resonance Intensity Ratios (Issp/Ippp) and Average Orientation Angles for the C≡N and $CH_3$ groups of Acetonitrile in Contact with SAMs and Bare Gold.

| System | $\nu_{ss}^{CN}$ resonance | | $\nu_{ss}^{CH_3}$ resonance | |
|---|---|---|---|---|
| | Issp/Ippp | Avg orientation angle (°) | Issp/Ippp | Avg orientation angle (°) |
| **D18SH** | 0.20 ± 0.02 | 48 | 0.18 ± 0.02 | 67 |
| **F1H17SH** | 0.45 ± 0.13 | 73 | 0.72 ± 0.14 | 8 |
| **F1H16SH** | 0.23 ± 0.03 | 57 | 0.42 ± 0.06 | 36 |
| **D1F6H10SH** | 0.16 ± 0.06 | 42 | 0.53 ± 0.06 | 26 |
| **Bare Au** | 0.32 ± 0.12 | 65 | 0.68 ± 0.16 | 14 |

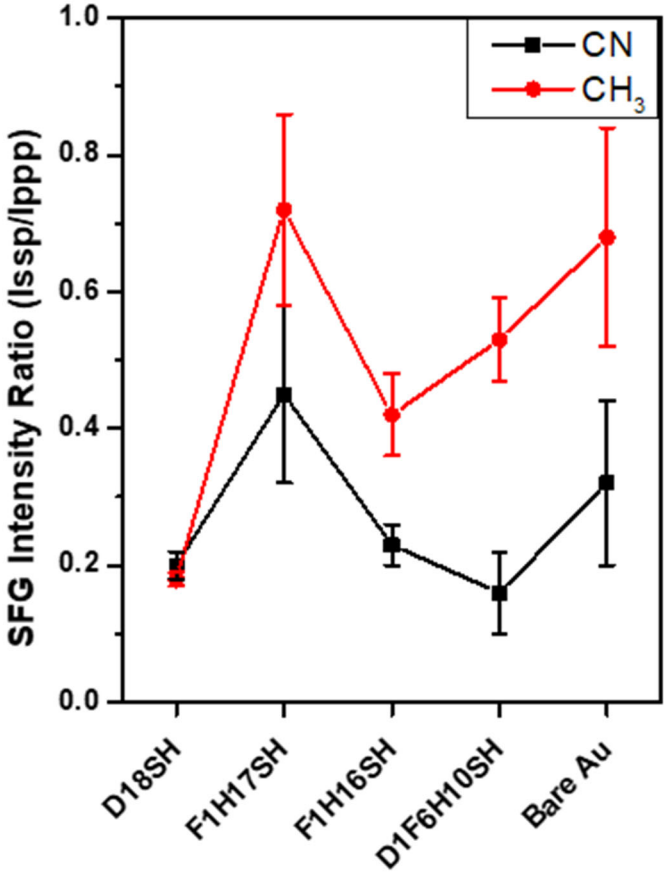


**Figure 3.12.** Resonance intensity ratios for acetonitrile in contact with SAMs and bare gold.

Apparent from Figure 3.12, the intensity ratios of the $CH_3$ and C≡N in the acetonitrile follow a similar pattern, as expected for a molecule with an overall $C_{\infty v}$ symmetry. The average tilt angles assuming a narrow distribution of orientations, as well as the tilt angles derived from the Gaussian distribution of orientations with different widths, were determined using the simulated intensity ratio curves shown in Figure 3.13. The intensity ratios derived from the data fits of the $CH_3CN$/**D18SH** interface are shown in comparison to the simulation in Figure 3.13 to provide an example of the method used to determine the functional group orientations. The errors in the intensity ratios were used to determine the range of tilt angles for each functional group and are depicted by the asymmetric error bars in Figure 3.14, which shows the final results from the orientation analysis assuming a narrow distribution in the calculated orientations.

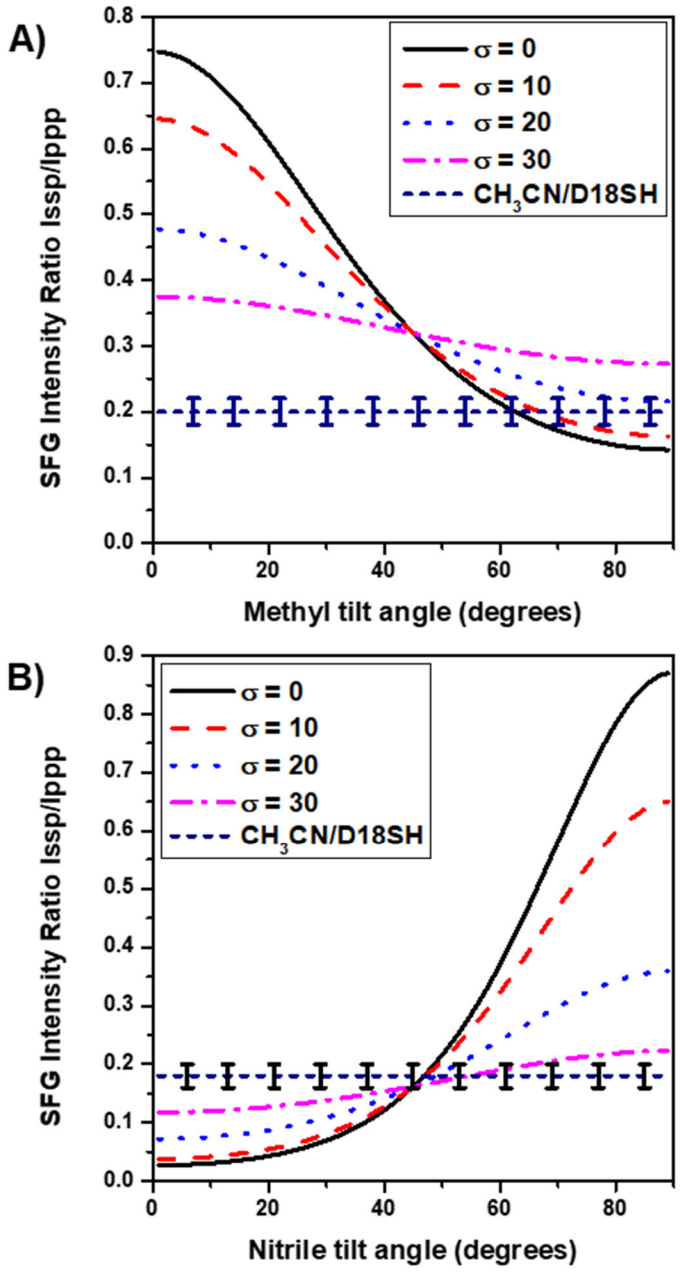


**Figure 3.13.** Simulated intensity ratio (Issp/Ippp) curve (black solid lines) in response to molecular orientation for the a) $CH_3$ and b) C≡N groups at the acetonitrile/SAM interface. Also shown are the curves for orientational distributions, σ, with a width of 10° (red dash), 20° (blue dot), and 30° (magenta dash dot). The purple dashed lines and corresponding error bars denote the intensity ratios for the a) $CH_3$ and b) C≡N groups of the acetonitrile at the **D18SH** interface. These were used to determine the range of tilt angles for each functional group.

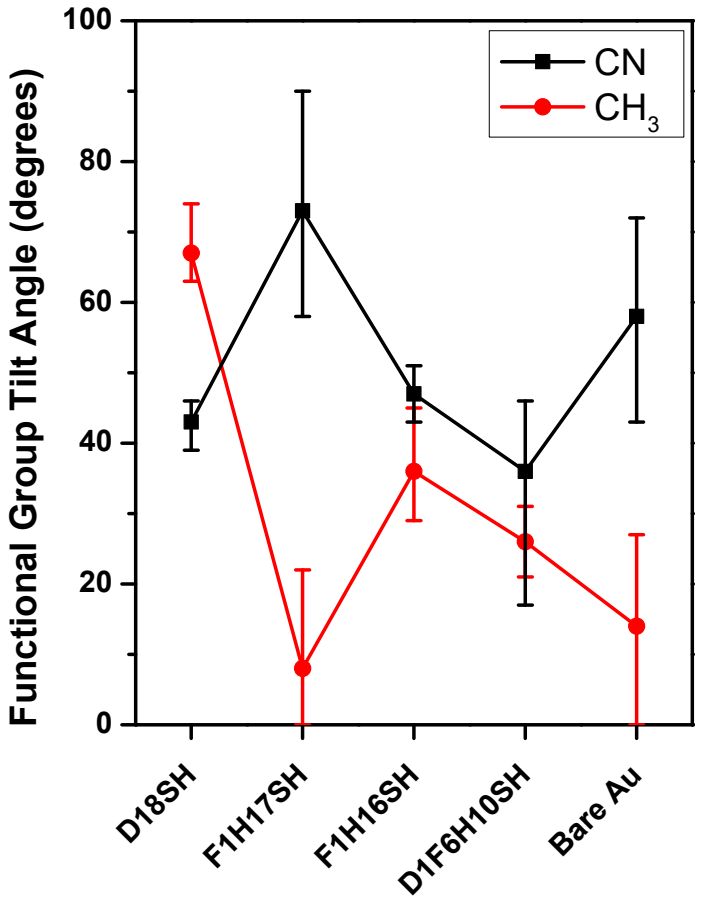


**Figure 3.14.** Average orientations and their asymmetric errors for the C≡N and $CH_3$ groups of $CH_3CN$ atop the SAMs and bare gold calculated using a $\sigma = 0°$ distribution of orientations.

However, because acetonitrile is in liquid form, a narrow distribution of orientations is not a perfect model for the interactions at the interface. The true nature of the arrangement of acetonitrile molecules at the interface is a distribution of possible orientations, i.e. the acetonitrile molecules could have their functional groups pointing in the same direction, but at different degrees of tilt from the surface normal. It is also possible that adjacent acetonitrile molecules are oriented with their functional groups pointing in oppositely directions, so that some molecules will have the $CH_3$ pointing away

from the surface and others will have the $CH_3$ pointing towards the surface. Both instances will influence the intensities of the resonances in the SFG spectra; if the distribution of orientations is high, the intensity of the resonances decreases. On the other hand, a smaller distribution in the orientation, in which the acetonitrile molecules at the SAM interface are tilted at the same angle and oriented with the functional groups pointing in the same direction, will enhance the detected SFG signal. This is shown by the apparent discrepancy in the tilt angles of the functional groups as shown in Figure 3.14. The overall $C_{\infty v}$ symmetry of acetonitrile forces the C-axes of each functional group into a collinear geometry, and therefore, should give consistent functional group tilt angles with respect to the surface normal. It is apparent from Figure 3.14 that the tilt angles calculated for the $CH_3$ and C≡N groups in acetonitrile at the **D18SH** interface were not consistent with one another, indicating that the simulated orientation curve did not follow the experiment. The same inconsistency in functional group tilt angles was noted for the $CH_3CN$ at the **F1H17SH** surface.

In order to preserve the internal $C_3$ axis of the acetonitrile molecule and keep consistency in its tilt angles, the following unknown parameters were varied in the simulated curve: the hyperpolarizability ratio, R, described in detail in Chapter 2 and typically derived from Raman depolarization data, and the refractive index value, nm, of the light fields going through the SAM. Previous reports have found an average orientation angle of 30° for the terminal methyl group belonging to an octadecanethiol SAM on gold.[48] The intensity ratio from the fitting analysis of the $CD_3$ symmetric stretch from **D18SH** was found to be $0.12 \pm 0.03$. Using these two values as the basis for the analysis, the R value was varied until the curve intersected with the point (0.12, 30), returning a value of 0.43

for the hyperpolarizability ratio of $CD_3$ when nm = 1.3 (the average value between bulk acetonitrile and the real component of the Au refractive index at the SFG wavelength). The new R value was then used to determine the orientations of the $CH_3$ groups in acetonitrile, however, only the $CH_3$ tilt angle of acetonitrile at the **D18SH** interface was consistent, giving an average of 46°, in comparison to 43° for the tilt angle of C≡N for the same surface. Note, the remaining $CH_3$ intensity ratios did not fit into the curve.

The next test case assumed that if the $CD_3$ group of the **D18SH** SAM was tilted at a 30° angle from the surface normal, then the $CH_3$ in the acetonitrile must also be tilted at that angle. This generated an R value of 0.75 which gave a nearly horizontal curve that once again did not fit with all the intensity ratios. Varying the hyperpolarizability ratio of the C≡N group produced similar negative results. Changing the value of the refractive index of the SAM only shifted the orientation curve as a whole but did not vary the shape, so only some but not all the intensity ratios matched to the curve. These tests show the limits of the orientation analysis from SFG when the true hyperpolarizabilities of the molecules in a solid-liquid system are unknown. It also is possible that undetermined correction factors must be applied to account for the change in the local fields at metal surfaces. Figure 3.12 does not show an obvious trend in the intensity ratios of the functional groups, meaning that for the current simulation, no matter how the R value is manipulated the average orientation values of the $CH_3CN$ choromophores atop the SAMs will not necessarily be consistent. Given that, Figure 3.14 clearly shows that the $CH_3CN$ tilt angles at the **F1H16SH** and **D1F6H10SH** interfaces were consistent and can be used as evidence that the orientations derived from SFG must be directly due to the oriented dipoles at the SAM surfaces.

### 3.3.4. Comparison of Wettability Data to SFG Orientation Analysis

Qualitative observations from the SFG orientation analysis can be compared to previous wettability data to provide information about how the liquid structure at the interface influences the advancing contact angles observed for acetonitrile atop each of these SAMs. The contact angles reported by Zenasni, et. al for the SAMs are listed in Table 3.9.[7]

**Table 3.9.** Advancing Contact Angles of Acetonitrile in Contact with the SAMs in this Study. Contact Angles Were Reproducible to ± 1° for Each of the Samples Tested..[7]

| SAM | Advancing contact angle for $CH_3CN$ |
|---|---|
| **D18SH** | 68° |
| **F1H17SH** | 48° |
| **F1H16SH** | 53° |
| **D1F6H10SH** | 46° |

The data show that the least wettable surface (highest contact angle) is the fully hydrocarbon surface with a 68° contact angle. The large amplitude of the SFG intensity of the peaks for the $CH_3CN$/**D18SH** interface could point to a high degree of organization in the molecules at the interface. The weaker Debye (dipole-induce dipole) interaction between polar acetonitrile and a hydrocarbon surface, compared to stronger Keesom interactions between the liquid molecules,[12] likely causes the liquid to optimize the intermolecular forces at play by forming an ordered layer at the interface. While repulsion between the dipoles of the liquid molecules arranged parallel to each other is expected, adjacent molecules can tilt so as to approach a lower-energy head-to-tail configuration.[46]

Another possibility involves the liquid adopting a multi-layered system to reduce the overall interaction energy, for which the upper layers leading into the bulk would be centrosymmetric and therefore invisible to the SFG. Hatch et. al. suggested that acetonitrile forms head-to-tail dimers at the solid-liquid interface with zirconia.[12] Ding et. al. provided insight into the literature surrounding $CH_3CN$ orientation at dielectric surfaces in conjunction with their own study to provide evidence for a well-ordered layer of acetonitrile molecules tethered through hydrogen bonding at a silica surface with progressively less ordered layers extending into the bulk of the liquid.[13] Although the systems in this study do not exhibit hydrogen bonding,[4] Keesom interactions between the liquid molecules could cause them to adopt a similar multi-layered arrangement near the surface.

The amplitudes of the resonance intensities for the acetonitrile molecules atop the three fluorinated surfaces are lower than that of the $CH_3CN$/**D18SH** system. Strong interactions between adjacent $CH_3CN$ molecules arranged above the **D18SH** interface, could lead to a narrow distribution of oriented molecules, which would explain the higher SFG intensity of the $CH_3CN$ modes at the $CH_3CN$/**D18SH** interface in comparison to the $CH_3CN$/FSAM interface. Strong interactions between the liquid and FSAM surfaces could increase the distribution of orientations at the interface and lower the SFG intensity of the $CH_3CN$ modes. Combining the findings from the reorientation of the polar acetonitrile molecules in relation to the dipole-terminated FSAM surfaces, and the fact that fluorinated monolayers are more loosely-packed than a fully hydrocarbon monolayer,[7] the lower SFG intensity of the vibrational modes at the $CH_3CN$/FSAM interface can be attributed, at least

in part, to a larger distribution of molecular orientations as $CH_3CN$ molecules intercalate into the FSAMs.

This is in direct agreement with the contact angle values of the FSAMs, which decrease by more than 10° compared a to hydrocarbon SAM, as shown in Table 3.9. This interpretation of the SFG results is also in direct agreement with a previous report which concluded that the significantly increased wettability of fluorinated SAMs in comparison to hydrocarbon SAMs was attributed to the strong dipole-dipole interactions between the dipole-terminated SAMs and the polar liquid,[4] indicating that acetonitrile can penetrate into fluorinated monolayers better than hydrocarbon monoalyers. Nevertheless, conclusions made from the comparison between macroscopic wettability in terms of contact angles and the microscopic information from SFG must be considered with caution. The solid-liquid interactions at the interface are only one piece of a puzzle that must be joined with other data, such as surface energy of the solid-air interface and the liquid-liquid interactions that make up the surface tension at the liquid-air interface, in order to form a complete representation of the factors that affect the wettability of a surface.

## 3.4. Conclusions

Interactions at the nanoscale solid-liquid interface can have a large impact on the macroscale wetting properties of thin films. As one of a limited number of techniques which can probe such interfaces, sum frequency generation (SFG) spectroscopy was employed to study the interactions between a common contacting liquid and model fluorinated surfaces generated using alkanethiol monolayer self-assembly onto gold. The films used in this study served to investigate how polar liquids, such as acetonitrile in this

case, reorient when exposed to different environments by varying the functional groups and, therefore, the dipole, at the terminus of the SAM. The elemental composition of the monolayers as well as the conformational order of the monolayers confirmed with surface infrared spectroscopy and SFG, shows that the SAMs formed densely-packed, well-ordered, trans-extended chains on the gold surfaces that are suitable model surfaces for the study outlined in this chapter. Because sum frequency generation signal is only allowed from noncentrosymmetric media, this spectroscopic technique supplied vibrational spectra of the solid-liquid interface between acetonitrile and the SAMs.

In order to determine the origin of the peaks versus dips in the SFG spectra, contributions to the SFG signal from the $CaF_2/CH_3CN$ and $CH_3CN$/Au interfaces had to be ruled out, as well as IR absorption by the bulk liquid layer of acetonitrile. SFG in both the C–H and C≡N stretching regions showed the $CH_3CN$ peaks pointing up or down depending on the SAM underneath. This corroborates previous reports identifying the source of the interaction between the polar contacting liquids and the partially fluorinated self-assembled monolayers as a dipole-dipole interaction.[7] The solid-liquid SFG spectra shown herein are the first to clearly show the dipole-dipole interactions at the nanoscale between contacting liquids and functionalized surfaces and are a useful stepping stone for future work at the solid-liquid interface.

## 3.5. References

1. Bonn, D.; Eggers, J.; Indekeu, J.; Meunier, J.; Rolley, E., Wetting and Spreading. *Rev. Mod. Phys.* **2009,** *81*, 739–805.

2. Buck, M.; Himmelhaus, M., Vibrational Spectroscopy of Interfaces by Infrared–Visible Sum Frequency Generation. *J. Vac. Sci. Technol. A* **2001,** *19*, 2717–2736.

3. Eisenthal, K. B., Liquid Interfaces Probed by Second-Harmonic and Sum-Frequency Spectroscopy. *Chem. Rev.* **1996,** *96*, 1343–1360.

4. Graupe, M.; Takenaga, M.; Koini, T.; Colorado, R., Jr.; Lee, T. R., Oriented Surface Dipoles Strongly Influence Interfacial Wettabilities. *J. Am. Chem. Soc.* **1999,** *121*, 3222–3223.

5. Colorado, R., Jr.; Lee, T. R., Wettabilities of Self-Assembled Monolayers on Gold Generated from Progressively Fluorinated Alkanethiols. *Langmuir* **2003,** *19*, 3288–3296.

6. Tao, F.; Bernasek, S. L., Understanding Odd−Even Effects in Organic Self-Assembled Monolayers. *Chem. Rev.* **2007,** *107*, 1408–1453.

7. Zenasni, O.; Marquez, M. D.; Jamison, A. C.; Lee, H. J.; Czader, A.; Lee, T. R., Inverted Surface Dipoles in Fluorinated Self-Assembled Monolayers. *Chem. Mater.* **2015,** *27*, 7433–7446.

8. Marquez, M. D. Modulating Surface Dipoles in Fluorinated Thin Films. Ph.D. Thesis, University of Houston, December 2017.

9. Bera, B.; Carrier, O.; Backus, E. H. G.; Bonn, M.; Shahidzadeh, N.; Bonn, D., Counteracting Interfacial Energetics for Wetting of Hydrophobic Surfaces in the Presence of Surfactants. *Langmuir* **2018,** *34*, 12344–12349.

10. Checco, A.; Cai, Y.; Gang, O.; Ocko, B. M., High Resolution Non-Contact AFM Imaging of Liquids Condensed onto Chemically Nanopatterned Surfaces. *Ultramicroscopy* **2006,** *106*, 703–708.

11. Hatch, S. R.; Polizzotti, R. S.; Dougal, S.; Rabinowitz, P., Surface Vibrational Spectroscopy of the Vapor/Solid and Liquid/Solid Interface of Acetonitrile on $ZrO_2$. *Chem. Phys. Lett.* **1992,** *196*, 97–102.

12. Hatch, S. R.; Polizzotti, R. S.; Dougal, S.; Rabinowitz, P., In Situ Surface Vibrational Spectroscopy of the Vapor/Solid and Liquid/Solid Interfaces of Acetonitrile on $ZrO_2$. *J. Vac. Sci. Technol. A* **1993,** *11*, 2232–2238.

13. Ding, F.; Hu, Z.; Zhong, Q.; Manfred, K.; Gattass, R. R.; Brindza, M. R.; Fourkas, J. T.; Walker, R. A.; Weeks, J. D., Interfacial Organization of Acetonitrile: Simulation and Experiment. *J. Phys. Chem. C* **2010,** *114*, 17651–17659.

14. Jang, J. H.; Lydiatt, F.; Lindsay, R.; Baldelli, S., Quantitative Orientation Analysis by Sum Frequency Generation in the Presence of Near-Resonant Background Signal: Acetonitrile on Rutile $TiO_2$ (110). *J. Phys. Chem. A* **2013,** *117*, 6288–6302.

15. Strunk, M. R.; Williams, C. T., Aliphatic Nitrile Adsorption on $Al_2O_3$ and $ZrO_2$ As Studied by Total Internal Reflection Sum-Frequency Spectroscopy. *Langmuir* **2003,** *19*, 9210–9215.

16. Gobrogge, E. A.; Walker, R. A., Binary Solvent Organization at Silica/Liquid Interfaces: Preferential Ordering in Acetonitrile–Methanol Mixtures. *J. Phys. Chem. Lett.* **2014,** *5*, 2688–2693.

17. Baldelli, S.; Mailhot, G.; Ross, P.; Shen, Y.-R.; Somorjai, G. A., Potential Dependent Orientation of Acetonitrile on Platinum (111) Electrode Surface Studied by Sum Frequency Generation. *J. Phys. Chem. B* **2001,** *105*, 654–662.

18. Roke, S.; Kleyn, A. W.; Bonn, M., Femtosecond Sum Frequency Generation at the Metal–Liquid Interface. *Surface Science* **2005,** *593*, 79–88.

19. Ong, T. H.; Davies, P. B.; Bain, C. D., Sum-Frequency Spectroscopy of Monolayers of Alkoxy-Terminated Alkanethiols in Contact with Liquids. *Langmuir* **1993,** *9*, 1836–1845.

20. Anderson, M. R.; Evaniak, M. N.; Zhang, M., Influence of Solvent on the Interfacial Structure of Self-Assembled Alkanethiol Monolayers. *Langmuir* **1996,** *12*, 2327–2331.

21. Henry, M. C.; Wolf, L. K.; Messmer, M. C., In Situ Examination of the Structure of Model Reversed-Phase Chromatographic Interfaces by Sum-Frequency Generation Spectroscopy. *J. Phys. Chem. B* **2003,** *107*, 2765–2770.

22. Bain, C. D., Sum-Frequency Vibrational Spectroscopy of the Solid/Liquid Interface. *J. Chem. Soc., Faraday Trans.* **1995,** *91*, 1281–1296.

23. Clark, A. J., 5.2.1.3 Method 3: From Organostannyllithium, Sodium, Potassium, and Magnesium Compounds by Reactions with Electrophiles. *Sci. Synth.* **2003,** *5*, 213.

24. Frey, S.; Heister, K.; Zharnikov, M.; Grunze, M.; Tamada, K.; Colorado, R., Jr.; Graupe, M.; Shmakova, O. E.; Lee, T. R., Structure of Self-Assembled Monolayers of Semifluorinated Alkanethiols on Gold and Silver Substrates. *Isr. J. Chem.* **2000,** *40*, 81–97.

25. Porter, M. D.; Bright, T. B.; Allara, D. L.; Chidsey, C. E. D., Spontaneously Organized Molecular Assemblies. 4. Structural Characterization of *n*-Alkyl Thiol Monolayers on Gold by Optical Ellipsometry, Infrared Spectroscopy, and Electrochemistry. *J. Am. Chem. Soc.* **1987,** *109*, 3559–3568.

26. Ngo, D.; Baldelli, S., Adsorption of Dimethyldodecylamine Oxide and Its Mixtures with Triton X-100 at the Hydrophilic Silica/Water Interface Studied Using Total Internal Reflection Raman Spectroscopy. *J. Phys. Chem. B* **2016,** *120*, 12346–12357.

27. Zhang, H.; Romero, C.; Baldelli, S., Preparation of Alkanethiol Monolayers on Mild Steel Surfaces Studied with Sum Frequency Generation and Electrochemistry. *J. Phys. Chem. B* **2005,** *109*, 15520–15530.

28. Wang, H.-F.; Gan, W.; Lu, R.; Rao, Y.; Wu, B.-H., Quantitative spectral and orientational analysis in surface sum frequency generation vibrational spectroscopy (SFG-VS). *Int. Rev. Phys. Chem.* **2005,** *24*, 191–256.

29. Hirose, C.; Yamamoto, H.; Akamatsu, N.; Domen, K., Orientation Analysis by Simulation of Vibrational Sum Frequency Generation Spectrum: CH Stretching Bands of the Methyl Group. *J. Phys. Chem.* **1993,** *97*, 10064–10069.

30. Hirose, C.; Akamatsu, N.; Domen, K., Formulas for the Analysis of Surface Sum-Frequency Generation Spectrum by CH Stretching Modes of Methyl and Methylene groups. *J. Chem. Phys.* **1992,** *96*, 997–1004.

31. Laibinis, P. E.; Whitesides, G. M.; Allara, D. L.; Tao, Y. T.; Parikh, A. N.; Nuzzo, R. G., Comparison of the Structures and Wetting Properties of Self-Assembled Monolayers of *n*-Alkanethiols on the Coinage Metal surfaces, Copper, Silver, and Gold. *J. Am. Chem. Soc.* **1991,** *113*, 7152–7167.

32. Castner, D. G.; Hinds, K.; Grainger, D. W., X-ray Photoelectron Spectroscopy Sulfur 2p Study of Organic Thiol and Disulfide Binding Interactions with Gold Surfaces. *Langmuir* **1996,** *12*, 5083–5086.

33. Nanaie, H.; Guirgis, G. A.; Durig, J. R., Torsional Spectra of Molecules with Two $C_{3v}$ rotors—XXV. Rotational and Vibrational Spectra, $r_0$ Structure, Barriers to Internal Rotation and Ab Initio Calculations for 2,2-Difluoropropane. *Spectrochim. Acta, Part A* **1993,** *49*, 2039–2056.

34. Murto, J.; Kivinen, A.; Korppi-Tommola, J.; Viitala, R.; Hyömäki, J.; Swahn, C.-G., Fluoroalcohols. Part 18. Infrared and Raman Spectra of the Perfluorinated t-Butyl Alcohols $(CF_3)_3COH$ and $(CF_3)_3COD$. *Acta. Chem. Scand.* **1973,** *27*, 107–120.

35. Chidsey, C. E. D.; Loiacono, D. N., Chemical Functionality in Self-Assembled Monolayers: Structural and Electrochemical Properties. *Langmuir* **1990,** *6*, 682–691.

36. MacPhail, R. A.; Strauss, H. L.; Snyder, R. G.; Elliger, C. A., Carbon-Hydrogen Stretching Modes and the Structure of *n*-Alkyl Chains. 2. Long, All-Trans Chains. *J. Phys. Chem.* **1984,** *88*, 334–341.

37. Pace, E. L.; Noe, L. J., Infrared Spectra of Acetonitrile and Acetonitrile-$d_3$. *J. Chem. Phys.* **1968,** *49*, 5317–5325.

38. Marzocchi, M. P.; Dobos, S., Infrared Spectra and Crystal Structure of $CH_3CN$ and $CD_3CN$. Polarization and Intensity Measurements. *Spectrochim. Acta, Part A* **1974,** *30A*, 1437–1444.

39. Love, J. C.; Estroff, L. A.; Kriebel, J. K.; Nuzzo, R. G.; Whitesides, G. M., Self-Assembled Monolayers of Thiolates on Metals as a Form of Nanotechnology. *Chem. Rev.* **2005,** *105*, 1103–1170.

40. Quinet, O.; Champagne, B.; Rodriguez, V., Experimental and theoretical investigation of the Raman and hyper-Raman spectra of acetonitrile and its derivatives. *J. Chem. Phys.* **2006,** *124*, 244312.

41. Solomun, T.; Christmann, K.; Baumgaertel, H., Interaction of Acetonitrile and Benzonitrile with the Gold (100) Surface. *J. Phys. Chem.* **1989,** *93*, 7199–7208.

42. Ojha, A. K.; Chandra, G.; Roy, A., A Study on Adsorption of Acetonitrile on Gold Nanorods by Non-Resonant Raman Measurements and Density Functional Theory Calculations. *Nanotechnology* **2008,** *19*, 095706.

43. Ward, R. N.; Davies, P. B.; Bain, C. D., Orientation of Surfactants Adsorbed on a Hydrophobic Surface. *J. Phys. Chem.* **1993,** *97*, 7141–7143.

44. Ward, R. N.; Duffy, D. C.; Davies, P. B.; Bain, C. D., Sum-Frequency Spectroscopy of Surfactants Adsorbed at a Flat Hydrophobic Surface. *J. Phys. Chem.* **1994,** *98*, 8536–8542.

45. Saito, K.; Peng, Q.; Qiao, L.; Wang, L.; Joutsuka, T.; Ishiyama, T.; Ye, S.; Morita, A., Theoretical and Experimental Examination of SFG Polarization Analysis at Acetonitrile–Water Solution Surfaces. *Phys. Chem. Chem. Phys.* **2017,** *19*, 8941–8961.

46. Zhang, D.; Gutow, J.; Eisenthal, K. B., Vibrational Spectra, Orientations, and Phase Transitions in Long-Chain Amphiphiles at the Air/Water Interface: Probing the Head and Tail Groups by Sum Frequency Generation. *J. Phys. Chem.* **1994,** *98*, 13729–13734.

47. Zhuang, X.; Miranda, P. B.; Kim, D.; Shen, Y. R., Mapping Molecular Orientation and Conformation at Interfaces by Surface Nonlinear Optics. *Phys. Rev. B* **1999,** *59*, 12632–12640.

48. Jacob, J. D. C.; Lee, T. R.; Baldelli, S., In Situ Vibrational Study of the Reductive Desorption of Alkanethiol Monolayers on Gold by Sum Frequency Generation Spectroscopy. *J. Phys. Chem. C* **2014,** *118*, 29126–29134.

# Chapter 4: Sum Frequency Generation Spectroscopy of the Solid-Liquid Interface of "Buried Dipoles" in Partially Fluorinated Self-Assembled Monolayers on Gold

## 4.1. Introduction

The influence of the addition of fluorinated moieties to the carbon backbones of alkanethiols on the structure[1-3] and properties[4-11] of self-assembled monolayers (SAMs) has been a topic of interest for the more than 35 years due to the valuable physical properties of fluorinated coatings, such as their reduced friction,[7] tunable surface tension,[12] and transport properties[8] in comparison to their hydrocarbon counterparts. Systematic studies on the effects of varying the amount of fluorocarbons along the chain,[10,13-14] the chain length of the underlying[5,9,15] and overlying[16] hydrocarbon segments, and the effect of changing the direction of the terminal dipole[17] have been undertaken with the sole purpose of developing a thorough understanding of fluorinated surfaces and their inherent characteristics. The current study aims to add to that body of work by examining the wetting behaviors of fluorinated surfaces from the viewpoint of the interactions at the interface between selectively fluorinated SAMs and various contacting liquids. Having characterized the properties of a terminal trifluoromethyl group in an alkanethiol SAM,[5-7,14,17-19] and its relative conformation at the solid-liquid interface in Chapter 5, it is natural to also probe the effect of a difluoromethylene group on the overall structure and properties of the resulting monolayer films.

Herein, a difluoromethylene group was successively buried into the carbon backbone of an alkanethiol chain with 18 total carbon atoms, the structures of which are portrayed in Figure 4.1. The structure and wetting behavior of the films produced from partially fluorinated adsorbates made up of difluorooctadecanethiols, referred to as the buried $CF_2$ series (**H1F1H16SH**, **H2F1H15SH**, **H3F1H14SH**, and **H4F1H13SH**), were compared to those of SAMs generated from the fully hydrocarbon 1-octadecanethiol (**H18SH**) and $CF_3$-terminated 18,18-trifluorooctadecane-1-thiol (**F1H17SH**) which have the same overall chain length.

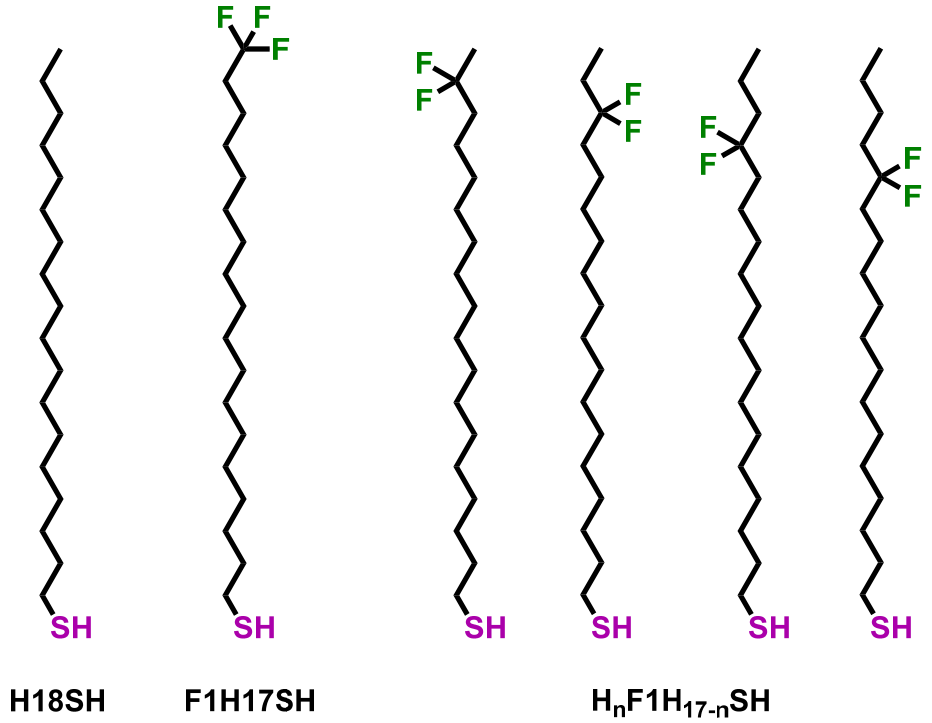


**Figure 4.1.** The molecular structures of the buried $CF_2$ series of adsorbates used in this study: 1-octadecanethiol (**H18SH**), 18,18-trifluorooctadecane-1-thiol (**F1H17SH**), and the difluorooctadecanethiols with the $CF_2$ placed progressively deeper into the carbon chain (from left to right: **H1F1H16SH**, **H2F1H15SH**, **H3F1H14SH**, and **H4F1H13SH**).

Prior research conducted on the films produced from these molecules determined that the addition of an underlying $CF_2$ moiety caused an increased wettability for the films compared to that of the fully hydrocarbon SAM due to physical attractions (mainly van der Waals interactions).[20] Consideration of the collective ellipsometric thickness, contact angle, X-ray photoelectron (XPS) and surface infrared spectroscopic data showed that although the SAMs formed overall well-ordered films, the terminal alkyl segments above the $CF_2$ group must have some disorder in their conformation.[20] The study outlined here provides molecular-scale evidence for this hypothesis by taking advantage of the interface specificity of vibrational sum frequency generation spectroscopy to probe the order and orientation of the terminal groups of these adsorbates on gold.

Vibrational sum frequency generation (SFG) spectroscopy is detailed elsewhere,[21-22] and is a surface-sensitive second-order nonlinear spectroscopic technique that under the electric-dipole approximation can only give signal at interfaces where the local centrosymmetry of the system is broken. Therefore, SFG spectroscopy generates a surface vibrational spectrum of molecules oriented at an interface by scanning in the region of the infrared that corresponds to their vibrational modes. The SFG reports on fluorinated monolayers are limited to the air-liquid interface of surfactants on water,[23-27] as well as a few examples of the air-solid interface of fluorinated SAMs used as reference molecules in non-SAM-related studies.[28-29] A clear understanding of the interactions at the solid-liquid interface of fluorinated coatings, developed using self-assembled monolayers on gold as a model surface for the investigation, can provide valuable insight to aid in the future design of materials with tailored responses to liquid contacting media.

In the following report, the findings from the solid-air and solid-liquid interface of the specifically-fluorinated monolayer films are combined with their ellipsometric thickness and complimentary surface-sensitive spectroscopic results from XPS and polarization-modulation infrared reflection-absorption spectroscopy (PM-IRRAS) to provide a thorough representation of the surface interactions that produce the macroscopic wetting phenomena outlined in a preceding report.[20]

## 4.2. Experimental Procedures

### 4.2.1. Materials and Methods

The partially fluorinated alkanethiols, 17,17-difluorooctadecane-1-thiol (**H1F1H16SH**), 16,16-difluorooctadecane-1-thiol (**H2F1H15SH**), 15,15-difluorooctadecane-1-thiol (**H3F1H14SH**), 14,14-difluorooctadecane-1-thiol (**H4F1H13SH**), and 18,18,18-trifluorooctadecane-1-thiol (**F1H17SH**) were synthesized according to procedures found in the literature.[17,20] The reference adsorbate, 1-octadecanethiol (**H18SH**), was purchased from Sigma-Aldrich and used as received. Absolute ethanol (200 proof, from Aaper Alcohol and Chemical Co.) and tetrahydrofuran (THF, from J.T. Baker) were used as received for the alkanethiols solutions and rinsing of the gold slides.

### 4.2.2. Monolayer Formation and Characterization

#### 4.2.2.1. Substrate Preparation

The substrates used for SAM formation were prepared by the thermal evaporation of 100 nm of gold (99.999% gold shot purchased from Kamis, Inc.) onto polished single-crystal silicon(100) wafers purchased from University Wafer. In order to aid in the

adhesion of the gold to the silicon wafer, an initial 10 nm of chromium (99.9% chromium rod purchased from R. D. Mathis Company) were evaporated onto the bare silicon wafer under vacuum at a pressure of ~$2 \times 10^{-6}$ torr with a deposition rate of 0.5 Å/s.

#### 4.2.2.2. Monolayer Formation and Characterization

The gold wafers were broken into 3x1 cm slides, rinsed with pure ethanol, and dried with a stream of ultra-pure nitrogen gas before measuring their optical constants with a Rudolph Auto EL III ellipsometer using a HeNe laser (632.8 nm) beam set at a 70° incident angle. Immediately after the measurement, the slides were immersed in 1 mM solutions of the alkanethiols and left to equilibrate for 48 h in the dark. The slides were then rinsed with THF and ethanol and dried with ultrapure nitrogen gas prior to taking ellipsometric thickness measurements. A value of 1.45 for the refractive index of an organic monolayer was used, consistent with the literature value used for SAMs.[30] The thicknesses reported are the average of nine measurements (three per point on the slide with three points tested per slide).

A PHI 5700 X-Ray photoelectron spectrometer using a monochromatic Kα X-ray source (hν = 1486.7 eV) set to 90° with respect to the axis of the hemispherical energy analyzer was used to collect the X-Ray photoelectron spectroscopy (XPS) spectra for the self-assembled monolayers. The photoelectron takeoff angle was set to 45° from the surface with a 23.5 eV pass energy. A survey spectrum was gathered before running high resolution spectra with a resolution of 0.1 eV. The high resolution spectra were aligned using the Au $4f_{7/2}$ peak at 84.0 eV as a reference.

Polarization-modulation infrared reflection absorption spectroscopy (PM-IRRAS) was measured under a constant nitrogen purge using a using a Nicolet Nexus 670 Fourier transform spectrometer equipped with a Hinds Instruments PEM-90 photoelastic modulator adjusting a ZnSe window to modify the IR polarization. The spectra were collected with a mercury-cadmium-telluride (MCT) detector in reflection geometry at an IR beam incident angle of 80° from the surface normal. Sample spectra were collected with a resolution of 2 $cm^{-1}$ in the C–H stretching region from 2750–3100 $cm^{-1}$ for 512 scans and in the C–F stretching region from 1100–1500 $cm^{-1}$ for 1024 scans.

A home-built instrument used to obtain advancing and receding contact angle measurements was constructed using a Matrix Technologies micro-Electrapette 25 with disposable pipette tips in conjunction with imaging optics (a 12X zoom lens with 12mm fine focus working with a 2X extension tube and the image detected on a 1.3MP CMOS camera) purchased from Thorlabs, Inc. Videos of the contacting liquids being dispensed and withdrawn at a rate of 1 μL/s following the dynamic sessile drop procedure, in which the pipette tip stays in contact with the drop, were collected. ImageJ was used to acquire a still image of the drops before they moved laterally on the slide and to measure the resulting advancing ($\theta_a$) contact angles. The average of six measurements, one from each corner of the drop with three different spots measured per slide, were used as the final reported contact angle values. The following set of polar and nonpolar contacting liquids of the highest purity available were tested: water ($H_2O$ – Millipore water with a resistivity of 18.2 Ω), acetonitrile (ACN – Sigma-Aldrich), dimethyl sulfoxide (DMSO – Sigma Aldrich), hexadecane (HD – Aldrich), and perfluorodecalin (PFD – Synquest Labs). Deuterated analogs of the hydrogen-containing contacting liquids were used for

spectroscopic measurements because they do not absorb the IR radiation at the frequencies scanned in the spectroscopy.

Sum frequency generation (SFG) spectroscopy measurements were collected using home-built instruments as detailed in Chapter 2. Briefly, a pulsed 1064 nm laser (EKSPLA PL-2251A Nd:YAG laser) was used to pump two LaserVision optical parametric generation and amplification (OPG/OPA) systems to generate the visible (532 nm) and tunable IR beams used in the vibrational sum frequency experiment. The co-propagating visible and IR beams overlap spatially and temporally at the sample surface with incidence angles of 50° and 60° degrees, respectively, while the newly generated beam at the sum of the input frequencies is reflected off the surface, steered into a monochromator for wavelength filtering, and detected with a photomultiplier tube. The sample slides were kept under constant dry nitrogen purge throughout the duration of the solid-air scans. To acquire the solid-liquid spectra, the samples were then transferred into a separate Teflon cell, covered in the contacting liquid, and enclosed with an IR-transparent $BaF_2$ window to minimize exposure to air and to prevent the absorption and/or scattering of the beams by the liquid.

The vibrational SFG spectra reported here are the average of at least 10 scans taken at a scan rate of 1 $cm^{-1}/s$ with an average of 20 laser shots per data point in both the C–H (2800–3050 $cm^{-1}$) and C–F (1100–1425 $cm^{-1}$) stretching regions. Both of the polarization combinations of the beams permissible for a metal surface were acquired, namely ppp and ssp, for which the letters denote the polarizations of the SFG, visible, and IR beams (in that order) with respect to the surface normal. Each ppp spectrum was fit using Mathematica 11 according to Equation 4.1 below,[22]

$$I_{SFG} \propto \left|\chi_R^{(2)} + \chi_{NR}^{(2)}\right|^2 = \left|\sum_q \frac{A_q}{\omega_q - \omega_{IR} - i\Gamma_q} + A_{NR}e^{i\epsilon}\right|^2 \quad 4.1$$

where $I_{SFG}$ denotes the intensity of the SFG signal, $\chi_R^{(2)}$ and $\chi_{NR}^{(2)}$ are the resonant and non-resonant contributions to the second-order nonlinear susceptibility, and $A_q$ and $\Gamma_q$ are the amplitude and linewidth of the q$^{th}$ vibrational mode at the frequency $\omega_q$. The frequency of the input infrared beam is denoted by $\omega_{IR}$, and $A_{NR}$ and $\epsilon$ are the non-resonant amplitude and phase of the gold substrates, respectively. The vibrational resonances used to fit the spectra followed the mode assignments as listed in Table 4.3.

The fitting curve parameters listed in Table 4.3 were used in the determination of the average orientation (tilt angle) of the functional groups in the FSAMs at the solid-air interface. In regards to the SAMs with a terminal methyl group, the ratio of the intensities of the symmetric and antisymmetric methyl C–H stretching modes were compared to a simulated orientation curve (shown in Chapter 2 for the **H3F1H14SH**, **H4F1H13SH**, and **H18SH**, and shown later in this chapter for the **H1F1H16SH** and **H2F1H15SH**) of intensity ratio versus tilt angle defined as the angle between the methyl $C_3$ axis (the terminal C–C axis) and the surface normal. The same analysis was used for the solid-liquid interface after taking into account the change in the Fresnel factors at the solid-liquid interface. Details for method used to fit the data and analyze the orientation of the functional groups are given in Chapter 2 following the procedures set in the literature.[22,31-32]

## 4.3. Results and Discussion

### 4.3.1. Characterization of the SAMs

#### 4.3.1.1. Ellipsometric Thickness Assessment

The monolayers were allowed to self-assemble for 48 h at room temperature before thickness measurements were obtained in order to afford sufficient time for the formation of densely-packed well-ordered films.[33] The average ellipsometric thickness results listed in Table 4.1 show that the SAMs display thickness values consistent with their overall chain length, assuming a chain tilt of 30° from the surface normal, with the **H18SH** (21 ±1 Å) and **F1H17SH** (18 ±1 Å) values in agreement with the literature.[5,17,33] The overall thickness of the films was not affected by the addition of a fluorinated methylene, as all the films have similar thickness (~21 Å), within the standard deviation of the values. The film derived from the $CF_3$-terminated adsorbate is thinner than the rest of the molecules possibly due to a lack in long-range order in the SAM related to the larger van der Waals diameter of the $CF_3$ group (2.7 Å) compared to the $CH_3$ group (2.0 Å),[6] since previous reports have shown that there is no difference in lattice spacing between the $CF_3$-terminated and regular alkanethiol SAMs and negligible difference in the refractive index used in the calculation of the thickness values.[5] Given the thickness results, the following results for the elemental analysis, molecular conformation, and structure of the SAMs can be considered keeping in mind that the thickness of the SAMs from the buried $CF_2$ series is similar to the reference molecules **H18SH** and **F1H17SH**.

**Table 4.1**. Average Ellipsometric Thickness, within ±1 Å, for the SAMs Formed from Normal And Partially Fluorinated Alkanethiols on Gold.

| Adsorbate | Thickness (Å) |
|---|---|
| **H18SH** | 22 |
| **F1H17SH** | 19 |
| **H1F1H16SH** | 22 |
| **H2F1H15SH** | 21 |
| **H3F1H14SH** | 23 |
| **H4F1H13SH** | 22 |

#### 4.3.1.2. XPS Analysis of the Monolayer Films

X-ray photoelectron spectroscopy has been used to determine the binding characteristics and elemental environment of self-assembled monolayers and can give information about the structure of SAMs on the surface.[1,3,15,17,34-36] Figure 4.2 shows the high resolution spectra for the sulfur, carbon, and fluorine in the SAMs and Table 4.2 lists the observed binding energies and their assignments.

Analysis of the S 2p region, shown in Figure 4.2A, shows a 1:2 peak ratio of the S $2p_{1/2}$ and $2p_{3/2}$ doublet with emission maxima at 163.2 and 162.0 eV, respectively, attributed to the binding energy of sulfur bound to gold. However, the doublets for the **H1F1H16SH** and **H3F1H14SH** SAMs display nearly 1:1 peak ratios and include shoulders centered around 164 eV, revealing the presence of a sulfur species often labeled as the disulfide,[35,37-38] or "unbound" sulfur,[15,39] signifying that not all molecules are bound to the Au. Notwithstanding, further analysis of the data via the S/Au intensity ratio, normalized by the corresponding ratio for **H18SH**, shows that the packing density is above 83 ± 5% for the fluorinated molecules, indicating that densely-packed monolayers were

formed despite having unbound thiol present in the XPS spectra. Experiments with vibrational spectroscopy are shown in a later section to determine the extent of the disorder in the SAMs caused by the lower packing densities of the fluorinated SAMs compared to the fully hydrocarbon SAM.

The C 1s high resolution spectra, shown in Figure 4.2B, show one peak at 285 eV for the **H18SH** monolayer, attributed to the $CH_3/CH_2$ units. The fluorinated SAM spectra have two peaks, one at ~284.9 eV and ~290.0 eV in accordance with having both hydrocarbon and fluorocarbon groups in the alkane chain, respectively. Analysis of the C 1s region shows that the peak attributed to the hydrocarbons ($CH_2$ and $CH_3$) is shifted to lower binding energies (284.8 eV) for the **F1H17SH** and **H1F1H16SH** monolayers in comparison to the **H18SH** monolayer (285.0 eV). The peak for the remaining partially fluorinated SAMs (**H2F1H15SH, H3F1H14SH,** and **H4F1H13SH)** appears at the same binding energy, within the resolution of the instrument, as the **H18SH** monolayer (284.9 eV). As shown in Table 4.2, the peak for the C 1s core electrons attributed to the $CF_2$ group in the buried $CF_2$ SAMs, which has a binding energy of 290.1 eV for the **H1F1H16SH** monolayer, shifts to lower binding energies as the $CF_2$ gets further into the film, in agreement with the trend in the binding energies of $CH_3/CH_2$ peak.

Studies have shown that densely-packed monolayer films can obstruct the discharging of positive surface charge produced by the use of X-rays, thereby increasing in the binding energy of the emitted electrons, while poorly-insulating loosely-packed chains do not.[15] Because the packing density of the SAMs determined by the S/Au ratio demonstrated that the SAMs have a similar overall density of molecules on the surface, the apparent shift to lower binding energies of the C 1s core electrons as the $CF_2$ moiety is

buried into the chain could indicate a decrease in the chain packing density at the terminus of the monolayers. This implies that the $CF_3$-terminated monolayer and the monolayer with the terminal $CH_3$-$CF_2$ may be the least densely-packed, with the termini of the monolayers getting increasingly dense as the number of hydrocarbons above the $CF_2$ moiety increases.

The F 1s region XPS spectra in Figure 4.2C clearly outline the difference in binding energy between the $CF_3$ (~688.3 eV) and the $CF_2$ moieties (~687.2 eV), with the $CF_2$ peak of the **H1F1H16SH** SAM showing a higher binding energy (687.5 eV) than its counterparts that are located further into the carbon chain of the molecules. Because the buried $CF_2$ molecules are all the same chain length and near to the same thickness by ellipsometry, the $CF_2$ peak would be expected to be at the same binding energy for all the monolayers. The binding energy of the F 1s electrons in $CF_3$-terminated SAMs was found to be lower than that of SAMs derived from the **H1F6HnSH** (n = 10–13) series;[17] the change in binding energy was attributed to a final state effect in the XPS spectra due to increasing the distance of the core hole from the screening electrons of the Au substrate.[17] Therefore, shifts in the emission peak maxima to higher binding energy can be attributed to the increased distance between the $CF_2$ and the Au surface. This is confirmed by the F 1s peak of the **F1H17SH** SAM, which shows the highest binding energy in the series of molecules used in this study, corresponding to the $CF_3$ group at the top of the film (i.e., furthest fluorocarbon from the Au substrate).

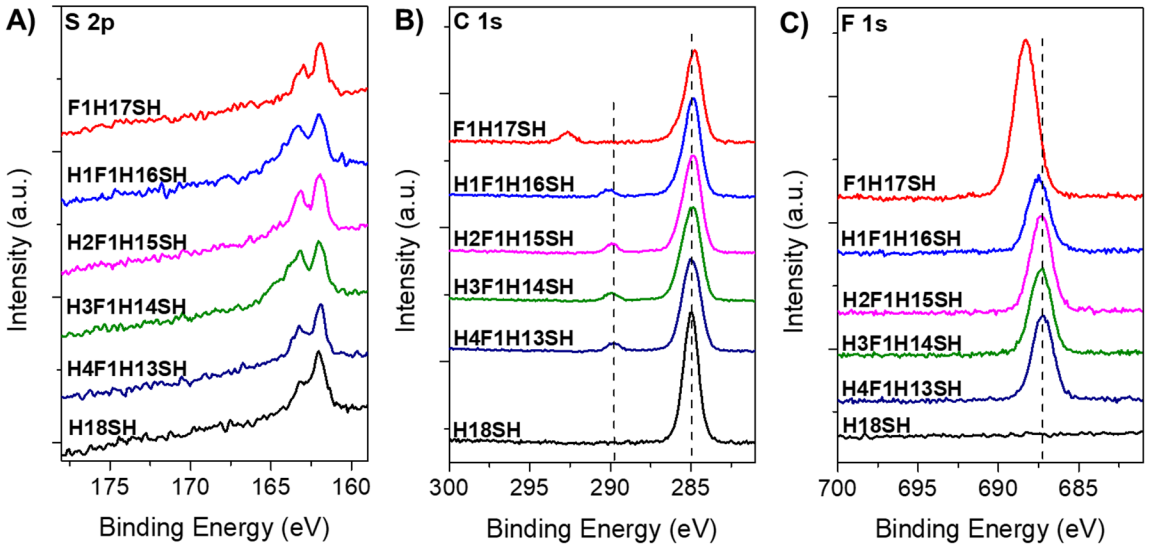


**Figure 4.2**. High resolution XPS spectra of the $CF_2$ buried series in the a) S 2p, b) C 1s, and c) F 1s regions. The dashed lines are centered for the $CF_2$ peak in the **H4F1H13SH** spectra and serve to highlight the shifts in the binding energies of the emission maxima for the different molecules. The XPS spectra shown here are not normalized.

**Table 4.2.** Emission Maxima Binding Energies, in eV, for the Peaks in the S 2p, C 1s, and F 1s XPS Spectra for the SAMs.

| **Adsorbate** | **S $2p_{3/2}$ (eV)** | **C 1s ($CH_2$/$CH_3$ peak) (eV)** | **C 1s ($CF_3$ and $CF_2$ peaks) (eV)** | **F 1s (eV)** |
|---|---|---|---|---|
| **F1H17SH** | 161.9 | 284.8 | 292.7 | 688.3 |
| **H1F1H16SH** | 162.0 | 284.8 | 290.1 | 687.5 |
| **H2F1H15SH** | 162.0 | 284.9 | 290.0 | 687.3 |
| **H3F1H14SH** | 162.0 | 284.9 | 289.9 | 687.2 |
| **H4F1H13SH** | 161.9 | 284.9 | 289.7 | 687.2 |
| **H18SH** | 162.0 | 285.0 | - | - |

#### 4.3.1.3. Conformational Order Using PM-IRRAS

Polarization-modulation infrared reflection absorption spectroscopy (PM-IRRAS) is a surface-sensitive infrared technique that provides the vibrational spectrum for the full chain of the alkanethiol monolayers assembled on the gold substrates. Figure 4.3 shows the PM-IRRAS spectra in the C–H stretching region (between 2800 and 3050 $cm^{-1}$) for the SAMs in this study. The two most intense peaks in the spectra are assigned to the methylene symmetric, $\nu_{ss}^{CH_2}$, and antisymmetric, $\nu_{as}^{CH_2}$, stretches attributed to the methylene groups making up the backbone of the monolayers, while the lower intensity resonances are assigned to the methyl symmetric, $\nu_{ss}^{CH_3}$, and antisymmetric, $\nu_{ss}^{CH_3}$, stretches.[40-41] The spectra of the monolayers generated from the buried $CF_2$ series of molecules display blue-shifted C–H stretching resonance frequencies in both the $CH_3$ and $CH_2$ groups due to the proximity of these groups to the fluorinated carbon atom as will be discussed further in the SFG section.

The PM-IRRAS spectra were used to determine the order in the bulk structure of the chains defined by the relative crystallinity in the monolayer. The C–H stretching region of alkanethiol SAMs has long been used to give insight into the conformational order of the monolayers by observing the shift in the band position of the methylene antisymmetric stretch, $\nu_{as}^{CH_2}$, where a resonance frequency at 2918 $cm^{-1}$ indicates a crystalline-like, ordered structure, and frequencies above 2920 $cm^{-1}$ for the $\nu_{as}^{CH_2}$ denote a liquid-like, disordered structure in the alkane chains.[9,30,42] As shown in Figure 4.3, all the SAMs have the $\nu_{as}^{CH_2}$ peak position at 2918 $cm^{-1}$, signaling that the bulk of the SAMs are well-ordered and trans-extended on the surface.[30] However, the broadening of the peak at 2918 $cm^{-1}$ for the $CF_2$

buried SAMs, in comparison to the **F1H17SH** and **H18SH** films, implies that the physical state of the films could be more liquid-like,[4] as is investigated further in the SFG section. The peak positions and band assignments of the vibrational modes observed in the surface infrared and SFG spectra are listed in Table 4.3, as determined from band assignments in the literature.[40-41,43-48]

**Table 4.3.** Peak Positions and Assignments of the C–H Stretching Vibrations for the Indicated SAMs

| **Adsorbate** | $\nu_{ss}^{CH_2}$ **(cm$^{-1}$)** | $\nu_{ss}^{CH_3}$ **(cm$^{-1}$)** | $\nu_{as}^{CH_2}$ **(cm$^{-1}$)** | $\nu_{as}^{CH_3}$ **(cm$^{-1}$)** |
|---|---|---|---|---|
| **H18SH** | 2850 | 2877 | 2918 | 2964 |
| **F1H17SH** | 2849 | - | 2918 | - |
| **H1F1H16SH** | 2850 | 2955* | 2918 | 3009* |
| **H2F1H15SH** | 2849 | 2954* | 2918 | 2984* |
| **H3F1H14SH** | 2850 | 2881 | 2918 | 2970 |
| **H4F1H13SH** | 2848 | 2878 | 2918 | 2965 |

The peak assignments marked with an asterisk (*) are determined from bulk Raman and IR studies of similar molecules.[43-48]

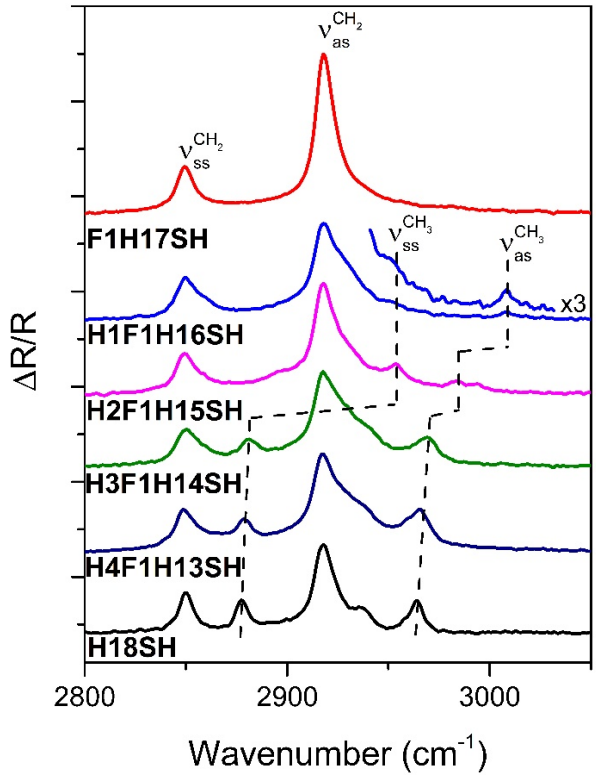


**Figure 4.3**. PM-IRRAS spectra of the SAMs generated from **H18SH**, **F1H17SH**, and the buried $CF_2$ series of alkanethiols in the C–H stretching region, 2800–3050 cm$^{-1}$. The dashed lines follow the shifts in frequencies of the methyl stretches for each of the molecules. The $CH_3$ stretches for the **H1F1H16SH** SAM are magnified for easy viewing.

#### 4.3.1.4. Terminal Group Orientation at the Air-Solid Interface with SFG

Sum frequency generation (SFG) spectroscopy is an inherently interface-specific technique that only gives signal from non-centrosymmetric environments; thus, the terminal methyl group of an alkanethiol monolayer will generate SFG signal, while the locally centrosymmetric methylene chain will not. Therefore, SFG spectroscopy was used to probe the air-SAM and SAM-liquid interfaces in situ to determine the orientation of the SAM terminal groups with respect to the surface normal. Figure 4.4 shows the experimental SFG spectra and their best fits for the SAMs generated from **H18SH**, **F1H17SH**, and the buried $CF_2$ series of adsorbates in the C–H stretching region, between

2800 $cm^{-1}$ and 3050 $cm^{-1}$, using the ppp and ssp polarization combinations. The resonances shown in the spectra belong to the methyl and methylene stretching modes, as described next. It is immediately apparent from the spectra in Figure 4.4 that the further the $CF_2$ group is buried into the backbone of the alkane chain, the more the spectrum resembles that of the fully alkylated chain, with the resonance positions of the methyl group in the **H1F1H16SH** monolayer being the most shifted to higher frequencies and the resonances of the functional groups in the **H4F1H13SH** SAM being at nearly identical frequencies to those of the SAM generated from **H18SH**, as seen with the PM-IRRAS spectra in Figure 4.3.

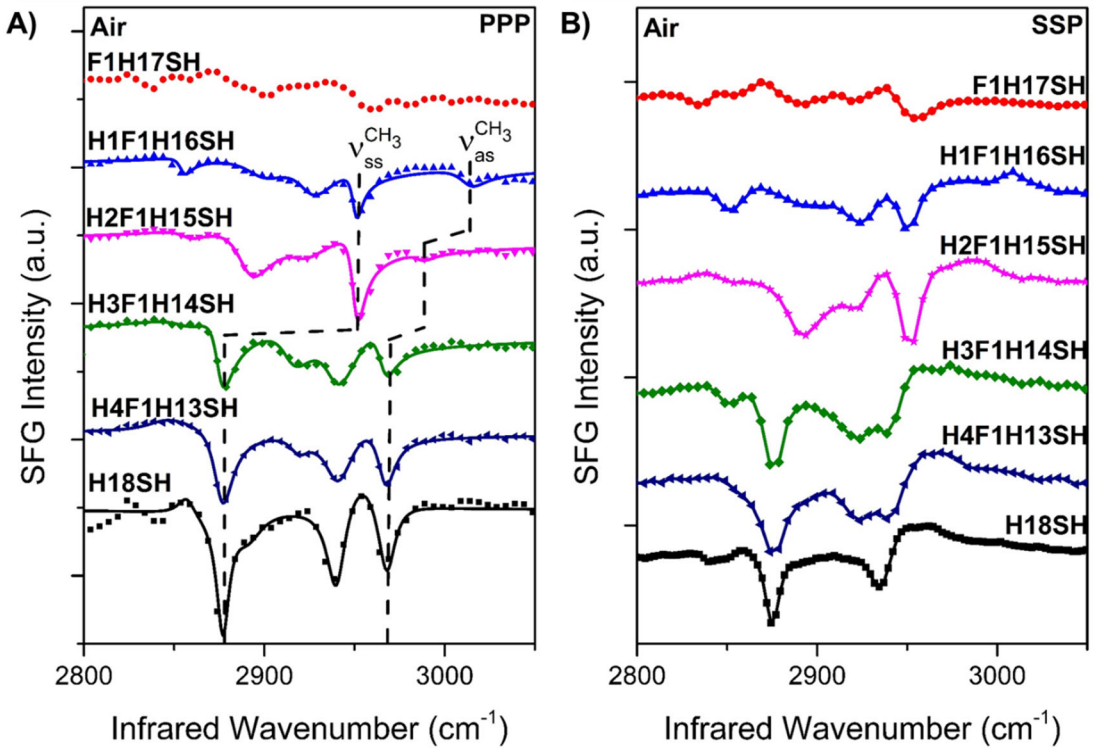


**Figure 4.4**. SFG spectra of the SAMs generated from **H18SH**, **F1H17SH**, and the buried $CF_2$ series of alkanethiols in the C–H stretching region in A) ppp and B) ssp polarization combinations. The dashed lines follow the shifts in frequencies of the methyl stretches for each of the different molecules. *For A) the symbols represent the experimental data, and the solid lines are the best fits.*

The experimental SFG spectra for the SAMs generated from **H18SH**, **H3F1H14SH**, and **H4F1H13SH** were fit to six resonances, including those listed in Table 4.3, the methyl and methylene symmetric and antisymmetric stretching modes, as well as the methyl symmetric stretching Fermi resonance band at 2936 $cm^{-1}$, and a degenerate but opposite phase antisymmetric methyl stretching band at 2955 $cm^{-1}$.[49] The **H1F1H16SH** and **H2F1H15SH** spectra were fit to five resonances. First were the symmetric methylene stretches at ~2855 $cm^{-1}$, made SFG-active due to the break in the local centrosymmetry of the alkane chain, and ~2900 $cm^{-1}$, assigned to the shifted band frequency for the methylene groups adjacent to the $CF_2$.[43-44] Then, the broad Fermi resonance band of the methylene symmetric stretching modes was centered at ~2925 $cm^{-1}$, and finally the methyl symmetric and antisymmetric stretching bands, as assigned in Table 4.3.[4,43-45,47] The appearance of the methylene resonances in the SFG spectra of the $CF_2$ buried SAMs indicates that there is disorder at the termini of the monolayers. This detail about the interfacial structure of the films provides an explanation for the peak broadening of the $\nu_{as}^{CH_2}$ resonance in the PM-IRRAS spectra shown in Figure 4.3.

The parameters derived from the spectrum fits are listed in Table 4.4 and include the amplitude and linewidth of the methyl symmetric and antisymmetric stretching bands. Table 4.4 includes the intensity ratio between the symmetric and antisymmetric stretching modes and was multiplied by a factor of 1.24 to account for the Fermi resonance contribution to the symmetric methyl mode in the **H3F1H14SH**, **H4F1H13SH**, and **H18SH** spectra.[31-32] The large shift in frequency of the $\nu_{ss}^{CH_3}$ band for the **H1F1H16SH** and **H2F1H15SH** monolayers (2955 $cm^{-1}$),[43] due to the proximity of their methyl groups

to the $CF_2$ group, also shifts the $\nu_{ss}^{CH_3}$ away from the overtone of the methyl asymmetric bending mode (~2900 $cm^{-1}$) that has been noted to couple to the $\nu_{ss}^{CH_3}$ of the methyl group in a fully alkane chain.[40,50] Therefore, the $\nu_{ss}^{CH_3}$ band for the **H1F1H16SH** and **H2F1H15SH** may not display Fermi resonance coupling, and thus the $CH_3$ intensity ratios were left as calculated.

**Table 4.4.** Resonance Amplitudes and Linewidths Derived from the Spectrum Fits of the Methyl Stretching Vibrations of the Indicated SAMs.

| Adsorbate | $A_{ss}^{CH_3}$ | $\Gamma_{ss}^{CH_3}$ | $A_{ss}^{CH_3}$ | $\Gamma_{ss}^{CH_3}$ | $I_{ss}/I_{as}$ |
|---|---|---|---|---|---|
| **H18SH** | 0.36 ± 0.01 | 4.11 ± 0.15 | 0.21 ± 0.03 | 4.14 ± 0.45 | 3.70 ± 1.11 |
| **H1F1H16SH** | 0.29 ± 0.01 | 8.06 ± 0.37 | 0.14 ± 0.02 | 9.99 ± 1.16 | 6.59 ± 2.60 |
| **H2F1H15SH** | 0.34 ± 0.01 | 5.33 ± 0.11 | 0.13 ± 0.02 | 11.39 ± 1.30 | 31.28 ± 11.46 |
| **H3F1H14SH** | 0.32 ± 0.01 | 6.12 ± 0.17 | 0.19 ± 0.03 | 6.43 ± 0.66 | 3.96 ± 1.20 |
| **H4F1H13SH** | 0.37 ± 0.01 | 6.20 ± 0.15 | 0.25 ± 0.03 | 5.77 ± 0.46 | 2.35 ± 0.56 |

The ratio of intensities of the methyl stretching resonances in the SFG spectra of the adsorbates (excluding the **F1H17SH**) at the solid-air interface were used to determine the average orientation of the terminal group, defined as the angle of the terminal C–C bond with respect to the surface normal. The ratios were compared to simulated curves that show the relationship between intensity ratio and $CH_3$ tilt angle with respect to the surface normal. Because of the electron-withdrawing nature of the $CF_2$ groups, the depolarization ratios of the $CH_3$ bands used in the analysis were different depending on

their proximity to the $CF_2$ group, producing different simulated orientation curves for the functional groups in different SAMs. Therefore, the curves were tailored to the molecules so that the **H1F1H16SH** and **H2F1H15SH** theoretical orientation curves were different than the one used for **H3F1H14SH**, **H4F1H13SH**, and **H18SH**. The orientation analysis gives a reference point for adsorbate terminal group tilt angle before contact with liquids and can provide an explanation for some of the phenomena discussed in the thickness and XPS sections. The average tilt angles of the methyl groups are plotted in Figure 4.5 with asymmetric error bars that denote the range of possible tilt angles, based on the error in the intensity ratios listed in Table 4.4.

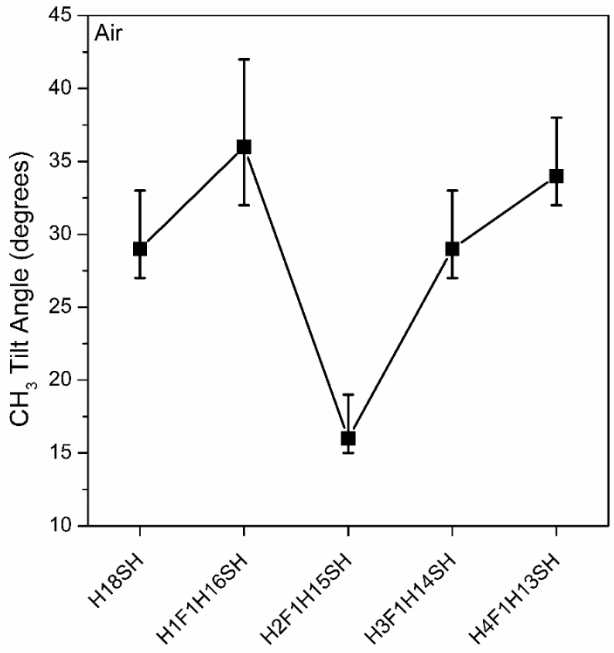


**Figure 4.5**. The tilt angles, derived from SFG orientation analysis, of the terminal methyl ($CH_3$) groups of the SAMs generated from **H18SH**, and the buried $CF_2$ series of alkanethiols at the air-solid interface. The asymmetric error bars denote the range of angles based on the error in the intensity ratios listed in Table 4.3.

Observing the consequences of fluorinating one carbon atom on the resonance frequencies and intensities of the adjacent methyl and methylene groups can provide insight into the process by which these molecules may interact with their environment. Several factors can affect the intensity of a vibrational mode in SFG spectroscopy: IR/Raman cross-section (the lower the cross-sections, the lower the intensities); order (orientational distribution -- the more molecules are oriented in the same manner, the more contribution to the final intensity of the resonance); and orientation (due to the IR surface selection rules of metals, the more tilted the transition dipole is -- pointing away from the surface normal -- the less intense it will appear in the spectra). Proximity to the electron-withdrawing $CF_2$ was observed to shift the C–H stretching resonances to higher frequencies for the methyl and methylene groups, as highlighted by the dashed lines in the surface IR (Figure 4.3) and SFG spectra (Figure 4.4).

The highly electron-withdrawing nature of the fluorine atoms may cause a shortening of the bond between the carbon and hydrogen atoms in the hydrocarbon functional groups adjacent to the fluorocarbon, leading to a lower overall change in the polarizability of the C–H bond (a lower cross-section), and to lower intensities of the C–H stretching peaks observed in the SFG spectra for the **H1F1H16SH**, in comparison to the intensities of the peaks for the remaining films in the buried $CF_2$ series. However, a broad distribution of orientations in the terminal methyl of **H1F1H16SH**, denoting a fluid structure at the interface, could also decrease the SFG signal intensity. Orientation distribution analysis using the tilt angle distribution curves shown in Figure 4.6A for the $CH_3$ in the **H1F1H16SH** SAM shows that the methyl group can have an average orientation ranging from 24°–36° (a range of 12°) from the surface normal. This is a much

broader range in comparison to the **H2F1H15SH** $CH_3$ group for which the range for the average tilt angle is from 15°–20° (a range of 5°), as shown in Figure 4.6B. Similar analysis performed on the $CH_3$ tilt angles of the terminal groups in the remaining SAMs showed distribution angle ranges of 14° for **H3F1H13SH**, 4° for **H4F1H13SH**, and 2° for **H18SH**. Therefore, the SAMs with an even number of hydrocarbons at the terminus (**H2F1H15SH**, **H4F1H13SH**, and **H18SH**) were more well-ordered (and their $\nu_{ss}^{CH_3}$ band was more intense) than those formed from alkanethiols with an "odd" number of hydrocarbon groups at the terminus (**H1F1H16SH** and **H3F1H14SH**). This is in line with the appearance of clear methylene resonances in the SFG spectra in Figure 4.4 for the methyl and propyl-terminated buried $CF_2$ SAMs, indicating exposure of methylene groups at the interface. Therefore, the broad distributions of orientations causing a change in the structure at the termini of the monolayers can be expected to contribute to the wettability behavior of the films.

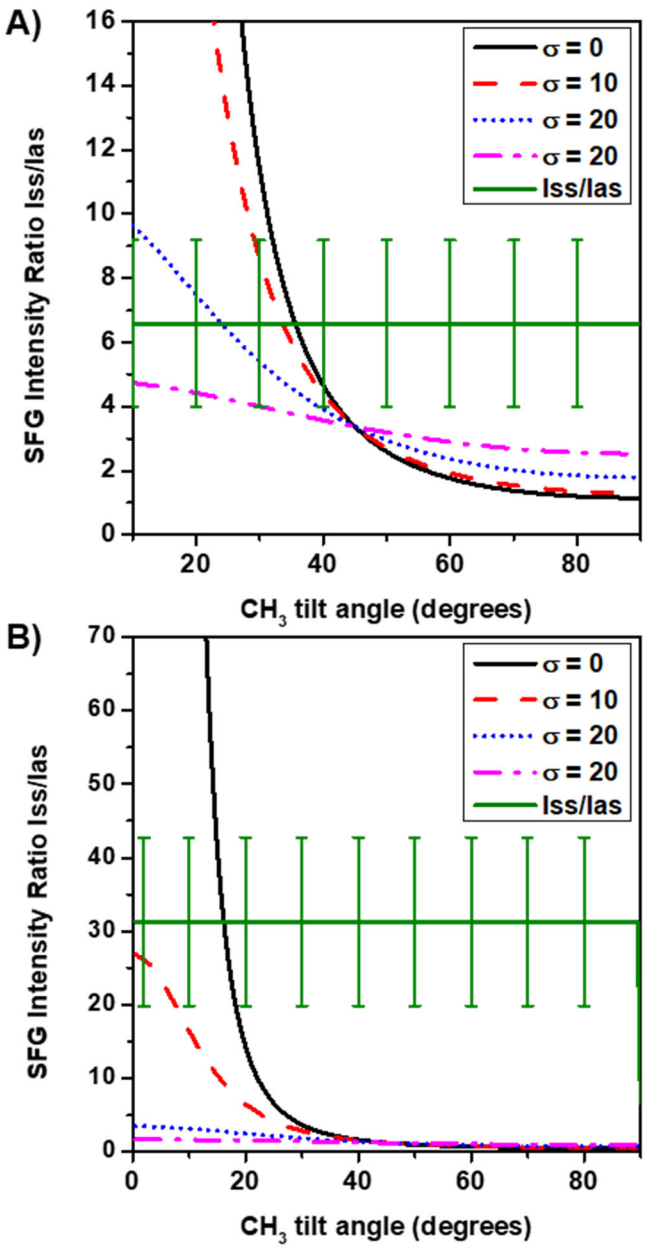


**Figure 4.6**. The orientation distribution curves for the terminal methyl ($CH_3$) groups of the SAMs generated from A) **H1F1H16SH** and B) **H2F1H15SH** at the air-solid interface. Note that the curves are not the same. The black solid, red dash, blue dot, and magenta dash-dot lines are the orientation curves with a Gaussian distribution width of σ = 0°, 10°, 20°, and 30°, respectively. The horizontal green solid lines and error bars represent the intensity ratio of the symmetric to antisymmetric $CH_3$ stretching resonances of A) **H1F1H16SH** and B) **H2F1H15SH** as derived from the fits to the experimental data shown in Figure 4.4.

The average tilt angles of the methyl groups at the air-solid interface can provide information on the influence of the fluorine atoms on the configuration of the neighboring hydrocarbons. Figure 4.5 shows that in the case of **H1F1H16SH**, proximity of the $CH_3$ to the bulky $CF_2$ group causes the methyl group to tilt slightly more than the same group in **H18SH**. This could be due to larger distance between the methyl groups of adjacent adsorbates, in accordance with the lower packing density shown by the XPS data, decreasing the probability for van der Waals interactions. Because the distribution of orientations for these methyl groups is broad, the group is likely not interacting strongly with neighboring methyl groups, so that it is more freely reorienting about the molecular axis than the methyl groups in the non-fluorinated analogue, **H18SH**.

For the **H2F1H15SH** monolayer, the methyl group is tilted more upright than for the other SAMs. If the terminal groups are in a trans configuration there could be repulsion between the fluorine atoms in the $CF_2$ and the hydrogen atoms in the terminal $CH_3$; the ethyl group would then reorient to reduce the amount of repulsion between $CF_2$ groups in adjacent molecules, as shown by the illustration in Figure 4.7. For the propyl-terminated and butyl-terminated films, the terminal methyl is tilted similarly to that of the **H18SH**, possibly due to having three or more hydrocarbons to interact favorably through van der Waals interactions with adjacent adsorbates.

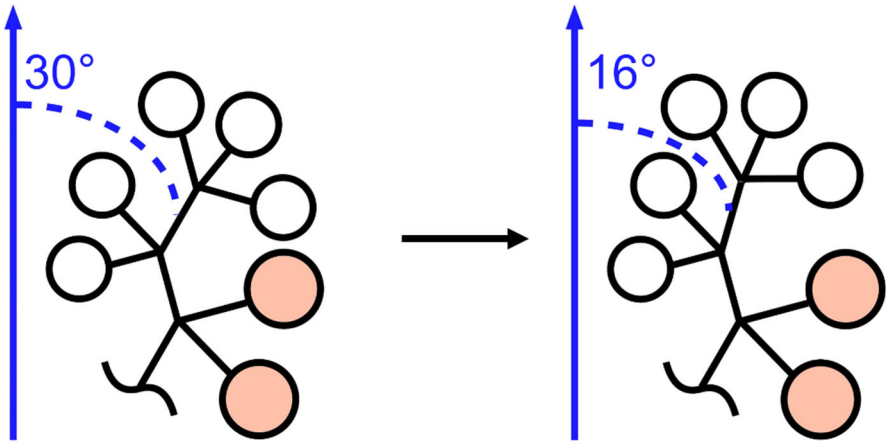


**Figure 4.7**. An illustration of the orientation of the terminal methyl ($CH_3$) group of the SAM generated from **H2F1H15SH** at the air-solid interface. The white circles represent hydrogen atoms, while the pink filled circles represent fluorine atoms. The left side of the image represents the methyl group of the **H2F1H15SH** monolayer if it was tilted at the same angle as the methyl group in **H18SH**. The right side shows the tilt angle of the methyl group in **H2F1H15SH**, as determined through SFG orientation analysis. The blue solid arrows point in the direction of the surface normal (the z-axis).

#### 4.3.1.5. Contact Angle Measurements

To visualize the macroscopic wetting behavior of the SAMs on gold with different contacting liquids, the advancing contact angles of several liquids in contact with the SAMs were measured. Several contacting liquids were tested, including the polar liquids water ($H_2O$), acetonitrile ($CH_3CN$), and dimethylsulfoxide (DMSO), a nonpolar hydrocarbon liquid, hexadecane (HD), and a nonpolar fluorocarbon liquid, perfluorodecalin (PFD). Representative images for the advancing contact angles of the polar liquids are shown in Figure 4.8, the nonpolar liquids in Figure 4.9, and the contact angle values are plotted in Figure 4.10. The films show an increase in the contact angle (less wettable) of all the liquids tested as the $CF_2$ is buried further into the backbone of the alkane chain; the wettability decreases in order from methyl to ethyl to propyl and finally butyl-terminated

buried $CF_2$ films. The most striking difference in the contact angles comes from the molecule with a fluorocarbon atom positioned adjacent to the terminal methyl group, **H1F1H16SH**. This film is more wettable with each of the wetting liquids than any of the other films in the series, with contact angles at least 5° lower than the rest of the films in this study.

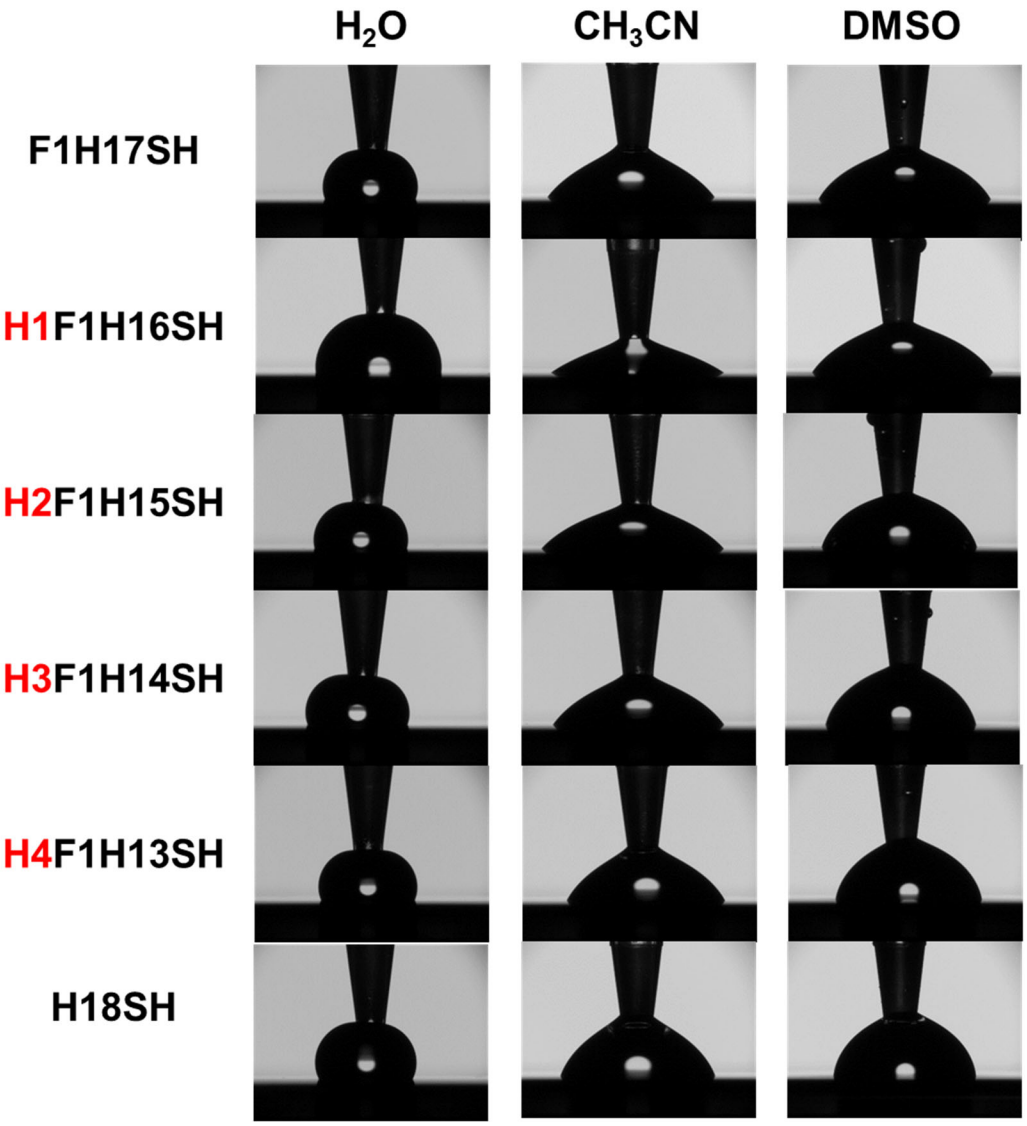


**Figure 4.8**. Representative images of the contact angles of the polar contacting liquids, water ($H_2O$), acetonitrile ($CH_3CN$), and dimethylsulfoxide (DMSO) atop the SAMs generated from **F1H17SH**, **H18SH**, and the buried $CF_2$ series of alkanethiols.

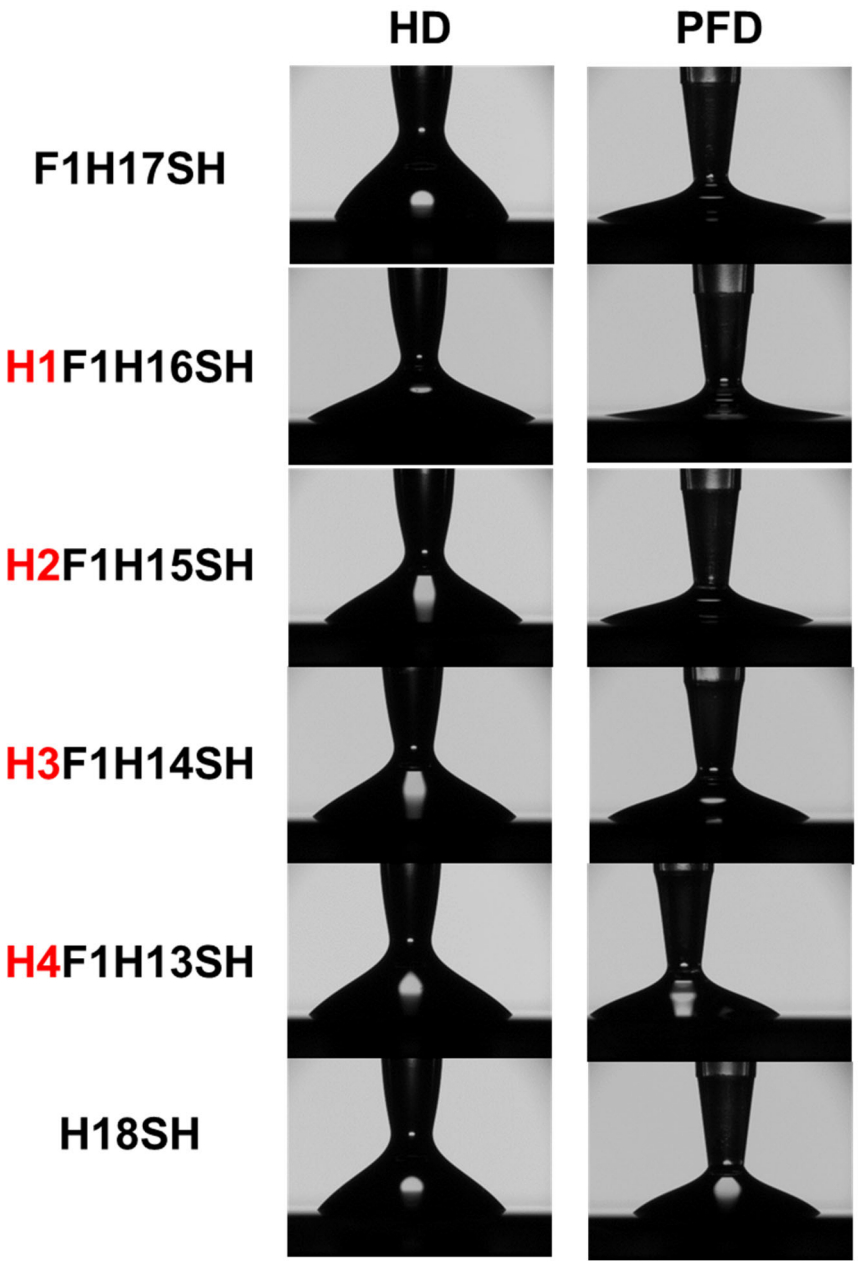


**Figure 4.9**. Representative images of the contact angles of the nonpolar contacting liquids, hexadecane (HD) and perfluorodecalin (PFD) atop the SAMs generated from **F1H17SH**, **H18SH**, and the buried $CF_2$ series of alkanethiols.

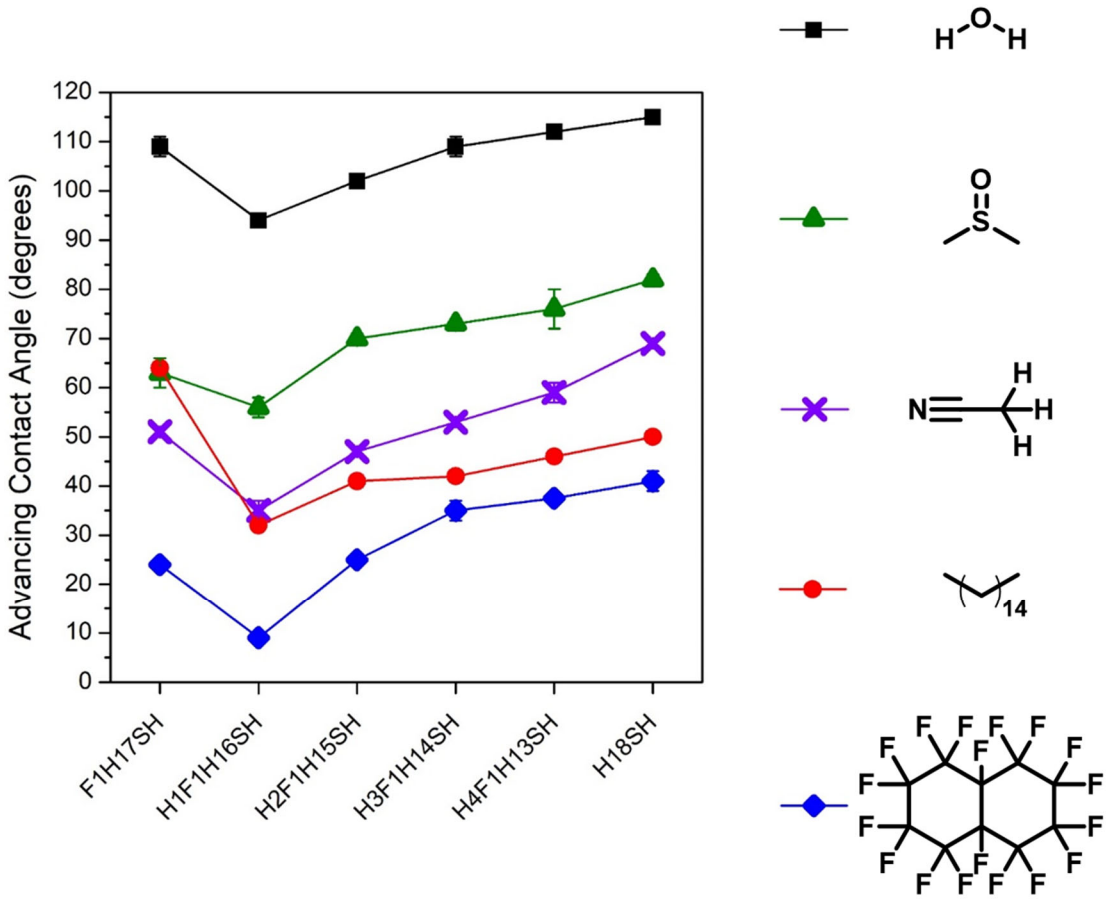


**Figure 4.10**. The advancing contact angles of the liquids in contact with the SAMs generated from **F1H17SH**, **H18SH**, and the buried $CF_2$ series of alkanethiols. Error bars not shown fall within the range of the symbol. The structures of the liquids shown from top to bottom are water ($H_2O$), acetonitrile ($CH_3CN$), dimethylsulfoxide (DMSO), hexadecane (HD), and perfluorodecalin (PFD).

The advancing contact angles of the polar liquids, $H_2O$, DMSO, and $CH_3CN$ are shown in Figure 4.10. The **F1H17SH** SAM has a lower contact angle with the polar solvents than the fully hydrocarbon **H18SH** due to stronger favorable interactions between the terminal $CF_3$-$CH_2$ dipole and the polar contacting liquids versus the weaker induced-dipole to dipole interactions between the $CH_3$-$CH_2$ terminus and the polar liquid. The buried $CF_2$ SAMs show an increase in the contact angle (less wettable) as the $CF_2$ moiety

is buried deeper into the film, indicating that the interaction between a terminal $CH_3$-$CF_2$ moiety is more favorable than a $CH_3$-$CH_2$. Previous reports on the wetting behavior of water on ether-terminated SAMs on Au, showed that the water contact angle stopped changing when the alkyl chain atop the O atom was four hydrocarbons or longer.[51] Bain and Whitesides noted that it was likely that the water molecules could penetrate into the short alkyl chains at the surface of the monolayer, but because of unfavorable energetics between water and hydrocarbons, the hydrogen bonding between water and the ether group was unable to overcome the concomitant hydrophobic interactions when the alkyl chains were above a certain length.[51] Therefore, water contact angles were unable to reveal the presence of the ether group at the interface once the ether group was buried under four or more hydrocarbons.[51] Similarly, as the length of the alkyl chain above the $CF_2$ moiety in the SAMs used in this study increased, the favorable interaction between the polar liquids and the small dipole created by the addition of a fluorinated group into the alkane chain decreased, thereby increasing the contact angle. This interaction will be discussed further with the solid-liquid interface SFG spectra.

For a linear nonpolar molecule, such as hexadecane, the hydrocarbon terminated SAMs would be expected to present a more wettable surface than fluorocarbon surface due to the self-associating interactions between hydrocarbons when in contact with fluorocarbons.[10] Therefore the trend in the wettability data should show a gradual decrease in the HD contact angle, from **F1H17SH** to the methyl-terminated **H1F1H16SH**, then the ethyl, propyl, and butyl-terminated films, until the fully hydrocarbon **H18SH** film shows the lowest contact angle. The presence of a terminal dipole at the surface would then lead to an oleophobic fluorinated film (i.e., less wettable with hexadecane). However, Figure

4.10 shows the lowest hexadecane contact angle was obtained for the monolayer generated from **H1F1H16SH**, (i.e., the most wettable surface). The results then show that the HD contact angle increases to match the angle of a fully hydrocarbon surface as the fluorocarbon is further buried into the film. Similarly, for the contact angles of the nonpolar, bulky, perfluorodecalin, chosen specifically to probe fluorine to fluorine interactions, a similar trend is observed as with hexadecane -- the methyl-terminated film is the most wettable and the butyl-terminated film has a similar wettability to that of the **H18SH** surface. The loss of one fluorine atom at the interface was not expected to increase the wettability of the **H1F1H16SH** in comparison to the **F1H17SH**; quite the opposite, a more hydrocarbon-rich surface, such as the $CH_3$-$CF_2$ terminated film, should have been less wettable than the $CF_3$-$CH_2$ terminated surface. Therefore, attractive fluorine-fluorine interactions were not the cause of the low contact angles in the case of the **H1F1H16SH**. The increase in the wettability of the **H1F1H16SH** film, in comparison to the **H18SH** surface, must then be due to a different phenomenon than that of dispersive and/or dipole–induced-dipole interactions.

The lower packing density suggested by XPS at the termini of the SAMs as the $CF_2$ is increasingly exposed at the surface makes it easier for the liquids to intercalate into the monolayer, causing disorder in the film at the interface. Bain and Whitesides noted that induced disorder in the top portion of ether-terminated monolayers when in contact with acetonitrile could be the reason for increased wettability of methyl-terminated ether SAMs over those with longer alkyl chains atop the oxygen atom.[51] Disorder in the film at the interface could lead to more exposure of the underlying methylene groups for the **H1F1H16SH** monolayer, thereby increasing the wettability of film. Therefore, a closer

inspection of the structure and the terminal functional group orientation at the solid-liquid interface by spectroscopically probing the interface between these films and $CD_3CN$ (a polar liquid) as well as PFD (fluorinated nonpolar liquid) may be used to explain the trends in wettability seen in this study

### 4.3.2. SFG Spectroscopy of the Solid-Liquid Interface

In order to elucidate the origin of the wettability trends highlighted in the previous section, the solid-liquid interface between the molecules and contacting liquids was probed. SFG was used to determine the orientation of the SAM terminal groups with respect to the contacting fluid in order to determine whether or not a change in the structure of the SAM upon contact with a liquid correlates to the macroscopic advancing contact angles of the liquids in contact with the films. Acetonitrile was chosen because its effect on the structure of SAMs has been probed before,[52-55] and the deuterated liquid is readily available for use in isolating the C–H stretches of the alkanethiols in the SFG spectra. The polar nature of the small molecule could give insight into the influence of dipoles on the orientation of the terminal groups in the fluorinated alkanethiols on the gold. Perfluorodecalin was used to provide insight into how fluorine-fluorine interactions cause the molecules on the surface to reorient. The SFG spectra in the C–H stretching region for each of the molecules in this study in contact with deuterated acetonitrile ($CD_3CN$) are shown in Figure 4.11A.

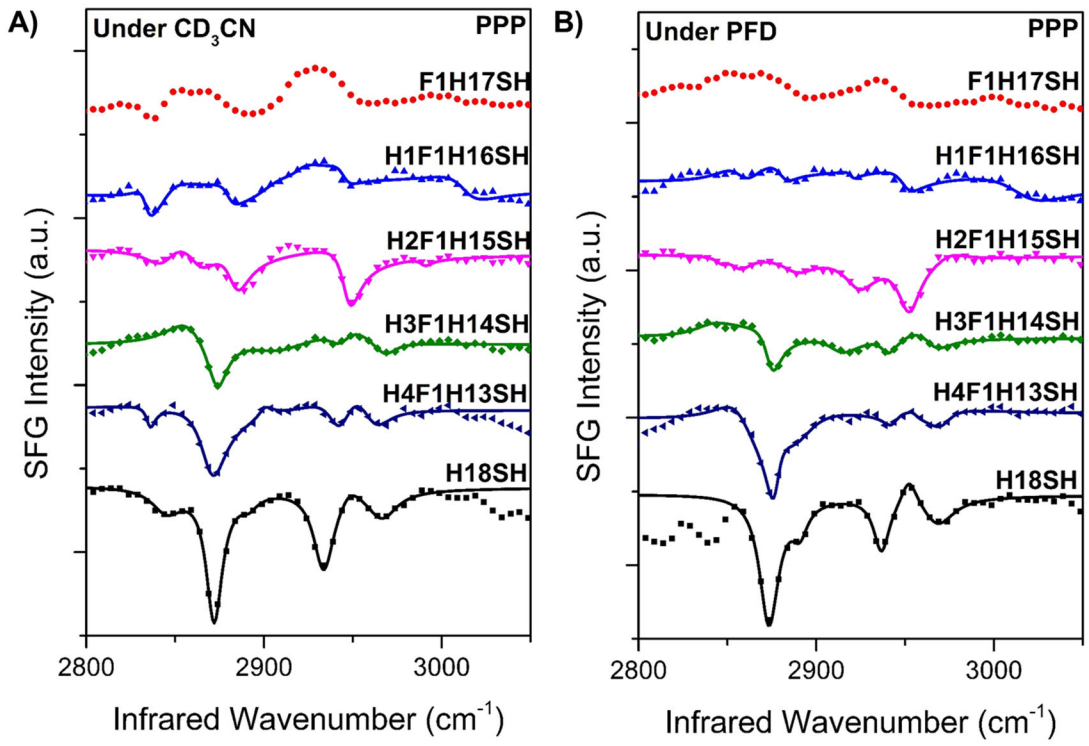


**Figure 4.11**. PPP SFG spectra of the SAMs generated from **H18SH**, **F1H17SH**, and the buried $CF_2$ series of alkanethiols in the C–H stretching region in contact with A) $CD_3CN$ and B) PFD. *The solid lines are the best fit curves for the experimental data and is represented by symbols.*

Figure 4.11A shows a marked decrease in the intensity of the methyl antisymmetric stretching resonances, as well as an increase in the presence of the methylene symmetric stretching dip at 2850 $cm^{-1}$. The ratio of the intensities of methyl symmetric to asymmetric stretching peaks seems to increase as well. Fitting of the solid-liquid interface SFG spectra and subsequent orientation analysis, the results of which are plotted in Figure 4.12 for the solid-liquid interface of the SAMs in contact with acetonitrile, shows that for the **H1F1H16SH** methyl groups the tilt angle changes dramatically compared to the solid-air interface, indicating that the methyl group went from a more upright orientation to nearly parallel to the surface. Figure 4.12 also compares the advancing contact angles of the films

with their terminal group tilt angles at the solid-liquid interface. The results show that the **H1F1H16SH** terminal C–C bond is lying flat (toward the surface), causing the $CF_2$ to be exposed at the interface. The increase in the intensity of the $\nu_{ss}^{CH_2}$ band at ~2850 $cm^{-1}$ also denotes an increase in gauche conformations at the interface that break the local centrosymmetry of the $CH_2$ groups near the interface and allow for SFG signal to be collected. These pieces of evidence indicate that the $CH_3CN$ molecules are indeed intercalating into the monolayer and changing the structure of the SAM at the interface by inducing some disorder. The penetration of the liquid into the SAM as well as the exposed $CH_3$-$CF_2$ dipole interacting favorably with the polar $CH_3CN$ molecules, leads to the low contact angles seen in the wettability results.

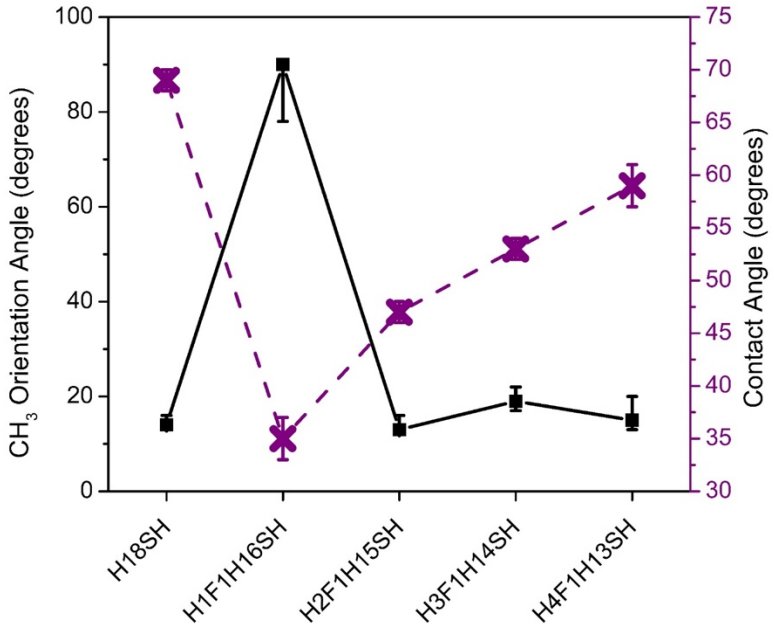


**Figure 4.12**. Methyl group tilt angles derived for the SAMs generated from **H18SH** and the buried $CF_2$ series of alkanethiols in contact with acetonitrile ($CD_3CN$) in comparison to the corresponding macroscopic advancing contact angles of $CH_3CN$.

Figure 4.12 shows that the **H2F1H15SH** methyl group remains at approximately the same tilt angle, while for the **H3F1H14SH**, **H4F1H13SH**, and **H18SH** monolayers the methyl group tilt angle decreases (the $CH_3$ adopts a more upright orientation), in comparison to the solid-air interface. While this shows that the interaction between acetonitrile and the films causes the terminal group of these four SAMs to point more upright (away from the surface), probably due to the intercalation of the $CH_3CN$ into the monolayer, the methyl group tilt angles of the **H2F1H15SH, H3F1H14SH**, **H4F1H13SH**, and **H18SH** SAMs are the same, within error. Since the terminal groups in these SAMs are oriented away from the surface, they could be increasingly masking possible interactions between the contacting liquids and $CF_2$ moiety, as it is buried deeper into the film. The contact angle data imply that the acetonitrile contact angle increases as the fluorocarbon is buried until the limit of penetration of the liquid disables the liquid from interacting with the $CF_2$, and the contact angle is at its highest as in the case of the **H18SH** monolayer.

The intensity ratios of the methyl stretching peaks in the SFG spectra of the solid-liquid interface between the SAMs and PFD, shown in Figure 4.11B, were used to calculate methyl tilt angles when in contact with PFD. Then, comparison between methyl group orientation angle and advancing contact angle was performed for the SAMs under perfluorodecalin, and is shown in Figure 4.13. The wettability of the films in PFD also follows the same trend as the $CH_3CN$, with the **H1F1H16SH** film being completely wettable. The orientation analysis results show that the terminal C–C bond of the **H1F1H16SH** SAM is parallel to the surface, thereby completely exposing the $CF_2$ group at the interface and allowing for favorable interactions with the fluorinated liquid. The

orientation of the terminal C–C of the **H2F1H15SH** SAM is tilted towards the surface, nearly to the same degree as in the case of the solid-air interface, giving it an upright orientation which can partially block the bulky PFD from accessing the $CF_2$, thereby producing a higher contact angle (less wettable surface). For the **H3F1H14SH** and **H4F1H13SH** monolayers, the methyl orientation angles are the same, within error, at the solid-liquid interface, and are lower than when the corresponding methyl groups are exposed to air. This shows that although the terminal C–C groups of these films are more upright than at the air-solid interface, implying that the PFD intercalates into the film, dispersive interactions between the hydrocarbons can partially overcome the interactions between the PFD and the buried $CF_2$, giving PFD contact angles that are similar to the fully hydrocarbon film **H18SH**. Therefore the increase in contact angle can be attributed to the fact that fluorocarbons interact less favorably with $CH_2$ groups than $CF_2$.[10,51,56]

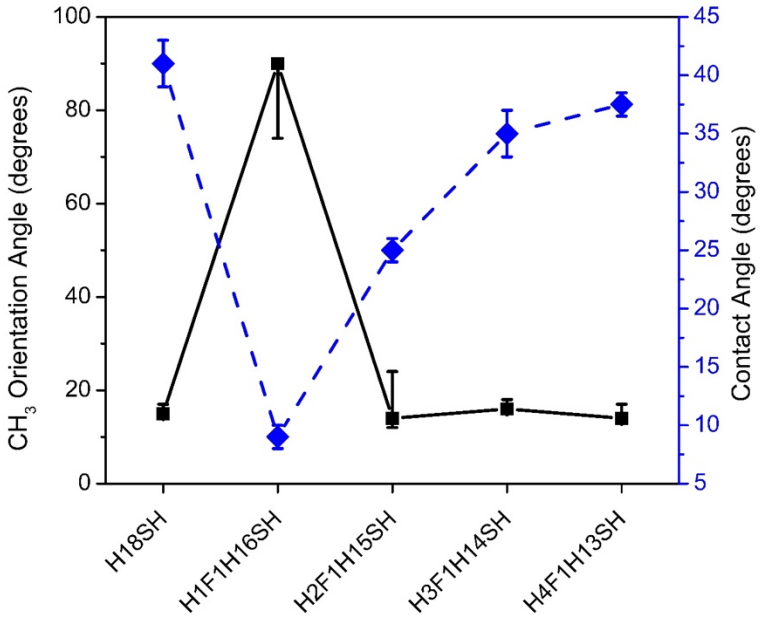


**Figure 4.13**. Methyl group tilt angles derived for the SAMs generated from **H18SH** and the buried $CF_2$ series of alkanethiols in contact with perfluorodecalin (PFD) in comparison to the corresponding macroscopic advancing contact angles.

To better understand the interaction between the contacting liquids and the films, the $CF_3$-$CH_2$ and the $CH_3$-$CF_2$ terminated surfaces can be compared. The analysis in Chapter 5 shows that the solid-liquid interface SFG spectrum for the **F1H17SH** SAM under acetonitrile has an increased intensity for the $\nu_{ss}^{CH_2}$ band at ~2850 $cm^{-1}$ in comparison to the solid-air interface, indicating that the $CF_3$-$CH_2$ dipoles are oriented in an ordered manner that exposes the methylene at the interface (possibly through a flat orientation of the terminal C–C). For the **F1H17SH** monolayer in contact with PFD, the methylene resonance disappeared, implying that intercalation of PFD into the film increases the disorder of the monolayer at the interface. The $CH_3$-$CF_2$ surface also contains a terminal dipole that appears to be parallel to the surface when in contact with the contacting liquids. Previous studies have shown that for both $CH_3CN$ and PFD, the $CF_3$-terminated surface is more wettable than the fully hydrocarbon surface, a phenomenon that has been attributed to the dipole-dipole interactions with the polar $CH_3CN$ and the fluorine-to-fluorine interactions with PFD.[10,12,17-18] The additional data provided by the **H1F1H16SH** surface implies that while the terminal dipole plays a strong role in the wettability of the $CF_3$-terminated SAMs, the inversion of this dipole by the fluorination of the second carbon in the chain makes the surface more wettable, as observed previously with the wettability of the **H1F6HnSH** SAMs.[17]

The increased wettability of the $CH_3$-$CF_2$ terminated surface has some contribution from the dipole, but the wettability behavior can also be attributed to the fact that the adsorbates are more separated at the terminus, as suggested by the XPS results, due to the addition of a bulky functional group in the middle of the chain, rather than at the terminus. A study on similarly buried $CF_2$ monolayers showed that the addition of a $CF_2$ group has

the ability to introduce conformational mobility to the upper alkyl chain, and therefore, introduce disorder into the monolayer.[57] Due to the lower packing density at the terminus, the **H1F1H16SH** film is less well-ordered than the **F1H17SH** film, as shown by the broad distribution of orientation angles for the methyl group in the **H1F1H16SH** monolayer, causing it to be the most wettable surface in this dataset. As the $CF_2$ group is increasingly concealed by the increase in hydrocarbon groups above it, and as the order in the film increases at the terminus due to increased van der Waals interactions between adjacent methylene groups, the contact angles increase (i.e., the wettability of the surface decreases).

## 4.4. Conclusions

Thin films with systematically buried fluorocarbon were generated and studied to understand the role of selective fluorination on the structure and macroscale properties of the final monolayer, specifically the wettability of the film. Taking the thickness results from ellipsometry, the monolayer conformation results from XPS and PM-IRRAS, and the interfacial structure results from SFG into account, the **H1F1H16SH** monolayer was deemed to be the least well-ordered at the interface and therefore the most wettable by each of the contacting liquids tested. The large orientational distribution of the methyl group in the **H1F1H16SH** SAM was noted as a possible reason for the observed lower intensities of the methyl peaks in the **H1F1H16SH** SFG spectra, as well as the high wettability of the monolayer, in comparison to the other SAMs in the series. The remaining monolayers generated from **H2F1H15SH**, **H3F1H14SH**, and **H4F1H13SH**, showed decreased wettability as the $CF_2$ group was systematically concealed in the alkane chain, although the methyl tilt angles for each monolayer were found to be aligned with the surface normal

(upright orientation) at the solid-liquid interface. The wettability of the film was shown to be influenced by the structure of the functional groups at the interface due to the ability of the termini of the fluorinated molecules to reorient more freely, compared to the methyl group of a fully hydrocarbon monolayer, due to the presence of a bulky $CF_2$ group in the chain. Therefore, for the self-assembled monolayers probed in this study, the order of the terminal groups and their structure at the interface appear to have a pronounced effect on the macroscopic wettability behavior of the thin films.

## 4.5. References


1. Lenk, T. J.; Hallmark, V. M.; Hoffmann, C. L.; Rabolt, J. F.; Castner, D. G.; Erdelen, C.; Ringsdorf, H., Structural Investigation of Molecular Organization in Self-Assembled Monolayers of a Semifluorinated Amidethiol. *Langmuir* **1994,** *10*, 4610–4617.
2. Alves, C. A.; Porter, M. D., Atomic Force Microscopic Characterization of a Fluorinated Alkanethiolate Monolayer at Gold and Correlations to Electrochemical and Infrared Reflection Spectroscopic Structural Descriptions. *Langmuir* **1993,** *9*, 3507–3512.
3. Frey, S.; Heister, K.; Zharnikov, M.; Grunze, M.; Tamada, K.; Colorado, R., Jr.; Graupe, M.; Shmakova, O. E.; Lee, T. R., Structure of Self-Assembled Monolayers of Semifluorinated Alkanethiols on Gold and Silver Substrates. *Isr. J. Chem.* **2000,** *40*, 81–97.

4. Chidsey, C. E. D.; Loiacono, D. N., Chemical Functionality in Self-Assembled Monolayers: Structural and Electrochemical Properties. *Langmuir* **1990,** *6*, 682–691.

5. Miura, Y. F.; Takenaga, M.; Koini, T.; Graupe, M.; Garg, N.; Graham, R. L., Jr.; Lee, T. R., Wettabilities of Self-Assembled Monolayers Generated from $CF_3$-Terminated Alkanethiols on Gold. *Langmuir* **1998,** *14*, 5821–5825.

6. Pflaum, J.; Bracco, G.; Schreiber, F.; Colorado, R., Jr.; Shmakova, O.; Lee, T.; Scoles, G.; Kahn, A., Structure and Electronic Properties of $CH_3$-and $CF_3$-terminated Alkanethiol Monolayers on Au (111): a Scanning Tunneling Microscopy, Surface X-ray and Helium Scattering Study. *Surf. Sci.* **2002,** *498*, 89–104.

7. Kim, H. I.; Graupe, M.; Oloba, O.; Koini, T.; Imaduddin, S.; Lee, T. R.; Perry, S. S., Molecularly Specific Studies of the Frictional Properties of Monolayer Films: A Systematic Comparison of $CF_3$-, $(CH_3)_2CH$-, and $CH_3$-Terminated Films. *Langmuir* **1999,** *15*, 3179–3185.

8. Bruce, R. C.; You, L.; Förster, A.; Pookpanratana, S.; Pomerenk, O.; Lee, H. J.; Marquez, M. D.; Ghanbaripour, R.; Zenasni, O.; Lee, T. R.; Hacker, C. A., Contrasting Transport and Electrostatic Properties of Selectively Fluorinated Alkanethiol Monolayers with Embedded Dipoles. *J. Phys. Chem. C* **2018,** *122*, 4881–4890.

9. Fukushima, H.; Seki, S.; Nishikawa, T.; Takiguchi, H.; Tamada, K.; Abe, K.; Colorado, R., Jr.; Graupe, M.; Shmakova, O. E.; Lee, T. R., Microstructure,

Wettability, and Thermal Stability of Semifluorinated Self-Assembled Monolayers (SAMs) on Gold. *J. Phys. Chem. B* **2000,** *104*, 7417–7423.

10. Colorado, R., Jr.; Lee, T. R., Wettabilities of Self-Assembled Monolayers on Gold Generated from Progressively Fluorinated Alkanethiols. *Langmuir* **2003,** *19*, 3288–3296.

11. Laffineur, F. A., D.; Plumier, F.; Pirlot, C.; Hevesi, L.; Delhalle, J.; Mekhalif, Z., Comparison Between $CH_3(CH_2)_{15}SH$ and $CF_3(CF_2)_3(CH_2)_{11}SH$ Monolayers on Electrodeposited Silver. *Langmuir* **2004,** *20*, 3240–3245.

12. Graupe, M.; Takenaga, M.; Koini, T.; Colorado, R., Jr.; Lee, T. R., Oriented Surface Dipoles Strongly Influence Interfacial Wettabilities. *J. Am. Chem. Soc.* **1999,** *121*, 3222–3223.

13. Colorado, R., Jr.; Graupe, M.; Shmakova, O. E.; Villazana, R. J.; Lee, T. R., Interfacial Properties on the Submicron Scale. *ACS Symp. Ser. 781* **2001,** 276–292.

14. Weinstein, R. D.; Moriarty, J.; Cushnie, E.; Colorado, R., Jr.; Lee, T. R.; Patel, M.; Alesi, W. R.; Jennings, G. K., Structure, Wettability, and Electrochemical Barrier Properties of Self-Assembled Monolayers Prepared from Partially Fluorinated Hexadecanethiols. *J. Phys. Chem. B* **2003,** *107*, 11626–11632.

15. Tamada, K.; Ishida, T.; Knoll, W.; Fukushima, H.; Colorado, R., Jr.; Graupe, M.; Shmakova, O. E.; Lee, T. R., Molecular Packing of Semifluorinated Alkanethiol Self-Assembled Monolayers on Gold: Influence of Alkyl Spacer Length. *Langmuir* **2001,** *17*, 1913–1921.

16. Marquez, M. D. Modulating Surface Dipoles in Fluorinated Thin Films. Ph.D. Thesis, University of Houston, December 2017.

17. Zenasni, O.; Marquez, M. D.; Jamison, A. C.; Lee, H. J.; Czader, A.; Lee, T. R., Inverted Surface Dipoles in Fluorinated Self-Assembled Monolayers. *Chem. Mater.* **2015,** *27*, 7433–7446.

18. Colorado, R., Jr.; Graupe, M.; Kim, H. I.; Takenaga, M.; Oloba, O.; Lee, S.; Perry, S. S.; Lee, T. R., Interfacial Properties on the Submicron Scale. *ACS Symp. Ser. 781* **2001,** 58–75.

19. Zenasni, O.; Jamison, A. C.; Lee, T. R., The Impact of Fluorination on the Structure and Properties of Self-Assembled Monolayer Films. *Soft Matter* **2013,** *9*, 6356–6370.

20. Jamison, A. C. Specifically Fluorinated Alkanethiol Adsorbates and Their Influence Upon the Formation of Self-Assembled Monolayers on Gold. Ph.D. Thesis, University of Houston, May 2011.

21. Bain, C. D., Sum-Frequency Vibrational Spectroscopy of the Solid/Liquid Interface. *J. Chem. Soc., Faraday Trans.* **1995,** *91*, 1281–1296.

22. Wang, H.-F.; Gan, W.; Lu, R.; Rao, Y.; Wu, B.-H., Quantitative Spectral and Orientational Analysis in Surface Sum Frequency Generation Vibrational Spectroscopy (SFG-VS). *Int. Rev. Phys. Chem.* **2005,** *24*, 191–256.

23. Tyrode, E.; Johnson, C. M.; Rutland, M. W.; Day, J. P. R.; Bain, C. D., A Study of the Adsorption of Ammonium Perfluorononanoate at the Air−Liquid Interface by Vibrational Sum-Frequency Spectroscopy. *J. Phys. Chem. C* **2007,** *111*, 316–329.

24. Iwahashi, T.; Miyamae, T.; Kanai, K.; Seki, K.; Kim, D.; Ouchi, Y., Anion Configuration at the Air/Liquid Interface of Ionic Liquid [bmim]OTf Studied by

Sum-Frequency Generation Spectroscopy. *J. Phys. Chem. B* **2008,** *112*, 11936–11941.

25. Volpati, D.; Chachaj-Brekiesz, A.; Souza, A. L.; Rimoli, C. V.; Miranda, P. B.; Oliveira, O. N.; Dynarowicz-Łątka, P., Semifluorinated Thiols in Langmuir Monolayers – A Study by Nonlinear and Linear Vibrational Spectroscopies. *J. Colloid Interface Sci.* **2015,** *460*, 290–302.

26. Even, M. A.; Lee, S.-H.; Wang, J.; Chen, Z., Detection and Spectral Analysis of Trifluoromethyl Groups at a Surface by Sum Frequency Generation Vibrational Spectroscopy. *J. Phys. Chem. B* **2006,** *110*, 26089–26097.

27. Karageorgiev, P.; Petrov, J. G.; Motschmann, H.; Moehwald, H., Why Fluorination of the Polar Heads Reverses the Positive Sign of the Dipole Potential of Langmuir Monolayers: A Vibrational Sum Frequency Spectroscopic Study. *Langmuir* **2013,** *29*, 4726–4736.

28. Cimatu, K.; Moore, H. J.; Barriet, D.; Chinwangso, P.; Lee, T. R.; Baldelli, S., Sum Frequency Generation Imaging Microscopy of Patterned Self-Assembled Monolayers with Terminal $-CH_3$, $-OCH_3$, $-CF_2CF_3$, $-C{=}C$, −Phenyl, and −Cyclopropyl Groups. *J. Phys. Chem. C* **2008,** *112*, 14529–14537.

29. Kato, M.; Oyaizu, N.; Shimazu, K.; Yagi, I., Oxygen Reduction Reaction Catalyzed by Self-Assembled Monolayers of Copper-Based Electrocatalysts on a Polycrystalline Gold Surface. *J. Phys. Chem. C* **2016,** *120*, 15814–15822.

30. Porter, M. D.; Bright, T. B.; Allara, D. L.; Chidsey, C. E. D., Spontaneously Organized Molecular Assemblies. 4. Structural Characterization of *n*-Alkyl Thiol

Monolayers on Gold by Optical Ellipsometry, Infrared Spectroscopy, and Electrochemistry. *J. Am. Chem. Soc.* **1987,** *109*, 3559–3568.

31. Hirose, C.; Akamatsu, N.; Domen, K., Formulas for the Analysis of Surface Sum-Frequency Generation Spectrum by CH Stretching Modes of Methyl and Methylene Groups. *J. Chem. Phys.* **1992,** *96*, 997–1004.

32. Hirose, C.; Yamamoto, H.; Akamatsu, N.; Domen, K., Orientation Analysis by Simulation of Vibrational Sum Frequency Generation Spectrum: CH Stretching Bands of the Methyl Group. *J. Phys. Chem.* **1993,** *97*, 10064–10069.

33. Bain, C. D.; Troughton, E. B.; Tao, Y. T.; Evall, J.; Whitesides, G. M.; Nuzzo, R. G., Formation of Monolayer Films by the Spontaneous Assembly of Organic Thiols from Solution onto Gold. *J. Am. Chem. Soc.* **1989,** *111*, 321–335.

34. Laibinis, P. E.; Whitesides, G. M.; Allara, D. L.; Tao, Y. T.; Parikh, A. N.; Nuzzo, R. G., Comparison of the Structures and Wetting Properties of Self-Assembled Monolayers of *n*-Alkanethiols on the Coinage Metal Surfaces, Copper, Silver, and Gold. *J. Am. Chem. Soc.* **1991,** *113*, 7152–7167.

35. Castner, D. G.; Hinds, K.; Grainger, D. W., X-Ray Photoelectron Spectroscopy Sulfur 2p Study of Organic Thiol and Disulfide Binding Interactions with Gold Surfaces. *Langmuir* **1996,** *12*, 5083–5086.

36. Tsao, M.-W.; Rabolt, J. F.; Schönherr, H.; Castner, D. G., Semifluorinated/Hydrogenated Alkylthiol Thin Films: A Comparison between Disulfides and Thiol Binary Mixtures. *Langmuir* **2000,** *16*, 1734–1743.

37. Heister, K.; Zharnikov, M.; Grunze, M.; Johansson, L. S. O.; Ulman, A., Characterization of X-ray Induced Damage in Alkanethiolate Monolayers by High-Resolution Photoelectron Spectroscopy. *Langmuir* **2001,** *17*, 8–11.

38. Lindberg, B. J.; Hamrin, K.; Johansson, G.; Gelius, U.; Fahlman, A.; Nordling, C.; Siegbahn, K., Molecular Spectroscopy by Means of ESCA II. Sulfur Compounds. Correlation of Electron Binding Energy with Structure. *Phys. Scr.* **1970,** *1*, 286–298.

39. Heeg, J.; Schubert, U.; Küchenmeister, F., Mixed Self-Assembled Monolayers of Terminally Functionalized Thiols at Gold Surfaces Characterized by Angle Resolved X-ray Photoelectron Spectroscopy (ARXPS) Studies. *Fresenius' J. Anal. Chem.* **1999,** *365*, 272–276.

40. MacPhail, R. A.; Strauss, H. L.; Snyder, R. G.; Elliger, C. A., Carbon-Hydrogen Stretching Modes and the Structure of *n*-Alkyl Chains. 2. Long, All-Trans Chains. *J. Phys. Chem.* **1984,** *88*, 334–341.

41. Snyder, R. G.; Schachtschneider, J. H., Vibrational Analysis of the *n*-Paraffins—I: Assignments of Infrared Bands in the Spectra of $C_3H_8$ through *n*-$C_{19}H_{40}$. *Spectrochim. Acta* **1963,** *19*, 85–116.

42. Tsao, M. W.; Hoffmann, C. L.; Rabolt, J. F.; Johnson, H. E.; Castner, D. G.; Erdelen, C.; Ringsdorf, H., Studies of Molecular Orientation and Order in Self-Assembled Semifluorinated *n*-Alkanethiols: Single and Dual Component Mixtures. *Langmuir* **1997,** *13*, 4317–4322.

43. Durig, J. R.; Yu, Z.; Guirgis, G. A., Conformational Stability, Barriers to Internal Rotation, Vibrational Assignment, and Ab Initio Calculations of 2,2-Difluorobutane. *J. Mol. Struct.* **1999,** *509*, 115–135.

44. Durig, J. R.; Guirgis, G. A.; Li, Y. S., Microwave, Raman, and Far Infrared Spectra, Barrier to Internal Rotation, and Dipole Moment of 2,2-Difluoropropane. *J. Chem. Phys.* **1981,** *74*, 5946–5953.

45. McNaughton, D.; Evans, C., High-Resolution FTIR Spectrum of Jet-Cooled $CH_3CHF_2$. *J. Phys. Chem.* **1996,** *100*, 8660–8664.

46. Smith, D. C.; Saunders, R. A.; Nielsen, J. R.; Ferguson, E. E., Infrared and Raman Spectra of Fluorinated Ethanes. IV. The Series $CH_3$–$CH_3$, $CH_3$–$CH_2F$, $CH_3$–$CHF_2$, and $CH_3$–$CF_3$. *J. Chem. Phys.* **1952,** *20*, 847–859.

47. Nanaie, H.; Guirgis, G. A.; Durig, J. R., Torsional Spectra of Molecules with Two $C_{3v}$ Rotors—XXV. Rotational and Vibrational Spectra, $r_0$ Structure, Barriers to Internal Rotation and Ab Initio Calculations for 2,2-Difluoropropane. *Spectrochim. Acta, Part A* **1993,** *49*, 2039–2056.

48. Li, Y. S.; Cox, F. O.; Durig, J. R., Low-Resolution Microwave, Infrared, and Raman Spectra, Conformational Stability, and Vibrational Assignment of 2,2,2-Trifluoroethyl Methyl Ether. *J. Phys. Chem.* **1987,** *91*, 1334–1344.

49. Bain, C. D.; Davies, P. B.; Ong, T. H.; Ward, R. N.; Brown, M. A., Quantitative Analysis of Monolayer Composition by Sum-Frequency Vibrational Spectroscopy. *Langmuir* **1991,** *7*, 1563–1566.

50. Wang, L.; Ishiyama, T.; Morita, A., Theoretical Investigation of C–H Vibrational Spectroscopy. 2. Unified Assignment Method of IR, Raman, and Sum Frequency

Generation Spectra of Ethanol. *The Journal of Physical Chemistry A* **2017,** *121*, 6701–6712.

51. Bain, C. D.; Whitesides, G. M., Depth Sensitivity of Wetting: Monolayers of ω-Mercapto Ethers on Gold. *J. Am. Chem. Soc.* **1988,** *110*, 5897–5898.

52. Ong, T. H.; Ward, R. N.; Davies, P. B.; Bain, C. D., Microscopic Basis of Wetting: an In Situ Study of the Interaction Between Liquids and an Organic Monolayer. *J. Am. Chem. Soc.* **1992,** *114*, 6243–6245.

53. Anderson, M. R.; Evaniak, M. N.; Zhang, M., Influence of Solvent on the Interfacial Structure of Self-Assembled Alkanethiol Monolayers. *Langmuir* **1996,** *12*, 2327–2331.

54. Ong, T. H.; Davies, P. B.; Bain, C. D., Sum-Frequency Spectroscopy of Monolayers of Alkoxy-Terminated Alkanethiols in Contact with Liquids. *Langmuir* **1993,** *9*, 1836–1845.

55. Henry, M. C.; Wolf, L. K.; Messmer, M. C., In Situ Examination of the Structure of Model Reversed-Phase Chromatographic Interfaces by Sum-Frequency Generation Spectroscopy. *J. Phys. Chem. B* **2003,** *107*, 2765–2770.

56. Whitesides, G. M.; Laibinis, P. E., Wet Chemical Approaches to the Characterization of Organic Surfaces: Self-Assembled Monolayers, Wetting, and the Physical-Organic Chemistry of the Solid-Liquid Interface. *Langmuir* **1990,** *6*, 87–96.

57. O'Hagan, D.; Kumadaki, I.; Petty, M.; Takaya, H.; Pearson, C., Synthesis and Langmuir Isotherms of Difluorostearic Acids. *J. Fluorine Chem.* **1998,** *90*, 133–138.

# Chapter 5. Sum Frequency Generation Spectroscopy of Partially Fluorinated Self-Assembled Monolayers on Underpotentially Deposited Silver and Bare Gold

## 5.1. Introduction

Chemical interactions occur at interfaces, and in order to understand the chemistry, buried interfaces, particularly the solid-liquid interface, must be studied due to the implications the interactions at these boundaries have on the macroscopic properties of a surface. Studies performed on model hydrophobic surfaces composed of alkanethiol self-assembled monolayers on gold show that the interfacial structure of the thin film has important consequences on the wettability.[1] The alkyl chains are known to be tilted ~30° from the surface normal in order to maximize van der Waals interactions between adjacent chains.[2-4] Furthermore, a change in the number of carbon atoms in the chain changes the orientation (upright or tilted) of the terminal functional group.[2,5] The change in the orientation of the terminal group has been shown to cause an "odd-even" effect in the interfacial properties of the surfaces.[1,5-6] In this effect, odd-numbered carbon chains (i.e. $CH_3(CH_2)_{16}SH$) on gold, heretofore referred to as *odd SAMs*, have the final C–C axis tilted away from the surface normal, exposing the terminal methyl and methylene groups to the interface. Whereas with even-numbered chains (i.e. $CH_3(CH_2)_{17}SH$), referred to as *even SAMs* in this study, have a more upright oriented terminal C–C axis and, therefore, do not allow for methylene exposure at the interface.[2] This is shown schematically in Figure 1.1 in Chapter 1. The difference in structure results in a more wettable odd SAM by contacting

liquids than the even SAM, due to increased dispersive interactions with the exposed methylene group, producing what is termed the "odd-even" effect in the wettability.

In addition to structural effects, fluorination of the carbon chain has also been shown to strongly influence the interfacial properties of the SAMs.[7-13] A recent study by Zenasni et. al. using trifluoromethyl-terminated and methyl-terminated partially-fluorinated alkanethiol SAMs (FSAMs) observed that the "odd-even" trends in the wettability of fully hydrocarbon SAMs were generally opposite for the $CF_3$-terminated surfaces.[14] They attributed the change to the addition of a FC–HC dipole with the negative pole pointing away from the surface. Research has shown that the SAMs generated from $CF_3$-termianted alkanethiols exhibit identical structural features as the analogous alkanethiol SAMs.[15] Consequently, the orientation of the terminal dipole present in $CF_3$-terminated SAMs follow the orientation of be terminal C–C axis (i.e., tilted away for the odd SAM and upright for the even SAM). The tilted orientation of the terminal dipole in the odd SAM leads to compensation between dipoles, leading to weaker dipole-dipole interactions with contacting liquids (i.e., higher contact angles) compared to the uncompensated dipoles of the upright even SAM.

In order to probe the effect of the terminal dipole further, Zenasni and coworkers inverted the terminal dipole, HC–FC, by synthesizing $CH_3$-capped partially fluorinated alkanethiols in which the positive pole is exposed at the interface, opposite to the $CF_3$-terminated films. The wetting properties of the HC–FC FSAMs proved richer than those of the $CF_3$-terminated SAMs. The authors noted similar trends with the nonpolar contacting liquids between the two types of fluorinated surfaces, while those with the polar

liquids, protic and aprotic, were highly dependent on the nature of the dipole at the interface of the SAM as well as that of the contacting liquid.

Changing the substrate to which the molecules bind has also been shown to change the physical properties of the resulting film because the molecules adopt binding geometries to adopt the most favorable interaction with the surface, causing differences in the final structure of the film.[6,16-25] Studies of SAMs on Ag and Au agree that the hydrocarbon chains require less tilting on silver (10°–12° from the surface normal) than on gold (32°–38°) to bring about maximum favorable interactions with the substrate and neighboring adsorbates.[2,19,26] As with the studies performed on self-assembled monolayers generated from thiols on gold surfaces, "odd-even" effects in the wetting of SAMs on silver have been observed.[2,17,27] This kind of information aids in the design of surfaces with tailored wettability to their application.

Due to the difficulties arising from the use of readily-oxidizable metals such as silver and copper, several studies have employed the electrochemical underpotential deposition (UPD) of a monolayer of metal, such as silver, onto a more noble metal, such as gold, to generate substrates to study SAMs on different metal surfaces.[25,28-32] The deposition of one metal onto another at a potential less negative than the thermodynamic potential for bulk deposition can allow for precise control of the surface coverage, allowing for only a monolayer to be deposited.[33] In the case of UPD Ag on Au, Jennings and Laibinis noted that the monolayer of Ag did not appear to oxidize, due to the lack of oxygen peaks in their XPS spectra, and noted the superiority of the SAMs formed on UPD metal substrates over using the corresponding more oxidizable bulk metals.[30] These advantages make the use of UPD metals on Au attractive substrates for SAM studies.

The study herein makes use of electrochemical underpotential deposition to deposit a monolayer of silver onto a gold substrate and use the substrates to generate self-assembled monolayers with different surface structures. To probe buried interfaces such as the solid-liquid interface between a contacting liquid and a SAM, an interface-specific technique, such as sum frequency generation (SFG) spectroscopy, is necessary. Sum frequency generation spectroscopy, scanned in the vibrational stretching regions of the functional groups in this study, was used to determine the orientation of the terminal functional groups of the SAMs on Au and UPD Ag at the solid-air and solid-liquid interfaces. The goal of this project was to determine the effect of changing the substrate on the structure and physical properties of the self-assembled monolayer films generated from hydrocarbon alkanethiols -- $H(CH_2)_nSH$ (**HnSH**), where n = 17–20 (**H17SH**, **H18SH**, **H19SH**, and **H20SH**) -- their $CF_3$-terminated analogues -- $CF_3(CH_2)_nSH$ (**F1HnSH**), where n = 16–19 (**F1H16SH**, **F1H17SH**, **F1H18SH**, and **F1H19SH**) -- and their $CH_3$-terminated partially fluorinated alkanethiols analogues -- $CH_3(CF_2)_6(CH_2)_nSH$ (**H1F6HnSH**), where n = 10–13 (**H1F6H10SH**, **H1F6H11SH**, **H1F6H12SH**, and **H1F6H13SH**) -- on Au and UPD Ag, as shown in Figure 5.1.

This study means to determine the effect of the contacting liquid on the structure of the SAM with different substrates and whether or not the wettability trends observed in previous research could be reversed by changing the structure of the SAM through its headgroup binding interactions. The effect of the change in structure of the SAM, specifically in the orientation of the tail group furthest from the substrate, was probed *in situ* with two contacting liquids for the purpose of determining the realtionship between the macroscopic contact angles and the microscopic tail group orientation. The polar

aprotic liquid acetonitrile ($CD_3CN$) and the nonpolar fluorinated liquid perfluorodecalin (PFD) were chosen as the contacting liquids for the solid-liquid interface experiments conducted in this study due to their dramatic advancing contact angle results for the SAMs on Au.[14,34] Moreover, the lack of absorption of IR radiation in the C–H stretching range by the chosen liquids allow for a straightforward analysis of the vibrational modes of the SAMs in this region of the infrared spectrum.

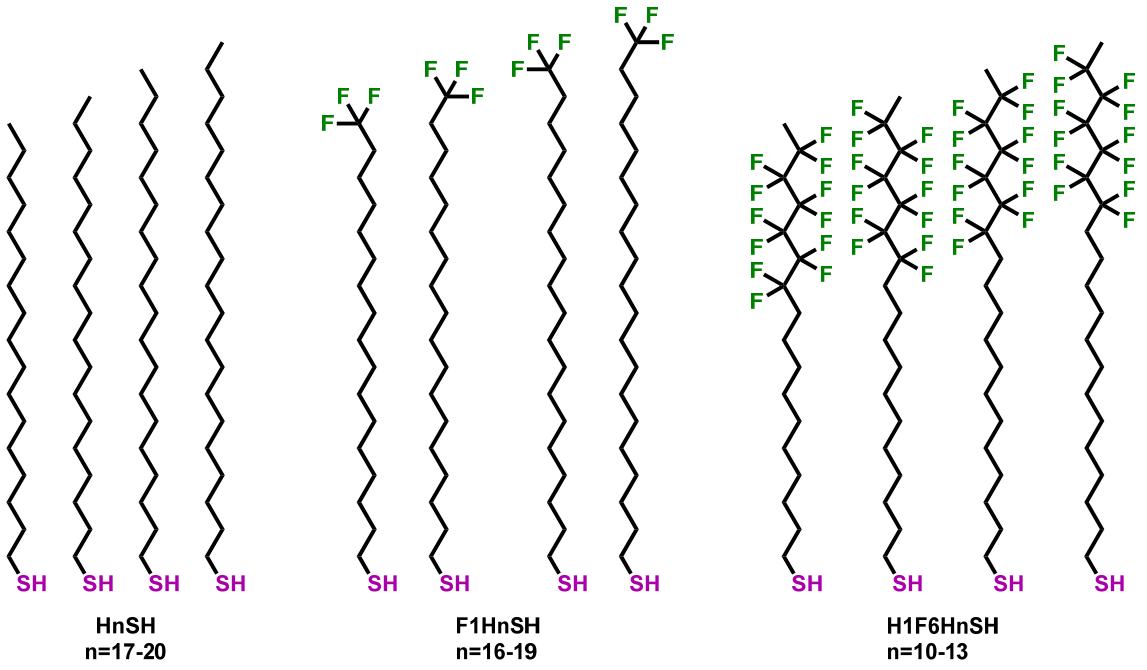


**Figure 5.1.** The alkanethiols used to generate self-assembled monolayers on gold and UPD silver in this study.

## 5.2. Experimental Procedures

### 5.2.1. Materials and Methods

Gold shot (99.999%) was purchased from Kamis, Inc. Chromium rods (99.9%) were purchased from R. D. Mathis Company. Single-side polished, single-crystal silicon (100) wafers were purchased from University Wafer. Absolute ethanol (200 proof,

from Decon Labs, Inc.) and tetrahydrofuran (THF, from J.T. Baker) were used as received for the 1 mM alkanethiol solutions and rinsing of the generated SAMs. Anhydrous acetonitrile-*d*$_3$ ($CD_3CN$, Sigma-Aldrich) and perfluorodecalin (PFD, Synquest Labs) were used as received without further purification.

Octadecanethiol 99.1% (**H18SH**) was purchased from Sigma-Aldrich and used as received. The remaining hydrocarbon adsorbates, 1-heptadecanethiol (**H17SH**), 1-nonadecanethiol (**H19SH**), and 1-eicosanethiol (**H20SH**) were prepared following a procedure from the literature.[1] The partially fluorinated adsorbates 17,17,17-trifluoroheptadecane-1-thiol (**F1H16SH**), 18,18,18-trifluorooctadecane-1-thiol (**F1H17SH**), 19,19,19-trifluorononadecane-1-thiol (**F1H18SH**), 20,20,20-trifluoroicosane-1-thiol (**F1H19SH**), 11,11,12,12,13,13,14,14,15,15,16,16-dodecafluoroheptadecane-1-thiol (**H1F6H10SH**), 12,12,13,13,14,14,15,15,16,16,17,17-dodecafluorooctadecane-1-thiol (**H1F6H11SH**), 13,13,14,14,15,15,16,16,17,17,18,18-dodecafluorononadecane-1-thiol (**H1F6H12SH**), 14,14,15,15,16,16,17,17,18,18,19,19-dodecafluoroicosane-1-thiol (**H1F6H13SH**) were synthesized according to procedures found in the literature.[14]

### 5.2.2. Monolayer Formation and Characterization

#### 5.2.2.1. Substrate Preparation

The substrates used for the self-assembled monolayer (SAM) formation were prepared by the thermal evaporation of 100 Å of chromium followed by 1000 Å of gold (99.999% purity from Kamis, Inc.) onto silicon (100) wafers purchased from University Wafer. The metals were evaporated under vacuum at a pressure of ~$2 \times 10^{-6}$ torr with a

deposition rate of 0.5 Å/s. The gold wafers were then cut into slides and stored in ultrapure Millipore water (with a resistivity of 18.2 Ω) until use for electrochemical measurements.

#### 5.2.2.2. Underpotential Deposition of Silver onto Gold

For cyclic voltammetry (CV), a Princeton Applied Research potentiostat/galvanostat model 263A was used to modulate the potential applied to, and to measure the current of the electrochemical system using PowerSuite software. A homemade glass flow cell, illustrated schematically in Figure 5.2, held three-electrodes used for electrochemical measurements using the gold slides as the working electrode (WE), a platinum wire as the counter electrode (CE), and mercury/mercurous sulfate in saturated $K_2SO_4$ as the reference electrode (RE). The reference electrode is +0.64 V relative the normal hydrogen electrode (NHE). The electrolyte for all the electrochemical measurements was 0.1 M sulfuric acid (Ultrex II Ultrapure Reagent from J. T. Baker) with 0.6 mM $Ag_2SO_4$ (99.999% trace metals basis from Aldrich) added for the underpotential deposition of silver onto the gold electrodes.

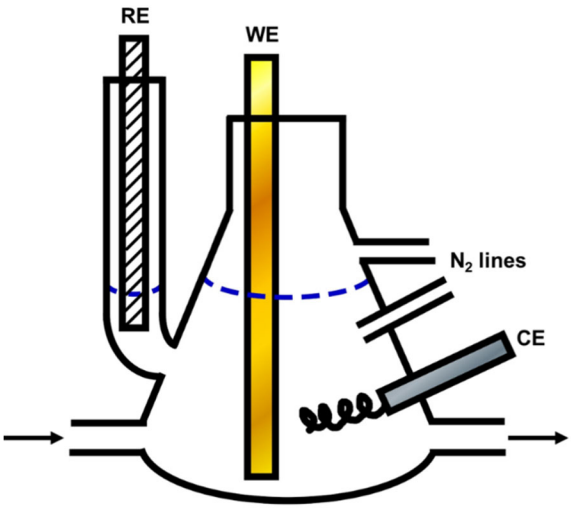


**Figure 5.2.** A schematic drawing of the glass electrochemistry cell used in this study. The RE, WE, and CE correspond to reference, working and counter electrodes, respectively. The blue dashed line represents the level of electrolyte in the cell, and the arrows point in the directions of the electrolyte flow through the cell. Two nitrogen lines are shown -- the bottom line purges the solution and is shut off during the voltammetry, and the top line keeps a continuous atmosphere of nitrogen above the electrolyte during the experiment. The top of the cell was loosely covered with Teflon tape to allow gas to pass through.

Gold slides were cycled ten times at a scan rate of 15 mV/s in deaerated sulfuric acid, rinsed with plenty of Millipore water, and stored in Millipore water until their use as the substrates for the self-assembled monolayers. For the deposition of silver, the cycled gold slides were cycled in deaerated silver solution ten times at a scan rate of 15 mV/s, then held at a potential of 0.15 V vs MSE for the underpotential deposition (UPD) of a monolayer of silver,[35] pulled out of the cell while held at potential, rinsed with copious Millipore water, and stored in Millipore water until analysis with ellipsometry. A representative cyclic voltammogram for gold is shown in Figure 5.3A with arrows pointing in the direction of the scan. Figure 5.3B shows a representative CV for Ag where the regions 1 (0.25–0.55 V vs MSE) and 2 (0.15–0.25 V vs MSE) correspond to the deposition

of the first full monolayer of Ag onto the Au slide and region 3 (~0.1 V vs MSE) begins the bulk deposition of metal.[35] Stripping voltammetry was performed by starting with a potential slightly negative of the UPD peak at 0.15 V vs MSE and oxidizing the electrode along the range shown in Figure 5.3B until the CVs stopped changing (about 30 scans).

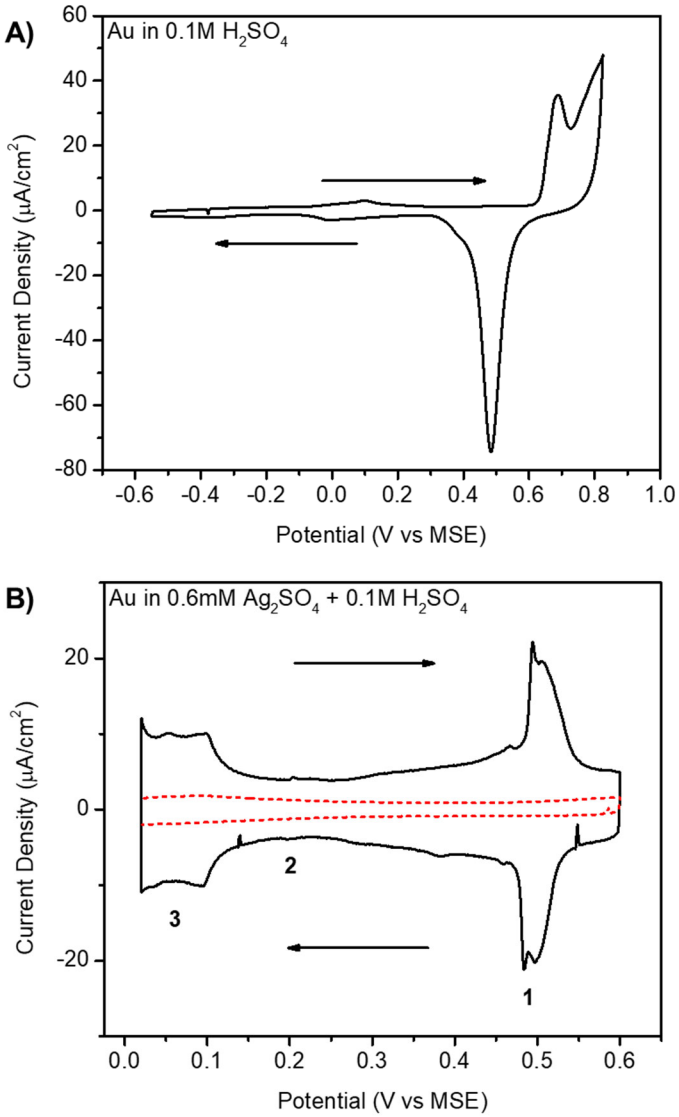


**Figure 5.3.** Representative cyclic voltammograms at a scan rate of 15 mV/s for A) bare gold and B) silver on gold in a sulfuric acid electrolyte. The arrows denote the direction of the scan. The red dashed line in B represents the Au CV in pure $H_2SO_4$ in the potential region shown. Regions 1–3 in the bottom figure denote the different layers of Ag deposited onto the gold, as described further in the text.[35]

#### 5.2.2.3. Monolayer Formation

The Au and UPD Ag slides were immersed in 1 mM solutions of the alkanethiols in absolute ethanol and left to equilibrate for 48 hours in the dark. The slides were then rinsed with THF and ethanol and dried with ultrapure nitrogen gas prior to use. The self-assembled monolayers were characterized using ellipsometry, X-ray photoelectron spectroscopy (XPS), and polarization-modulation infrared reflection-absorption spectroscopy (PM-IRRAS) before the SFG spectroscopic measurements.[34]

#### 5.2.2.4. Characterization Techniques

A PHI 5700 X-Ray photoelectron spectrometer using a monochromatic Kα X-ray source (hν = 1486.7 eV) set to 90° with respect to the axis of the hemispherical energy analyzer was used to collect the X-Ray photoelectron (XPS) spectra for the bare Au, bare UPD Ag, and self-assembled monolayers. The photoelectron takeoff angle was set to 45° from the surface with a 23.5 eV pass energy. A survey spectrum was gathered before running high resolution spectra with a resolution of 0.1 eV. The high resolution spectra were aligned using the Au $4f_{7/2}$ peak at a binding energy of 84.0 eV as a reference. The fractional coverage of UPD Ag, $\phi_{UPD}$, on the Au was calculated as detailed by Jennings and Laibinis[30] using Equation 5.1:

$$\phi_{UPD} = \left\{\left(\frac{I_{Au}}{I_{UPD}}\right)\left(\frac{I^{\circ}_{UPD}}{I^{\circ}_{Au}}\right) C_{SAM}\left[1 - exp\left(\frac{-a_{UPD}}{\lambda_{UPD(KE_{UPD})} * \cos\Theta}\right)\right] + \left[1 - exp\left(\frac{-a_{UPD}}{\lambda_{UPD(KE_{Au})} * \cos\Theta}\right)\right]\right\}^{-1} \quad (5.1)$$

where $I_{Au}$ and $I_{UPD}$ are the measured attenuated intensities of the Au and Ag peaks, respectively, and $\frac{I^{\circ}_{UPD}}{I^{\circ}_{Au}}$ = 0.97 and is the ratio of the sensitivity factors for the UPD Ag and Au. The $a_{UPD}$ is the diameter of an adatom (2.89 Å for silver), $\lambda_{UPD(KE_{Au})}$= 18 Å, and $\lambda_{UPD(KE_{UPD})}$ = 15 Å are the inelastic mean free paths through the UPD Ag layer for electrons of kinetic energy (KE) from the gold and the UPD silver, respectively.[30] The Θ is the angle of the detector to the surface normal, which for this study was 45°. The $C_{SAM}$ corresponds to the attenuation of the Au and Ag electrons due to the SAM and follows the relationship,

$$C_{SAM} = \frac{exp\left(\frac{-d_{SAM}}{\lambda_{SAM(KE_{UPD})} * \cos\Theta}\right)}{exp\left(\frac{-d_{SAM}}{\lambda_{SAM(KE_{Au})} * \cos\Theta}\right)} \tag{5.2}$$

where $\lambda_{SAM(KE_{Au})}$ = 40 Å and $\lambda_{SAM(KE_{UPD})}$ = 34 Å and are the attenuation strengths of photoelectrons of kinetic energy, KE, from the Au or Ag layers through the SAM.[30] The thickness of the SAM, $d_{SAM}$, is taken from the ellipsometry measurements.

Raman spectroscopy of the bulk alkanethiols was performed using a home-built TIR Raman spectrometer, which is detailed elsewhere.[36] The solid bulk alkanethiols were stored in glass vials, and the scattered light was collected with a spectrograph combined with a CCD camera (Andor iDus; Andor Technology) and resolved by high-frequency and low-frequency transmission gratings. The spectra were collected for 5 minutes each from 1000–2300 $cm^{-1}$ and 2750–3100 $cm^{-1}$ to probe the C–F and C–H stretching regions, respectively.

Attenuated total reflection infrared spectroscopy (ATR-IR) of the bulk alkanethiols was measured using a Thermo Scientific Nicolet iS10 FT-IR spectrometer with an ATR accessory using a diamond window. Alkanethiol spectra were collected with a resolution of 2 $cm^{-1}$ from 600–4000 $cm^{-1}$ for 128 scans.

Polarization-modulation infrared reflection absorption spectroscopy (PM-IRRAS) of the SAMs was measured under a constant nitrogen purge using a Nicolet Nexus 670 Fourier transform spectrometer equipped with a Hinds Instruments PEM-90 photoelastic modulator adjusting a ZnSe window to modify the IR polarization. The spectra were collected with a mercury-cadmium-telluride (MCT) detector in reflection geometry at an IR beam incident angle of 80° from the surface normal. Sample spectra were collected with a resolution of 2 $cm^{-1}$ in the C–F stretching region, from 1000–1500 $cm^{-1}$, for 1024 scans and the C–H stretching region, from 2800–3100 $cm^{-1}$, for 512 scans.

Sum frequency generation (SFG) spectroscopy of the SAMs was measured using a home-built spectrometer for which the details can be found elsewhere,[37] and in Chapter 2. Briefly, a pulsed, 20 Hz, 1064 nm beam from an EKSPLA Nd:YAG laser is used to pump a LaserVision optical parametric generation and amplification system (OPG/OPA) to produce a tunable-frequency infrared beam as well as a 532 nm visible beam. The two beams, with corresponding incidence angles of 60° and 50° with respect to the surface normal, were spatially and temporally aligned at the sample surface to produce a new beam with a frequency equal to the sum of the two input frequencies. This sum frequency generation (SFG) beam was filtered for wavelength purity, collected using a PMT, processed using a boxcar integrator, and the resulting averaged data points were plotted using a LabView program. The same Nd:YAG laser was used to pump a separate

OPG/OPA system fitted to generate infrared frequencies between 1000–2000 $cm^{-1}$ and which was used for the low-frequency SFG instrument as detailed in Chapter 2. The samples were scanned in the C–F (1100–1400 $cm^{-1}$) and C–H (2800–3050 $cm^{-1}$) stretching regions using ppp and ssp polarization combinations, where the letters denote the polarization of the SFG, visible, and IR beams, respectively. The final spectra are the average of at least 5 scans and have been normalized to the corresponding bare gold SFG spectrum to account for the gold response over the scanned IR frequencies.

A cell was designed and built for the solid-liquid SFG experiments and is described in Chapter 2. The cell consisted of a Teflon (PTFE) body into which the gold slide containing the SAM was placed. A cleaned glass pipette was used to place a few drops of contacting liquid onto the gold slide and a cleaned $BaF_2$ window was placed on top. A small Kalrez o-ring under the gold slide helped to press the sample against the window so as to minimize the amount of liquid between the slide and the window. A metal flange covered with Teflon tape was fastened over the window by tightening nuts at the bottom of the cell to press all the components together, as shown in Figure 2.15 in Chapter 2. The spectra were monitored for IR absorption with the reference channel of the SFG spectrometer, and, as expected, were found to have no absorption by the bulk liquid above the monolayer.

The theory of sum frequency generation spectroscopy has been thoroughly described by several groups,[38-40] and is detailed in Chapter 2. Briefly, SFG is a coherent second-order nonlinear process that under the electric-dipole approximation is only allowed from media that are non-centrosymmetric. Therefore, molecules in an isotropic bulk environment will not produce SFG signal, but interfacial molecules will because they

are at the boundaries where the centrosymmetry of the system is broken. The intensity of the SFG signal, $I_{SFG}$, is related to the intensities of the incident beams $I(\omega_{vis})$ and $I(\omega_{IR})$ at the frequencies $\omega_{vis}$ and $\omega_{IR}$ of the visible and infrared beams, respectively, as well as the effective second order nonlinear susceptibility, $\chi^{(2)}_{eff}$, via the following relationship,[38]

$$I_{SFG} \propto \left|\chi^{(2)}_{eff}\right|^2 I(\omega_{vis}) I(\omega_{IR}) \tag{5.3}$$

The susceptibility is the sample system's response to the optical fields probing it and is described by the sum of $\chi^{(2)}_{NR}$, the vibrationally non-resonant component coming from the interaction of the metal surface with the intense light fields, and the vibrationally resonant component, $\chi^{(2)}_{R}$, which contains molecular ensemble information and is maximized when the frequency of the IR beam is the same as the frequency of a normal mode. As described in Chapter 2, the resulting relationship between the intensity of the SFG beam and the susceptibility can be reduced to,

$$I_{SFG} \propto \left| \mathrm{A}_{NR} e^{i\epsilon} + \sum_q \frac{\mathrm{A}_q}{\omega_q - \omega_{\mathrm{IR}} - i\Gamma_q} \right|^2 \tag{5.4}$$

where $\mathrm{A}_q$, $\omega_q$, and $\Gamma_q$ are the amplitude, frequency, and line-width of the q$^{\text{th}}$ vibrational mode. Equation 5.4 was used to fit the SFG spectra, and the intensities of the resonances were calculated. The intensity ratio between to resonances in the same spectrum (i.e. for the C–H spectra of the SAMs) was compared to the simulated curves that relate intensity to functional group tilt angle, as described in detail in Chapter 2.

## 5.3. Results and Discussion

### 5.3.1. Substrate Characterization

Stripping voltammetry was used to determine the coverage, in monolayers, of silver deposited onto the polycrystalline gold slides.[30] The deposited layer(s) of Ag were removed from the Au by oxidizing the sample with cyclic voltammetry and calculating the amount of Ag using the calculations described below. Two different methods of UPD Ag substrate preparation were stripped in order to determine whether or not there was a change in the coverage of Ag when the slide was removed from the deposition solution while it was held at the UPD potential. The first method was performed as described in the experimental section, in which the Ag was deposited onto the bare Au, and the slide was taken out of solution while still under potential control. The UPD Ag slide was then placed back into the cell filled with purged, pure electrolyte, and the stripping scan commenced. The second method used the cell depicted in Figure 5.2 to flow fresh electrolyte solution into the cell while the slide was held at the UPD potential so that the slide never left the solution; the slide was held at the potential for two minutes in the Ag solution before the $N_2$ purged, pure electrolyte solution was introduced. Once the electrolyte had been replenished, over five times, the Ag stripping voltammetry scan begun. Representative cyclic voltammograms for the bare Au, Au in Ag solution, and UPD Ag stripping are shown in Figure 5.4A. Figure 5.4B showed that as the number of cycles increased, the current density of the Ag stripping peak decreased, due to removal of the silver from the gold substrate and its diffusion into the bulk solution.

The initial positive sweep of the Ag stripping voltammogram was analyzed to determine the UPD Ag coverage on the Au slides. The stripping voltammograms were

first normalized to the corresponding bare Au doublelayer current shown in Figure 5.4. The Ag stripping peak was then integrated and the area was divided by the scan rate and the geometric surface area of the slide to determine the Ag charge density. The charge density was then divided by the literature value of 222 μC/cm$^2$ for the charge density of a full monolayer of Ag on Au (111), which corresponds to $\phi_{UPD}$ = 0.8.[33,41] This value was chosen because it corresponds to an epitaxial layer of Ag on Au and because the evaporated gold used in this study is considered to be mostly (111) in character.[30]

The results from the stripping voltammetry are listed in Table 5.1. This analysis served two purposes. The first was as an indirect probe of oxide formation; the stripping voltammetry does not remove metal oxides, therefore if the silver coverage calculated from the flow cell experiment is higher than the coverage on the slide pulled out of solution, the formation of a layer of oxide on the UPD Ag after removal of the slide from the solution is likely. The second purpose was to determine coverage of the Au surface in order to conclude if the sulfur of the adsorbates could be binding to the Au as well as the Ag atoms. The results showed that the coverage of silver on the slides removed from solutions was higher than that for the slide that remained in the flow cell throughout the duration of the experiment. Such a low coverage ($\phi_{UPD}$ = 0.14 ± 0.01) on the slides in solution was possibly due to the experimental conditions used during the flow of fresh electrolyte. Although the slides prepared by the second method were treated in the same manner as those from the first method, replacement of the silver solution with pure sulfuric acid required stirring to completely remove the silver solution as the pure electrolyte was added, due to the design of the cell. The discrepancy in surface coverage by silver could then be attributed to fluctuations in the liquid level of the cell causing unavoidable variances in the

surface area covered by electrolyte, thereby preventing the silver from adhering on the gold electrode.

In terms of the samples taken out of solution, the UPD Ag coverage was 0.51 ± 0.03 which, within experimental error, agrees well with the literature.[30] However, the coverage determined from the voltammetry falls short of the $\phi_{UPD}$ = 0.8 for a full monolayer of silver on gold. Part of this discrepancy could be due to the calculation for the surface area of the gold slide; since the surface roughness before and after the voltammetry was unknown, no correction factor could be applied to account for it, yielding a smaller value for the coverage. Laibinis et. al. noted that coverages determined by coulometric measurements can underestimate surface coverage,[30] requiring a more surface-sensitive approach to be able to fulfill the second purpose of this experiment.

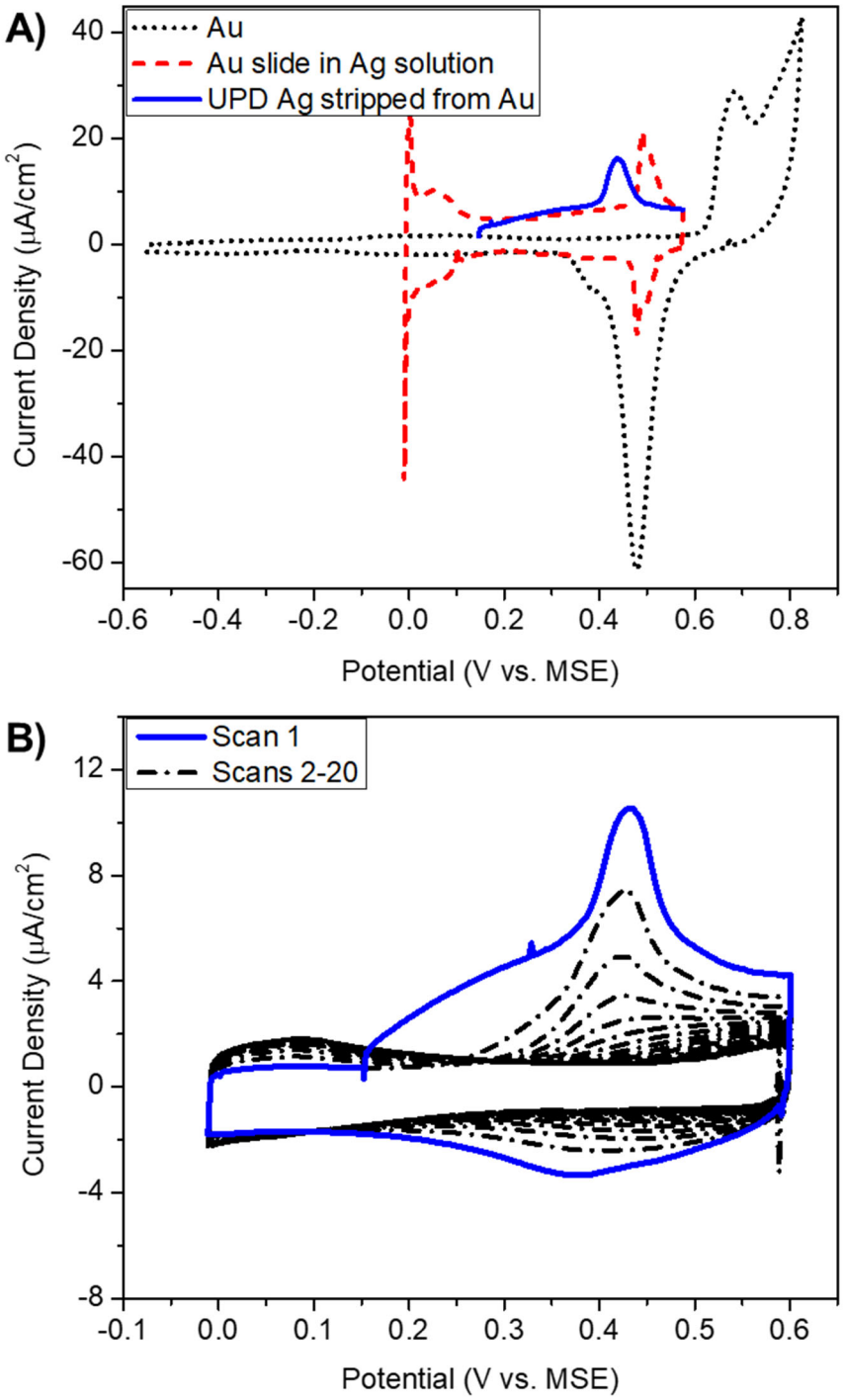


**Figure 5.4.** A) Overlapped voltammograms: Au in $H_2SO_4$ (black dot), Au in Ag solution (red dash), and the first scan of Ag stripped from Au (blue solid line). B) Stripping voltammetry of the UPD Ag monolayer from the Au surface. The blue solid line is the first scan while the black dash-dot lines are scans 2–20, showing a decrease in the current density of the Ag stripping (oxidation) peak as the number of scans increases.

Elemental analysis with XPS was used to determine the coverage of UPD Ag on Au using the method outlined by Laibinis.[30] The high resolution Au 4f and Ag 3d XPS spectra for the bare UPD Ag and HSAM-covered UPD Ag substrates are given in Figure 5.5. Since XPS quantifies both the Ag metal and its oxide, higher coverage values can be expected from the XPS analysis than the voltammetry. A comparison of the values in Table 5.1 show that the coverage of UPD Ag on Au calculated from the XPS data is almost double of that derived from the stripping voltammetry, and is at a full monolayer within experimental precision. Although these results indicate that the Au surface is fully terminated with silver atoms, studies have shown that the silver does not form a commensurate layer over the Au, but rather fills bridge sites as well as top-sites, creating an incommensurate surface.[42] If the Ag atoms are not close-packed to fully cover the Au surface, the sulfur headgroup of the alkanethiol could be bound to both Ag and Au atoms at the UPD Ag/Au substrate.

A study to determine the binding characteristics of propanethiolates on UPD Ag-modified Au found a preference for binding to Ag.[43] Sellers et. al. noted that there are two chemisorption modes (giving surface-S-C angles of 109° and 180°) of similar stability for the SAMs on Au (111) and it is possible for both modes to exist in small clusters that make the surface homogeneous on a macroscopic level.[2] Considering that this study uses polycrystalline substrates, the probability of such a phenomenon is high. Since "odd-even" effects in the wettability and the orientation of the terminal functional groups are evident (vide infra), the relative homogeneity of the samples observed on the macroscopic scale could be due to the preference of one chemisorption mode over another.[2] Within the resolution of the surface characterization techniques used in this study, the SAMs were

considered homogeneous, and the true nature of the bonding of the thiols to the metals remains undefined. However, since the literature agrees that alkanethiols bind to UPD Ag, the forthcoming discussion will follow that conclusion.

**Table 5.1.** Coverage Calculations from Stripping Voltammetry and XPS Measurements[a,b]

| Surface | $\phi_{UPD}$ from Stripping Voltammetry | | $\phi_{UPD}$ from XPS |
|---|---|---|---|
| | Sample in Flow Cell | Sample Removed from Solution | |
| **Au** | 0.14 ± 0.01 | 0.51 ± 0.03 | 0.79 ± 0.04 |
| **H17SH** | - | - | 0.65 ± 0.03 |
| **H18SH** | - | - | 0.67 ± 0.01 |
| **H19SH** | - | - | 0.69 ± 0.07 |
| **H20SH** | - | - | 0.63 ± 0.03 |
| **F1H16SH** | - | | 0.63 ± 0.02 |
| **F1H17SH** | - | - | 0.63 ± 0.01 |
| **F1H18SH** | - | - | 0.61 ± 0.03 |
| **F1H19SH** | - | - | 0.63 ± 0.01 |
| **H1F6H10SH** | - | - | 0.66 ± 0.01 |
| **H1F6H11SH** | - | - | 0.64 ± 0.05 |
| **H1F6H12SH** | - | - | 0.63 ± 0.04 |
| **H1F6H13SH** | - | - | 0.63 ± 0.05 |

[a]Coverage calculations using the XPS data were performed using the bare metal substrates as well as SAM-covered substrates to determine if there was a change in the Ag coverage with the addition of the monolayer.
[b]The standard deviations were determined from three separate sets of experiments.

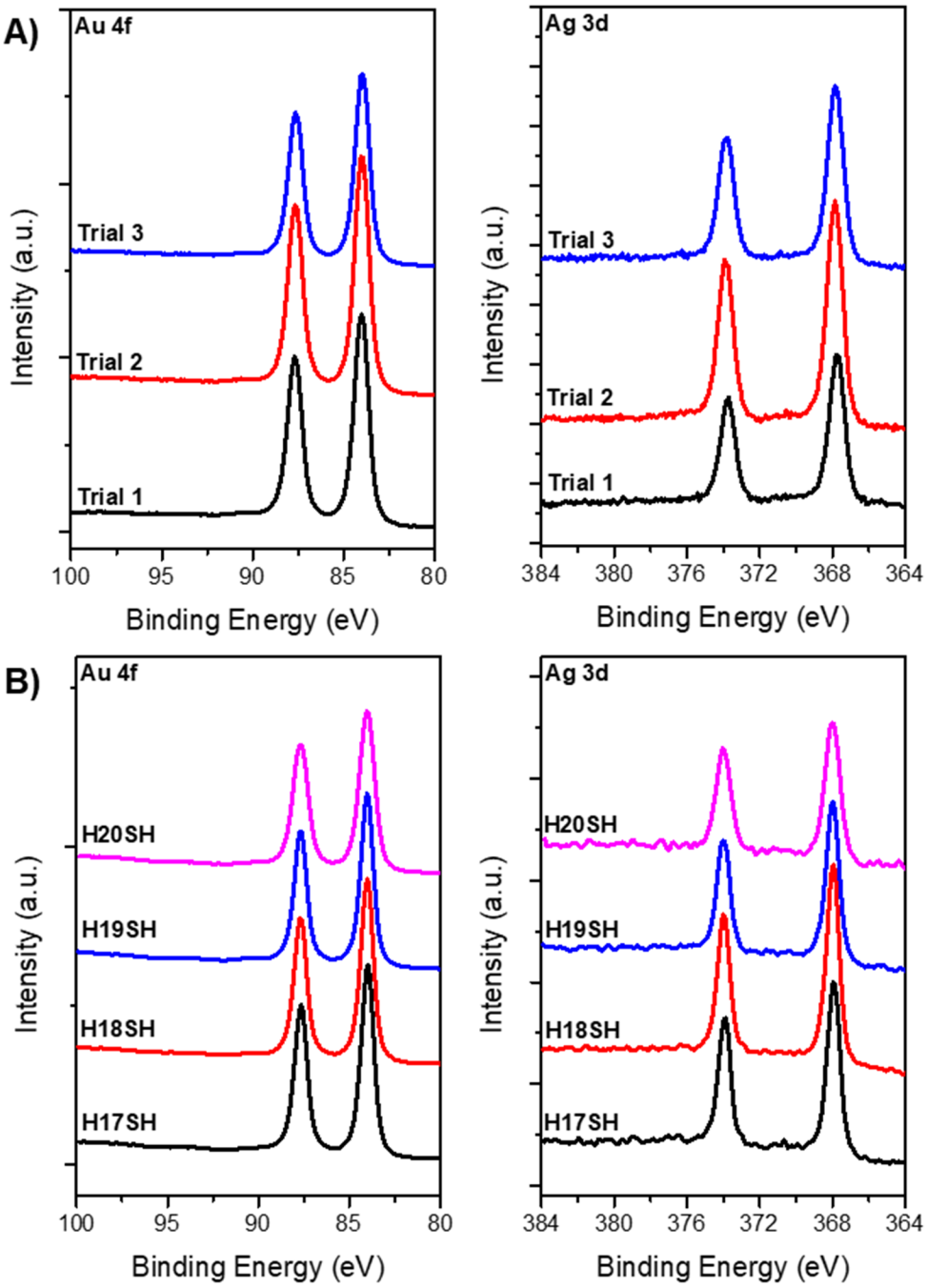


**Figure 5.5.** A) Representative high-resolution XPS spectra in the Au 4f and Ag 3d regions for bare samples of UPD Ag on Au. B) The Au 4f and Ag 3d spectra for the alkanethiol SAMs on UPD Ag substrates, as shown in a previous report.[34]

The XPS spectra in Figure 5.5 confirm the presence of the Au and Ag expected in each film and show the binding energies of the Ag $3d_{5/2}$ peaks at 368.0 eV for all the substrates studied, including the bare UPD Ag, which agrees with literature values.[30] The surface coverages determined from the XPS data for the bare UPD Ag substrates were higher by ~0.15 monolayers than the SAM covered surfaces, which seems to indicate a loss of Ag atoms with the adsorption of the monolayer. This is in contrast to the observations of Jennings and Laibinis who saw no change in the coverage of the Ag with the formation of a SAM.[30] However, it is possible that the lower Ag coverages of the SAMs were due to the electron screening model used to derive Equation 5.2 not being suitable for these experiments, or due to inhomogeneities in coverage[44] from surface reconstruction upon the adsorption of the SAMs onto the sample substrates[45] rather than the removal of bound Ag from the Au. To analyze this further, samples were made by the electrochemical deposition of Ag in the "bulk" region of the voltammogram (denoted by a number 3 in Figure 5.3). Using laser confocal microscopy combined with differential interference contrast microscopy, Azhagurajan et. al. found that this potential region deposited the second and third monolayers of Ag onto Au (111).[35] The samples were found to have surface coverages of $\phi_{UPD}$ = 0.79 ± 0.08 for an **H18SH** SAM on UPD Ag and $\phi_{UPD}$ = 0.83 ± 0.04 for the bare UPD Ag surfaces. By stripping voltammetry, the "bulk" Ag surfaces were calculated to have a surface coverage of $\phi_{UPD}$ = 0.47 ± 0.04 of a monolayer. Since the XPS and CV-determined coverages are the same for the monolayer and "bulk" regions of the Ag deposition, it is possible that due to the polycrystalline nature of the Au slides the surface Ag atoms merely became more close-packed and homogeneously distributed.

### 5.3.2. Vibrational Mode Assignments

Prior to analyzing the structure of the self-assembled monolayers, generated from the alkanethiols shown in Figure 5.1, from the point of view of surface-sensitive vibrational spectroscopies, PM-IRRAS and SFG, the complex vibrational modes of the fluorinated adsorbates must be assigned. The Raman and ATR-IR spectra for the bulk alkanethiols are presented in Figures 5.6 and 5.7 for the C–H stretching region and Figures 5.8 and 5.9 for the C–F stretching region, and were used to assign the peaks for the vibrational modes observed in this study. The resonance frequencies observed for the fully hydrocarbon alkanethiols (**HnSH**) are listed in Table 5.2, while Table 5.3 lists the frequencies for the $CF_3$-terminated alkanethiols (**F1HnSH**).

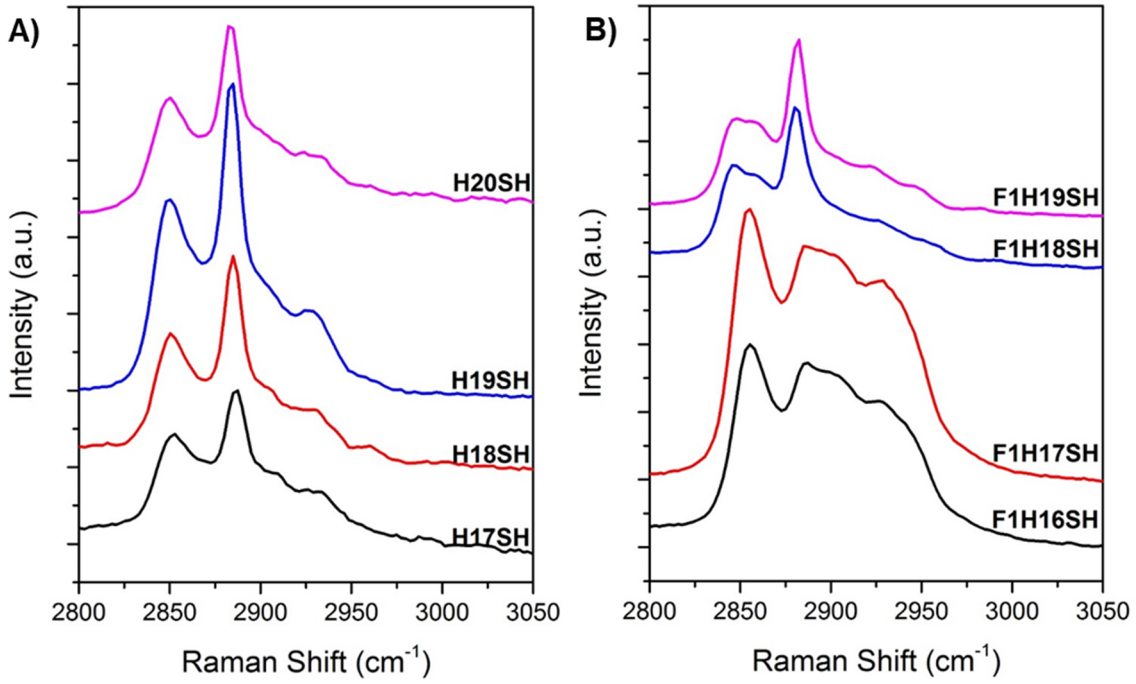


**Figure 5.6.** Raman spectra of the bulk A) **HnSH** alkanethiols and B) **F1HnSH** alkanethiols in the C–H stretching region, 2800–3050 $cm^{-1}$.

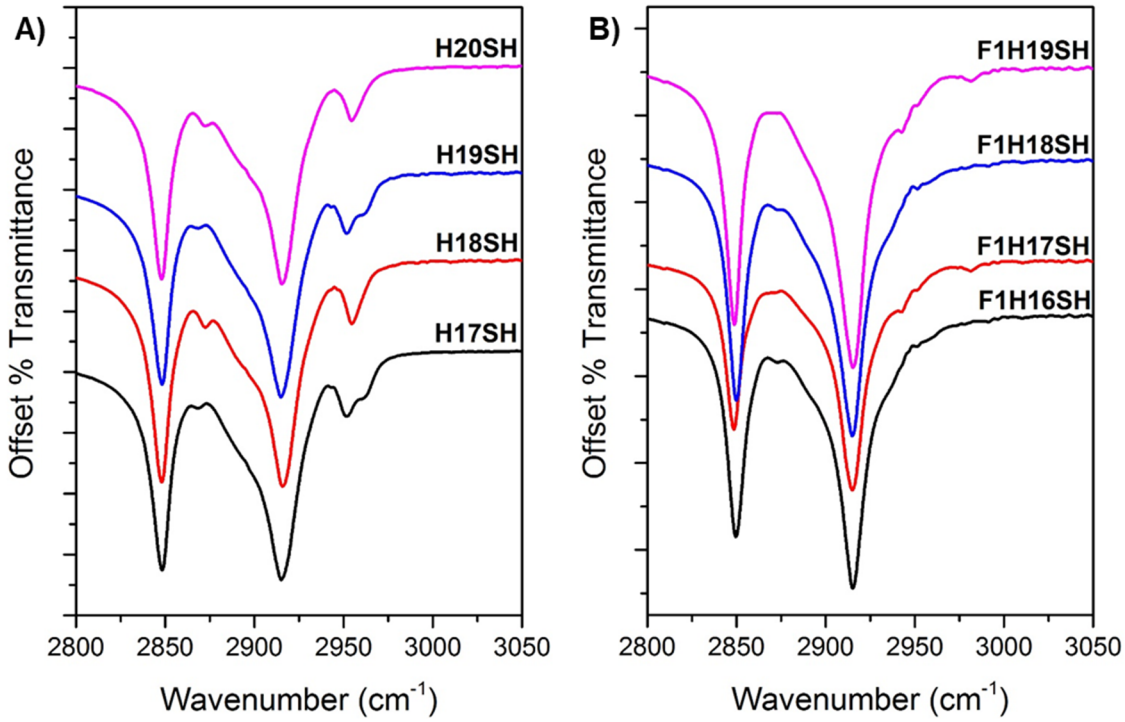


**Figure 5.7.** ATR-IR spectra of the bulk A) **HnSH** alkanethiols and B) **F1HnSH** alkanethiols in the C–H stretching region, 2800–3050 $cm^{-1}$.

**Table 5.2.** Observed Vibrational Mode Frequencies and their Assignments for the Fully Hydrocarbon Alkanethiols.

| Resonance Position ($cm^{-1}$) | | Assigned Mode[46-47] |
|---|---|---|
| IR | Raman | |
| 2848 | 2850 | $\nu_{ss}^{CH_2}$, $CH_2$ symmetric stretch |
| 2870 | - | $\nu_{ss}^{CH_3}$, $CH_3$ symmetric stretch |
| 2888 | 2887 | $\nu_{as}^{CH_2}$, $CH_2$ antisymmetric stretch |
| - | 2909 | $\nu_{FR}^{CH_2}$, $CH_2$ Fermi resonance |
| 2916 | 2923 | $\nu_{as}^{CH_2}$, $CH_2$ antisymmetric stretch |
| 2942 | 2934 | $\nu_{FR}^{CH_3}$, $CH_3$ symmetric stretch split by Fermi resonance |
| 2956 | - | $\nu_{as}^{CH_3}$, $CH_3$ antisymmetric stretch out-of-plane |
| 2962 | 2960 | $\nu_{as}^{CH_3}$, $CH_3$ antisymmetric stretch, in-plane |
| 1130 | 1131 | $\nu_{s}^{CC}$, C–C stretch (trans conformation)[46,48] |
| 1282-1300 | 1296 | $\nu_{w}^{CH_2}$, $CH_2$ wag[48] |
| 1375 | 1371 | $\delta_{s}^{CH_3}$, symmetric $CH_3$ bend[48-50] |
| 1435 | 1441 | $\delta_{s}^{CH_2}$, $CH_2$ bend[51] |
| 1461 | 1462 | $\delta_{a}^{CH_3}$, antisymmetric $CH_3$ bend[48-49]<br>$\delta_{s}^{CH_2}$, $CH_2$ bend[48,50] |
| 1472 | - | $\delta_{a}^{CH_3}$, antisymmetric $CH_3$ bend[50,52]<br>$\delta_{s}^{CH_2}$, $CH_2$ bend[48,50-51,53] |

The Raman spectra for the **HnSH** adsorbates in Figure 5.6A are in agreement with literature spectra of hydrogenated alkanethiols in crystal form,[46,51] with the two strongest resonances corresponding to the highest concentration of functional groups, the methylene ($CH_2$) stretching modes. The lowest frequency band in the C–H stretching region, at 2850 $cm^{-1}$, corresponds to the symmetric methylene stretch, $\nu_{ss}^{CH_2}$, and is followed by the band

at 2900 $cm^{-1}$, which is assigned to the symmetric stretch split by Fermi resonance with the overtone of the methylene bending mode, $\nu_{FR}^{CH_2}$.[47] Figure 5.6B shows the Raman spectra of the **F1HnSH** adsorbates. Along with exhibiting the $\nu_{ss}^{CH_2}$ and $\nu_{FR}^{CH_2}$ modes, the antisymmetric stretching vibration, $\nu_{as}^{CH_2}$, at 2920 $cm^{-1}$ for the longer-chained **F1HnSH** adsorbates, blue-shifts to ~2925 $cm^{-1}$ for **F1H16SH** and **F1H17SH**, likely due to the liquid-like nature of shorter-chain length compounds; note, the **F1H16SH** and **F1H17SH** appeared to melt at room temperature while the spectra were gathered.[51] The broad nature of the bands can also be attributed to the melting of the compound, since less crystalline compounds have a greater contribution to inhomogeneous broadening on the peak shape.

The aforementioned resonances are typical stretching frequencies for $CH_2$ groups in a hydrocarbon environment, however, the $CF_3$-terminus present in this set of adsorbates clearly affects the resonances, blue-shifting the $CH_2$ band frequencies higher than 2925 $cm^{-1}$. Infrared and Raman spectroscopic studies of small fluorinated molecules, such as $CF_3CH_3$,[54] $CF_3CH_2CF_3$,[55] $CF_3CH_2OCH_3$,[56] $CF_3CH_2CH_2Cl$,[57] as well as a $CF_3(CH_2)_3SH$,[58] have shown dramatic blue-shifts in the frequency of the $CH_2$ stretching modes due to their proximity to a fluorocarbon. Therefore, the resonances observed in Figure 5.8B at 2875 $cm^{-1}$ and ~2950 $cm^{-1}$ were assigned to the symmetric and antisymmetric stretching modes of the methylene closest to the $CF_3$ group (denoted as $*CH_2$), respectively.[56-57,59] Moreover, the infrared spectra of the **HnSH** adsorbates shown in Figure 5.7A clearly show the resonances belonging to the $CH_3$ group, while they are absent for the **F1HnSH** adsorbates, see spectra in Figure 5.7B. These resonances include the methyl symmetric stretching, $\nu_{ss}^{CH_3}$, at 2870 $cm^{-1}$, the symmetric stretch split by its Fermi resonance interacting

with the overtone of the methyl bending mode, $\nu_{FR}^{CH_3}$, at 2934 cm$^{-1}$, and the methyl antisymmetric stretch, $\nu_{as}^{CH_3}$, at 2962 cm$^{-1}$.

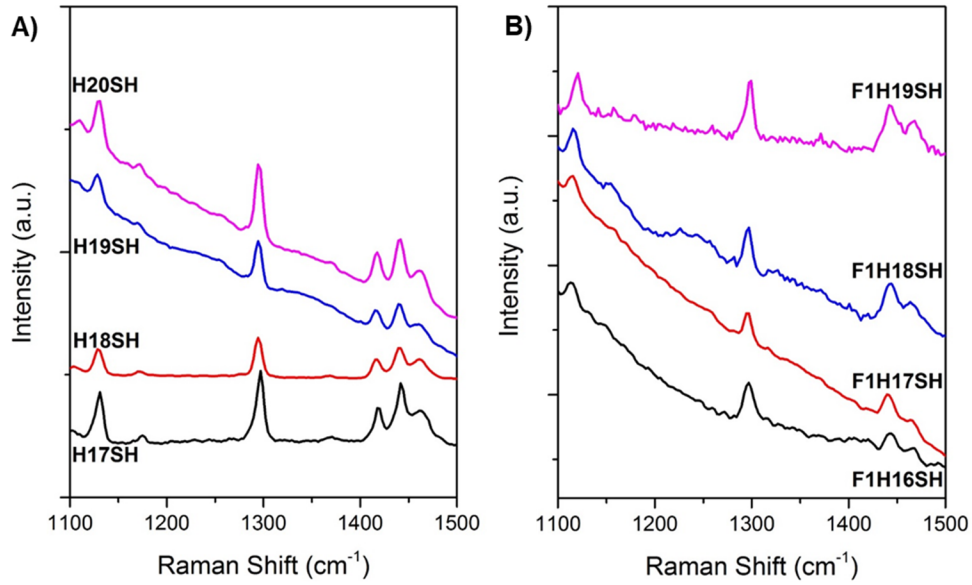


**Figure 5.8.** Raman spectra of the bulk A) **HnSH** alkanethiols and B) **F1HnSH** alkanethiols in the C–F stretching region, 1100–1500 cm$^{-1}$.

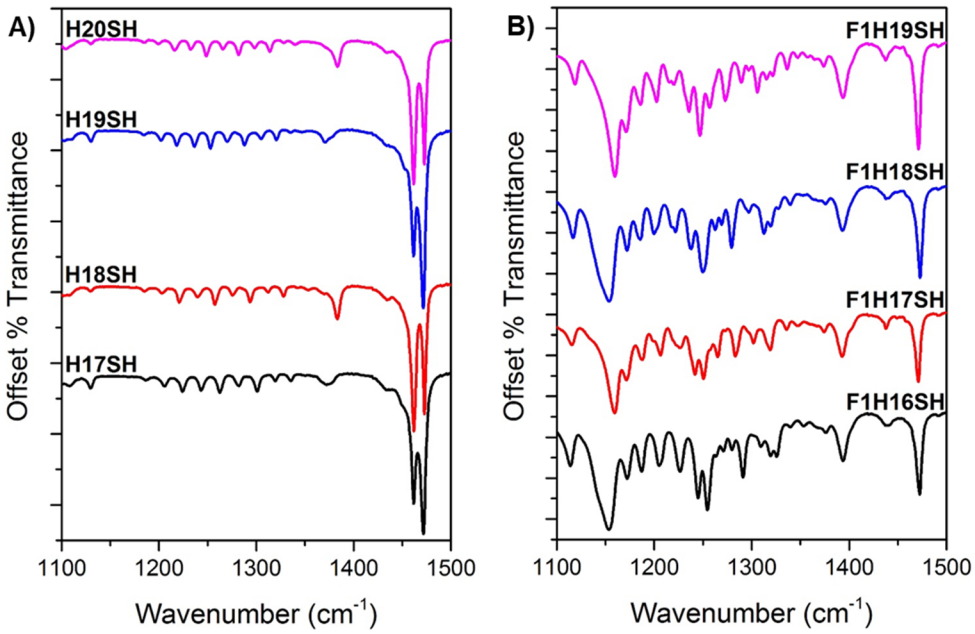


**Figure 5.9.** ATR-IR spectra of the bulk A) **HnSH** alkanethiols and B) **F1HnSH** alkanethiols in the C–F stretching region, 1100–1500 cm.

**Table 5.3.** Observed Vibrational Mode Frequencies and their Assignments for the $CF_3$-terminated Alkanethiols.

| Resonance Position ($cm^{-1}$) | | Assigned Mode |
|---|---|---|
| IR | Raman | |
| 2849 | 2847-2855 | $\nu_{ss}^{CH_2}$, $CH_2$ symmetric stretch§ |
| - | 2859 | $\nu_{ss}^{CH_2}$, $CH_2$ symmetric stretch[46] |
| 2873 | - | $\nu_{ss}^{*CH_2}$, *$CH_2$ symmetric stretch<br>$\nu_{FR}^{*CH_2}$, *$CH_2$ Fermi resonance† |
| 2888 | 2882-2903 | $\nu_{as}^{CH_2}$, $CH_2$ antisymmetric stretch<br>$\nu_{FR}^{CH_2}$, $CH_2$ Fermi resonance§ |
| 2915 | 2923-2928 | $\nu_{as}^{CH_2}$, $CH_2$ antisymmetric stretch§ |
| 2952 | 2948 | $\nu_{as}^{*CH_2}$, *$CH_2$ antisymmetric stretch, trans[56-57,59] |
| 1114-1119 | 1114-1120 | $\nu_{s}^{CC}$, C–C stretch[48] |
| 1153-1159 | 1160 (vw) | $\nu_{ss}^{CF_3}$, $CF_3$ symmetric stretch[57-58,60] |
| 1172 | 1175 (vw) | $\nu_{ss}^{CF_3}$, $CF_3$ symmetric stretch[56,60-61] |
| 1247-1255 | 1260 (vw) | $\nu_{as}^{CF_3}$, $CF_3$ antisymmetric stretch[58-60] |
| 1272-1291 | - | $\nu_{as}^{CF_3}$, $CF_3$ antisymmetric stretch[56,60-61] |
| 1289-1308 | 1298 | $\nu_{as}^{CF_3}$, $CF_3$ stretch with $\nu_{sb}^{CF_3}$ bend[56,59] |
| 1393 | - | $\delta_{s}^{CH_2}$, *$CH_2$ bend<br>$\nu_{s}^{CC}$, C–C stretch [57]<br>$\nu_{w}^{CH_2}$ *$CH_2$ wag[58] |
| 1438 | 1443 | $\delta_{s}^{CH_2}$, *$CH_2$ bend[57-59] |
| 1471 | 1467 | $\delta_{s}^{CH_2}$, $CH_2$ bend[48,53] |

§ Assignments taken from references[46-47]
† Assignments taken from references[56-57]
(vw) denotes bands that have very weak intensities

The low-frequency spectra presented in Figures 5.8 and 5.9 were used to assign the main vibrational modes of the $CF_3$ group. The assignments for the **HnSH** adsorbates in this study were limited to the bands that were observed in both IR and Raman, consisting

of chain stretches, $CH_2$ wagging and bending, the $CH_3$ symmetric (~1370 $cm^{-1}$), and $CH_3$ antisymmetric bending (~1460 $cm^{-1}$) modes (see Table 5.2). The low-frequency modes for the **F1HnSH** adsorbates were assigned based on available studies of similar molecules and observed similarities to the **HnSH** adsorbate spectra. There is disagreement in the literature about the assignment of the symmetric and antisymmetric vibrations of the $CF_3$ group, with some studies showing that the symmetric stretch is higher frequency than the antisymmetric,[54,62] and others showing the opposite.[63]

In a study involving perfluoroalkanes of different chain lengths, Shimoaka concluded that in C–F vibrations, the fluorine remains relatively unmoved, due to the lighter mass of carbon compared to fluorine, resulting in coupling of the vibration to the oscillation of the C–C backbone.[64] Since the $CF_3$ stretching Raman bands are weak, the bands at 1114–1120 $cm^{-1}$ were assigned to C–C stretching[48] vibrations, due to the increasing peak frequency as the number of carbon atoms increases. The bands at 1150 $cm^{-1}$ and 1175 $cm^{-1}$ were not found in the **HnSH** spectra, and therefore were assigned to the $CF_3$ symmetric stretching -- albeit the mode is strongly coupled to C–C stretches.[56] The bands at ~1250 $cm^{-1}$ were assigned as a mixture of $CF_3$ antisymmetric character and $CH_2$ twists and rocks.[58-59] The band at 1271 $cm^{-1}$, observed only in the IR spectra, was assigned to the $CF_3$ antisymmetric stretch, although Li et. al. recorded potential energy distributions that indicate this mode is coupled to the antisymmetric $CF_3$ bend and the C–C stretches.[56] The band ~1300 $cm^{-1}$ was assigned to $CF_3$ stretching in conjunction with $CF_3$ bending,[56,59] while the bands at ~1393 $cm^{-1}$ and ~1440 $cm^{-1}$ were attributed to $*CH_2$ bending[57-59] modes, see Table 5.3 for assignments.

The FT-IR transmission spectra for the **H1F6HnSH** adsorbates was provided in a previous report,[14] however, the authors were not able to assign the stretches associated with the $CH_3$. A deuterated analog, **D1F6H10SH**, was synthesized, according to the procedures outlined in Chapter 3, for the purposes of assigning the $CH_3$ stretching peaks and is discussed below. The C–H, C–D, and C–F stretching regions of the vibrational spectra are plotted in Figures 5.10–5.12. Their peak assignments are listed in Table 5.4. The IR and Raman spectra plotted in Figure 5.10 show a comparison between the **H1F6H10SH** and **D1F6H10SH** adsorbates, as well as a comparison to the $CF_3$-terminated analog, **F1H16SH**, and the normal alkanethiol, **H17SH**. Although the infrared spectra of the **H1F6H10SH** and **D1F6H10SH** adsorbates are similar, the Raman spectra clearly display the stretching frequencies of a $CH_3$ group adjacent to a fluorinated carbon chain (labeled as $*CH_3$) at 2961 and 3024 $cm^{-1}$. Upon deuteration of the terminal methyl group, the bands at 2961 and 3024 $cm^{-1}$ disappear, indicating that they belong to the methyl group and not the methylenes in the chain below the fluorinated moiety. The methyl stretching frequencies of the **H1F6H10SH** adsorbate are shifted to higher values than those of alkanethiols, **H17SH**, due to proximity of the methyl group to the electron-withdrawing fluorocarbons.[52,65] Moreover, the broad bands in the Raman spectrum and the shifted $\nu_{as}^{CH_2}$ resonance frequency at 2920 $cm^{-1}$, compared to 2915 $cm^{-1}$ for the solid alkanethiols, are indicative of the liquid-like nature of the molecules at the time the spectra was collected; we note that the compounds are waxy solids at room temperature.

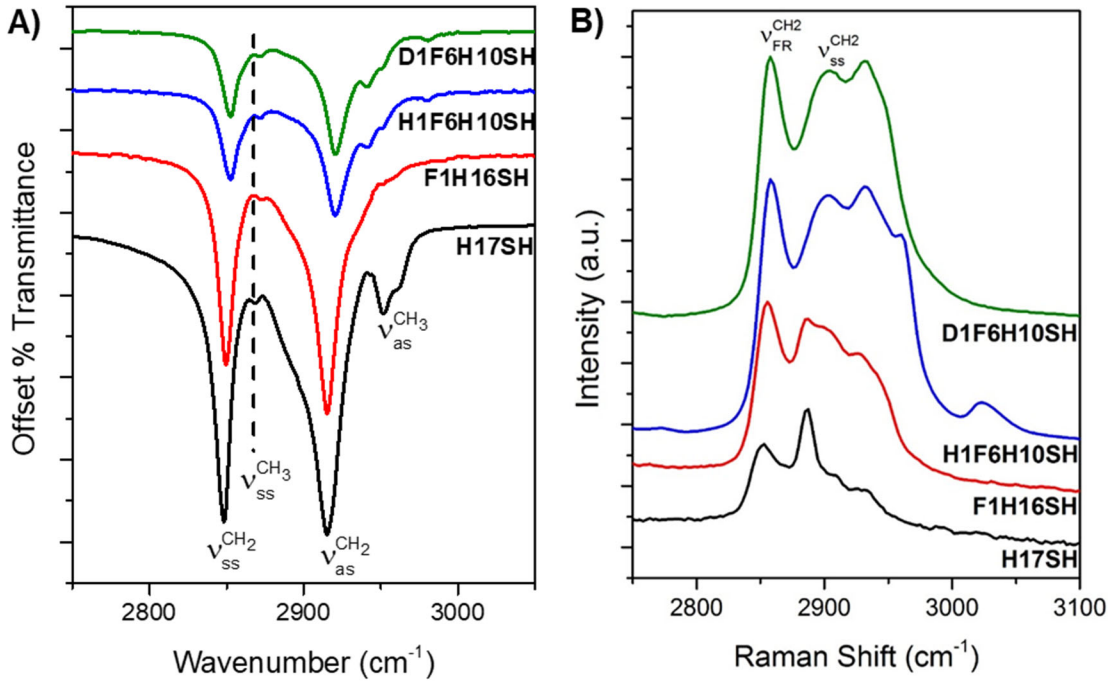


**Figure 5.10.** A) ATR-IR and B) Raman spectra of the bulk alkanethiols **H17SH**, **F1H16SH**, **H1F6H10SH**, and **D1F6H10SH** in the C–H stretching region between 2750–3100 cm$^{-1}$.

The $CD_3$ stretching region between 2000–2300 cm$^{-1}$, shown in Figure 5.11, reveals the methyl stretches of the **D1F6H10SH** molecule, with the symmetric stretching peak appearing at 2140 cm$^{-1}$ and the antisymmetric stretch at 2270 cm$^{-1}$.[66] Note, the stretches of the **D1F6H10SH** adsorbate appear at higher frequencies than the methyl stretching frequencies of deuterated octadecanethiol which appear at 2060 cm$^{-1}$ and 2212 cm$^{-1}$, respectively.[47] The peaks for the $CF_3$-capped molecule in the C–D region are attributed to overtones and combination bands of the C–C skeletal and $CF_3$ stretching modes.[67] The ATR-IR percent transmittance spectra shown in Figure 5.11 in the C–D stretching region fail to show resonances for the **D1F6H10SH** molecule. The absence of the $CD_3$ stretching bands is attributed to a low IR cross-section, considering that the methyl bands in the

**H1F6H10SH** counterpart already have low intensities compared to the methyl group of fully hydrocarbon molecules,[14] (as shown by the spectra in Figure 5.10A) which is possibly due to the methyl group's proximity to the electron-withdrawing fluorocarbons.[65] If the $CH_3$ bands in the partially-fluorinated alkanethiol have such low intensities, then the $CD_3$ bands would be below the detection limit of the IR spectrometer. Finally, the C–F stretching region, shown in Figure 5.12, indicates that the IR and Raman spectra are similar due to the only difference being the deuterated terminal group of the **D1F6H10SH** adsorbate. Use of the **D1F6H10SH** adsorbate aided in assigning bands observed in the low-frequency IR spectra plotted in Figure 5.12A. Specifically, the band at 1395 $cm^{-1}$ in the **H1F6H10SH** spectrum can be unequivocally assigned to the methyl group bending mode, however since the band at 1383 $cm^{-1}$ appears in both spectra, it can be attributed to the either $CF_2$ or $CH_2$; the peak at 1375 $cm^{-1}$ in the **F1H16SH** IR spectra may then also be attributed to the $CF_3$ or $CH_2$ modes, or a combination of modes from the two functional groups.

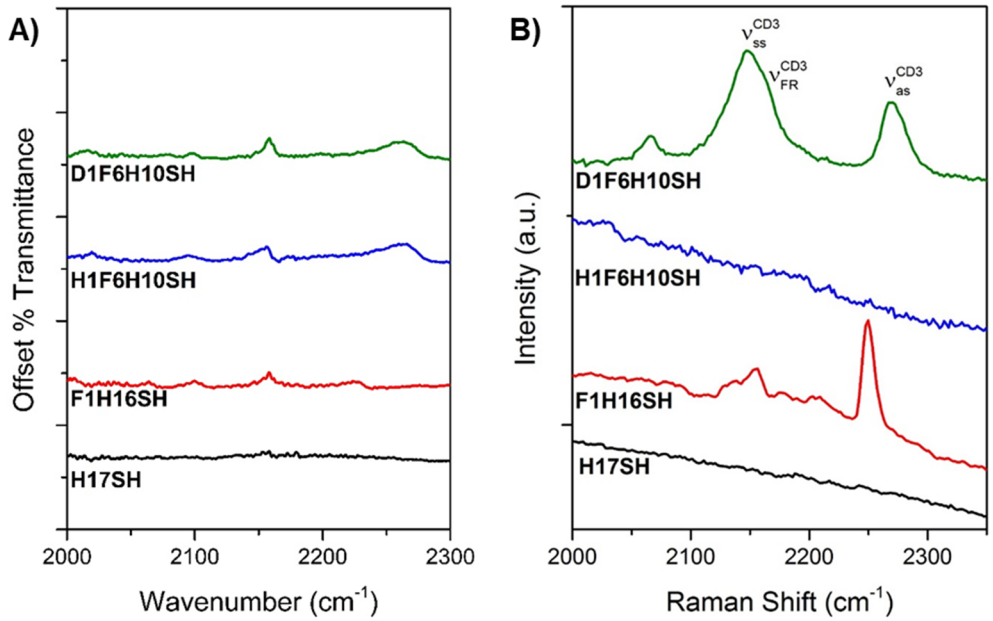


**Figure 5.11.** A) ATR-IR and B) Raman spectra of the bulk alkanethiols **H17SH**, **F1H16SH**, **H1F6H10SH**, and **D1F6H10SH** in the C–D stretching region, 2000–2350 cm$^{-1}$. The percent transmittance IR spectra are offset for clarity and are plotted with the same y-axis scale as the corresponding IR spectra in Figure 5.10.

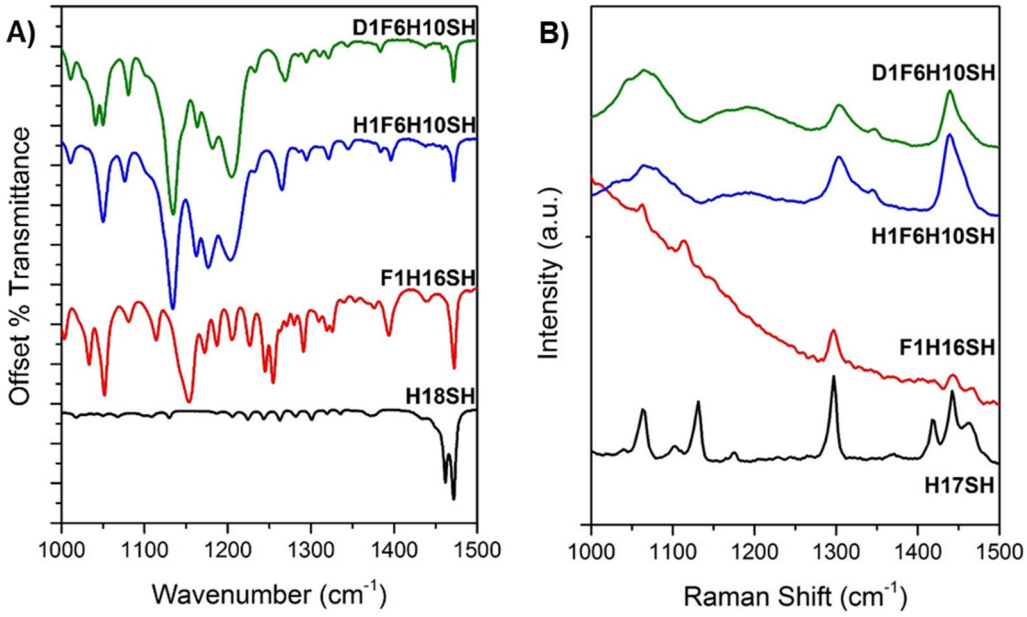


**Figure 5.12.** A) ATR-IR and B) Raman spectra of the bulk alkanethiols **H17SH**, **F1H16SH**, **H1F6H10SH**, and **D1F6H10SH** in the C–F stretching region between 1000–1500 cm$^{-1}$ (left).

**Table 5.4.** Observed Vibrational Mode Frequencies and their Assignments for the $CH_3$-terminated Alkanethiols.

| Resonance Position ($cm^{-1}$) | | Assigned Mode |
|---|---|---|
| IR | Raman | |
| 2852 | 2859 | $\nu_{ss}^{CH_2}$, $CH_2$ symmetric stretch§ |
| 2872 | - | $\nu_{ss}^{CH_2}$, *$CH_2$ symmetric stretch<br>$\nu_{FR}^{CH_2}$, *$CH_2$ Fermi resonance† |
| 2889 | 2903 | $\nu_{as}^{CH_2}$, $CH_2$ antisymmetric stretch<br>$\nu_{FR}^{CH_2}$, $CH_2$ Fermi resonance§ |
| 2920 | 2932 | $\nu_{FR}^{CH_2}$, *$CH_2$ Fermi resonance[52]<br>$\nu_{as}^{CH_2}$, $CH_2$ antisymmetric stretch§ |
| 2952 | 2961 | $\nu_{ss}^{CH_3}$, *$CH_3$ symmetric stretch[52,66,68] |
| - | 3024 | $\nu_{as}^{CH_3}$, *$CH_3$ antisymmetric stretch[52,66,68] |
| 1133 | - | $\nu_{ss}^{CF_2}$, $CF_2$ symmetric stretch[64] |
| 1162 | 1167 | $\nu_{ss}^{CF_2}$, $CF_2$ stretch[68] |
| 1203 | 1198 | $\nu_{s}^{CC}$, $CH_3$–$CF_2$ C–C stretch[52]<br>$\nu_{as}^{CF_2}$, $CF_2$ antisymmetric stretch<br>$\nu_{r}^{CH_3}$ $CH_3$ rock[66] |
| 1232 | - | $\nu_{ss}^{CF_2}$, $CF_2$ symmetric stretch[52] |
| 1295 | 1303 | $\nu_{t}^{CH_2}$, $CH_2$ twist[52]<br>$\nu_{s}^{CC}$, C–C stretch<br>$\delta_{b}^{CCC}$CCC bend<br>$\nu_{w}^{CF_2}$ $CF_2$ wag[69] |
| 1344 | 1347 | $CH_2$ or $CF_2$ |
| 1384 | - | $CH_2$ or $CF_2$ |
| 1396 | - | $\delta_{s}^{*CH_3}$, *$CH_3$ bend[52,66] |
| 1437 | 1439 | $\delta_{s}^{*CH_2}$, *$CH_2$ bend[52,70] |
| 1472 | - | $\delta_{s}^{CH_2}$, $CH_2$ bend[48,53] |

§ Assignments taken from references[46-47]
† Assignments taken from references[56-57]

### 5.3.3. Monolayer Characterization

Previous studies on alkanethiol films on Au[14] and UPD Ag[31] as well as probing the same films used here with PM-IRRAS, XPS and ellipsometry revealed that the HSAMs on Au and UPD Ag were well-ordered, with the SAMs formed on UPD Ag being more densely packed and ~3 Å thicker than the corresponding HSAM on Au.[34] The $CF_3$-terminated SAMs faired similarly well, with comparable packing densities and relative crystallinity to the corresponding-length HSAMs. As with the HSAMs, the thicknesses for the FSAMs were found to be higher on the UPD Ag substrates than the Au.[34] The $CH_3$-FSAMs were found to be thinner and less densely-packed than the $CF_3$-terminated SAMs,[14] and as was the case for the other two sets of SAMs, the $CH_3$-FSAMs formed thicker and more densely-packed monolayers UPD Ag.[34] Because the Au surfaces can be roughened during cyclic voltammetry,[71] reliable contact angles were unable to be obtained for the $CH_3$-FSAMs.

#### 5.3.3.1. Determination of Monolayer Structure with PM-IRRAS

The bulk structure of the self-assembled monolayers was probed with surface infrared spectroscopy. Polarization-modulation infrared reflection-absorption spectroscopy (PM-IRRAS) modulates the polarization of the input light from p-polarized to s-polarized with respect to the surface normal and takes the differential surface reflectivity

$$\frac{\Delta R}{R} = \frac{R_p - R_s}{R_p + R_s} \tag{5.5}$$

of the sample (taken at a grazing angle to the surface normal) to generate a surface IR spectrum of the molecules with the full bulk information of the thin film.[8,72] This is useful in characterizing the relative structural order (crystallinity) of the films and relative chain

orientation and can be tested by examining the frequency of the antisymmetric methylene stretch, $\nu_{as}^{CH_2}$. The peak for the methylene antisymmetric stretch, shown in Figures 5.13–5.15, is at 2918 $cm^{-1}$, which suggests that the alkane chains are well-ordered and trans-extended, making crystalline-like surfaces.[3] This peak has been shown to shift to higher frequencies when the monolayer is "liquid-like" and disordered, and shifts to lower frequencies when the monolayer is ordered and more crystalline in nature. A decrease in the full width at half maximum (FWHM) of the broad peak attributed to $\nu_{FR}^{CH_2}$ and $\nu_{as}^{CH_2}$ in the IR has also been noted to indicate more crystalline-like monolayers.[65,73] Therefore, if the FWHM and $\nu_{as}^{CH_2}$ peak position in the FT-IR spectra correspond to the molecules in a crystalline state, then the closer the PM-IRRAS peak is to the frequency of the FT-IR peak, the more crystalline the molecules are on the surface.[65,73]

As with any linear absorption spectroscopy, the intensity of PM-IRRAS resonances can be partially attributed to the concentration of functional groups contributing to that vibrational mode, however, the modulation of the polarization can also contribute to the final intensity of the peaks.[72] Therefore, the relative intensity of the resonance bands in the spectra is used and is described as the ratio of two bands in the same spectrum.[72] This ratio is related to the tilt of the molecule with respect to the surface because of the metal surface selection rule which states that transition dipole moments with a component perpendicular to the surface (aligned with the surface normal) will be enhanced, while those with a component parallel to the surface (tilted away from the surface normal) will be screened.[74]

The spectra in Figure 5.13 for the HSAMs on Au and UPD Ag in the C–H stretching region show a visible "odd-even" effect in the relative ratio of the methyl ($CH_3$) symmetric and antisymmetric stretches, $\nu_{ss}^{CH_3}:\nu_{as}^{CH_3}$, corresponding to the orientation of that functional group. The methyl peak ratio for the odd-numbered chain length SAMs (i.e., **H17SH** and **H19SH**) on Au is ~1:2, while for the even-numbered chain length SAMs (i.e., **H18SH** and **H20SH**) the ratio is ~1:1, as observed in other studies.[14,16,19] Changing the substrate to which the thiols bind produced a change in the ratio of intensities of the $CH_3$ symmetric and antisymmetric stretches in the IR spectra of the **HnSH** monolayers, as shown in Figure 5.13. The **HnSH** SAMs on UPD Ag have the opposite methyl intensity ratios, with the odd SAMs having a $\nu_{ss}^{CH_3}:\nu_{as}^{CH_3}$ ratio of ~1:1 and the even SAMs having a ratio of ~1:2. These changes in the trends for the relative ratios of the intensities are directly related to the orientation of the methyl group with respect to the surface normal.

Since the transition dipole moment for the antisymmetric stretch of the methyl group of an alkanethiol is perpendicular to the terminal C–C axis, the $CH_3$ antisymmetric stretch will be enhanced when the functional group is tilted away from the surface normal. Therefore, for the **HnSH** SAMs on Au, this means that the odd SAMs will be tilted away from the surface normal, while the even SAMs will be more upright, with respect to the surface normal. On the other hand, the **HnSH** SAMs on UPD Ag have methyl groups pointed upright for the odd SAMs and tilted away from the surface normal for the even SAMs. "Odd-even" effects in the IR spectroscopy of HSAMs on Au have been observed before.[53] A study by Chang et. al. on aromatic-derivatized alkanethiols deposited onto Au and Ag surfaces demonstrated the same trends in the "odd-even" behavior of the methyl stretching resonances shown by IR spectroscopy.[5] Studies of molecules with alkanoic acid,

rather than thiol, headgroups self-assembled onto Ag surfaces[27,75] have also exhibited the same "odd-even" effects in the structure of the tail group. These changes in structure led to changes in the physical properties of the films, as expanded upon in the wettability section.

The binding of the adsorbates to the UPD Ag surface had one more consequence -- the relative intensity between the methylene symmetric and antisymmetric stretches changed. The intensity ratio of those two resonances for the **HnSH** SAMs on Au is close to 1:2, whereas for the UPD Ag surface, the ratio is closer to 2:3. This can also be explained according to the surface selection rule. Previous studies have noted that SAMs formed on silver have lower chain tilt angles than the same SAMs on gold.[16,46] Therefore, as the chains tilt upright, aligning with the surface normal, the transition dipole moment for the methylene antisymmetric stretch, which is normal to the carbon backbone plane,[17] aligns more parallel to the surface, decreasing its peak intensity.[31] This dramatic decrease in the intensity ratio between the methylene stretching modes could be attributed to an overall upright orientation for the alkanethiol chain on the UPD Ag surface in comparison to the Au surface.

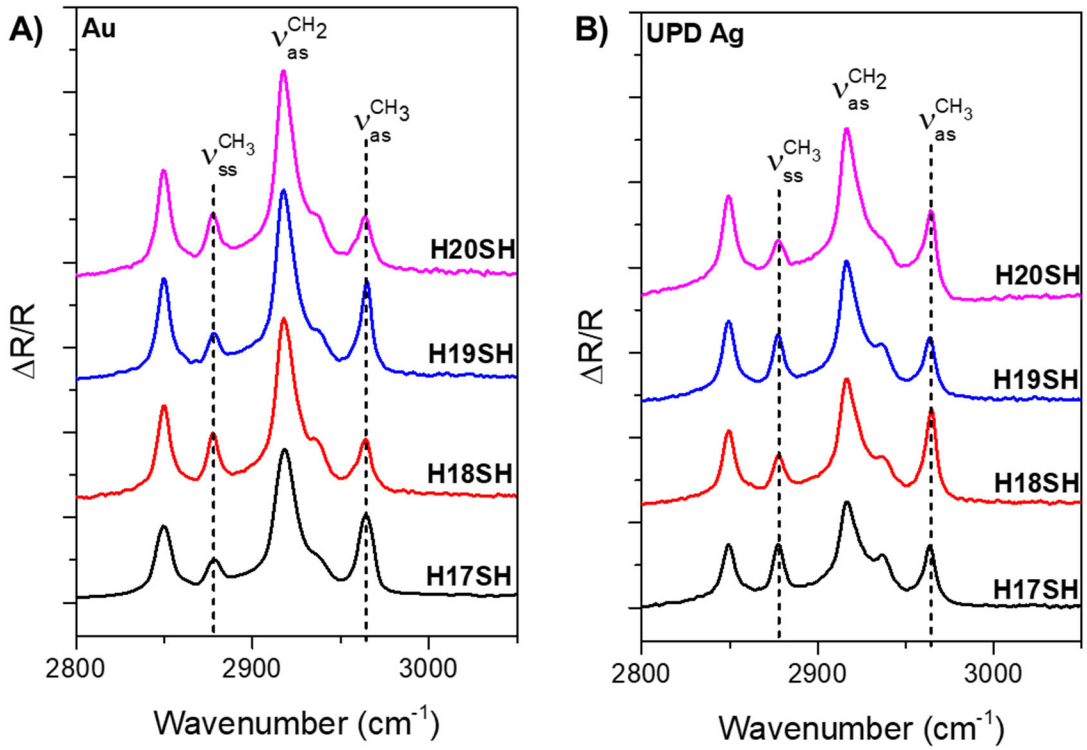


**Figure 5.13.** PM-IRRAS spectra of the **HnSH** SAMs on A) Au and B) UPD silver substrates in the C–H stretching region, 2800–3050 cm$^{-1}$.

Figure 5.14 shows the PM-IRRAS spectra in the C–H stretching region for the **F1HnSH** SAMs on Au and UPD Ag. The FSAM spectra clearly show that there are no methyl ($CH_3$) stretches, in agreement with the molecular structure of the adsorbates. As in the case of the **HnSH** SAMs, all of the FSAMs have their methylene antisymmetric stretch, $\nu_{as}^{CH_2}$, at 2918 cm$^{-1}$, indicative of well-ordered, trans-extended chains.[3] Moreover, the relative ratio in the $CH_2$ symmetric and antisymmetric stretching frequencies increases for the adsorbates on the UPD Ag surfaces, indicating, as was the case for the **HnSH** SAMs on UPD Ag, that the FSAMs are tilted more upright on the UPD Ag than the Au surface.

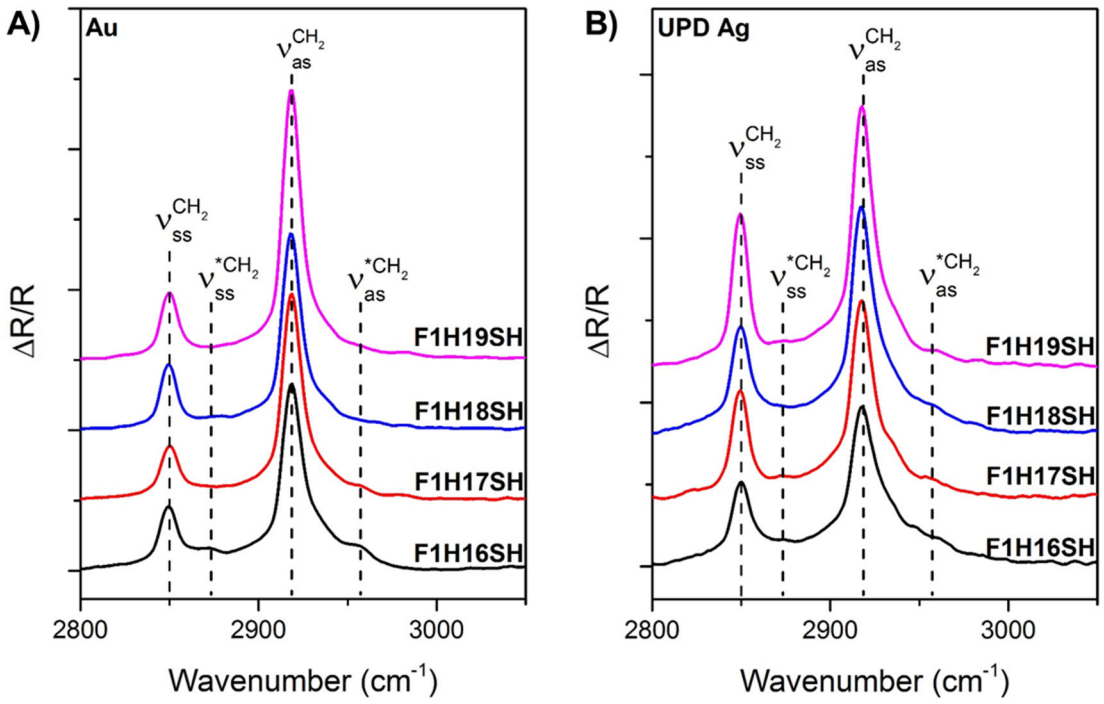


**Figure 5.14.** PM-IRRAS spectra of the **F1HnSH** SAMs on A) Au and B) UPD silver substrates in the C–H stretching region, 2800–3050 cm$^{-1}$.

Figure 5.15 shows the PM-IRRAS spectra for the **H1F6HnSH** adsorbates assembled onto Au and UPD Ag surfaces in the C–H stretching region. The blue-shifted methyl stretching resonances are small but visible in the spectra at 2963 cm$^{-1}$ and 3023 cm$^{-1}$, corresponding to the symmetric and antisymmetric modes, respectively. Figure 5.16 expands this region for better observation of these bands. From these spectra it is clear that the hydrocarbon chain below the fluorocarbon moiety is well-ordered on both surfaces, due to the position of the $\nu_{as}^{CH_2}$ at 2918 cm$^{-1}$; note that the $\nu_{as}^{CH_2}$ of the SAMs appeared at a lower frequency than the bulk IR spectra taken when the molecule was in a liquid-like state. A discussion of the relative order at the termini of the monolayers will be discussed later in the SFG section. As with the **HnSH** and **F1HnSH** SAMs, the ratio of $\nu_{as}^{CH_2}$:$\nu_{ss}^{CH_2}$ is larger

for the monolayers on Au than the UPD Ag, indicating that the carbon chains are tilted more upright and away from the surface on UPD Ag compared to the Au surface.

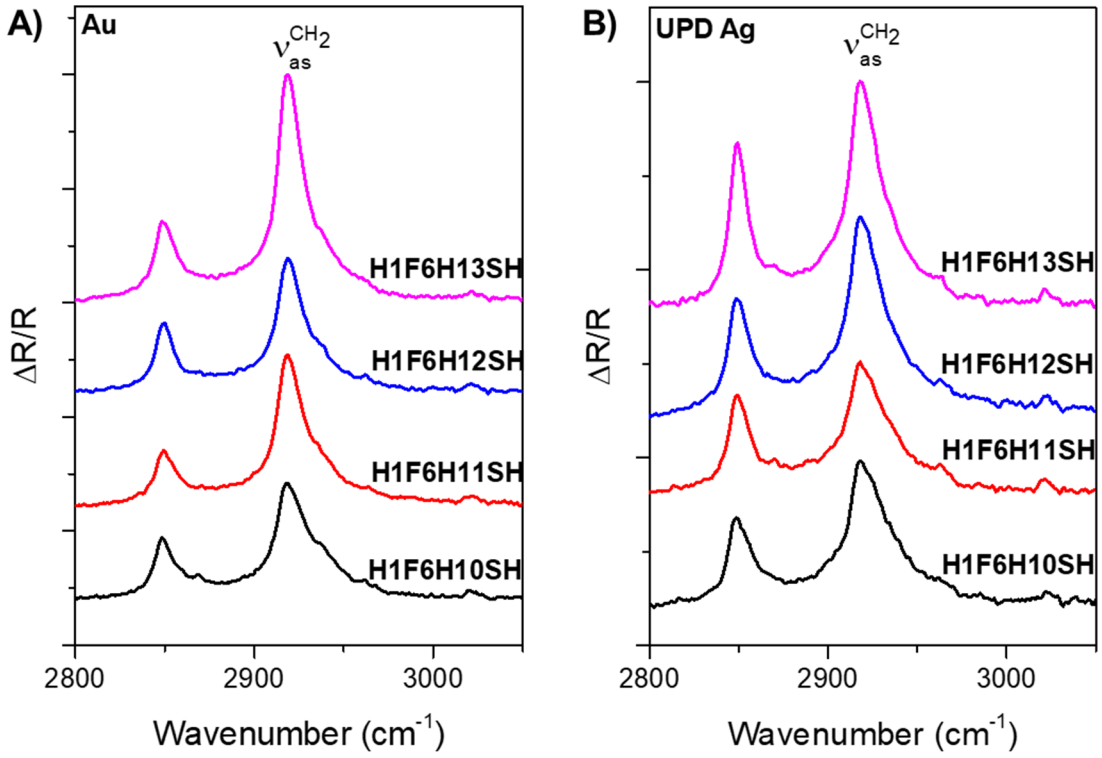


**Figure 5.15.** PM-IRRAS spectra of the **H1F6HnSH** SAMs on A) Au and B) UPD silver substrates in the C–H stretching region, 2800–3050 cm$^{-1}$.

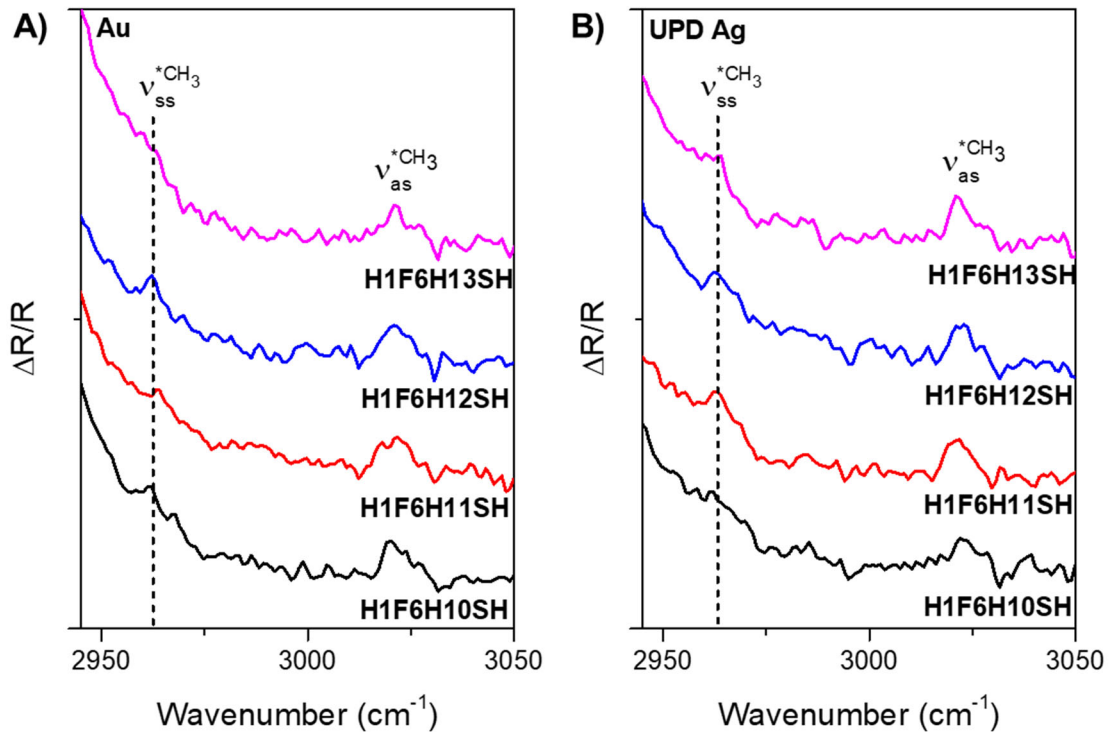


**Figure 5.16.** Expanded PM-IRRAS spectra of the **H1F6HnSH** SAMs on A) Au and B) UPD silver substrates in the C–H stretching region, 2950–3050 cm$^{-1}$.

The low-frequency PM-IRRAS spectra in the C–F stretching region of the **F1HnSH** SAMs and **H18SH**, which serves as a reference, are plotted in Figure 5.17. Although the Raman and IR spectra of the bulk materials exhibited bands in the low frequency region for the **HnSH** adsorbates, no resonances were within the detection limit of the PM-IRRAS, thus, only a representative spectrum for **H18SH** is provided. The band labeled on the spectra in Figure 5.17 is attributed mainly to the $CF_3$ symmetric stretching mode, $\nu_{ss}^{CF_3}$, however, the band is also coupled to skeletal stretching and $CH_2$ wagging modes. The band at ~1400 cm$^{-1}$ is attributed to a bending/wagging mode coupled to C–C stretching for the $CH_2$ adjacent to the $CF_3$ group, $\delta_s^{*CH_2}$. The spectra in Figure 5.17 display an "odd-even" effect in the relative ratio between the intensities of the $\nu_{ss}^{CF_3}$ and $\delta_s^{*CH_2}$

modes. For the FSAMs on gold, the odd FSAMs (**F1H16SH** and **F1H18SH**) have a higher ratio than the even SAMs (**F1H17SH** and **F1H19SH**). The opposite effect is observed for the FSAMs on UPD Ag, where the odd SAMs have a lower $\nu_{ss}^{CF_3}$: $\delta_s^{*CH_2}$ intensity ratio than the even SAMs. However, due to the coupled nature of the bands, the relative ratios cannot be used to determine the terminal $CF_3$ group orientation of the FSAMs. Therefore, a previous study used molecular modeling to determine the tilt angle of the terminal C–C bonds of the FSAMs with respect to the surface normal, and calculated tilt angles of ~17° for the even **F1HnSH** SAMs, and ~58° for the odd **F1HnSH** SAMs.[14]

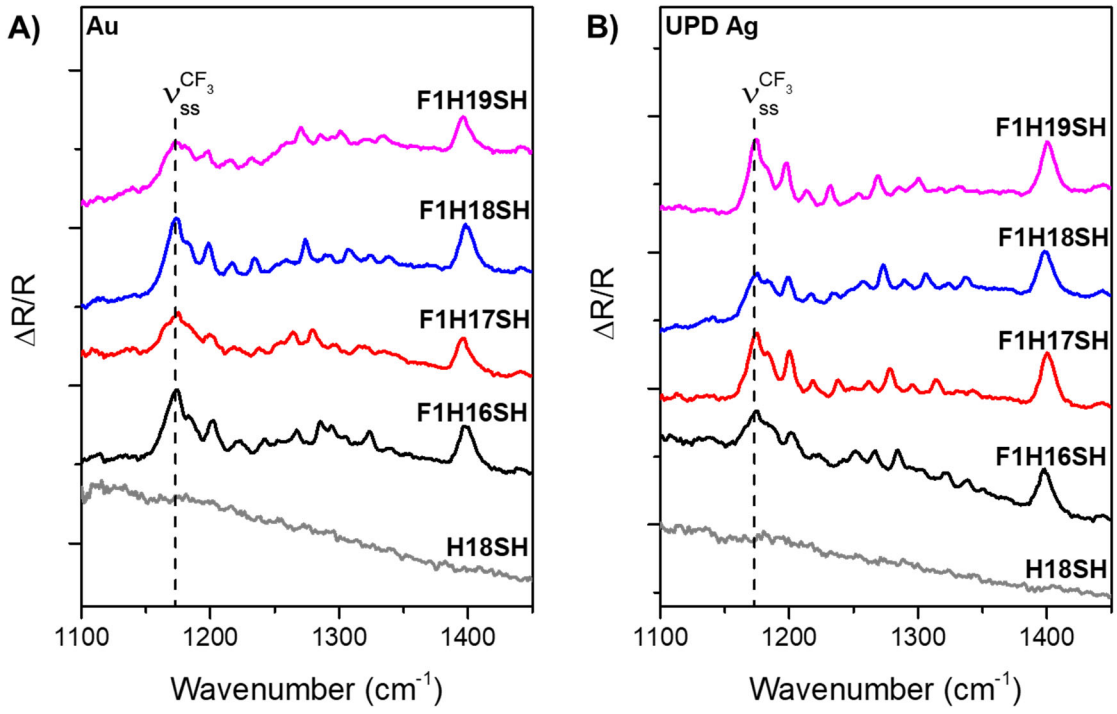


**Figure 5.17.** PM-IRRAS spectra for the **F1HnSH** SAMs and **H18SH** on A) Au and B) UPD silver substrates in the C–F stretching region, 1100–1450 cm$^{-1}$.

The low-frequency PM-IRRAS spectra shown in Figure 5.18 for the **H1F6HnSH** FSAMs failed to exhibit surface-driven orientational differences between the odd and even SAMs. Although the ratio in the relative intensity of the bands at 1140 cm$^{-1}$ and 1200 cm$^{-}$

[1] appears to change between the odd and even SAMs, previously reported bulk IR spectra[14] showed the same effect, implying that the change is due to chain packing and not chain orientation on the surface.

The assignment of the resonances in Figure 5.18 can be determined by comparison of the low-frequency PM-IRRAS of several fluorinated molecules. Figure 5.19 shows the PM-IRRAS spectra taken in the C–F stretching region, for certain FSAMs tested in this dissertation, **H18SH**, **F1H17SH**, **H1F1H16SH**, as well as those generated from $CF_3(CF_2)_7(CH_2)_{11}SH$ (**F8H11SH**), the HC–FC dipole molecule, **H1F6H11SH**. Figures 5.18 and 5.19 show that the resonances at ~1330 and ~1375 $cm^{-1}$, typically attributed to the axial $CF_2$ stretching modes (dipole moment parallel to the helical axis) are absent in the spectra of the **H1F6H11SH** SAM.[70,76-77] Fluorocarbon moieties of more than five fluorinated carbon atoms in SAMs are known to have upright orientations (~16° from the surface normal),[65,78] therefore, if the transition dipole moment is parallel to the helical axis, it will be perpendicular to the surface and will be enhanced due to the IR surface selection rules for metals.[10]

Colorado et. al. noted an increase in the wavenumber of these bands as the number of fluorocarbons in the chain increased, however, the analysis was performed exclusively on adsorbates with a $CF_3$-terminus.[79] The **H1F6HnSH** SAMs, with six $CF_2$ groups, should also exhibit two strong bands between 1320–1330 and 1365–1370 $cm^{-1}$,[10,79] however, the absence of these bands in the PM-IRRAS spectra confirm that the bands are predominantly composed of $CF_3$ stretching vibrations, in molecules with more than five fluorinated carbon atoms, as previously assigned by others.[80-81] Nonetheless, the small resonances at ~1340 and ~1384 $cm^{-1}$ -- attributed to a $CH_2$, $CF_2$, or coupled vibration – present in the PM-IRRAS

spectra of the **H1F6HnSH** SAMs lead to the possibility that those frequencies are due to the axial $CF_2$ vibrations shifted in frequency due to the absence of a terminal $CF_3$ group.

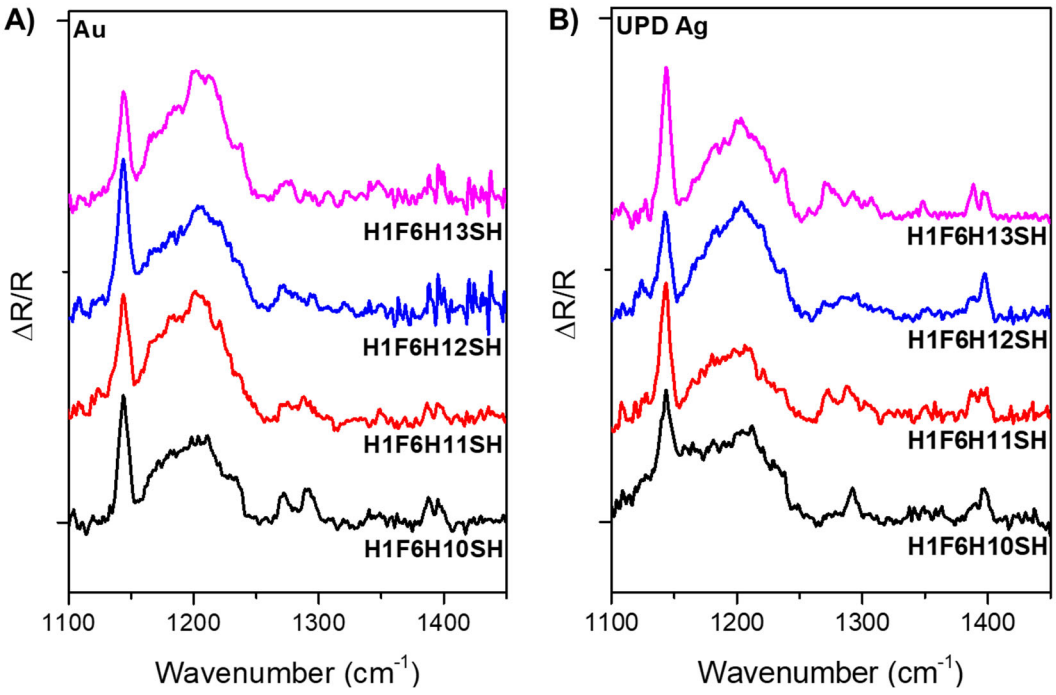


**Figure 5.18.** PM-IRRAS spectra for the **H1F6HnSH** SAMs and on A) Au and B) UPD silver substrates in the C–F stretching region, 1100–1450 $cm^{-1}$.

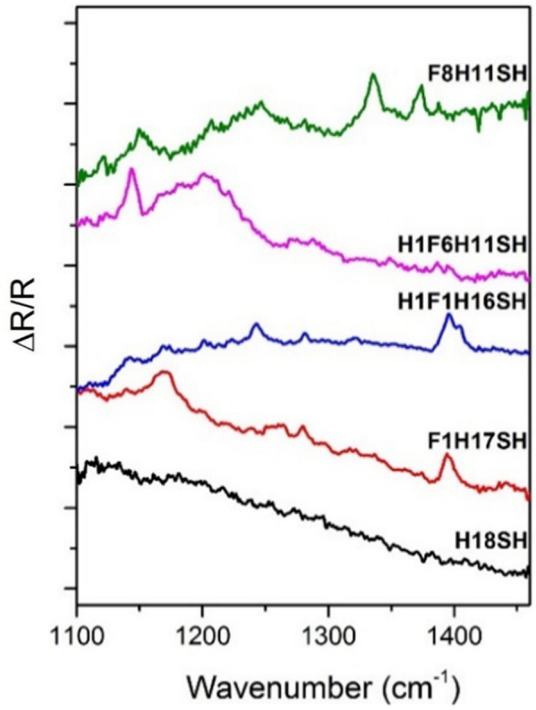


**Figure 5.19.** PM-IRRAS spectra for a perfluorocarbon-capped (**F8H11SH**), $CH_3$-terminated partially fluorinated (**H1F6H11SH**), buried $CF_2$ (**H1F1H16SH**), $CF_3$-terminated (**F1H17SH**), and fully alkanethiol (**H18SH**) SAMs on gold substrates in the C–F stretching region, 1100–1450 $cm^{-1}$.

### 5.3.3.2. Terminal Group Orientation at the Solid-Air Interface with SFG

To selectively probe the interfacial interactions between SAMs and contacting liquids we employed sum frequency generation (SFG) spectroscopy in the C–H and C–F stretching regions. Sum Frequency Generation spectroscopy uses powerful lasers at two different input wavelengths to cause a change in the polarization of the surface molecules, which in turn causes the emission of a beam with a frequency that is the sum of the input frequencies. The intensity of this SFG beam is dependent on the structure of the molecules; the functional group orientation information is contained in the susceptibility term of Equation 5.3. This relationship can be used to determine the orientation of any part of the molecule that is non-centrosymmetric, as that is one of the selection rules of the technique.

Signal from the vibrational normal modes probed by SFG can only be obtained when the modes are both Raman and IR active.

SFG signal is also dependent on the order of the system due to the relationship between the number density of oriented chromophores, N, and the SFG intensity, as shown in Equation 2.21 in Chapter 2. A decrease in the order of the system results in a decrease in the SFG signal, so that only well-oriented functional groups, such as the terminal methyl groups of densely-packed trans-extended SAM, give strong SFG signal.[82] For the systems analyzed in this study, SFG signal would be expected from the terminal functional group of the adsorbate ($CH_3$ or $CF_3$) and the methylene directly below it. However, the bulk of the methylene chains display a local centrosymmetry that will disable the chain from emitting SFG signal, unless the symmetry is broken as in the case of loosely-packed or disorganized alkanethiol monolayers that have gauche defects at the tail end of a trans-extended chain.[82]

The solid-air interface spectra, shown in Figures 5.20–5.22 for the C–H stretching region and 5.24 for the C–F stretching region, were included to provide contrast with the solid-liquid spectra as well as a reference for peak positions and functional group orientations. The SFG spectra shown in Figure 5.20 for the fully hydrocarbon SAMs generated from **HnSH** on Au and UPD Ag, show the typical methyl stretching resonances, $\nu_{ss}^{CH_3}$, $\nu_{FR}^{CH_3}$, $\nu_{as}^{CH_3}$, at 2875, 2936, and 2965 $cm^{-1}$, respectively, as dips in the ppp SFG spectra. The ssp spectra, Figures 5.20c and 5.20d, show only the symmetric stretches and the appearance of methylene symmetric and Fermi resonance modes , $\nu_{ss}^{CH_2}$ and $\nu_{FR}^{CH_2}$, at 2850, and 2900–2920, respectively, especially in the SAMs formed on UPD Ag, indicating the presence of gauche defects at the terminus of the chain. The oxidation of the UPD

silver surface is not suspected to play a role in the apparent disorder of the chains due to the finding by Laibinis et. al. who showed that oxidized bulk silver contained little to no silver oxide after SAM formation.[26] Defects in the structures of the SAMs could then be due to surface roughness of the substrates, however, surface Raman studies have shown that SAMs generated from long-chain alkanethiols form well-ordered surfaces even on electrochemically roughened Ag surfaces.[83] Similar studies on rough Au[1] and Ag[84-85] surfaces have concluded the same. Therefore, the complexity in the thiol-metal bonding chemistry causing a mismatch in the ideal lattice parameters for the alkyl chains versus the substrate-bound head groups could be the source of chain disorder.[3] Because the chains are long (more than 12 carbon atoms), the van der Waals interactions between molecules are strong enough to sustain the overall crystalline-like structure of the chain,[3] however, they may not be enough to prevent the formation of kinks at the end of the chain due to heterogeneous binding of the molecules to the substrates.

Since the methyl groups of these SAMs point away from the Au surface and produce dips in the spectra, the terminal groups ($CF_3$ and $*CH_3$) in the other sets of monolayers are expected to do the same. The **F1HnSH** adsorbates have small resonances in the C–H stretching region, shown Figure 5.21, attributed to the methylene group below the fluorinated segment,[82] and are assigned as the $\nu_{ss}^{*CH_2}$, $\nu_{FR}^{*CH_2}$, $\nu_{as}^{*CH_2}$, at 2875, 2900, and 2950 $cm^{-1}$, respectively. Literature on semi-fluorinated alkanes with ≥ 6 fluorocarbons noted the ability of methylene groups to rotate about their chain axis under a bulky fluorinated chain due to a lower packing density (greater spacing between chains) than for normal alkanes.[70] The methylene groups in the chain of the **HnSH** monolayers (tilted away from the surface normal to maximize van der Waals interactions) have been found to lack

free rotation around the molecular axis due to a high energy barrier for rotation.[4] A study by Pflaum and coworkers,[86] supports the notion that the methylenes adjacent to a bulky $CF_3$-terminus on a fluorinated alkanethiol have enough molecular mobility to break the local centrosymmetry of the chain causing for the $*CH_2$ vibrational modes to have blue-shifted stretching frequencies and become SFG active. Figure 5.21 shows an apparent "odd-even" effect in the relative amplitude of the methylene peaks that is opposite when the substrate is changed from Au to UPD Ag; this could due to the methylene modes reorienting (twisting) under the $CF_3$-terminus to achieve a lower surface energy,[14] which can cause changes in the intensity of the SFG peaks.

The SFG spectra for the monolayers generated from the **H1F6HnSH** adsorbates, shown in Figure 5.22, have resonances, $\nu_{ss}^{*CH_2}$, $\nu_{FR}^{*CH_2}$, attributed to the methylene below the fluorocarbon chain at 2875 and 2900–2920 $cm^{-1}$, and $\nu_{ss}^{*CH_3}$ and $\nu_{as}^{*CH_3}$ at 2960 and 3024 $cm^{-1}$, respectively, for the terminal methyl group. Interestingly, the ssp spectra, known to only display the symmetric C–H stretching modes for non-functionalized alkanethiols, have a clear upward-pointing peak for the $*CH_3$ antisymmetric stretch.

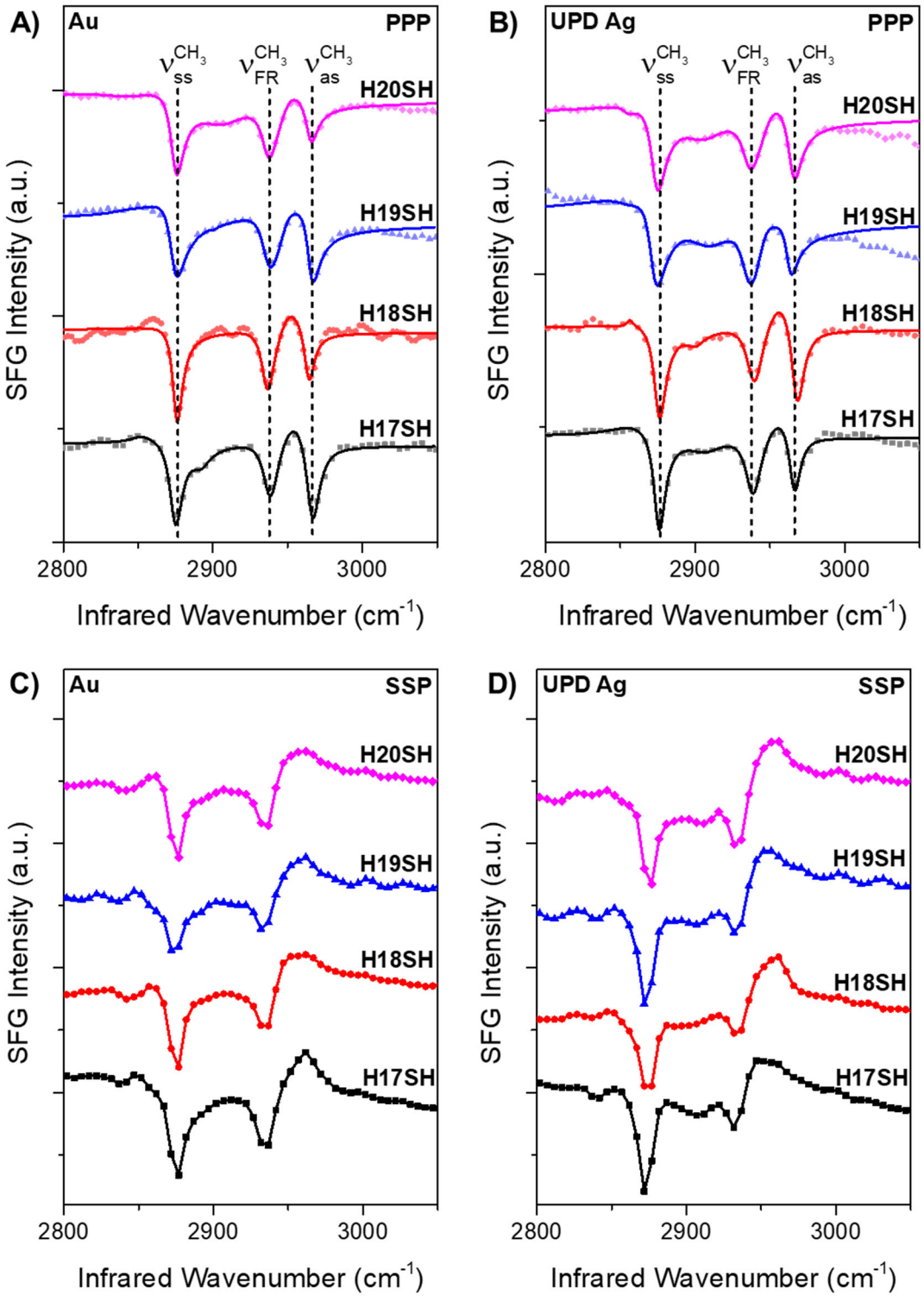


**Figure 5.20.** Solid-air SFG spectra in A/B) ppp and C/D) ssp polarization combinations for the **HnSH** SAMs on A/C) Au and B/D) UPD Ag in the C–H stretching region, 2800–3050 cm$^{-1}$. *Solid lines in A/B are the fits to the spectra.*

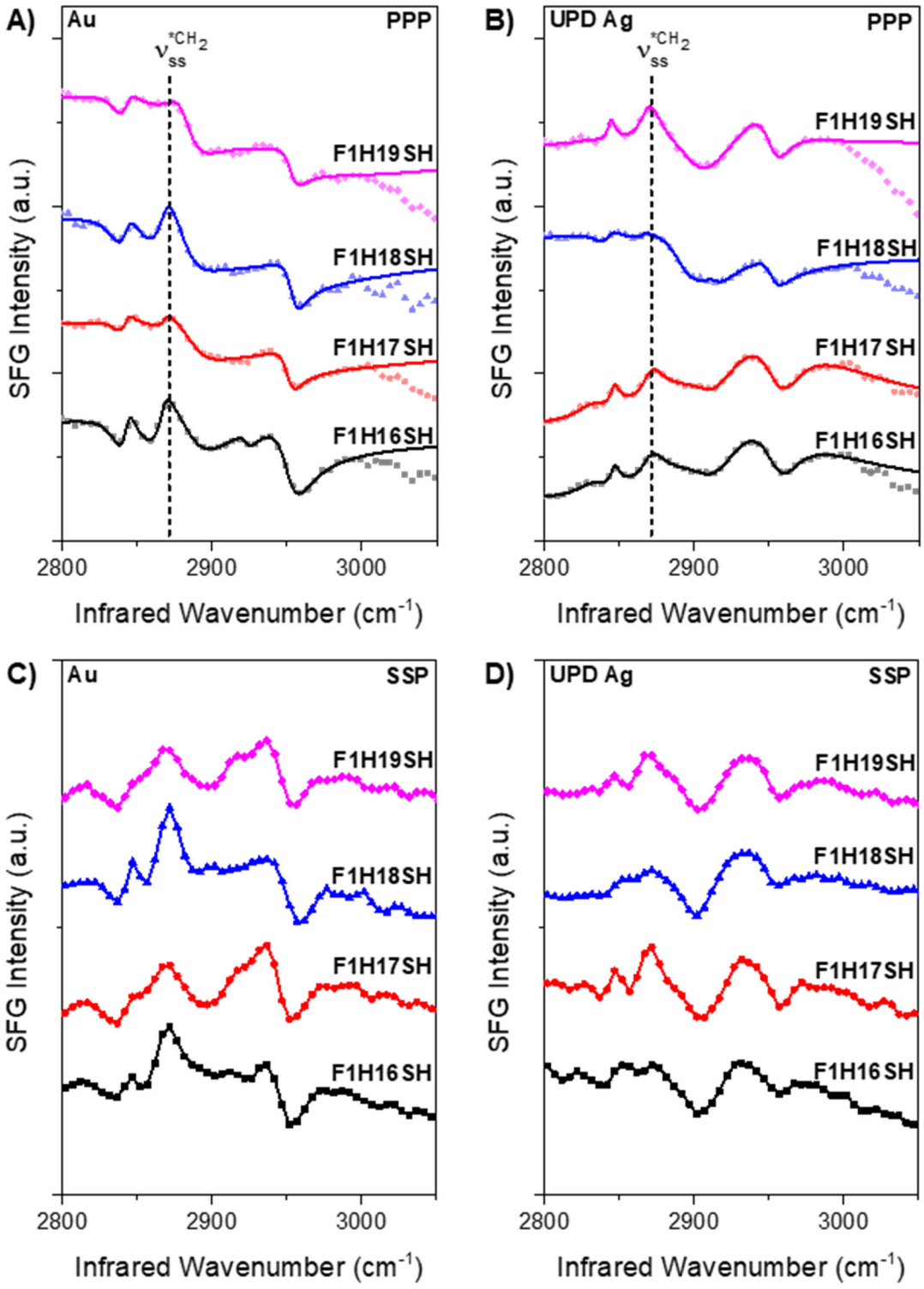


**Figure 5.21.** Solid-air SFG spectra in A/B) ppp and C/D) ssp polarization combinations for the **F1HnSH** SAMs on A/C) Au and B/D) UPD Ag in the C–H stretching region, 2800-3050 cm$^{-1}$. *Solid lines in A/B are the fits to the spectra.*

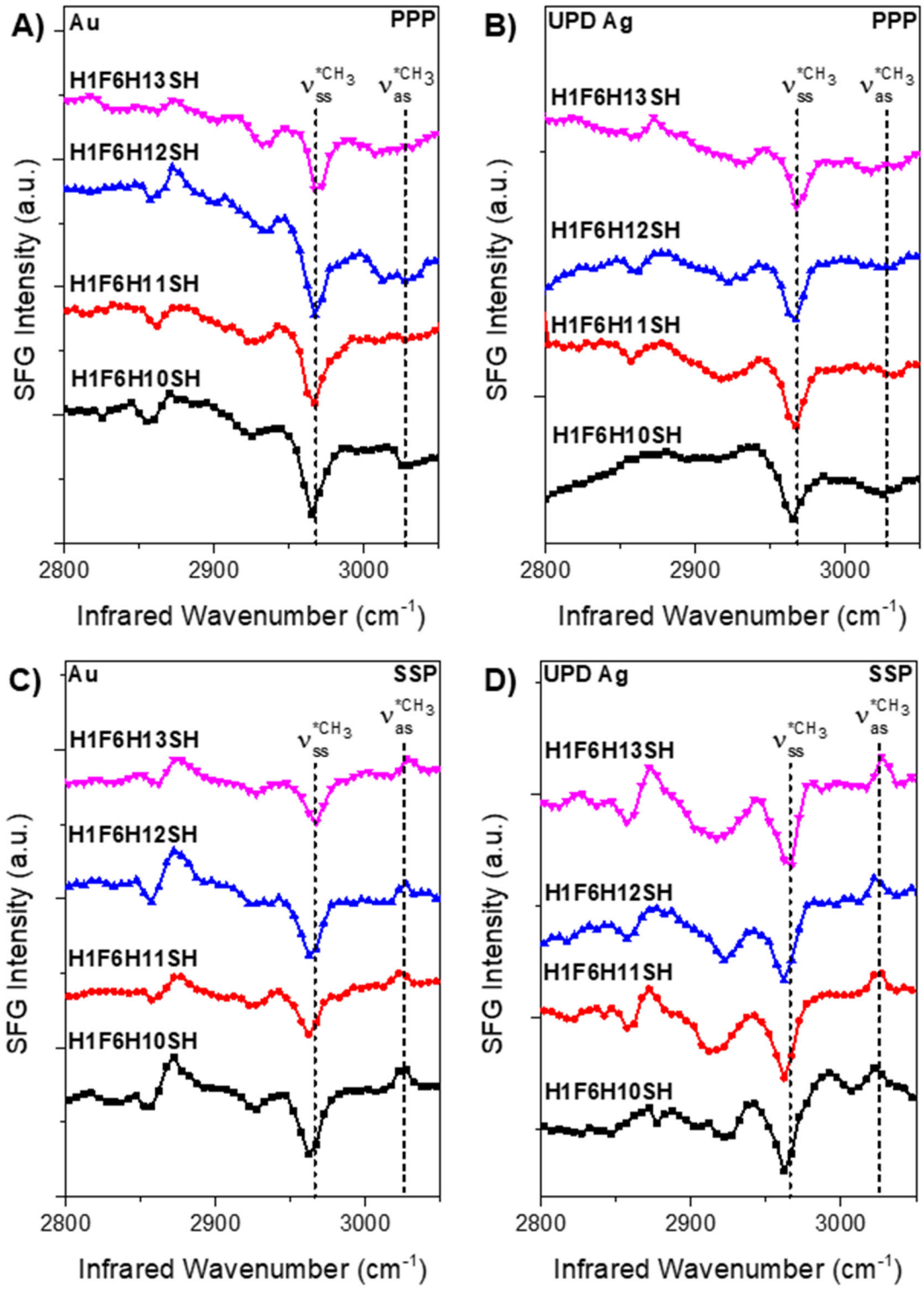


**Figure 5.22.** Solid-air SFG spectra in A/B) ppp and C/D) ssp polarization combinations for the **H1F6HnSH** FSAMs on A/C) Au and B/D) UPD Ag in the C–H stretching region, 2800-3050 cm$^{-1}$.

Using the assignments taken from Tables 5.2–5.4, the SFG spectra in Figures 5.20–5.22 and 5.24 were fit using Equation 5.4, and the calculated resonance intensities were compared to simulated curves for the intensity ratio versus functional group tilt angle, as described in Chapter 2. The orientation of the functional groups is defined by the tilt angle, θ, of the $C_3$-axis with respect to the surface normal. The parameters obtained from the spectrum fits for the C–H spectra of the SAMs generated from the **HnSH** and **H1F6HnSH** adsorbates are tabulated in Tables 5.5–5.6. Figure 5.23 shows the fitted spectra of the **H1F6HnSH** SAMs.

**Table 5.5.** Fitting Parameters for the C–H SFG Spectra of the $CH_3$-Terminated SAMs (**HnSH** and **H1F6HnSH**) on Au

| Adsorbate On Au | $A_{ss}$ ($CH_3$) | $\Gamma_{ss}$ ($CH_3$) | $A_{as}$ ($CH_3$) | $\Gamma_{as}$ ($CH_3$) | Ratio $I_{ss}/I_{as}$ |
|---|---|---|---|---|---|
| **H17SH** | 0.39 ± 0.02 | 5.01 ± 0.24 | 0.46 ± 0.05 | 5.46 ± 0.38 | 1.06 ± 0.31 |
| **H18SH** | 0.35 ± 0.01 | 4.01± 0.15 | 0.21 ± 0.03 | 4.12 ± 0.44 | 4.50 ± 1.66 |
| **H19SH** | 0.44 ± 0.02 | 6.86 ± 0.41 | 0.52 ± 0.16 | 6.15 ± 0.86 | 0.88 ± 0.61 |
| **H20SH** | 0.44 ± 0.02 | 4.65 ± 0.21 | 0.33 ± 0.14 | 5.31 ± 1.09 | 3.53 ± 3.36 |
| **H1F6H10SH** | 0.35 ± 0.01 | 8.10 ± 0.23 | 0.83 ± 0.08 | 43.04 ± 3.41 | 10.12 ± 2.56 |
| **H1F6H11SH** | 0.37 ± 0.02 | 7.75 ± 0.29 | 0.44 ± 0.14 | 49.88 ± 12.13 | 67.59 ± 60.95 |
| **H1F6H12SH** | 0.38 ± 0.01 | 8.06 ± 0.31 | 1.83 ± 0.11 | 43.70 ± 1.98 | 5.25 ± 2.55 |
| **H1F6H13SH** | -0.37 ± 0.02 | 5.01 ± 0.33 | -0.17 ± 0.04 | 9.99 ± 2.29 | 18.83 ± 12.80 |

The ratio of peak intensities for the **HnSH** SAMs was multiplied by a factor of 1.24 to account for the Fermi resonance contribution to the symmetric stretch peak at 2875 $cm^{-1}$.[39-40]

**Table 5.6.** Fitting Parameters for the C–H SFG Spectra of the $CH_3$-Terminated SAMs (**HnSH** and **H1F6HnSH**) on UPD Ag.

| Adsorbate on UPD Ag | $A_{ss}$ ($CH_3$) | $\Gamma_{ss}$ ($CH_3$) | $A_{as}$ ($CH_3$) | $\Gamma_{as}$ ($CH_3$) | Ratio $I_{ss}/I_{as}$ |
|---|---|---|---|---|---|
| **H17SH** | 0.31 ± 0.02 | 4.69 ± 0.23 | 0.09 ± 0.02 | 3.60 ± 0.59 | 10.6 ± 6.10 |
| **H18SH** | 0.26 ± 0.01 | 4.20 ± 0.15 | 0.24 ± 0.02 | 4.42 ± 0.32 | 2.11 ± 0.52 |
| **H19SH** | 0.30 ± 0.03 | 4.71 ± 0.41 | 0.14 ± 0.04 | 4.08 ± 0.76 | 5.02 ± 3.67 |
| **H20SH** | 0.40 ± 0.03 | 6.69 ± 0.21 | 0.34 ± 0.04 | 5.77 ± 0.51 | 1.79 ± 0.60 |
| **H1F6H10SH** | -0.71 ± 0.05 | 8.15 ± 0.56 | -0.44 ± 0.06 | 9.99 ± 1.24 | 3.97 ± 1.65 |
| **H1F6H11SH** | -0.50 ± 0.02 | 6.08 ± 0.27 | -0.10 ± 0.02 | 7.32 ± 1.75 | 35.82 ± 22.81 |
| **H1F6H12SH** | -0.48 ± 0.02 | 6.44 ± 0.35 | -0.11 ± 0.04 | 10.01 ± 3.69 | 50.17 ± 50.05 |
| **H1F6H13SH** | -0.29 ± 0.01 | 5.06 ± 0.29 | -0.15 ± 0.03 | 11.37 ± 2.37 | 18.59 ± 11.02 |

The ratio of peak intensities for the **HnSH** SAMs was multiplied by a factor of 1.24 to account for the Fermi resonance contribution to the symmetric stretch peak at 2875 $cm^{-1}$.[39-40]

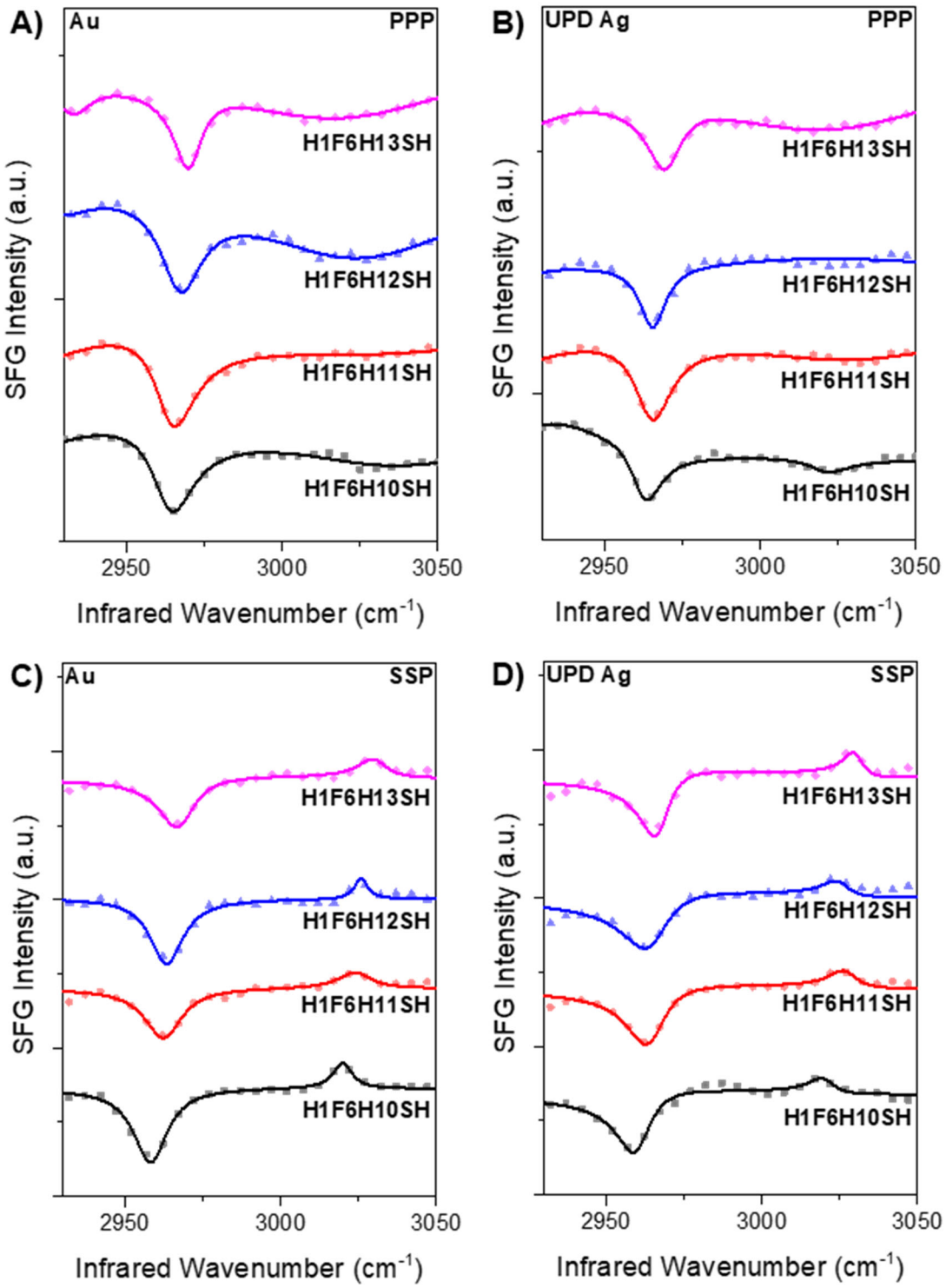


**Figure 5.23.** Fitted solid-air SFG spectra in A/B) ppp and C/D) ssp polarization combinations for the **H1F6HnSH** FSAMs on A/C) Au and B/D) UPD Ag in the C–H stretching region, 2800-3050 $cm^{-1}$. *Symbols denote the experimental data, and the solid lines denote the best fits to the spectra.*

The fluorinated monolayers were scanned in the C–F stretching region to probe the relative orientation of the fluorinated functional groups on the surface, and the resulting spectra are plotted in Figure 5.24. The **HnSH** SAM SFG spectra in the low-frequency region inconsistently showed a peak at 1385 $cm^{-1}$, attributed to the $\delta_s^{CH_3}$, symmetric $CH_3$ bend.[48-50] However, due to the irreproducibility in displaying the $\delta_s^{CH_3}$, as shown by Figure 5.24, the resonance was excluded from the current discussion. As in the PM-IRRAS spectra, the low-frequency SFG spectra show many bands in both ppp and ssp polarization combinations. Calculated potential energy distributions for the $CF_3$ stretching modes of similar molecules have shown that the modes are coupled strongly to other vibrations in the chain and cannot be separated.[54,56-57,59] Since the $CF_3$ bands are coupled to skeletal modes, the strongest band in the SFG (which has been assigned to mostly $CF_3$ symmetric stretching character) was fitted in both ssp and ppp polarization combinations to try to determine the orientation of the $CF_3$ group.

Since SFG intensities are the product of both the IR and Raman intensities for the transition in question, the small intensities for this mode in the Raman data (Figure 5.8) present a plausible reason for the low SFG intensities of the $CF_3$ stretches in the **F1HnSH** SAMs, Figure 5.24. Unfortunately, the low intensity and poor signal to noise ratio of the spectra did not allow for fitting within reasonable error limits, however, the relative intensities listed in Tables 5.7 and 5.8 were noted for the purpose of highlighting the "odd-even" effect in the amplitudes of the resonance designated as the $CF_3$ symmetric stretch, at 1175 $cm^{-1}$. The parameters obtained from the spectrum fits for the **F1HnSH** monolayers are provided in Tables 5.7–5.8 for the Au and UPD Ag substrates. Figure 5.25 shows the

fittings to the experimental spectra of the **F1HnSH** monolayers. The SFG spectra in the C–F stretching region failed to exhibit resonances for the **H1F6HnSH** SAMs, possibly due to the local centrosymmetry present in the six-fluorocarbon moiety.

**Table 5.7.** Fitting Parameters for the C–F SFG ssp and ppp Spectra for the **F1HnSH** SAMs on Au at the $CF_3$ Symmetric Stretching Frequency of ~1175 $cm^{-1}$.

| Adsorbate on Au | $A_{ssp}$ ($CF_3$) | $\Gamma_{ssp}$ ($CF_3$) | $A_{ppp}$ ($CF_3$) | $\Gamma_{ppp}$ ($CF_3$) | $I_{ssp}/I_{ppp}$ |
|---|---|---|---|---|---|
| **F1H16SH** | -0.86 ± 0.07 | 10.78 ± 0.91 | -1.02 ± 0.06 | 10.84 ± 0.52 | 0.71 ± 0.19 |
| **F1H17SH** | -0.22 ± 0.10 | 4.99 ± 2.60 | -0.94 ± 0.08 | 15.92 ± 1.02 | 0.54 ± 0.77 |
| **F1H18SH** | -0.76 ± 0.17 | 9.99 ± 2.18 | -0.79 ± 0.05 | 9.20 ± 0.53 | 0.77 ± 0.50 |
| **F1H19SH** | -0.50 ± 0.03 | 5.39 ± 0.32 | -1.03 ± 0.10 | 14.99 ± 1.26 | 0.15 ± 0.14 |

**Table 5.8.** Fitting Parameters for the C–F SFG ssp and ppp Spectra for the **F1HnSH** SAMs on UPD Ag at the $CF_3$ Symmetric Stretching Frequency of ~1175 $cm^{-1}$.

| Adsorbate on UPD Ag | $A_{ssp}$ ($CF_3$) | $\Gamma_{ssp}$ ($CF_3$) | $A_{ppp}$ ($CF_3$) | $\Gamma_{ppp}$ ($CF_3$) | $I_{ssp}/I_{ppp}$ |
|---|---|---|---|---|---|
| **F1H16SH** | -0.82 ± 0.17 | 9.85 ± 1.50 | -1.71 ± 0.10 | 19.94 ± 0.91 | 0.95 ± 0.51 |
| **F1H17SH** | -0.50 ± 0.24 | 6.17 ± 3.22 | -0.65 ± 0.03 | 7.89 ± 0.43 | 0.95 ± 1.35 |
| **F1H18SH** | -0.39 ± 0.32 | 8.00 ± 5.50 | -0.75 ± 0.05 | 13.49 ± 0.75 | 0.76 ± 1.63 |
| **F1H19SH** | -0.43 ± 0.27 | 6.00 ± 3.78 | -0.65 ± 0.02 | 8.70 ± 0.34 | 0.90 ± 1.62 |

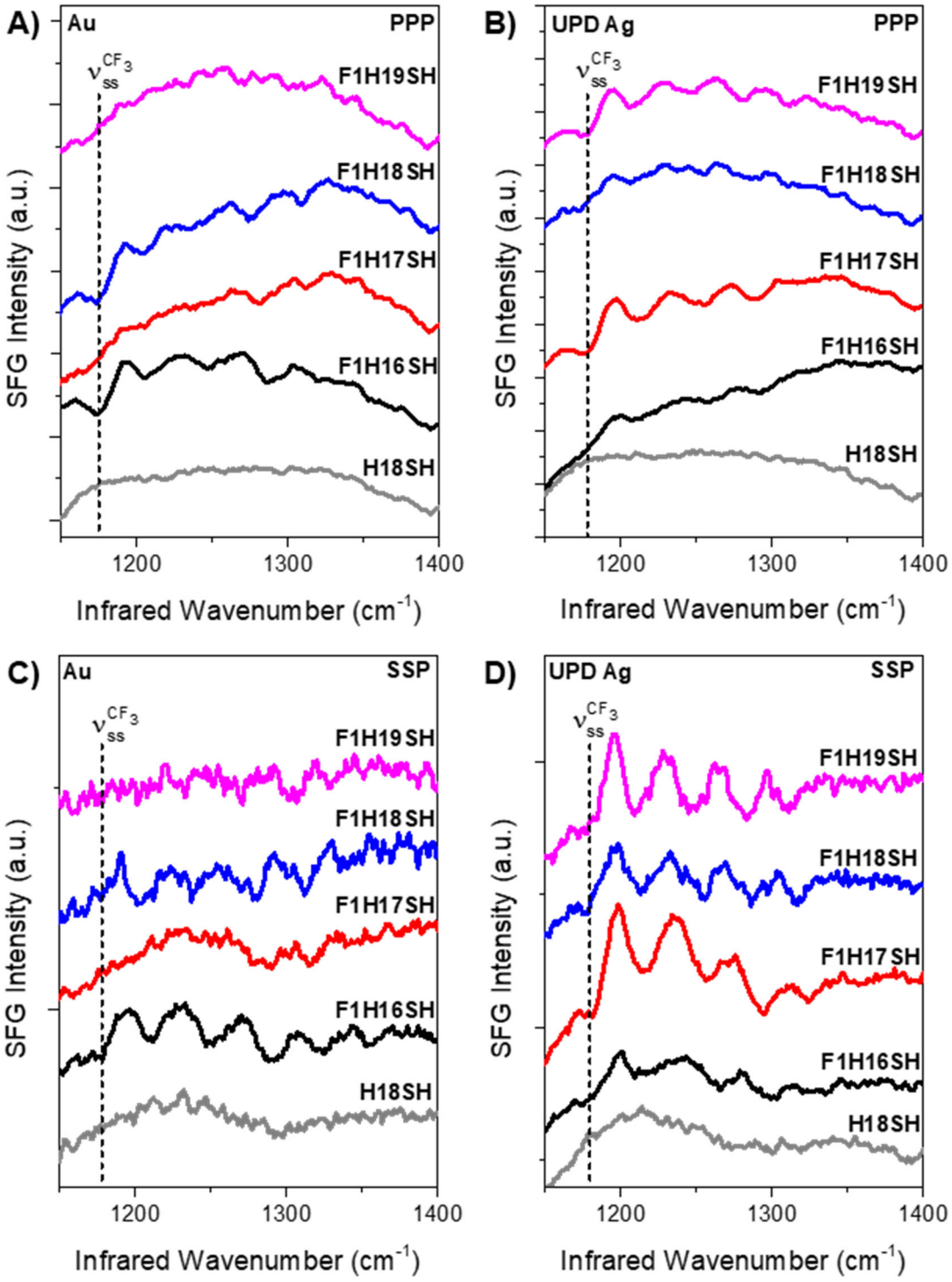


**Figure 5.24.** Solid-air SFG spectra in A/B) ppp and C/D) ssp polarization combinations for the **F1HnSH** SAMs on A/C) Au and B/D) UPD Ag in the C–F stretching region, 1150–1400 cm$^{-1}$.

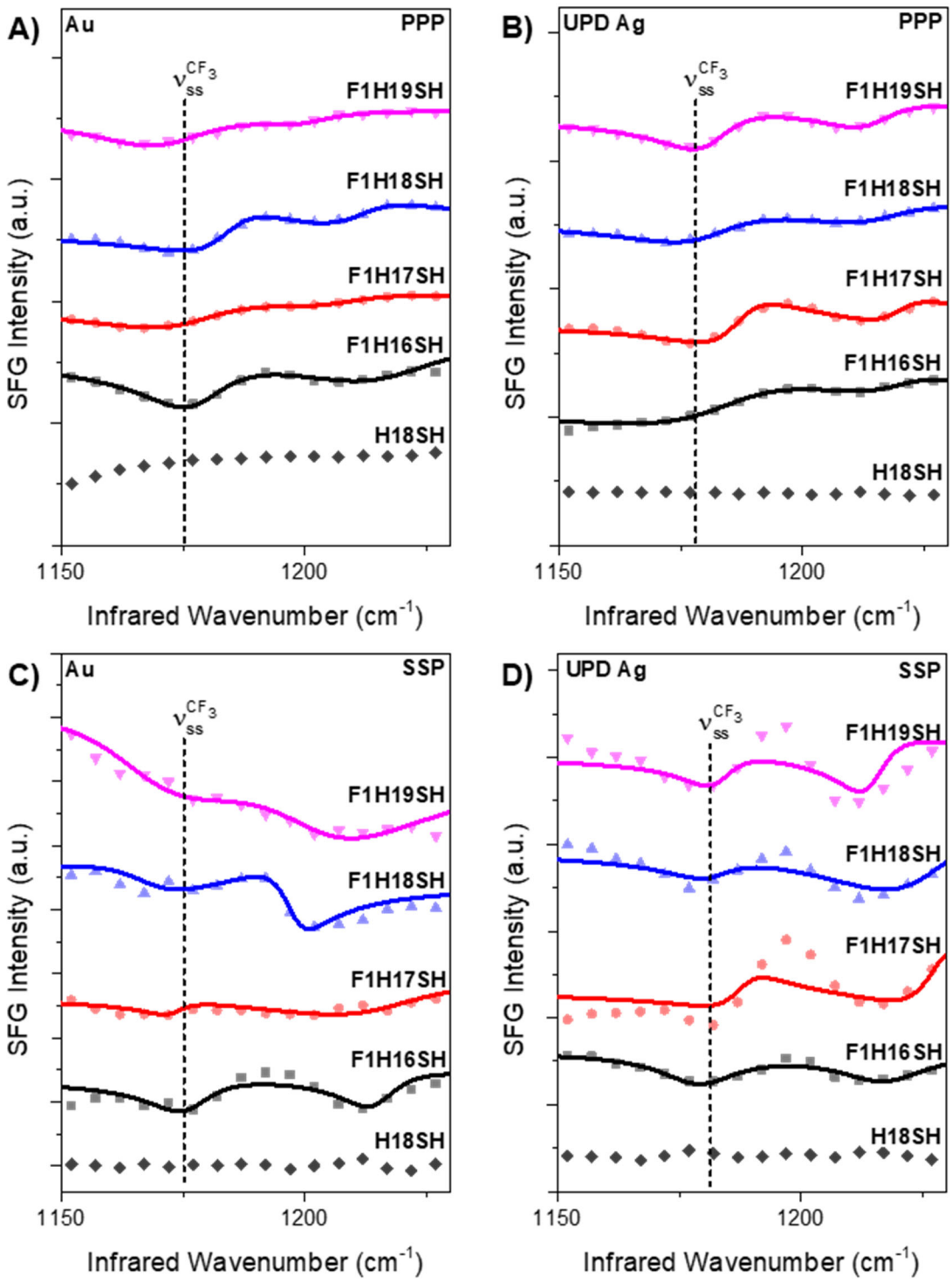


**Figure 5.25.** Fitted solid-air SFG spectra in A/B) ppp and C/D) ssp polarization combinations for the **F1HnSH** SAMs on A/C) Au and B/D) UPD Ag in the C–F stretching region, 1150-1230 cm$^{-1}$. *The symbols represent the experimental data, and the solid lines are the fits to the spectra.*

Figure 5.26 was generated using the intensity ratio results obtained from the fits to the SFG spectra to show the $CH_3$ and $CF_3$ orientations at the solid-air interface. For the simulation of the orientation curves, the refractive index of the surface was assumed to be that of evaporated gold for both the bare Au and UPD Ag surfaces, since the UPD Ag surface is covered by only a monolayer of silver and will not have the same optical properties as bulk silver. However, it is important to note that the refractive indices determined using ellipsometry at 632 nm for the Au and UPD Ag were on average $0.16 \pm 3.45i$ and $0.15 \pm 3.4i$, respectively. Therefore, some error intrinsic to the orientation curves was introduced due to the small differences in optical constants of the surfaces. Nonetheless, Figure 5.26A shows a clear "odd-even" effect in the orientation of the terminal groups of the **HnSH** SAMs on Au; where the methyl groups of the odd SAMs are tilted away from the surface normal, while the methyl groups of the even SAMs are more upright, in agreement with the PM-IRRAS results and previous SFG studies on the orientation of $CH_3$ groups of alkanethiols on Au.[87] The trend is reversed when the **HnSH** SAMs are on the UPD Ag substrates, indicating that the terminal groups of the odd SAMs are more upright than the even SAMs.

Figure 5.26B shows the $CF_3$ tilt angles determined using the intensity ratio between the symmetric stretch in the ssp and ppp polarization combinations. Due to the high error from the fits to the spectra, a trend is not evident in the orientation of the $CF_3$ groups. Beyond signal-to-noise ratio issues, a reliable simulated curve for the orientations of the $CF_3$ groups could not be obtained by the current analysis. This was due to the inability to determine the true hyperpolarizabilities for the symmetric stretching vibration due to its coupling to other vibrational modes.

Nonetheless, the value of the hyperpolarizability ratio, R, was varied between 1 and 4 to produce curves that complied with the intensity ratios from the experimental results (not shown). The simulated curves matched the experiment for values of $R \geq 3.4$. A value of R = 3.4 was applied to generate the curve used to calculate the $CF_3$ tilt angles plotted in Figure 5.26B. A simulation of $CF_3$ orientations by molecular modeling,[14] has shown that the **F1H16SH** SAM should have a terminal C–C tilt angle of ~ 58° -- this was not the case with the SFG orientation analysis using the Issp/Ippp ratio for the $CF_3$ symmetric stretching vibration. Despite the shortcomings with the intensity ratios, there is a visible "odd-even" effect in the amplitudes of the $CF_3$ symmetric stretch shown in Figure 5.24A and 5.24B, and if the hyperpolarizability, βccc, is known, the intensities for the mode can be directly related to the tilt angle of the functional group in order to determine the general trend for the orientation of the $CF_3$ group in air and under contacting liquids.

The previously determined $CF_3$ tilt angles of ~58° for odd SAMs and ~17° for even SAMs,[14] were used as a starting point to back-calculate the hyperpolarizability, βccc, and hyperpolarizability ratio, R, from the experimental data. Unfortunately, varying the values failed to exhibit such trends in the tilt angle, but rather gave the opposite trend; no matter what value for R or βccc was used in the simulation, the intensities determined from the experimental SFG spectra for the odd SAMs on Au gave lower tilt angles than the even SAMs on Au. The plot shown in Figure 5.27 shows the simulated intensity in the ppp spectrum versus orientation curve and the experimentally-determined intensities of the $CF_3$ symmetric stretching peaks for the FSAMs on Au. The discrepancy in "odd-even" trends indicates that the model used to determine the orientations from the SFG has faults and will need further analysis before it can be used. Undetermined correction factors may need

to be applied to account for the change in the local fields at metal surfaces in the low-frequency IR region. Despite the failure with the quantitative orientation analysis of the $CF_3$ groups, the data is reliable (due to its reproducibility) so that the amplitudes of the peaks can be trusted to provide qualitative information about the functional group orientation. If the trends observed with molecular modeling hold true, then the peaks in the SFG spectra with larger amplitudes correspond to $CF_3$ groups that are more tilted on the surface, while the lower amplitude peaks correspond to $CF_3$ groups that are more upright. In SFG, a decrease in the intensity of a mode typically implies an increase in the tilt angle with respect to the surface normal, thereby, lower SFG intensity is indicative of a more slanted functional group.

It is possible that the assignment of the peak at 1175 $cm^{-1}$ to a symmetric stretching mode is not accurate, and the band is instead related to the antisymmetric stretching of the $CF_3$ group. Several studies incorporating Raman and IR have shown that $CF_3$-terminated propylsilanes have a band at 1143 $cm^{-1}$ that is assigned to the $CF_3$ antisymmetric stretch, while a band at 1271 $cm^{-1}$ contains symmetric stretching character.[88-90] If those assignments are to be followed, then the larger amplitudes of the $CF_3$ bands in the odd FSAMs can be reasonably related to an increase in the tilt of the $CF_3$ group, as is the case for the higher $CH_3$ antisymmetric stretching peak intensity an odd alkanethiol SAM (in comparison to the $\nu_{as}^{CH_3}$ intensity for an even SAM), corresponding to a greater tilt of the $CH_3$ with respect to the surface normal. Notwithstanding the disagreement in the literature for peak assignments of the $CF_3$ group, the fact that the "odd-even" effect in the amplitude of the $CF_3$ stretching mode inverts between the Au and UPD Ag surfaces indicates that the

orientation of the terminal group in the SAMs changes depending on the substrate to which the molecules are bound.

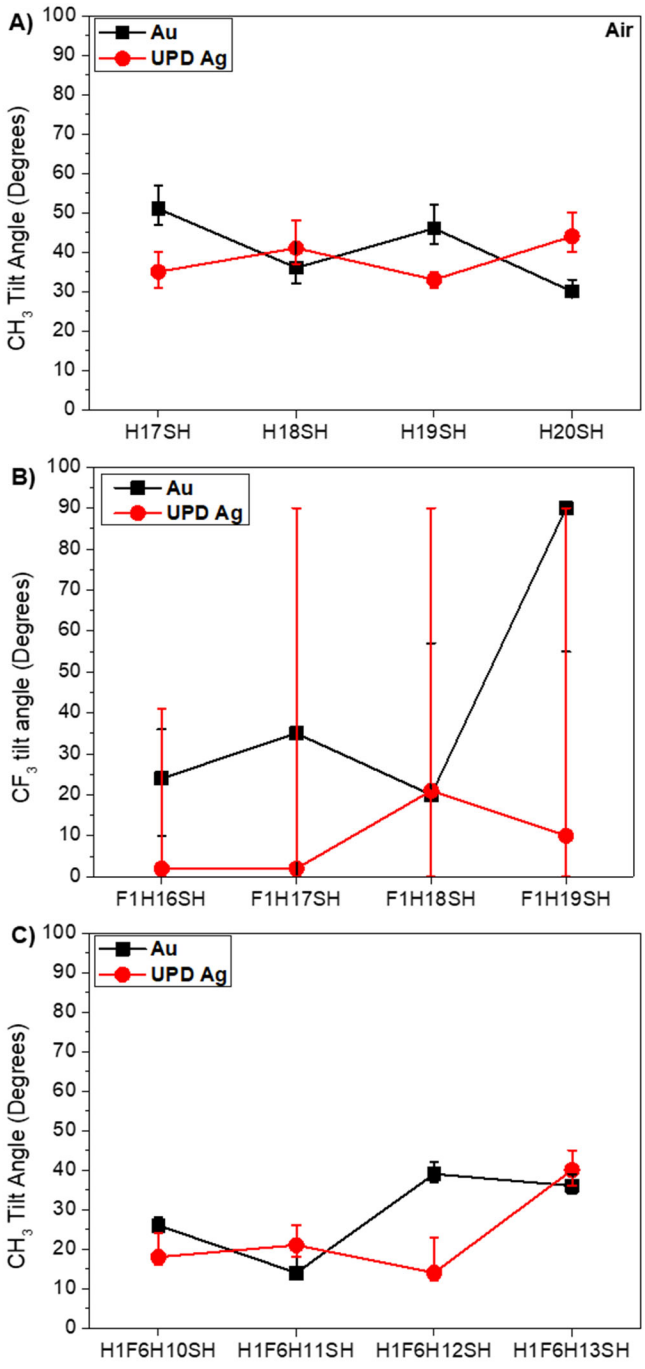


**Figure 5.26.** Solid-air average terminal functional group orientations calculated from the SFG spectra of the $CH_3$ in the **HnSH** SAMs, $CF_3$ in the **F1HnSH** SAMs, and $CH_3$ in the **H1F6HnSH** SAMs.

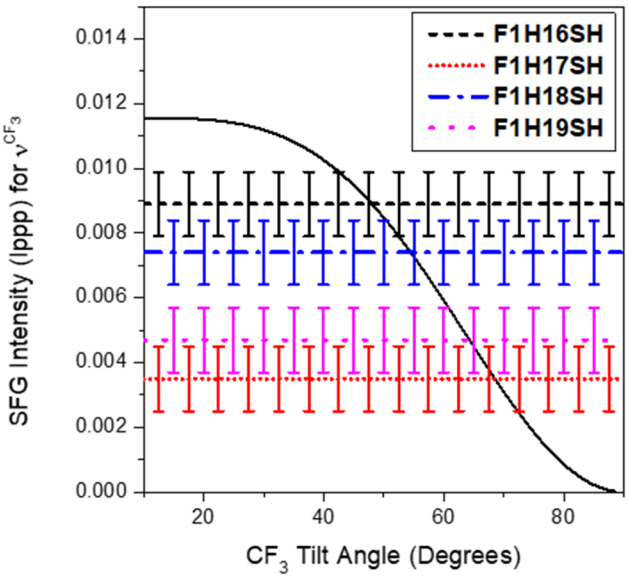


**Figure 5.27.** Simulated curve (black solid line) for the SFG intensity of the $CF_3$ stretching vibration at 1175 $cm^{-1}$ as a function of its average tilt angle for the **F1HnSH** SAMs on Au. The lines with error bars represent the SFG intensities calculated from the fits to the experimental spectra for the **F1HnSH** SAMs on Au. The top two intensities belong to the odd SAMs, while the bottom two are for the even SAMs.

The **H1F6HnSH** SAMs on Au and UPD Ag exhibit an "odd-even" trend in the terminal methyl group tilt angle matching that of the **HnSH** SAMs on Au and UPD Ag, respectively, and is shown in Figure 5.26C. Although there seems to be a reversal in "odd-even" trends for the **H1F6HnSH** SAMs on Au versus UPD Ag, three of the SAMs on UPD Ag fail to show a difference in the overall $CH_3$ tilt angle, within error. The upright orientation of the methyl groups in the three aforementioned SAMs indicate that the SAMs on UPD Ag lack an "odd-even" effect for the average tilt angle, possibly due to the fact that the chains as a whole are aligned to the surface normal.[5] In other words, if the overall tilt of the alkyl chains is more upright on the surface, the terminal methyl groups will adopt the same average orientation, regardless of overall chain length, as shown by the **H1F6HnSH** SAMs.

### 5.3.4. SFG Spectroscopy of the Solid-Liquid Interface

#### 5.3.4.1. The Solid-Liquid Interface of the HnSH SAMs

SFG signal can only be obtained from functional groups in an environment of non-centrosymmetry, such as at an interface, therefore, this technique was chosen to probe the interface between the liquids and the terminal groups of the SAMs to examine how the SAM structure changes when in contact with acetonitrile-*d*$_3$ ($CD_3CN$) and perfluorodecalin (PFD). Orientation analysis was performed on the SFG spectra of the SAMs under the liquids to offer detail about the structure of the SAM at the liquid interface. The fitted data were then used to deduce the orientation of each functional group -- denoted as the tilt angle, θ, of the $C_3$-axis with respect to the surface normal -- by using the intensity ratio between the symmetric and antisymmetric methyl stretching vibrations in the ppp SFG spectra. The simulated orientation curves were also corrected for the change in Fresnel factors at the solid-liquid interface. SFG spectra were obtained for all the monolayers before, during, and after contact with the wetting liquids. The spectra taken before and after contact with a wetting liquid were exactly the same, revealing the reversibility of the structural changes induced by interactions between the SAMs and the liquids, and confirming reports that contact with wetting liquids prompt structural changes isolated to the tail groups of monolayers, while the main methylene backbone retains its relative crystallinity.[85,91]

Acetonitrile is a small polar aprotic molecule which has been used to test the contribution of dipole interactions at SAM surfaces.[14] Figure 5.28 contains the experimental SFG spectra for the solid-liquid interfaces between the SAMs generated from the **HnSH** adsorbates and the contacting liquids, acetonitrile and pefluorodecalin. The fits

to the spectra in Figure 5.28 were used to determine values for the intensity ratios of the methyl symmetric and antisymmetric stretches of the **HnSH** SAMs and **H1F6HnSH** FSAMs (vide infra) on Au and UPD Ag, which were then used to calculate the average $CH_3$ tilt angles at the solid-liquid interface. The ratios and corresponding average $CH_3$ tilt angles are listed in Table 5.9. These tilt angles, along with their asymmetric error bars, denoting the range of tilt angles based on the error in the intensity ratios, are plotted in Figure 5.29A for the **HnSH** SAMs on Au and UPD Ag in contact with acetonitrile. A comparison between the tilt angles of the $CH_3$ group for the **HnSH** SAMs at the solid-air interface in Figure 5.26A and those for the **HnSH** SAMs in contact with acetonitrile in Figure 5.29A shows that the methyl groups in the SAMs are tilted more upright when in contact with the wetting liquid. This decrease in the tilt angle of the terminal group is likely caused by the methyl groups reorienting to accommodate the penetration of the liquid into the monolayer.

A PM-IRRAS study by Anderson et. al.[91] on the structural changes of alkanethiol monolayers on Au in contact with $CD_3CN$ concluded that acetonitrile partially solvates the monolayers, increasing the fluidity of the alkyl chains and causing them to reorient into a perpendicular alignment relative to the substrate. A partial rotation of the methyl group due to solvent-monolayer interactions with $CD_3CN$ has been noted previously,[92] and is shown by distinguishable broadening of the higher frequency band corresponding to the $\nu_{as}^{CH_3}$ mode. The spectra in Figure 5.28 clearly display this broadening of the antisymmetric methyl stretching mode. The intercalation of the small $CD_3CN$ molecules into the SAM causes an increase in the disorder of the terminal functional groups, as shown by comparing the spectra in Figure 5.28A and 5.28B for the solid-liquid interfaces with those of the

corresponding solid-air interfaces in Figure 5.20. The spectra in Figure 5.28 show an increase in the intensities of the methylene stretching vibrations, indicating gauche conformations present at the interface.[92] The peak frequencies of the **HnSH** SAMs in contact with acetonitrile red-shifted by ~5 $cm^{-1}$, closer to the peak frequencies of the bulk molecules collected from IR and Raman spectroscopy. This is consistent with previous reports that attributed the red-shift of the methyl peaks from **H18SH** in contact with $CD_3CN$ to the change in the environment of the methyl groups from air (where they are able to rotate freely) to a bulk-phase, more dense, environment, where their movement can be restricted by dispersive interactions between the methyl group of the liquid and the hydrocarbon monolayer.[92-93]

There is experimental evidence in the literature that suggests the methyl-to-methyl interaction between hydrocarbon SAMs and acetonitrile.[82,94-96] Ward et. al.[95-96] studied various surfactants adsorbed onto a **D18SH** on Au surface and noted that the surfactants preferred to orient with their terminal methyl group pointing toward the **D18SH** terminal methyl. Finally, although the "odd-even" effect in the orientation of the methyl group of the **HnSH** SAMs on Au stays intact, even when in contact with the liquid, for the **HnSH** SAMs formed on UPD Ag the "odd-even" effect is lost, and the methyl groups of the different chain-length monolayers have nearly the same tilt angle, within error. This could be due to the more perpendicular alignment of the chains to the UPD Ag substrate, causing the terminal methyl groups of the SAMs to be oriented with the same tilt as was the case for the $*CH_3$ groups of the **H1F6HnSH** SAMs at the solid-air interface.

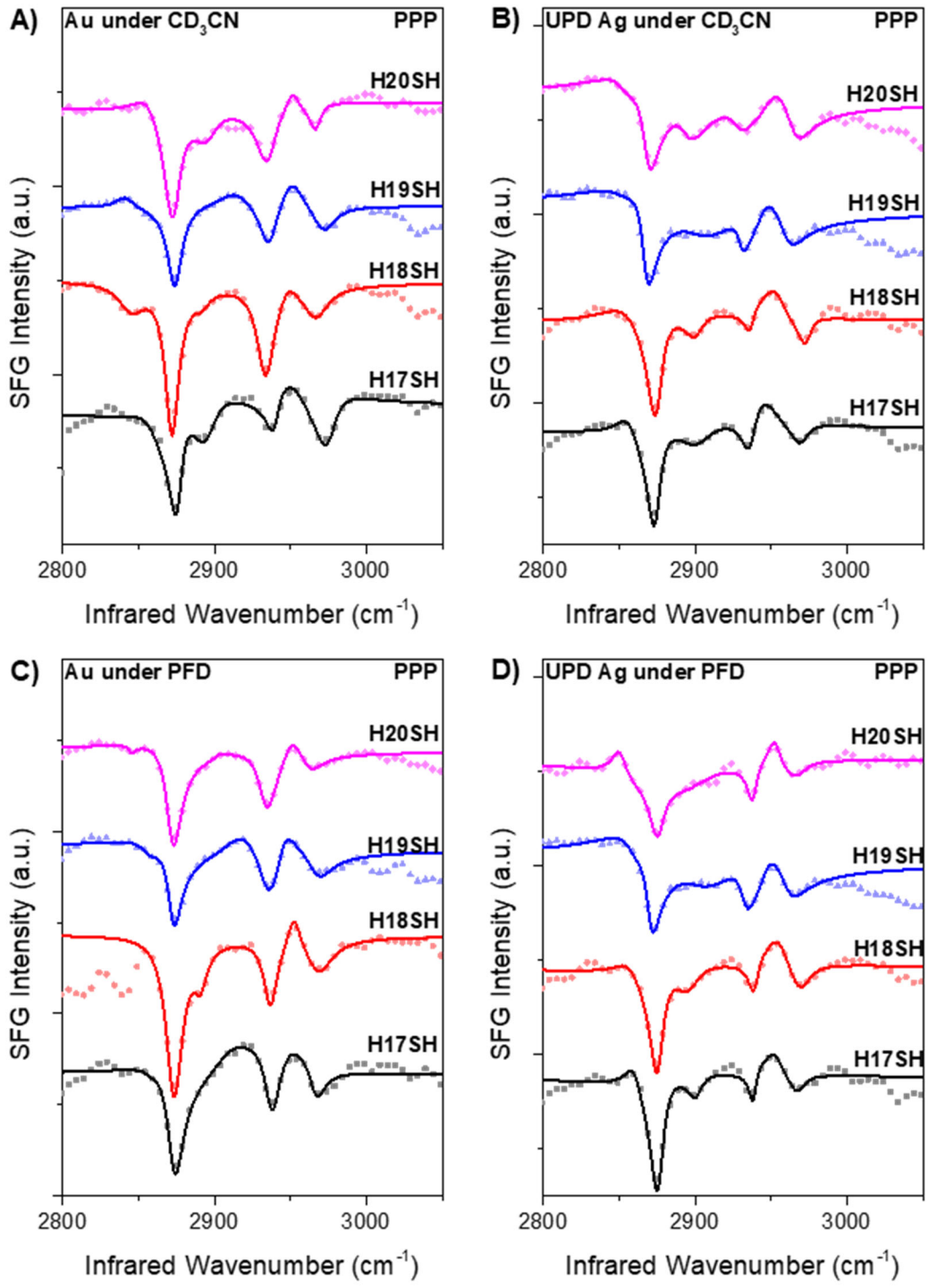


**Figure 5.28.** Solid-liquid SFG spectra in the ppp polarization combination for the **HnSH** SAMs formed on A/C) Au and B/D) UPD Ag in contact with A/B) $CD_3CN$ and C/D) PFD in the C–H stretching region. *The solid lines are the fits to the spectra, and the symbols represent the experimental data.*

**Table 5.9.** The Intensity Ratios and Methyl Group Tilt Angles Derived from the SFG Fitting Analysis for the **HnSH** and **H1F6HnSH** SAMs on Au and UPD Ag in Contact with $CD_3CN$.

| Adsorbate | Au | | UPD Ag | |
|---|---|---|---|---|
| | Ratio $I_{ss}/I_{as}$[a] | Tilt angle[b] | Ratio $I_{ss}/I_{as}$[a] | Tilt angle[b] |
| **H17SH** | 4.63 ± 2.77 | 24° | 23.81 ± 15.62 | 15° |
| **H18SH** | 30.25 ± 10.93 | 14° | 14.70 ± 5.68 | 17° |
| **H19SH** | 10.87 ± 3.18 | 19° | 6.77 ± 4.53 | 22° |
| **H20SH** | 19.55 ± 8.42 | 16° | 4.84 ± 2.77 | 24° |
| **H1F6H10SH** | 1.41 ± 1.16 | 26° | 0.33 ± 0.25 | 43° |
| **H1F6H11SH** | 1.42 ± 1.18 | 26° | 0.85 ± 0.71 | 31° |
| **H1F6H12SH** | 0.36 ± 0.32 | 48° | 0.55 ± 0.48 | 36° |
| **H1F6H13SH** | 0.46 ± 0.20 | 10° | 0.39 ± 0.15 | 40° |

[a]The ratio of peak intensities for the **HnSH** SAMs was multiplied by a factor of 1.24 to account for the Fermi resonance contribution to the symmetric stretch peak at 2875 $cm^{-1}$.[39-40]
[b]The error in the tilt angle is presented as a range of angles in Figure 5.29A.

Perfluorodecalin is a nonpolar liquid used in previous studies to determine the values for the dispersive component of the surface tension of a fluorinated surface, and eventually, the work of adhesion in order to describe the contribution of dispersive interactions to the surface energies that dictate the interfacial properties of fluorinated surfaces.[7,9] The SFG spectra for the SAMs in contact with PFD, plotted in Figure 5.28C and 5.28D, show similar disordering behavior, increase in the presence of gauche defects, to the $CD_3CN$/HSAM interfaces, which is revealed by the increase in methylene

contributions to the spectra. The antisymmetric methyl stretching peaks broadened, as in the case of the $CD_3CN$ interface, but the frequency of the resonances failed to shift, implying that although there may be some rotation of the methyl group to accommodate the bulky contacting liquid, the non-ideal dispersive interactions between fluorocarbons and hydrocarbons allow for more movement in the methyl group at this interface than at the $CH_3CN$ interface. The orientation analysis of the methyl groups under PFD, listed in Table 5.10 and displayed in Figure 5.29B, shows that the methyl groups are upright (tilted away from the surface normal) in comparison to their more slanted conformations at the solid-air interface. The SAMs on gold portray an "odd-even" effect in the tilt of the methyl groups comparable to the "odd-even" trends at the solid-air interface. However, as was the case for the $CD_3CN$/HSAM interface, the tilt angles for the methyl groups of SAMs on UPD Ag failed to showed changes, within the error of the fitting.

**Table 5.10.** Intensity Ratios and Tilt Angles Derived from the SFG Fitting Analysis for the **HnSH** and **H1F6HnSH** SAMs on Au in Contact with PFD.

| Adsorbate | Au | | UPD Ag | |
|---|---|---|---|---|
| | **Ratio $I_{ss}/I_{as}$**[a] | **Tilt angle**[b] | **Ratio $I_{ss}/I_{as}$**[a] | **Tilt angle**[b] |
| **H17SH** | 9.94 ± 5.52 | 20° | 34.97 ± 23.90 | 14° |
| **H18SH** | 27.19 ± 10.49 | 15° | 19.76 ± 15.01 | 16° |
| **H19SH** | 10.49 ± 3.67 | 19° | 6.50 ± 4.87 | 22° |
| **H20SH** | 27.85 ± 18.10 | 15° | 13.68 ± 12.30 | 18° |
| **H1F6H10SH** | 3.52 ± 2.34 | 20° | 2.07 ± 1.87 | 23° |
| **H1F6H11SH** | 3.67 ± 2.45 | 20° | 2.43 ± 1.56 | 23° |
| **H1F6H12SH** | 3.55 ± 2.35 | 20° | 0.68 ± 0.15 | 33° |
| **H1F6H13SH** | 0.51 ± 0.17 | 36° | 0.43 ± 0.28 | 39° |

[a]The ratio of peak intensities for the **HnSH** SAMs was multiplied by a factor of 1.24 to account for the Fermi resonance contribution to the symmetric stretch peak at 2875 $cm^{-1}$.[39-40]
[b]The error in the tilt angle is presented as a range of angles in Figure 5.29B.

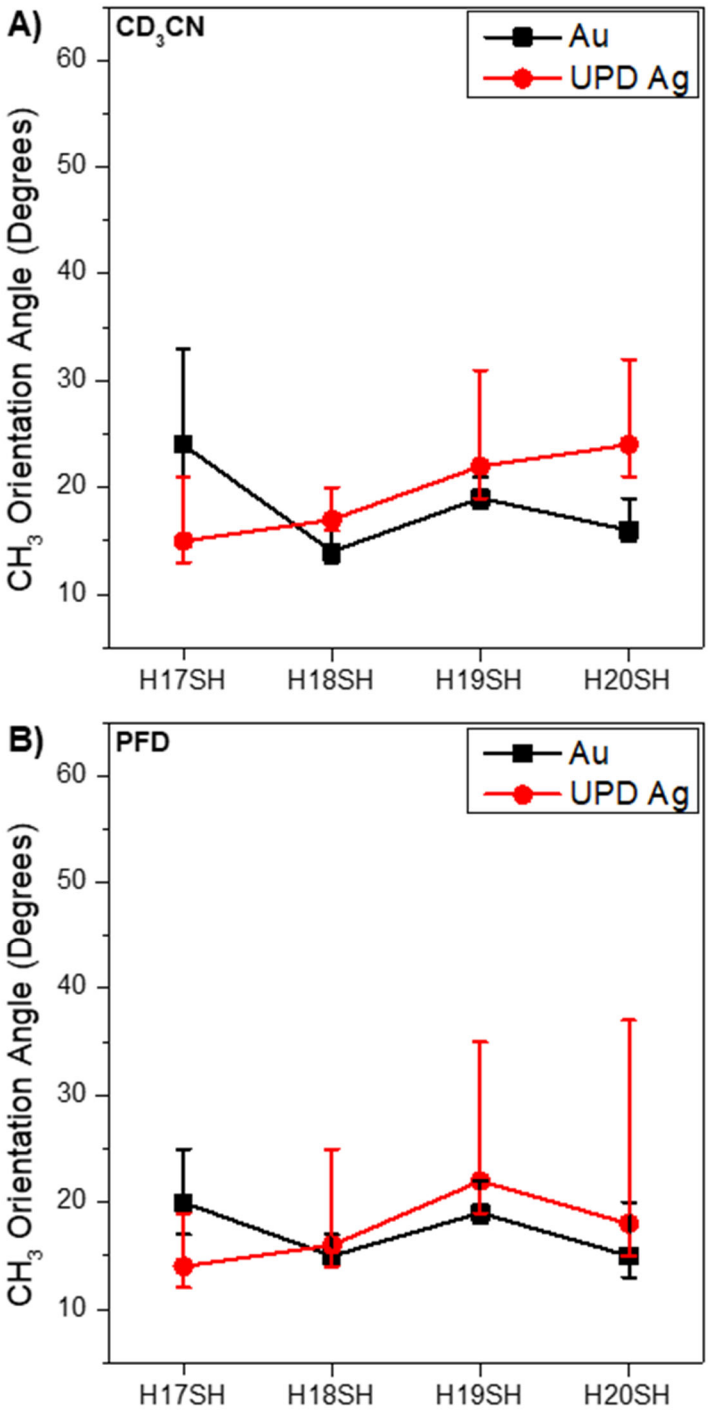


**Figure 5.29.** Methyl tilt angles determined from the SFG resonance intensity ratios for the **HnSH** SAMs on Au and UPD Ag in contact with A) acetonitrile and B) perfluorodecalin. *Asymmetric error bars denote the range of orientations derived from the error in the intensity ratios*.

### 5.3.4.2. The Solid-Liquid Interface of the F1HnSH SAMs

The C–H spectra of the FSAMs in contact with acetonitrile, depicted in Figures 5.30A and 5.30B, show a marked increase in the amplitude of the methylene stretches in comparison to the solid-air interface spectra in Figure 5.21. The overall increase in the intensities can be attributed to either an increase in the tilt of the terminal C–C bond -- which would cause the $CH_2$ symmetric stretch transition dipole to align with the z-axis leading to enhancement in the intensity -- an increase in gauche defects due to a reorientation of the polar terminal groups upon interacting with the polar liquid, or to an increase in the orientational order of the SAMs at the interface. To determine the reason, the C–F spectra for the FSAMs in contact with acetonitrile, shown by representative spectra of **F1H18SH** on UPD Ag at the solid-air and solid-liquid interface, are presented in Figure 5.31. The solid-liquid spectra display a ~25 $cm^{-1}$ red-shift of the $CF_3$ symmetric stretching peak from 1170 $cm^{-1}$ to 1145 $cm^{-1}$. As was the case with the $CD_3CN$/HSAM interface, the peak shifted to the frequency observed for the bulk molecules collected from IR and Raman spectroscopy.

Therefore, it is possible that the change in the environment of the fluoromethyl groups from air (where they are able to rotate freely) to a dense, bulk-like environment restricts the rotation of the $CF_3$ group due to the strong dipole-dipole interactions between the terminal groups of the FSAMs and the liquid molecules. To probe further, a second polar aprotic liquid with a slightly higher dipole moment to $CD_3CN$, deuterated dimethylsulfoxide ($d_6$-DMSO) was tested in the C–H and C–F regions, and representative spectra are shown in Figure 5.32. As with the $CD_3CN$, the interactions between the FSAMs and $d_6$-DMSO caused an increase in methylene intensity in the C–H stretching region and

a red-shift of 25 $cm^{-1}$ in the frequency of the $CF_3$ stretching mode. The overall intensities of the peaks did not change upon exposure to the liquid, implying that the terminal groups are not necessarily reorienting. Therefore, the increase in the intensity of the methylene modes can be attributed to an increase in the order (and therefore the number of oriented dipoles) in the system attributed to the restricted rotation of the $CF_3$ group interacting with the polar liquids. Table 5.11 lists the $CH_2$ amplitudes derived from the SFG spectra for the FSAMs in contact with $CD_3CN$. "Odd-even" effects in the amplitude of the methylene stretches were visible for the $CD_3CN$/FSAM interface spectra, however, no change in the trends with a change in substrate, UPD Ag, were observed.

In contrast to the observations from the polar liquid atop the **F1HnSH** interfaces, the C–H SFG spectra of the **F1HnSH** SAMs in contact with perfluorodecalin, shown in Figures 5.30C and 5.30D, show an almost complete disappearance of the methylene resonances. This points to a high degree of disorder in the SAM when in contact with PFD, possibly due to favorable interactions between the fluorinated SAM termini and the fluorinated liquid.[14] Attractive forces at the interface can cause partial solvation of the tail groups by PFD and allow for the functional groups to have greater degrees of motion, thereby decreasing the number of oriented groups that contribute to the SFG signal (increasing the distribution of molecular orientations as PFD molecules intercalate into the SAMs) and decreasing the mode intensities in the spectra. Disorder in the monolayer caused the vibrational bands to be within the noise level of the spectra so that satisfactory fits could not be obtained for the **F1HnSH** SAMs in contact with PFD. Unfortunately, due to the overlap in the stretching frequencies for PFD and the **F1HnSH** SAMs, the solid-liquid SFG spectra in the C–F stretching region could not be tested.

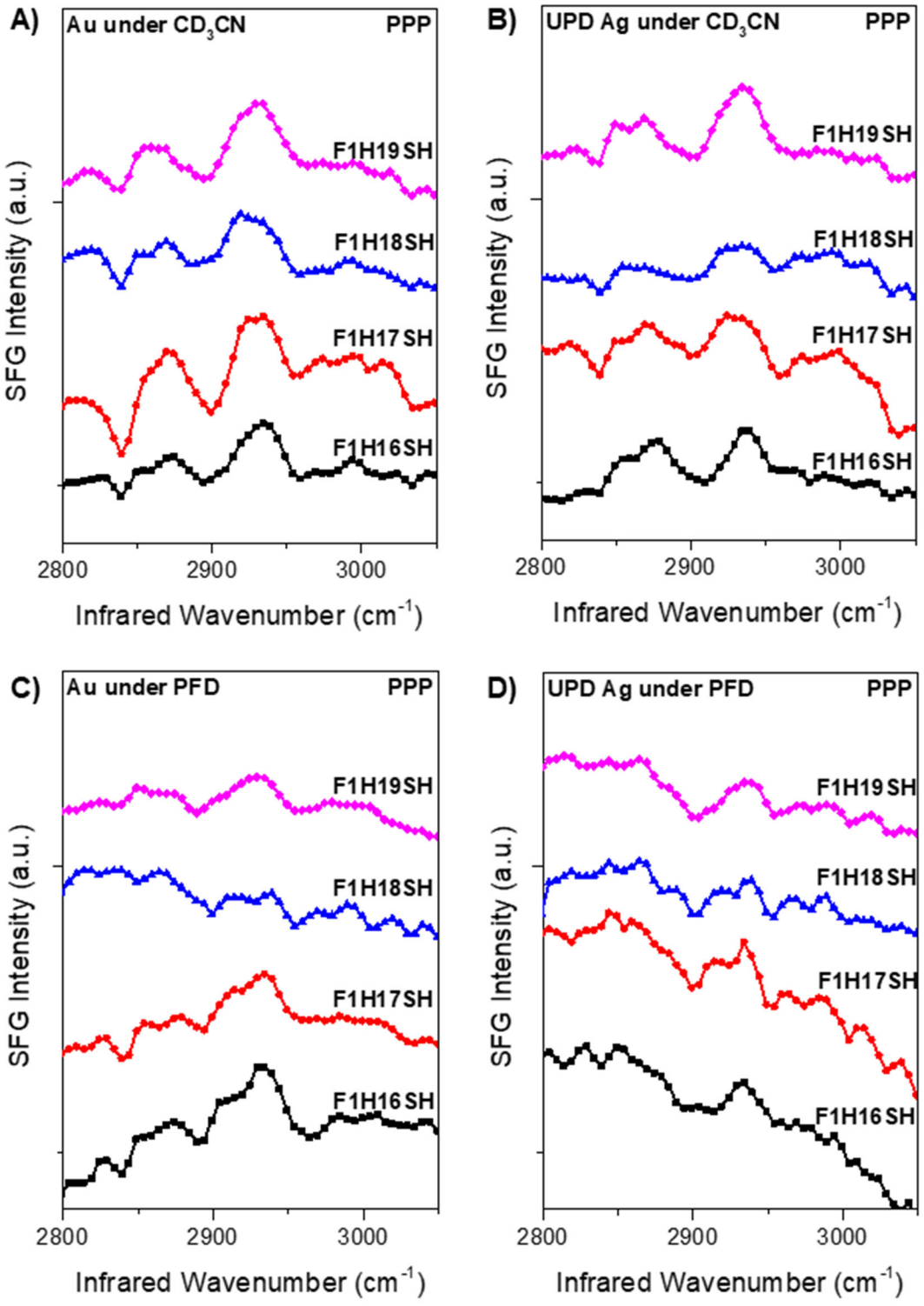


**Figure 5.30.** Solid-liquid SFG spectra in the ppp polarization combination for the **F1HnSH** SAMs formed on A/C) Au and B/D) UPD Ag in contact with A/B) $CD_3CN$ and C/D) PFD in the C–H stretching region.

**Table 5.11.** Fitting Parameters for the $CH_2$ stretching mode at 2843 $cm^{-1}$ in the SFG Spectra for the $CF_3$-terminated SAMs on Au in Contact with $CD_3CN$.

| Adsorbate | Au | | | UPD Ag | | |
|---|---|---|---|---|---|---|
| | $A_{ppp}$ | $\Gamma_{ppp}$ | Ippp | $A_{ppp}$ | $\Gamma_{ppp}$ | Ippp |
| **F1H16SH** | -0.04 ± 0.01 | 3.30 ± 0.39 | 1.5E-4 ± 4.6E-5 | -0.04 ± 0.01 | 4.77 ± 1.24 | 7.0E-5 ± 5.0E-5 |
| **F1H17SH** | -0.27 ± 0.01 | 7.49 ± 0.34 | 1.3E-3 ± 1.5E-4 | -0.07 ± 0.01 | 4.37 ± 0.39 | 2.6E-4 ± 6.3E-5 |
| **F1H18SH** | -0.09 ± 0.01 | 4.93 ± 0.41 | 3.3E-4 ± 7.5E-5 | -0.05 ± 0.01 | 5.05 ± 0.50 | 9.8E-5 ± 2.7E-5 |
| **F1H19SH** | -0.11± 0.01 | 6.62 ± 0.66 | 2.7E-4 ± 7.3E-5 | -0.06 ± 0.01 | 3.61 ± 0.35 | 2.8E-4 ± 7.2E-5 |

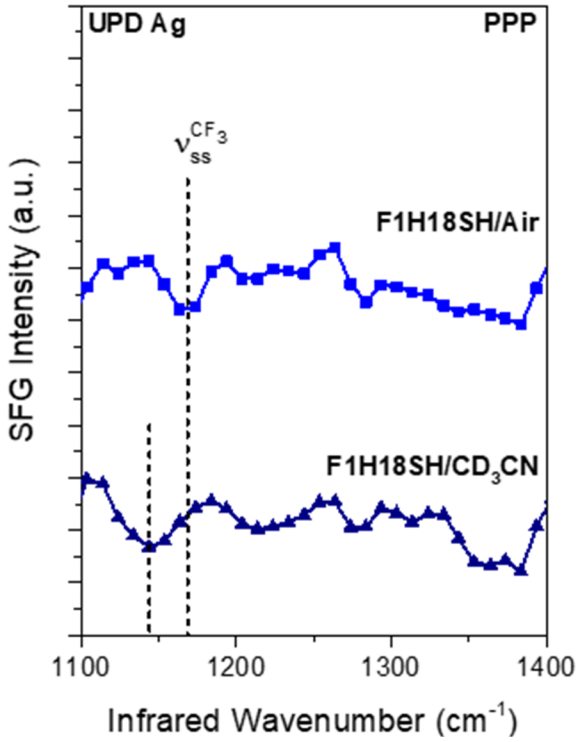


**Figure 5.31.** Solid-liquid SFG spectra in the ppp polarization combination for the **F1H18SH** SAM on UPD Ag in contact with $CD_3CN$ in the C–F stretching region.

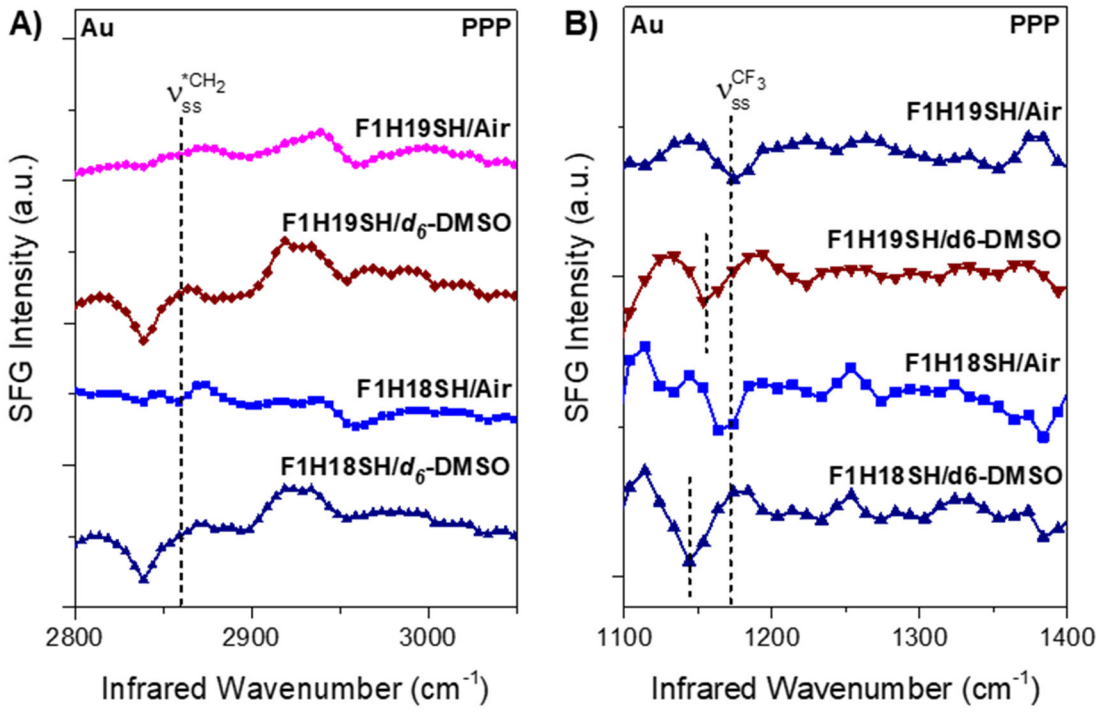


**Figure 5.32.** Solid-liquid SFG spectra in the ppp polarization combination for the **F1HnSH** SAMs on Au in contact with $d_6$-DMSO in the A) C–H and B) C–F stretching region.

### 5.3.4.3. The Solid-Liquid Interface of H1F6HnSH SAMs

Figures 5.33A and 5.33B show the SFG spectra for the solid-liquid interface between acetonitrile and the SAMs generated from the **H1F6HnSH** series. A comparison of these spectra to the solid-air interface spectra in Figure 5.22 shows a significant decrease in the amplitude of the *$CH_3$ symmetric stretching resonance and a decrease in the overall signal-to-noise ratio. As with the PFD/**F1HnSH** SAM interface, this indicates a strong interaction between the acetonitrile molecules and the **H1F6HnSH** SAMs, likely causing a reorientation of the terminal functional groups. The intensity ratios and average orientation angles derived from the SFG spectra of the $CD_3CN$/**H1F6HnSH** interfaces are given in Table 5.9. and the tilt angles are plotted in Figure 5.34A. The SFG results indicate

that the *$CH_3$ tilts to a more slanted configuration under $CD_3CN$ than at the solid-air interface, providing an explanation for the decrease in the SFG intensity. XPS analysis of these SAMs showed that the packing density at the surface near the $CH_3$–$CF_2$ dipole is lower in comparison to the fully hydrocarbon and $CF_3$-terminated monolayers.[34] Consequently, the acetonitrile molecules will easily permeate into the monolayer and increase the fluidity of the terminal groups.

The interaction between the **H1F6HnSH** SAMs and the PFD broadened the band corresponding to the *$CH_3$ symmetric stretching resonance in Figures 5.33C and 5.33D, but did not decrease its overall intensity. Figure 5.34B (constructed from the results listed in Table 5.10) shows that the average orientation angles for the **H1F6HnSH** SAMs in contact with PFD did not change compared to the *$CH_3$ tilt angles at the solid-air interface (shown in Figure 5.26). These results indicate that the interaction between bulky PFD and the inverted dipole interfaces is one of little intercalation of the liquid into the monolayer, although some rotation of the terminal group occurs (evidenced by the broadening of the peak), plausibly allows for additional exposure of the $CF_2$ at the interface with the fluorinated liquid.

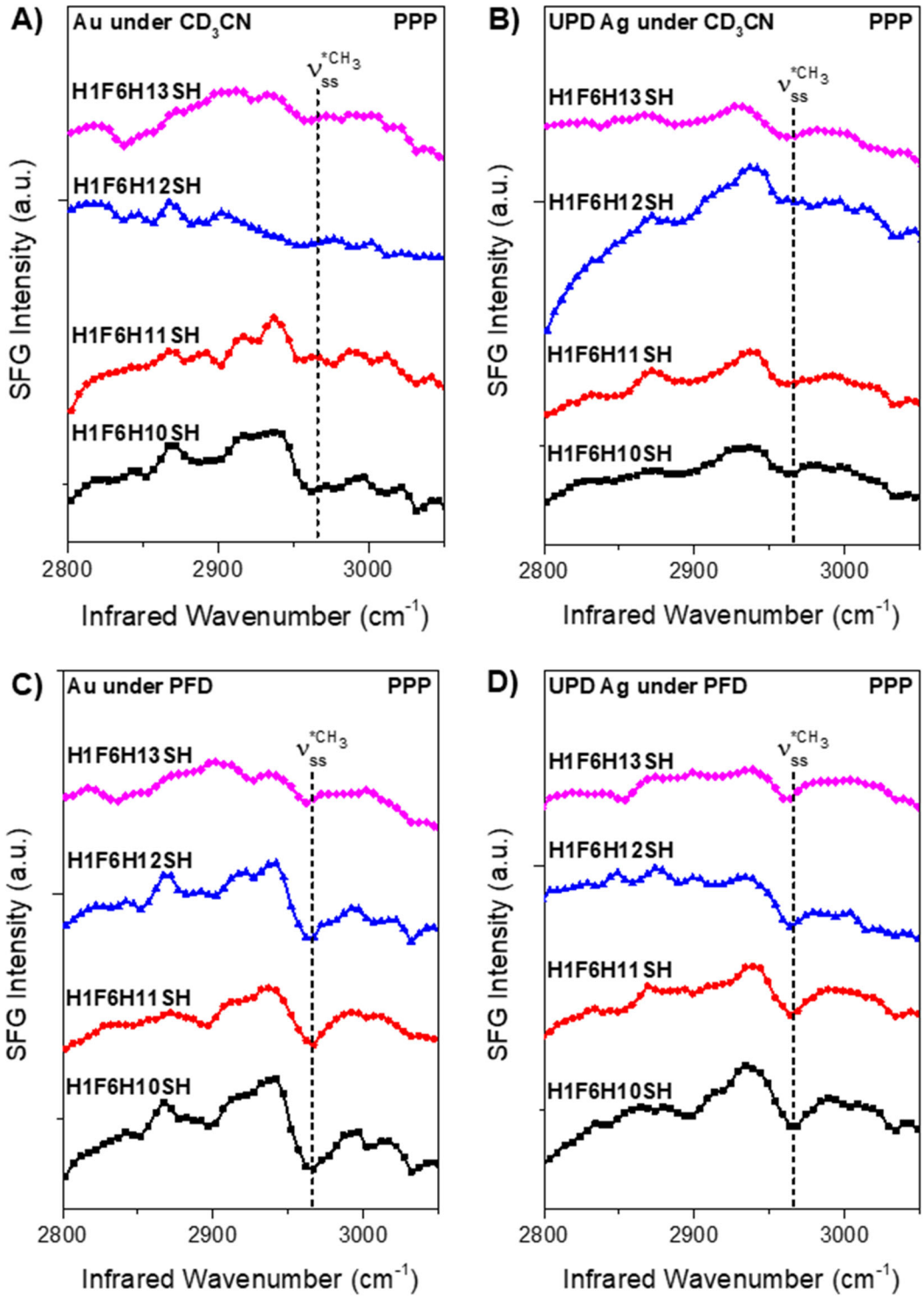


**Figure 5.33.** Solid-liquid SFG spectra in the ppp polarization combination for the **H1F6HnSH** SAMs formed on A/C) Au and B/D) UPD Ag in contact with A/B) $CD_3CN$ and C/D) PFD in the C–H stretching region.

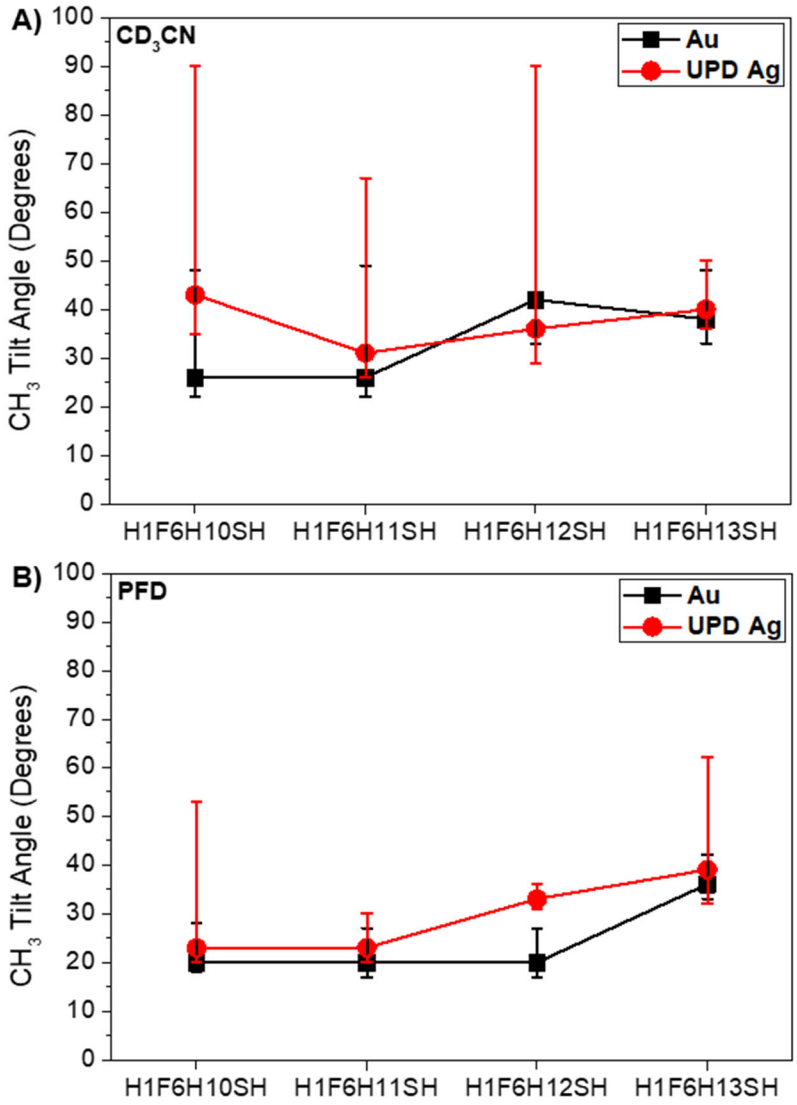


**Figure 5.34.** Methyl tilt angles determined from the SFG resonance intensity ratios for the **H1F6HnSH** SAMs on Au and UPD Ag in contact with A) acetonitrile and B) perfluorodecalin. *Asymmetric error bars denote the range of orientations derived from the error in the intensity ratios*.

### 5.3.5. Comparison of Orientation and Wettability Trends

The SFG orientation analysis and amplitude ratios can be compared to previously collected wettability data to determine if there is a correlation between the SFG results and the advancing contact angles observed for acetonitrile and perfluorodecalin on each of the

sets of SAMs. The advancing contact angles reported before[34] are plotted in comparison to the tilt angles, determined by analysis of the SFG data, in Figures 5.35–5.39.

The comparisons plotted in Figures 5.35 and 5.36 for the **HnSH** SAMs on Au show a clear correlation between the SFG determined microscopic orientation angles and the macroscopic advancing contact angles for the wetting liquids on the surfaces. The data in Figures 5.35A and 5.36A show that as the tilt angle of the terminal methyl group increases (the terminal C–C bond aligns away from the surface normal and closer to the substrate) the contact angle decreases, indicating an increase in the wettability of the film. This is due to the increased exposure of the $CH_2$ group adjacent to the terminal $CH_3$ at the interface with the liquid, allowing for more favorable dispersive interactions between the liquids and the monolayer. This result is in accordance with previous reports that have shown that the structure of self-assembled monolayer has a marked effect on the wettability of the resulting film.[5,14,75] For the **HnSH** SAMs on UPD Ag, however, this conclusion does not hold true. The orientations of the terminal methyl groups in Figures 5.35B and 5.36B fail to show "odd-even" effects, yet the advancing contact angles do. This discrepancy could be due to the nuances between microscopic structure and macroscopic wetting behavior. The solid-liquid interactions at the interface are only one parameter that can affect the contact angle of a liquid on a SAM -- the surface energy of the solid-air interface and the liquid-liquid interactions that make up the surface tension at the liquid-air interface must be considered in order to form a complete representation of the factors that affect the wettability of a surface.[97]

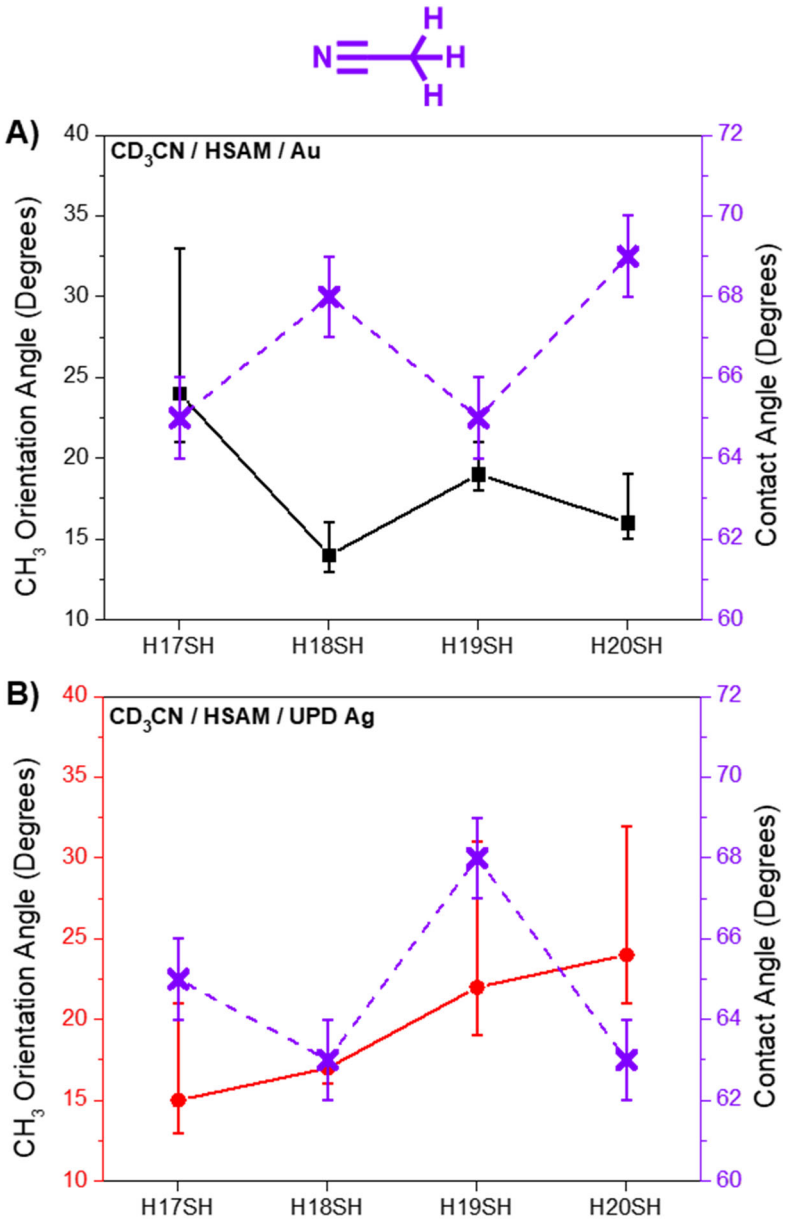


**Figure 5.35.** Comparison between the methyl tilt angles of the **HnSH** SAMs on A) Au and B) UPD Ag in contact with acetonitrile and the corresponding advancing contact angles (purple x symbols). *The dashed lines between the contact angle data are guides to the eye. The asymmetric error bars for the tilt angles denote the range of orientations derived from the error in the intensity ratios. The structure of acetonitrile is shown above the plots for reference.*

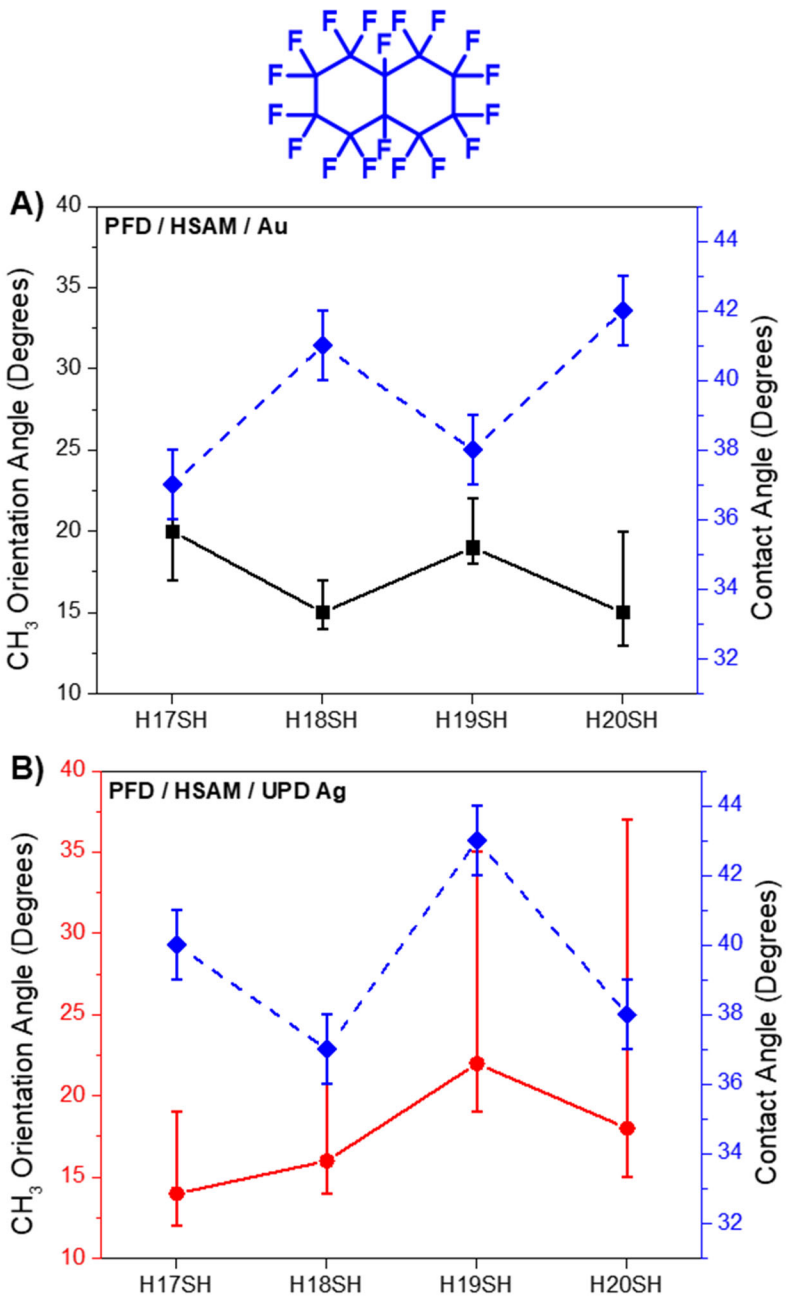


**Figure 5.36.** Comparison between the methyl tilt angles of the **HnSH** SAMs on A) Au and B) UPD Ag in contact with perfluorodecalin and the corresponding advancing contact angles (blue diamonds). *The dashed lines between the contact angle data are guides to the eye. The asymmetric error bars for the tilt angles denote the range of orientations derived from the error in the intensity ratios. The structure of perfluorodecalin is shown above the plots for reference.*

Figure 5.37 shows the amplitudes of the $CH_2$ symmetric stretching vibration of the **F1HnSH** SAMs in comparison to the macroscopic contact angles of acetonitrile. This comparison gives insight into the effect of the exposure of the methylene group at the interface to the contact angle. The amplitudes for both the SAMs on Au and UPD Ag surfaces follow the same trend, although there is a reversal in the "odd-even" effect seen in the wettability, implying that regardless of the degree of methylene exposure at the surface, the wettability will change for the **F1HnSH** SAMs with an overall change in chain length. This indicates that the wetting behavior of the $CF_3$-terninated films is directly related to the strength of the dipole at the interface and not just a change in orientation of the terminal group. Zenasni and coworkers noted that for the odd SAMs (**F1H16SH** and **F1H18SH**), the $CF_3$ group is tilted away from the surface normal, making an array of head-to-tail arranged dipoles at the interface that can compensate each other, leading to a weaker interaction.[14] The even SAMs (**F1H17SH** and **F1H19SH**) will have $CF_3$ groups upright (slight tilt), which will form a surface of oriented dipoles, leading to a stronger interaction. The SFG results indicate that the strength of these dipoles plays an important role in the final wettability of the films.

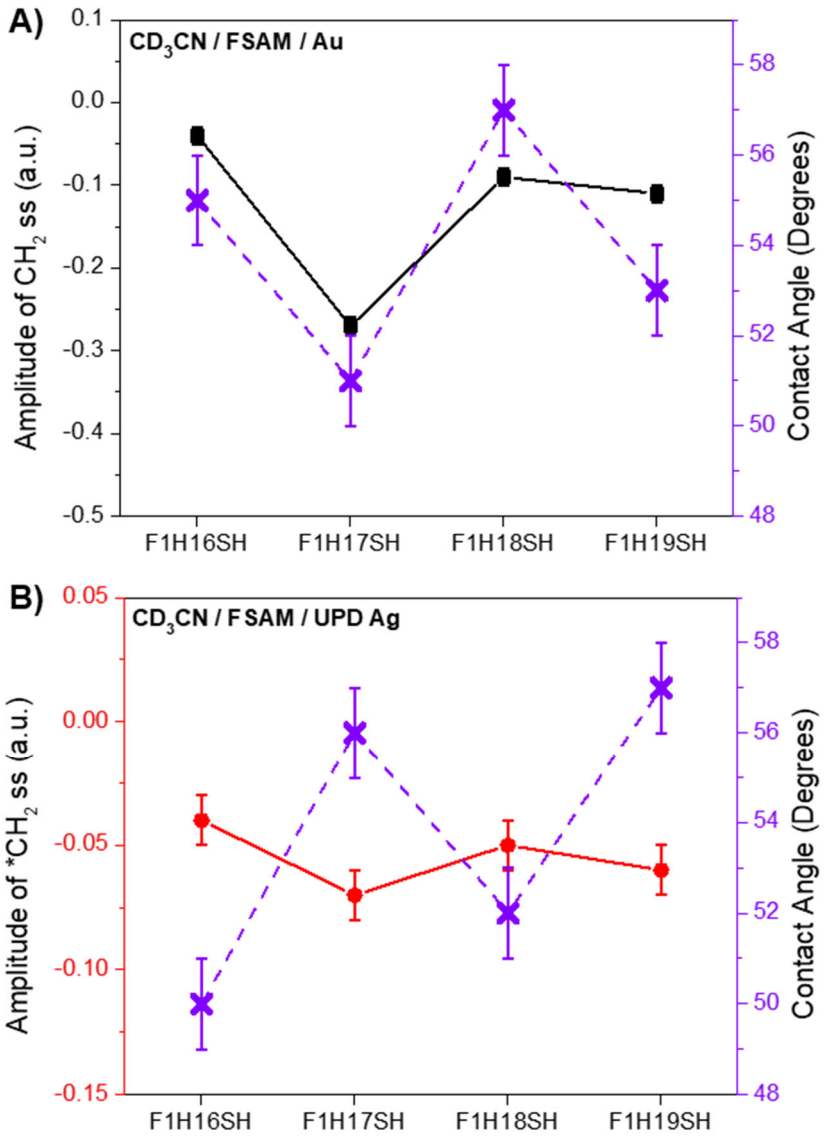


**Figure 5.37.** Comparison between the methylene peak amplitudes for the **F1HnSH** SAMs on A) Au and B) UPD Ag in contact with acetonitrile and the corresponding advancing contact angles (purple x symbols). *The dashed lines between the contact angle data are guides to the eye. Error bars that are not visible fall within the symbol.*

Figures 5.38 and 5.39 show comparisons between the *$CH_3$ tilt angles with respect to the surface normal and the advancing contact angles for acetonitrile and perfluorodecalin, respectively. The results from the SFG spectra found that there is no "odd-even" effect in the tilt angle of the *$CH_3$ for the SAMs formed on either the Au or

UPD Ag surfaces, in contact with the acetonitrile, as shown in Figure 5.38. The wettability data follow suit for the Au surface, showing no relationship between total chain length and the contact angle. This was attributed to disorder in the chains because of low packing densities and the use of a potentially electrochemically-roughened Au substrate.[34] However, the SAMs formed on UPD Ag, which, due to the more upright tilt of the alkane chain with respect to the surface, showed increased packing densities than the corresponding SAMs formed on Au, also showed a clear "odd-even" effect in the wettability, as shown in Figure 5.38B. This indicates that the packing density of the SAMs played a large role in determining the wetting behavior of these films, although the orientation of the terminal *$CH_3$ group did not.

Similar to the acetonitrile interfaces, comparison between the *$CH_3$ group tilt angle and the wettability with perfluorodecalin failed to show a correlation for the **H1F6HnSH** SAMs on Au, as shown by Figure 5.39A. Figure 5.39B shows that the SAMs on UPD Ag, however, did demonstrate an "odd-even" effect in the wettability, with the lower tilt angle for the *$CH_3$ group in the **H1F6H11SH** SAM (more upright) corresponding to a higher contact angle (less wettable surface) and the higher tilt angle (more slanted) configuration of the **H1F6H12SH** SAM corresponding to a lower contact angle (more wettable surface). This was in accordance with the results from the interfaces of the liquids and the HSAMs, however, since only two out of the four molecules in the set could be related to the wettabilities, the relationship cannot be generalized for the films generated from the $CH_3$-terminated alkanethiols.

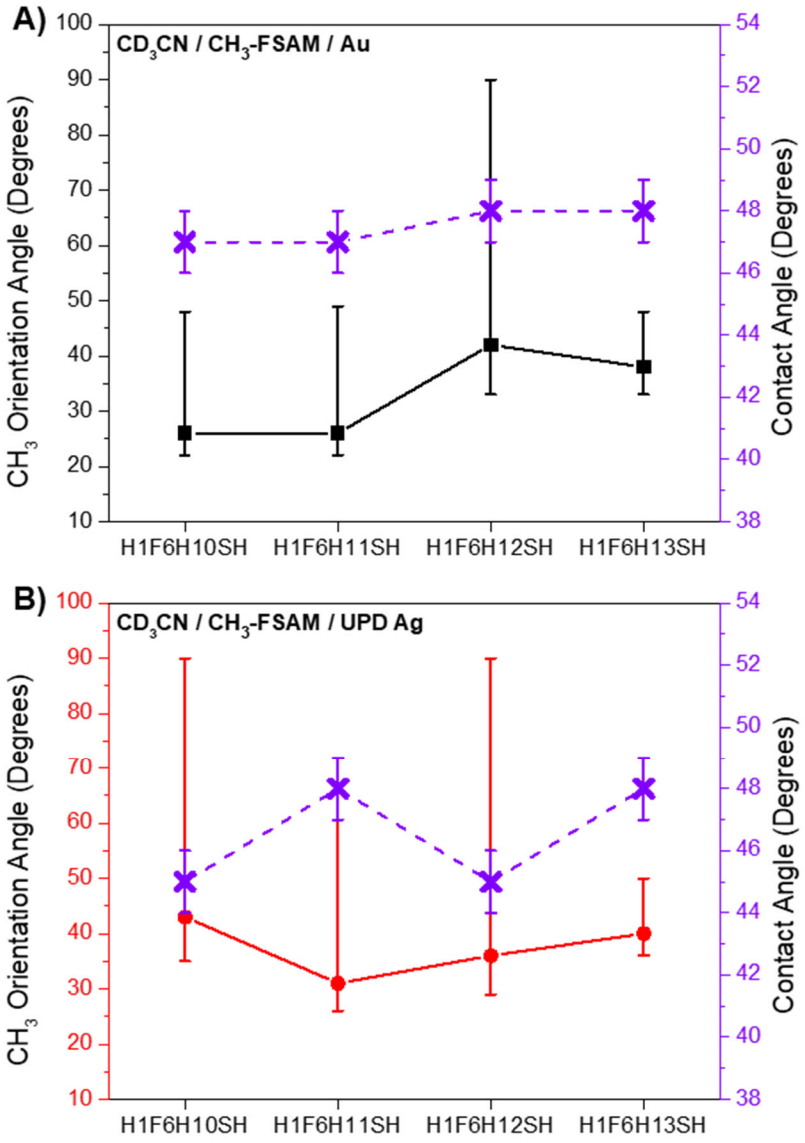


**Figure 5.38.** Comparison between the methyl tilt angles of the **H1F6HnSH** SAMs on A) Au and B) UPD Ag in contact with acetonitrile and the corresponding advancing contact angles (purple x symbols). *The dashed lines between the contact angle data are guides to the eye. Asymmetric error bars for the tilt angles denote the range of orientations derived from the error in the intensity ratios.*

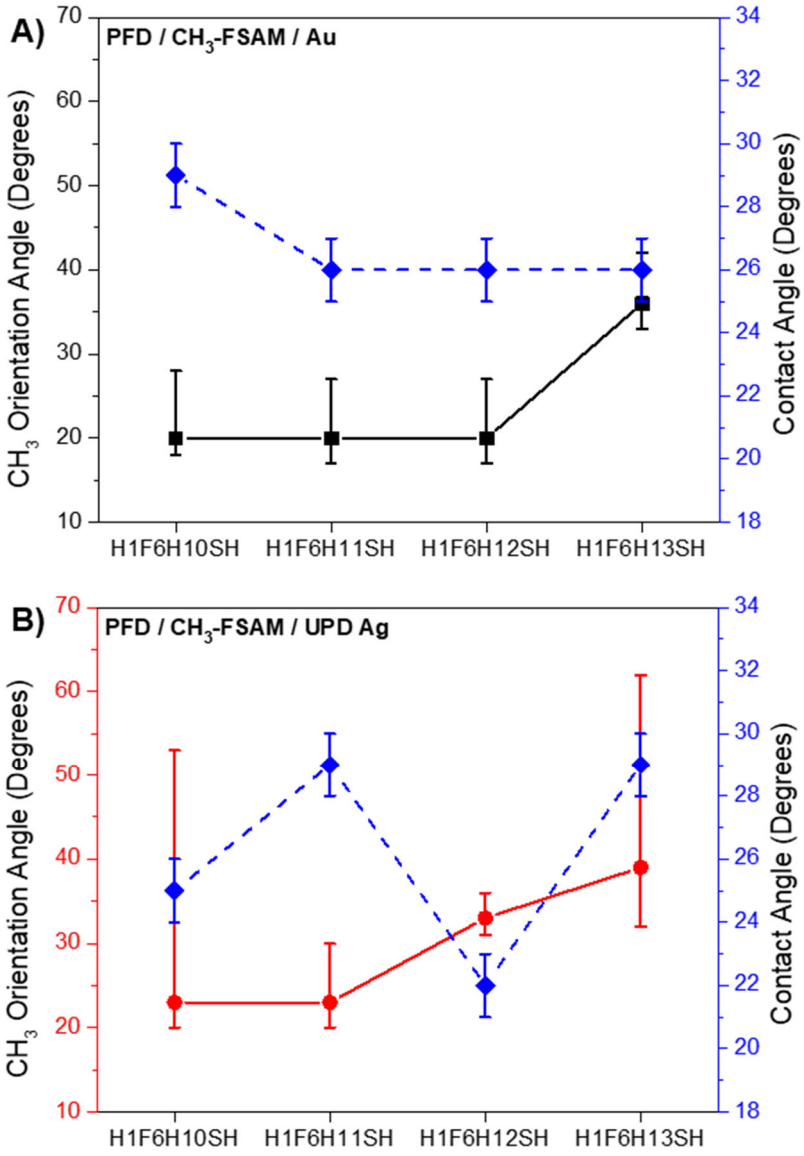


**Figure 5.39.** Comparison between the methyl tilt angles of the **H1F6HnSH** SAMs on A) Au and B) UPD Ag in contact with perfluordecalin and the corresponding advancing contact angles (blue diamonds). *The dashed lines between the contact angle data are guides to the eye. Asymmetric error bars for the tilt angles denote the range of orientations derived from the error in the intensity ratios.*

## 5.4. Conclusions

Interactions at the nanoscale solid-liquid interface can have a large impact on the macroscopic wetting properties of thin films. As one of a limited number of techniques

which can probe such interfaces, we have employed sum frequency generation (SFG) spectroscopy to study the interactions between contacting liquids and model fluorinated surfaces generated using alkanethiol monolayer self-assembled onto gold. The polar and nonpolar liquids used in this study were used to investigate how the terminal functional groups of a SAM reorient when exposed to different environments. Since sum frequency generation signal is only allowed from noncentrosymmetric media, this spectroscopic technique supplied the vibrational spectra at the solid-liquid interface between acetonitrile or perfluorodecalin and self-assembled monolayers formed from the adsorbates **HnSH** (n = 17–20), **F1HnSH** (n = 16–19), and **H1F6HnSH** (n = 11–13) onto Au and underpotentially-deposited Ag substrates. The substrates were characterized using stripping voltammetry and XPS to determine that a full monolayer of silver was formed on the gold substrates. Elemental sample composition collected by XPS as well as surface-sensitive vibrational spectroscopy (PM-IRRAS and SFG) confirmed that the SAMs formed densely-packed, well-ordered, trans-extended chains on the gold and UPD Ag surfaces.

This study showed that there was an "odd-even" effect in the orientations of the terminal groups on gold surfaces and an opposite trend when the SAMs were formed on a underpotentially-deposited monolayer of silver onto gold. Namely, on the Au surfaces the $CH_3$ groups were tilted toward the surface for the odd-chain length SAMs, and were more upright for the even-chain length SAMs. On the UPD Ag surfaces the trend in tilt angles of the $CH_3$ groups were opposite that of Au -- the $CH_3$ groups were more upright for the odd-numbered chain length SAMs and more tilted for the even-numbered chain length SAMs.

The solid-liquid interface of the SAMs and acetonitrile as well as perfluorodecalin were probed with SFG spectroscopy to determine the effect of the contacting liquids on the structure of the SAM terminal group. The tilt angle of the terminal methyl group in the **HnSH** SAMs was shown to become more upright when in contact with both liquids, attributed to the intercalation of the contacting liquids into the SAMs and the subsequent reorientation of the terminal group. The $CF_3$ group of the **F1HnSH** SAMs was shown to interact strongly with both liquids, with an increased disorder at the terminus of the monolayer. Furthermore, the aforementioned SAM exhibited a red-shift in the frequency of the $CF_3$ symmetric stretch when in contact with polar liquids, due to dipole-dipole interactions.

The tilt angles of the terminal $CH_3$ groups in the monolayers generated from the **H1F6HnSH** adsorbates were shown to align toward the surface, opposite to the behavior of the **HnSH** SAMs when in contact with acetonitrile. This was due to a strong dipole-dipole interaction between the polar contacting liquids and the partially fluorinated self-assembled monolayers causing the liquid to penetrate into the film and solvate the terminal methyl groups.[14] Although the advancing contact angles of the **HnSH** SAMs on Au and UPD Ag were shown to have an "odd-even" effect dependent on the chain length of the alkanethiol adsorbate, the SFG results showed no differences in the tilt angles of the methyl groups of the SAMs on the UPD Ag substrate. The solid-liquid spectra for the **F1HnSH** and **H1F6HnSH** monolayers also showed no difference in tilt angles between odd and even chains on Au or UPD Ag. Therefore, factors other than the structure of the monolayer contribute to the final wettability of the films. However, the microscopic terminal group

orientation results from the SFG analysis can provide useful information necessary to guide the interpretation of the macroscopic contact angles.

The solid-liquid SFG spectra provided herein show the interactions between contacting liquids and functionalized surfaces at the buried solid-liquid interface and are a useful stepping stone for future work at this interface. It may be possible to use studies, such as the one detailed here, to infer the wettability behavior of surfaces with different contacting liquids.

## 5.5. References


1. Bain, C. D.; Troughton, E. B.; Tao, Y. T.; Evall, J.; Whitesides, G. M.; Nuzzo, R. G., Formation of Monolayer Films by the Spontaneous Assembly of Organic Thiols from Solution onto Gold. *J. Am. Chem. Soc.* **1989,** *111*, 321–335.
2. Sellers, H.; Ulman, A.; Shnidman, Y.; Eilers, J. E., Structure and Binding of Alkanethiolates on Gold and Silver Surfaces: Implications for Self-Assembled Monolayers. *J. Am. Chem. Soc.* **1993,** *115*, 9389–9401.
3. Porter, M. D.; Bright, T. B.; Allara, D. L.; Chidsey, C. E. D., Spontaneously Organized Molecular Assemblies. 4. Structural Characterization of *n*-Alkyl Thiol Monolayers on Gold by Optical Ellipsometry, Infrared Spectroscopy, and Electrochemistry. *J. Am. Chem. Soc.* **1987,** *109*, 3559–3568.
4. Ulman, A.; Eilers, J. E.; Tillman, N., Packing and Molecular Orientation of Alkanethiol Monolayers on Gold Surfaces. *Langmuir* **1989,** *5*, 1147–1152.

5. Chang, S.-C.; Chao, I.; Tao, Y.-T., Structure of Self-Assembled Monolayers of Aromatic-Derivatized Thiols on Evaporated Gold and Silver Surfaces: Implication on Packing Mechanism. *J. Am. Chem. Soc.* **1994,** *116*, 6792–6805.

6. Tao, F.; Bernasek, S. L., Understanding Odd−Even Effects in Organic Self-Assembled Monolayers. *Chem. Rev.* **2007,** *107*, 1408–1453.

7. Graupe, M.; Takenaga, M.; Koini, T.; Colorado, R., Jr.; Lee, T. R., Oriented Surface Dipoles Strongly Influence Interfacial Wettabilities. *J. Am. Chem. Soc.* **1999,** *121*, 3222–3223.

8. Fukushima, H.; Seki, S.; Nishikawa, T.; Takiguchi, H.; Tamada, K.; Abe, K.; Colorado, R., Jr.; Graupe, M.; Shmakova, O. E.; Lee, T. R., Microstructure, Wettability, and Thermal Stability of Semifluorinated Self-Assembled Monolayers (SAMs) on Gold. *J. Phys. Chem. B* **2000,** *104*, 7417–7423.

9. Colorado, R., Jr.; Lee, T. R., Wettabilities of Self-Assembled Monolayers on Gold Generated from Progressively Fluorinated Alkanethiols. *Langmuir* **2003,** *19*, 3288–3296.

10. Weinstein, R. D.; Moriarty, J.; Cushnie, E.; Colorado, R., Jr.; Lee, T. R.; Patel, M.; Alesi, W. R.; Jennings, G. K., Structure, Wettability, and Electrochemical Barrier Properties of Self-Assembled Monolayers Prepared from Partially Fluorinated Hexadecanethiols. *J. Phys. Chem. B* **2003,** *107*, 11626–11632.

11. Colorado Jr, R.; Lee, T. R., Physical Organic Probes of Interfacial Wettability Reveal the Importance of Surface Dipole Effects. *J. Phys. Org. Chem.* **2000,** *13*, 796–807.

12. Yuan, Y.; Yam, C. M.; Shmakova, O. E.; Colorado, R., Jr.; Graupe, M.; Fukushima, H.; Moore, H. J.; Lee, T. R., Solution-Phase Desorption of Self-Assembled Monolayers on Gold Derived From Terminally Perfluorinated Alkanethiols. *J. Phys. Chem. C* **2011,** *115*, 19749–19760.

13. Miura, Y. F.; Takenaga, M.; Koini, T.; Graupe, M.; Garg, N.; Graham, R. L.; Lee, T. R., Wettabilities of Self-Assembled Monolayers Generated from $CF_3$-Terminated Alkanethiols on Gold. *Langmuir* **1998,** *14*, 5821–5825.

14. Zenasni, O.; Marquez, M. D.; Jamison, A. C.; Lee, H. J.; Czader, A.; Lee, T. R., Inverted Surface Dipoles in Fluorinated Self-Assembled Monolayers. *Chem. Mater.* **2015,** *27*, 7433–7446.

15. Kim, H. I.; Graupe, M.; Oloba, O.; Koini, T.; Imaduddin, S.; Lee, T. R.; Perry, S. S., Molecularly Specific Studies of the Frictional Properties of Monolayer Films: A Systematic Comparison of $CF_3$-, $(CH_3)_2CH$-, and $CH_3$-Terminated Films. *Langmuir* **1999,** *15*, 3179–3185.

16. Laibinis, P. E.; Whitesides, G. M.; Allara, D. L.; Tao, Y. T.; Parikh, A. N.; Nuzzo, R. G., Comparison of the Structures and Wetting Properties of Self-Assembled Monolayers of *n*-Alkanethiols on the Coinage Metal Surfaces, Copper, Silver, and Gold. *J. Am. Chem. Soc.* **1991,** *113*, 7152–7167.

17. Walczak, M. M.; Chung, C.; Stole, S. M.; Widrig, C. A.; Porter, M. D., Structure and Interfacial Properties of Spontaneously Adsorbed n-Alkanethiolate Monolayers on Evaporated Silver Surfaces. *J. Am. Chem. Soc.* **1991,** *113*, 2370–2378.

18. Hines, M. A.; Todd, J. A.; Guyot-Sionnest, P., Conformation of Alkanethiols on Au, Ag(111), and Pt(111) Electrodes: A Vibrational Spectroscopy Study. *Langmuir* **1995,** *11*, 493–497.

19. Laibinis, P. E.; Bain, C. D.; Nuzzo, R. G.; Whitesides, G. M., Structure and Wetting Properties of ω-Alkoxy-*n*-Alkanethiolate Monolayers on Gold and Silver. *J. Phys. Chem.* **1995,** *99*, 7663–7676.

20. Zharnikov, M.; Frey, S.; Rong, H.; Yang, Y. J.; Heister, K.; Buck, M.; Grunze, M., The Effect of Sulfur–Metal Bonding on the Structure of Self-Assembled Monolayers. *Phys. Chem. Chem. Phys.* **2000,** *2*, 3359–3362.

21. Love, J. C.; Estroff, L. A.; Kriebel, J. K.; Nuzzo, R. G.; Whitesides, G. M., Self-Assembled Monolayers of Thiolates on Metals as a Form of Nanotechnology. *Chem. Rev.* **2005,** *105*, 1103–1170.

22. Woodruff, D., The Role of Reconstruction in Self-Assembly of Alkylthiolate Monolayers on Coinage Metal Surfaces. *Appl. Surf. Sci.* **2007,** *254*, 76–81.

23. Sheen, C. W.; Shi, J. X.; Maartensson, J.; Parikh, A. N.; Allara, D. L., A New Class of Organized Self-Assembled Monolayers: Alkane Thiols on Gallium Arsenide (100). *J. Am. Chem. Soc.* **1992,** *114*, 1514–1515.

24. Allara, D. L.; Nuzzo, R. G., Spontaneously Organized Molecular Assemblies. 1. Formation, Dynamics, and Physical Properties of n-Alkanoic Acids Adsorbed from Solution on an Oxidized Aluminum Surface. *Langmuir* **1985,** *1*, 45–52.

25. Lin, S.-Y.; Tsai, T.-K.; Lin, C.-M.; Chen, C.-h.; Chan, Y.-C.; Chen, H.-W., Structures of Self-Assembled Monolayers of *n*-Alkanoic Acids on Gold Surfaces

Modified by Underpotential Deposition of Silver and Copper: Odd−Even Effect. *Langmuir* **2002,** *18*, 5473–5478.

26. Laibinis, P. E.; Fox, M. A.; Folkers, J. P.; Whitesides, G. M., Comparisons of Self-Assembled Monolayers on Silver and Gold: Mixed Monolayers Derived from $HS(CH_2)_{21}X$ and $HS(CH_2)_{10}Y$ (X, Y = $CH_3$, $CH_2OH$) have Similar Properties. *Langmuir* **1991,** *7*, 3167–3173.

27. Tao, Y. T., Structural Comparison of Self-Assembled Monolayers of n-Alkanoic Acids on the Surfaces of Silver, Copper, and Aluminum. *J. Am. Chem. Soc.* **1993,** *115*, 4350–4358.

28. Jennings, G. K.; Laibinis, P. E., Underpotentially Deposited Metal Layers of Silver Provide Enhanced Stability to Self-Assembled Alkanethiol Monolayers on Gold. *Langmuir* **1996,** *12*, 6173–6175.

29. Burgess, J. D.; Hawkridge, F. M., Octadecyl Mercaptan Sub-Monolayers on Silver Electrodeposited on Gold Quartz Crystal Microbalance Electrodes. *Langmuir* **1997,** *13*, 3781–3786.

30. Jennings, G. K.; Laibinis, P. E., Self-Assembled *n*-Alkanethiolate Monolayers on Underpotentially Deposited Adlayers of Silver and Copper on Gold. *J. Am. Chem. Soc.* **1997,** *119*, 5208–5214.

31. Chen, I. W. P.; Chen, C.-C.; Lin, S.-Y.; Chen, C.-h., Effect of Underpotentially Deposited Adlayers on Sulfur Bonding Schemes of Organothiols Self-Assembled on Polycrystalline Gold: sp or sp3 Hybridization. *J. Phys. Chem. B* **2004,** *108*, 17497–17504.

32. Aitchison, H.; Lu, H.; Hogan, S. W. L.; Früchtl, H.; Cebula, I.; Zharnikov, M.; Buck, M., Self-Assembled Monolayers of Oligophenylenecarboxylic Acids on Silver Formed at the Liquid–Solid Interface. *Langmuir* **2016,** *32*, 9397–9409.

33. Herrero, E.; Buller, L. J.; Abruña, H. D., Underpotential Deposition at Single Crystal Surfaces of Au, Pt, Ag and Other Materials. *Chem. Rev.* **2001,** *101*, 1897–1930.

34. Marquez, M. D. Modulating Surface Dipoles in Fluorinated Thin Films. University of Houston, 2017.

35. Azhagurajan, M.; Itoh, T.; Itaya, K., Ultra-High-Resolution Differential Interference Microscopy of Ag Deposition on an Ultraflat Au(111). *J. Phys. Chem. C* **2016,** *120*, 16221–16227.

36. Ngo, D.; Baldelli, S., Adsorption of Dimethyldodecylamine Oxide and Its Mixtures with Triton X-100 at the Hydrophilic Silica/Water Interface Studied Using Total Internal Reflection Raman Spectroscopy. *The Journal of Physical Chemistry B* **2016,** *120*, 12346–12357.

37. Zhang, H.; Romero, C.; Baldelli, S., Preparation of Alkanethiol Monolayers on Mild Steel Surfaces Studied with Sum Frequency Generation and Electrochemistry. *J. Phys. Chem. B* **2005,** *109*, 15520–15530.

38. Wang, H.-F.; Gan, W.; Lu, R.; Rao, Y.; Wu, B.-H., Quantitative Spectral and Orientational Analysis in Surface Sum Frequency Generation Vibrational Spectroscopy (SFG-VS). *Int. Rev. Phys. Chem.* **2005,** *24*, 191–256.

39. Hirose, C.; Yamamoto, H.; Akamatsu, N.; Domen, K., Orientation analysis by simulation of vibrational sum frequency generation spectrum: CH stretching bands of the methyl group. *J. Phys. Chem.* **1993,** *97*, 10064–10069.

40. Hirose, C.; Akamatsu, N.; Domen, K., Formulas for the Analysis of Surface Sum-Frequency Generation Spectrum by CH Stretching Modes of Methyl and Methylene Groups. *J. Chem. Phys.* **1992,** *96*, 997–1004.

41. Corcoran, S. G.; Chakarova, G. S.; Sieradzki, K., An in-situ STM investigation of the underpotential deposition of Ag on Au(111) electrodes. *J. Electroanal. Chem.* **1994,** *377*, 85-90.

42. Chen, C. H.; Vesecky, S. M.; Gewirth, A. A., In situ atomic force microscopy of underpotential deposition of silver on gold(111). *J. Am. Chem. Soc.* **1992,** *114*, 451–458.

43. Fonticelli, M. H.; Benítez, G.; Carro, P.; Azzaroni, O.; Salvarezza, R. C.; Gonzalez, S.; Torres, D.; Illas, F., Effect of Ag Adatoms on High-Coverage Alkanethiolate Adsorption on Au(111). *J. Phys. Chem. C* **2008,** *112*, 4557-4563.

44. Oyamatsu, D.; Nishizawa, M.; Kuwabata, S.; Yoneyama, H., Underpotential Deposition of Silver onto Gold Substrates Covered with Self-Assembled Monolayers of Alkanethiols To Induce Intervention of the Silver between the Monolayer and the Gold Substrate. *Langmuir* **1998,** *14*, 3298–3302.

45. Hsieh, M.-H.; Chen, C.-h., Scanning Tunneling Microscopy Observations of Butanethiol Self-Assembled Monolayers on Ag Underpotential Deposition Modified Au(111). *Langmuir* **2000,** *16*, 1729-1733.

46. Bryant, M. A.; Pemberton, J. E., Surface Raman Scattering of Self-Assembled Monolayers Formed from 1-Alkanethiols: Behavior of Films at Gold and Comparison to Films at Silver. *J. Am. Chem. Soc.* **1991,** *113*, 8284–8293.

47. MacPhail, R. A.; Strauss, H. L.; Snyder, R. G.; Elliger, C. A., Carbon-hydrogen stretching modes and the structure of *n*-alkyl chains. 2. Long, all-trans chains. *J. Phys. Chem.* **1984,** *88*, 334–341.

48. Snyder, R. G.; Schachtschneider, J. H., Vibrational analysis of the n-paraffins—I: Assignments of infrared bands in the spectra of C3H8 through n-C19H40. *Spectrochim. Acta* **1963,** *19*, 85-116.

49. Kato, H. S.; Noh, J.; Hara, M.; Kawai, M., An HREELS Study of Alkanethiol Self-Assembled Monolayers on Au(111). *J. Phys. Chem. B* **2002,** *106*, 9655–9658.

50. Snyder, R. G., Vibrational spectra of crystalline n-paraffins: Part I. Methylene rocking and wagging modes. *J. Mol. Spectrosc.* **1960,** *4*, 411-434.

51. Knoll, W.; Philpott, M. R.; Golden, W. G., Surface infrared and surface enhanced Raman vibrational spectra of monolayer assemblies in contact with rough metal surfaces. *J. Chem. Phys.* **1982,** *77*, 219-225.

52. Durig, J. R.; Yu, Z.; Guirgis, G. A., Conformational stability, barriers to internal rotation, vibrational assignment, and ab initio calculations of 2,2-difluorobutane. *J. Mol. Struct.* **1999,** *509*, 115-135.

53. Nuzzo, R. G.; Dubois, L. H.; Allara, D. L., Fundamental Studies of Microscopic Wetting on Organic Surfaces. 1. Formation and Structural Characterization of a Self-Consistent Series of Polyfunctional Organic Monolayers. *J. Am. Chem. Soc.* **1990,** *112*, 558–569.

54. Stengle, T. R.; Taylor, R. C., Raman spectra and vibrational assignments for 1,1,1-trihaloethanes and their deuterium derivatives. *J. Mol. Spectrosc.* **1970,** *34*, 33-46.

55. Bürger, H.; Pawelke, G., Schwingungsspektren und Normalkoordinatenanalyse von $CF_3$-Verbindungen—XX. Infrarot- und Raman-Spektren von $(CF_3)_2CH_2$ und $(CF_3)_2CD_2$. *Spectrochim. Acta, Part A* **1979,** *35*, 517–523.

56. Li, Y. S.; Cox, F. O.; Durig, J. R., Low-Resolution Microwave, Infrared, and Raman Spectra, Conformational Stability, and Vibrational Assignment of 2,2,2-Trifluoroethyl Methyl Ether. *J. Phys. Chem.* **1987,** *91*, 1334–1344.

57. Kuramshina, G. M.; Pentin, Y. A., The Stable Form of 1, 1, 1-Trifluoro-3-chloropropane Molecules in the Crystal II Modification. *J. Chem. Thermodyn.* **1979,** *11*, 1115–1121.

58. Napier, M. E.; Friend, C. M., Effect of Fluorination on Thiol Reactivity: Reaction of 4,4,4-Trifluorobutanethiol on Mo(110). *Langmuir* **1996,** *12*, 1800-1806.

59. Förner, W.; Badawi, H. M., Ab Initio Calculations of Vibrational Frequencies, Potential Functions of Internal Rotations and Vibrational Infrared and Raman Spectra for 3,3,3-Trifluoropropanal. *J. Mol. Model.* **2000,** *6*, 99-111.

60. Forbes, J. G.; Gellman, A. J., The β-Hydride Elimination Mechanism in Adsorbed Alkyl Groups. *J. Am. Chem. Soc.* **1993,** *115*, 6277–6283.

61. Karageorgiev, P.; Petrov, J. G.; Motschmann, H.; Moehwald, H., Why Fluorination of the Polar Heads Reverses the Positive Sign of the Dipole Potential of Langmuir Monolayers: A Vibrational Sum Frequency Spectroscopic Study. *Langmuir* **2013,** *29*, 4726–4736.

62. Iwahashi, T.; Miyamae, T.; Kanai, K.; Seki, K.; Kim, D.; Ouchi, Y., Anion Configuration at the Air/Liquid Interface of Ionic Liquid [bmim]OTf Studied by Sum-Frequency Generation Spectroscopy. *J. Phys. Chem. B* **2008,** *112*, 11936–11941.

63. Dai, Q.; Gellman, A. J., Fluorinated Alcohols on Clean and Preoxidized Silver (110) Surfaces: HREELS and TDS Studies. *J. Phys. Chem.* **1991,** *95*, 9443–9448.

64. Shimoaka, T.; Sonoyama, M.; Amii, H.; Takagi, T.; Kanamori, T.; Hasegawa, T., Study of Perfluoroalkyl Chain-Specific Band Shift in Infrared Spectra on the Chain Length. *J. Phys. Chem. A* **2017,** *121*, 8425–8431.

65. Chidsey, C. E. D.; Loiacono, D. N., Chemical Functionality in Self-Assembled Monolayers: Structural and Electrochemical Properties. *Langmuir* **1990,** *6*, 682–691.

66. Nanaie, H.; Guirgis, G. A.; Durig, J. R., Torsional Spectra of Molecules with Two $C_{3v}$ Rotors—XXV. Rotational and Vibrational Spectra, $r_0$ Structure, Barriers to Internal Rotation and Ab Initio Calculations for 2,2-Difluoropropane. *Spectrochim. Acta, Part A* **1993,** *49*, 2039–2056.

67. Murto, J.; Kivinen, A.; korppi-tommola, J.; Viitala, R.; Hyömäki, J.; Swahn, C.-G., Fluoroalcohols. Part 18. Infrared and Raman Spectra of the Perfluorinated t-Butyl Alcohols $(CF_3)_3COH$ and $(CF_3)_3COD$. *Acta Chem. Scand.* **1973,** *27*, 107–120.

68. McNaughton, D.; Evans, C., High-Resolution FTIR Spectrum of Jet-Cooled $CH_3CHF_2$. *J. Phys. Chem.* **1996,** *100*, 8660–8664.

69. Rabolt, J. F.; Fanconi, B., Raman Scattering from Finite Polytetrafluoroethylene Chains and a Highly Oriented TFE-HFP Copolymer Monofilament. *Macromolecules* **1978,** *11*, 740–745.

70. Rabolt, J. F.; Russell, T. P.; Twieg, R. J., Structural Studies of Semifluorinated *n*-Alkanes. 1. Synthesis and Characterization of $F(CF_2)_n(CH_2)_mH$ in the Solid State. *Macromolecules* **1984,** *17*, 2786–2794.

71. Whelan, C. M.; Smyth, M. R.; Barnes, C. J.; Attard, G. A.; Yang, X., Surface Structural Transitions Induced by Repetitive Underpotential Deposition of Ag on Au (111). *J. Electroanal. Chem.* **1999,** *474*, 138–146.

72. Buffeteau, T.; Desbat, B.; Turlet, J. M., Polarization Modulation FT-IR Spectroscopy of Surfaces and Ultra-thin Films: Experimental Procedure and Quantitative Analysis. *Appl. Spectrosc.* **1991,** *45*, 380–389.

73. Evans, S. D.; Urankar, E.; Ulman, A.; Ferris, N., Self-Assembled Monolayers of Alkanethiols Containing a Polar Aromatic Group: Effects of the Dipole Position on Molecular Packing, Orientation, and Surface Wetting Properties. *J. Am. Chem. Soc.* **1991,** *113*, 4121–4131.

74. Greenler, R. G., Infrared Study of Adsorbed Molecules on Metal Surfaces by Reflection Techniques. *J. Chem. Phys.* **1966,** *44*, 310–315.

75. Tao, Y. T.; Lee, M. T.; Chang, S. C., Effect of Biphenyl and Naphthyl Groups on the Structure of Self-Assembled Monolayers: Packing, Orientation, and Wetting Properties. *J. Am. Chem. Soc.* **1993,** *115*, 9547–9555.

76. Tsao, M. W.; Hoffmann, C. L.; Rabolt, J. F.; Johnson, H. E.; Castner, D. G.; Erdelen, C.; Ringsdorf, H., Studies of Molecular Orientation and Order in Self-

Assembled Semifluorinated *n*-Alkanethiols: Single and Dual Component Mixtures. *Langmuir* **1997,** *13*, 4317–4322.

77. Lenk, T. J.; Hallmark, V. M.; Hoffmann, C. L.; Rabolt, J. F.; Castner, D. G.; Erdelen, C.; Ringsdorf, H., Structural Investigation of Molecular Organization in Self-Assembled Monolayers of a Semifluorinated Amidethiol. *Langmuir* **1994,** *10*, 4610-4617.

78. Tamada, K.; Nagasawa, J.; Nakanishi, F.; Abe, K.; Hara, M.; Knoll, W.; Ishida, T.; Fukushima, H.; Miyashita, S.; Usui, T.; Koini, T.; R. Lee, T., Structure of SAMs Generated from Functionalized Thiols on Gold. *Thin Solid Films* **1998,** *327-329*, 150–155.

79. Colorado, R., Jr. ; Graupe, M.; Shmakova, O. E.; Villazana, R. J.; Lee, T. R., Structural Properties of Self-Assembled Monolayers (SAMs) on Gold Generated from Terminally Fluorinated Alkanethiols. *ACS Symp. Ser.* **2001,** *781*, 276-292.

80. Tyrode, E.; Johnson, C. M.; Rutland, M. W.; Day, J. P. R.; Bain, C. D., A Study of the Adsorption of Ammonium Perfluorononanoate at the Air−Liquid Interface by Vibrational Sum-Frequency Spectroscopy. *J. Phys. Chem. C* **2007,** *111*, 316–329.

81. Kristalyn, C. B.; Watt, S.; Spanninga, S. A.; Barnard, R. A.; Nguyen, K.; Chen, Z., Investigation of Sub-Monolayer, Monolayer, and Multilayer Self-Assembled Semifluorinated Alkylsilane Films. *J. Colloid Interface Sci.* **2011,** *353*, 322–330.

82. Bain, C. D., Sum-Frequency Vibrational Spectroscopy of the Solid/Liquid Interface. *J. Chem. Soc., Faraday Trans.* **1995,** *91*, 1281–1296.

83. Bryant, M. A.; Pemberton, J. E., Surface Raman scattering of self-assembled monolayers formed from 1-alkanethiols at silver [electrodes]. *J. Am. Chem. Soc.* **1991,** *113*, 3629–3637.

84. Thompson, W. R.; Cai, M.; Ho, M.; Pemberton, J. E., Hydrolysis and Condensation of Self-Assembled Monolayers of (3-Mercaptopropyl)trimethoxysilane on Ag and Au Surfaces. *Langmuir* **1997,** *13*, 2291-2302.

85. Sandroff, C. J.; Garoff, S.; Leung, K. P., Surface-Enhanced Raman Study of the Solid/Liquid Interface: Conformational Changes in Adsorbed Molecules. *Chem. Phys. Lett.* **1983,** *96*, 547–551.

86. Pflaum, J.; Bracco, G.; Schreiber, F.; Colorado, R., Jr.; Shmakova, O.; Lee, T.; Scoles, G.; Kahn, A., Structure and Electronic Properties of $CH_3$-and $CF_3$-Terminated Alkanethiol Monolayers on Au (111): a Scanning Tunneling Microscopy, Surface X-Ray and Helium Scattering Study. *Surf. Sci.* **2002,** *498*, 89–104.

87. Jacob, J. D. C.; Lee, T. R.; Baldelli, S., In Situ Vibrational Study of the Reductive Desorption of Alkanethiol Monolayers on Gold by Sum Frequency Generation Spectroscopy. *J. Phys. Chem. C* **2014,** *118*, 29126–29134.

88. Klaeboe, P.; Guirgis, G. A.; Witkowski, W. A.; Horn, A.; Nielsen, C. J., Vibrational Spectroscopic Studies, Conformations and Quantum Chemical Calculations of 3,3,3-Trifluoropropylsilane and 3,3,3-Trifluoropropylsilane-$d_3$. *J. Raman Spectrosc.* **2006,** *37*, 29–51.

89. Guirgis, G. A.; Horn, A.; Klaeboe, P.; Nielsen, C. J., Vibrational Spectroscopic Studies, Conformations and Ab Initio Calculations of 3,3,3-Trifluoropropyltrichlorosilane. *Spectrochim. Acta, Part A* **2005,** *61*, 1335–1346.

90. Gruodis, A.; Aleksa, V.; Powell, D. L.; Klaeboe, P.; Nielsen, C. J.; Guirgis, G. A.; Durig, J. R., Vibrational Spectroscopic Studies, Conformations and Ab Initio Calculations of 1,1,1-Trifluoropropyltrifluorosilane. *J. Raman Spectrosc.* **2003,** *34*, 711–724.

91. Anderson, M. R.; Evaniak, M. N.; Zhang, M., Influence of Solvent on the Interfacial Structure of Self-Assembled Alkanethiol Monolayers. *Langmuir* **1996,** *12*, 2327–2331.

92. Ong, T. H.; Davies, P. B.; Bain, C. D., Sum-Frequency Spectroscopy of Monolayers of Alkoxy-Terminated Alkanethiols in Contact with Liquids. *Langmuir* **1993,** *9*, 1836–1845.

93. Ong, T. H.; Ward, R. N.; Davies, P. B.; Bain, C. D., Microscopic Basis of Wetting: an In Situ Study of the Interaction Between Liquids and an Organic Monolayer. *J. Am. Chem. Soc.* **1992,** *114*, 6243–6245.

94. Ding, F.; Hu, Z.; Zhong, Q.; Manfred, K.; Gattass, R. R.; Brindza, M. R.; Fourkas, J. T.; Walker, R. A.; Weeks, J. D., Interfacial Organization of Acetonitrile: Simulation and Experiment. *The Journal of Physical Chemistry C* **2010,** *114*, 17651–17659.

95. Ward, R. N.; Davies, P. B.; Bain, C. D., Orientation of Surfactants Adsorbed on a Hydrophobic Surface. *J. Phys. Chem.* **1993,** *97*, 7141–7143.

96. Ward, R. N.; Duffy, D. C.; Davies, P. B.; Bain, C. D., Sum-Frequency Spectroscopy of Surfactants Adsorbed at a Flat Hydrophobic Surface. *J. Phys. Chem.* **1994,** *98*, 8536–8542.

97. Bonn, D.; Eggers, J.; Indekeu, J.; Meunier, J.; Rolley, E., Wetting and Spreading. *Rev. Mod. Phys.* **2009,** *81*, 739–805.

# Chapter 6. Conclusions

The dissertation has endeavored to present how sum frequency generation (SFG) spectroscopy can be applied to the study of solid-liquid interfaces between alkanethiol self-assembled monolayers (SAMs) and contacting liquids. Chapters 1 and 2 gave a broad overview of the current scientific progress and fundamental theory for the understanding of this subject. The studies outlined in the ensuing chapters demonstrate the advantages of using sum frequency generation spectroscopy as a tool for the furthering of the fundamental understanding related to chemical interactions at the solid-liquid interface and their role in determining macroscopic surface properties.

Chapter 3 presented the SFG spectroscopy of liquid acetonitrile in contact with monolayers generated from a deuterated hydrocarbon alkanethiol, of the form $CD_3(CD_2)_{17}SH$, and partially fluorinated alkanethiols, of the form $CF_3(CH_2)_{16}SH$, $CF_3(CH_2)_{17}SH$, and $CD_3(CF_2)_6(CH_2)_{10}SH$, self-assembled onto evaporated gold substrates. Varying the functional groups ($CH_3$ versus $CF_3$) and, therefore, the dipole, at the boundary between the SAM and the polar liquid acetonitrile, produced peaks or dips for the resonances in the SFG spectra due to the reorientation of the acetonitrile liquid when exposed to different interfacial environments. Contributions to the SFG signal from the $CaF_2/CH_3CN$ and $CH_3CN$/Au interfaces were shown to not affect the SFG signal from the $CH_3CN$/SAM interface. The construction of a custom cell for solid-liquid spectroscopy minimized infrared absorption by the bulk liquid layer of acetonitrile atop the SAM on gold as shown by using a reference SFG signal collected simultaneously with the sample SFG signal. This study provided in-situ spectroscopic evidence identifying the source of

the interaction between polar contacting liquids, such as acetonitrile, and functionalized surfaces composed of partially fluorinated self-assembled monolayers as a dipole-dipole interaction.

Chapter 4 presented the SFG spectroscopy at the solid-air and solid-liquid interface of partially fluorinated octadecanethiols with the molecular formulas $CH_3CF_2(CH_2)_{16}SH$ (**H1F1H16SH)**, $CH_3CH_2CF_2(CH_2)_{15}SH$ (**H2F1H15SH)**, $CH_3(CH_2)_2CF_2(CH_2)_{14}SH$ (**H3F1H14SH),** and $CH_3(CH_2)_3CF_2(CH_2)_{13}SH$ (**H4F1H13SH**) adsorbed onto gold substrates, in which the difluoromethylene group was progressively buried into the bulk of the monolayer. The effects of the $CF_2$ position on the alkane chain on the structure and wetting properties of the final monolayer were described using ellipsometric thickness measurements as well as X-ray photoelectron, polarization-modulation reflection absorption infrared, and SFG spectroscopies. The thickness results from ellipsometry, elemental analysis results from XPS, molecular chain conformation results from PM-IRRAS, and the interfacial structure results from SFG showed that the **H1F1H16SH** monolayer was the least ordered monolayer at the interface, and therefore, the most wettable by each of the contacting liquids tested with contact angle measurements. The remaining monolayers in the series, generated from **H2F1H15SH**, **H3F1H14SH**, and **H4F1H13SH**, showed decreased wettability (higher contact angles) as the $CF_2$ group was systematically concealed by the terminal hydrocarbon moiety, with the results of the **H4F1H13SH** film nearly matching those of a fully hydrocarbon monolayer.

The SFG methyl tilt angle analysis showed that the methyl groups of all the monolayers were aligned with the surface normal (upright orientation) at the solid-liquid interface, due to the ability of the liquids to intercalate into, and partially solvate, the

terminal functional groups of the alkanethiol films. The hydrocarbon moieties positioned above the bulky $CF_2$ group at the interface were thus shown to reorient more freely at the solid-liquid interface in comparison to the methyl group of a fully hydrocarbon monolayer. The SFG spectroscopy of the solid-liquid interface between monolayers with a progressively buried $CF_2$ moiety showed that the order of the terminal groups and their structure at the interface have a significant effect on the macroscopic wettability behavior of the resulting thin films.

In Chapter 5, the SFG spectroscopy of three series of molecules -- fully hydrocarbon ($CH_3(CH_2)_nSH$, **HnSH**, where n = 16–19), $CF_3$-terminated ($CF_3(CH_2)_nSH$, **F1HnSH**, where n = 16–19), and $CH_3$-terminated partially-fluorinated alkanethiols ($CH_3(CF_2)_6(CH_2)_nSH$, **H1F6HnSH**, where n = 10–13) -- self-assembled onto gold and underpotentially deposited (UPD) silver surfaces was presented. The SFG terminal group orientation analysis at the solid-air interface showed that the adsorption of the thiols onto different metal surfaces caused a change in the "odd-even" effects of the terminal functional group orientation. On the Au surfaces, the terminal groups were shown to be tilted away from the surface normal for the odd chain-length SAMs, and were more upright for the even chain-length SAMs. On the UPD Ag surfaces the trend in tilt angles of the $CH_3$ groups were opposite that of Au -- the $CH_3$ groups were more upright for the odd SAMs and more tilted for the even SAMs.

The solid-liquid interface of the SAMs and acetonitrile as well as perfluorodecalin were probed with SFG spectroscopy to determine the effect of the contacting liquids on the structure of the SAM terminal group. The tilt angle of the terminal groups of the SAMs generated from **HnSH** were shown to become more upright when in contact with both

liquids, attributed to the intercalation of the contacting liquids into the SAMs and the subsequent reorientation of the terminal group. The $CF_3$ group of the **F1HnSH** SAMs was shown to interact strongly with both liquids, with an increased disorder at the terminus of the monolayer. For the **H1F6HnSH** adsorbates, the tilt angles of the terminal $CH_3$ groups were shown to align toward the surface, opposite to the behavior of the **HnSH** SAMs when in contact with acetonitrile. This was due to a strong dipole-dipole interaction between the polar contacting liquids and the partially fluorinated self-assembled monolayers, causing the liquid to penetrate into the film and solvate the terminal methyl groups. Although the advancing contact angles of the SAMs on Au and UPD Ag were shown to have an "odd-even" effect dependent on the chain length of the alkanethiol adsorbate, the SFG results showed no differences in the tilt angles of the methyl groups of the SAMs on Au and UPD Ag substrates. Therefore, the structure of the monolayer at the interface was shown to be a less significant contributing factor to the final wettability of the films.

The studies of the buried solid-liquid interface detailed in this dissertation demonstrate the interactions between contacting liquids and functionalized surfaces and were shown to be a useful stepping stone for future work at this interface. Studies such as these may be used in the future to infer the direction of the terminal dipole of a SAM, its energy of interaction, and eventually the wettability behavior of the resulting thin film in order to specifically tailor the surfaces to any desired application.